
Adaptive rotor concepts for system-friendly offshore wind turbines

Daniel Ribnitzky

Bei der Fakultät für Mathematik und Naturwissenschaften
der Carl von Ossietzky Universität Oldenburg
zur Erlangung des Grades und Titels eines

DOKTORS DER INGENIEURWISSENSCHAFTEN

DR.-ING.

angenommene Dissertation

von Herrn Daniel Ribnitzky
geboren in Herrenberg, Deutschland



Gutachter: Prof. Dr. Martin Kühn

Zweitgutachter: Prof. Dr. Gerard Schepers

Tag der Disputation: 29.10.2025

Abstract

In this thesis, the Hybrid-Lambda Rotor design methodology is introduced, which enables very large rotors for offshore wind turbines in order to increase the energy capture in light winds, but still limiting the loads to foster a lightweight and cost-effective blade design. The methodology features a non-uniform distribution of axial induction along the blade span and a design for two different tip speed ratios (TSRs, λ). This is coupled to the control strategy which consists of two operating modes below rated wind speed. A light-wind mode (high TSR) for maximal aerodynamic efficiency and a strong-wind mode (low TSR) where the load limitation technique is applied. By lowering the TSR and simultaneously pitching to feather, the angle of attack distribution is tilted with a decreasing trend towards the blade tip. Thus, the lever arm of the resulting flapwise bending forces is reduced and the load limitation can be applied with reduced losses, compared to conventional approaches such as solely pitching to feather. A sophisticated aero-servo-elastic simulation model is set up, using an aero-elastic blade optimization routine. The concept is investigated in several design load cases and a techno-economic evaluation is carried out.

Further, the concept is scaled to wind tunnel size, introducing a novel scaling approach which aims to match the non-uniform distribution of axial induction and to reproduce the change in the angle of attack distribution. The experimental investigations reveal that switching between the operating modes works similarly as for the full-scale model. The unique wake characteristics of the Hybrid-Lambda Rotor are investigated experimentally as well as with mid-fidelity simulations, revealing three advantages. First, the thrust coefficient and corresponding wake deficit in the strong-wind mode is significantly reduced which increases the wind farm efficiency over a wide range of wind speeds. Second, the low induction design of the outer part of the blade leads to an outer annulus with increased wind speeds, compared to a wake deficit profile of a conventional turbine. And third, an additional shear layer and vortex system is formed between the outer annulus and the inner wake core which further enhances wake diffusion.

A control methodology is set up for the Hybrid-Lambda Rotor which allows to track two different TSRs below rated wind speed and enables a transition region with constant rotational speed to switch between the two operating modes. Different versions for the pitch controller are formulated which approach the objective of limiting the loads in different ways, including among others a load feedback and a wind speed feed-forward architecture. The control algorithms are implemented on the scaled model turbine and experimentally evaluated under reproducible, turbulent inflow conditions in the wind tunnel. A thorough explanation of the scaling methodology ensures the transferability of the results from the wind tunnel tests to full-scale applications.

Further research could investigate the performance of the Hybrid-Lambda Rotor in large wind farms and clusters. Despite the significantly larger rotor diameter, the reduced wake effects could enable to use the same absolute turbine spacing as for conventional turbines with the same rated power. Or, if the same annual energy production is targeted, a smaller number of Hybrid-Lambda turbines would be required.

Zusammenfassung

In dieser Arbeit wird die Hybrid-Lambda-Rotor Entwurfsmethodik vorgestellt, wodurch sehr große Rotoren für Offshore-Windenergieanlagen ermöglicht werden. Dies erhöht den Energieertrag bei schwachem Wind und begrenzt gleichzeitig die Lasten, um ein kostengünstiges Rotorblattdesign in Leichtbauweise zu ermöglichen. Die Methode zeichnet sich durch eine ungleichmäßige Verteilung der axialen Induktion entlang des Rotorblattes aus und beinhaltet ein Design für zwei verschiedene Schnelllaufzahlen (tip speed ratio, TSR, λ). Dies ist eng mit der Regelungsstrategie verknüpft, welche aus zwei Betriebsmodi unterhalb der Nennwindgeschwindigkeit besteht. Ein Schwachwindmodus (hohes TSR) für maximale aerodynamische Effizienz und ein Starkwindmodus (niedriges TSR), in dem die Lastbegrenzung angewendet wird. Durch das Absenken des TSRs und gleichzeitiges Pitchen der Rotorblätter wird die Anstellwinkelverteilung mit abnehmender Tendenz zur Blattspitze hin gekippt. Dadurch wird der Hebelarm der resultierenden Schubkräfte reduziert und die Lastbegrenzung kann mit geringeren Verlusten angewandt werden als bei konventionellen Ansätzen, wie z.B. durch alleiniges Pitchen der Rotorblätter. Es wird ein detailliertes aero-servo-elastisches Simulationsmodell erstellt, wobei eine aero-elastische Optimierung des Rotorblattes verwendet wird. Das Konzept wird anhand mehrerer Auslegungslastfälle untersucht und eine technisch-wirtschaftliche Bewertung wird durchgeführt.

Darüber hinaus wird das Konzept auf Windkanalgröße skaliert. Hierbei wird ein innovativer Skalierungsansatz eingeführt, der darauf abzielt, die ungleichmäßige Verteilung der axialen Induktion und die Änderung der Anstellwinkelverteilung zu reproduzieren. Die experimentellen Untersuchungen zeigen, dass das Umschalten zwischen den Betriebsmodi in vergleichbarer Weise funktioniert wie beim Modell in Originalgröße.

Die einzigartigen Nachlaufeigenschaften des Hybrid-Lambda-Rotors werden sowohl experimentell als auch mit Mid-Fidelity-Simulationen untersucht, wobei sich drei Vorteile herausstellen. Erstens sind der Schubbeiwert und das resultierende Nachlaufdefizit im Starkwindmodus deutlich reduziert, was die Effizienz im Windpark über einen breiten Bereich von Windgeschwindigkeiten erhöht. Zweitens führt das Design mit

reduzierter Induktion im äußeren Teil des Rotorblattes zu einem äußeren Ring mit höheren Windgeschwindigkeiten, verglichen mit einem Nachlaufprofil einer konventionellen Windenergieanlage. Und drittens bilden sich eine zusätzliche Scherschicht und ein Wirbelsystem zwischen dem äußeren Ring und dem inneren Nachlaufkern, was die Erholung des Nachlaufs verbessert.

Es wird außerdem eine Regelungsmethodik für den Hybrid-Lambda-Rotor entwickelt, die es ermöglicht, zwei verschiedene TSRs unterhalb der Nennwindgeschwindigkeit zu verfolgen und einen Übergangsbereich mit konstanter Drehzahl zu schaffen, um zwischen den beiden Betriebsarten umschalten zu können. Für den Pitch-Regler werden verschiedene Varianten formuliert, wobei das Ziel der Lastbegrenzung auf unterschiedliche Weise implementiert wird, u.a. mittels eines Rückkopplungssignals der Lastmessung und mittels einer Windgeschwindigkeitsmessung stromauf des Rotors als Vorsteuerungssignal. Die Regelalgorithmen werden auf der skalierten Modellwindenergieanlage implementiert und experimentell unter reproduzierbaren, turbulenten Einströmbedingungen im Windkanal evaluiert. Eine gründliche Erläuterung der Skalierungsmethodik gewährleistet die Übertragbarkeit der Ergebnisse von den Windkanaltests auf die Anwendungen im Originalmaßstab.

In weiterer Forschung könnte die Leistung des Hybrid-Lambda-Rotors in großen Windparks und Clustern untersucht werden. Trotz des deutlich größeren Rotordurchmessers könnten die reduzierten Nachlaufeffekte es ermöglichen, denselben absoluten Turbinenabstand wie bei herkömmlichen Turbinen mit derselben Nennleistung zu verwenden. Oder, wenn dieselbe jährliche Energieproduktion angestrebt wird, wäre eine geringere Anzahl von Hybrid-Lambda-Turbinen erforderlich.

Contents

Abstract / Zusammenfassung	iii
List of Figures	xi
List of Tables	xix
List of Abbreviations	xxi
1 Introduction	1
1.1 Motivation	1
1.2 State of the art	2
1.2.1 Specific rating of wind turbines	3
1.2.2 Traditional aerodynamic blade design	4
1.2.3 Conventional wind turbine controllers	5
1.2.4 Conventional scaling approaches in wind energy applications . .	7
1.3 Thesis objectives	9
1.4 Structure of the thesis	10
2 Hybrid-Lambda: a low-specific-rating rotor concept for offshore wind turbines	13
2.1 Introduction	14
2.2 Methodology	17
2.2.1 Aerodynamic concept: the Hybrid-Lambda Rotor	17
2.2.2 Design and simulation methodology	22
2.2.3 Structural design, aeroelastic simulation and optimization meth- odology	23
2.3 Results	26
2.3.1 Aerodynamic blade design	27
2.3.2 Aerodynamics, loads and power in steady-inflow BEM simulations	30
2.3.3 Optimization of the structural blade and tower design	35

2.3.4	Aeroelastic load simulations	38
2.3.5	Techno-economic evaluation	49
2.4	Discussion	52
2.5	Conclusions	56
3	Rotor and wake aerodynamic analysis of the Hybrid-Lambda concept	59
3.1	Introduction	60
3.2	The rotor concept	62
3.3	Methods	62
3.4	Results	64
3.4.1	Comparison of BEM and FVW results	64
3.4.2	Wake investigations using FVW	66
3.4.3	Wake investigations using LES and actuator line model	68
3.5	Discussion	71
3.6	Conclusions	71
4	A scaling methodology for the Hybrid-Lambda Rotor	75
4.1	Introduction	76
4.2	Scaling methodology of the Hybrid-Lambda Rotor	79
4.2.1	Geometric scaling vs. aerodynamic redesign	80
4.2.2	Scaling objectives	80
4.2.3	Adaptation of design TSRs	81
4.2.4	Design and scaling constraints	83
4.2.5	Inputs to the aerodynamic redesign	85
4.2.6	Deriving the control schedule and time scaling factor	86
4.2.7	Verifying the constraints and closing the design loop	88
4.3	Experimental and simulation methodology	89
4.3.1	Experimental set-up	89
4.3.2	Measurement equipment and experimental matrix	91
4.3.3	Measurement data post-processing and uncertainty estimation	93
4.3.4	Simulations	95
4.4	Results	96
4.4.1	Rotor-integrated quantities	96
4.4.2	Radially resolved quantities	99
4.4.3	Dynamic response to gust events	102
4.4.4	Wake characterization	103
4.5	Discussion	108

Contents	ix
4.6 Conclusions	111
5 Experimental investigation of wind turbine controllers for the Hybrid-Lambda Rotor	113
5.1 Introduction	114
5.2 Methodology	116
5.2.1 The Hybrid-Lambda control methodology	117
5.2.2 Scaling considerations	125
5.2.3 Measurement set-up and post-processing	129
5.2.4 Test cases	130
5.2.5 Calculation of pitch actuation and blade fatigue loads	131
5.3 Results	132
5.3.1 Wind steps	132
5.3.2 Gusts	135
5.3.3 Turbulent wind fields	138
5.3.4 Waked inflow	139
5.3.5 Pitch actuation and blade fatigue loads	142
5.4 Discussion	144
5.5 Conclusions	147
5.6 Appendix	149
6 Conclusions and Outlook	153
6.1 Conclusions	153
6.2 Suggestions for further research	158
References	161
List of publications	173
Acknowledgements	179
Curriculum Vitae	181
Erklärung	183

List of Figures

Figure 1.1	Qualitative control schedule of a conventional horizontal axis wind turbine.	6
Figure 1.2	Overview of the thesis structure.	12
Figure 2.1	(a) Desired axial induction along the blade span for the operating modes in light wind (blue) and strong wind (yellow). (b) Schematic overview of the design criteria of the Hybrid-Lambda concept.	18
Figure 2.2	Rotational speed and pitch schedule over wind speed; crosses indicate operational points shown in Figs. 2.6 and 2.8 with corresponding colours.	20
Figure 2.3	Design and optimization workflow of the Hybrid-Lambda concept. Definitions: round bullet points, free design variables; square bullet points, constraints; diamonds, outputs; $f(\dots)$, as a function of (\dots) ; LW, light wind; SW, strong wind.	21
Figure 2.4	Chord distribution over radius.	28
Figure 2.5	Twist over non-dimensional radius.	28
Figure 2.6	Axial induction: light-wind mode (blue), transition (red), strong-wind mode (yellow), peak shaving (dashed, purple), rated power (dash-dotted, green) and design value 0.21 (dash-dotted, black).	30
Figure 2.7	Inflow angle distribution for a varying TSR (assuming constant $a = 1/3$ over the blade length).	32
Figure 2.8	Angle of attack (BEM): light-wind mode (blue), transition to strong-wind mode (red) and strong-wind mode (yellow).	33
Figure 2.9	Power output of the Hybrid-Lambda Rotor (solid red) compared to the reference turbine (blue) and a scaled reference turbine (dashed green and dotted black).	34
Figure 2.10	Thrust coefficient of the Hybrid-Lambda Rotor (RBM limited) compared to the reference turbine.	35

Figure 2.11 Comparison of structural parameters between initial (dashed lines) and optimized (solid lines) blade design: relative thickness distribution (a) , spar cap thickness distribution (b) , strains in the spar caps (SS, suction side; PS, pressure side) (c) and blade mass relative to the cubic scaling law of the IEA 15 MW blade mass (d)	36
Figure 2.12 Mass and stiffness distribution for the optimized Hybrid-Lambda blade (red) and the IEA 15 MW blade (blue).	38
Figure 2.13 Campbell diagram for optimized blade and tower design. Safety margins of 10 % for 1P and 3P excitations are shown in grey.	38
Figure 2.14 Transition of operating modes in a wind field with the normal turbulence model and a mean wind speed of 7.5 ms^{-1} ; background colours indicate the desired operating modes: green, light wind; red, strong wind; yellow, transitioning between the operating modes.	42
Figure 2.15 Ultimate loads in solid bars for the Hybrid-Lambda Rotor and in hatched bars for the IEA 15 MW reference turbine; only critical loads are displayed. Abbreviations: EWSH, extreme wind shear horizontal; EWSV, extreme wind shear vertical; f-a BM, fore–aft bending moment; s-s BM, side–side bending moment.	44
Figure 2.16 Extreme vertical wind shear profiles according to IEC 61400-1 (2019) for the Hybrid-Lambda Rotor and the IEA 15 MW reference turbine.	47
Figure 2.17 Out-of-plane forces per unit length under extreme vertical wind shear (EWSV 2): for the Hybrid-Lambda Rotor (a) and for the IEA reference turbine (b) . Resulting lever arms are indicated with vertical black lines.	48
Figure 2.18 Weibull distributions for three reference sites.	49
Figure 2.19 Gross energy yield, wind speed distribution (FINO1 cluster-wake affected) and market value of wind power.	50
Figure 2.20 Reduction in the cost of valued energy and the LCoE relative to the reference turbine for the cluster-wake-affected wind speed distribution.	52
Figure 2.21 Estimation of turbine component costs for the IEA 15 MW (blue) and the optimized Hybrid-Lambda turbine (red).	52
Figure 3.1 Axial induction distribution (left) and angle of attack distribution (right) for operating point 1 (solid lines) and operating point 2 (dashed lines), comparing BEM (blue) and FVW (red)	65
Figure 3.2 Averaged axial velocity component for steady uniform inflow	

	(FVW). Top: Hybrid-Lambda Rotor; bottom: IEA 15-MW turbine; left: Operating point 1 (6.8 ms^{-1}); and right: Operating point 3 (10.2 ms^{-1}).	67
Figure 3.3	Normalized wake deficit profiles (FVW, steady uniform) for operating point 1 (left) and 3 (right). Dashed lines indicate 70% rotor radius. Red: Hybrid-Lambda Rotor; and blue: IEA 15-MW turbine.	67
Figure 3.4	Left: Averaged axial velocity component for numeric turbulent wind field (FVW), light-wind mode (top: Hybrid-Lambda Rotor; bottom: IEA 15-MW turbine); right: Normalized wake deficit profiles	68
Figure 3.5	Neutral stratification: Normalized wake deficit profiles from LES (light-wind mode)	69
Figure 3.6	Stable stratification: Normalized wake deficit profiles from LES (light-wind mode)	69
Figure 3.7	Stable stratification: Averaged axial velocity component for LES (light-wind mode); top: Hybrid-Lambda Rotor; and bottom: IEA 15-MW turbine with coordinates normalized with the diameter of the IEA 15-MW rotor for both plots	70
Figure 4.1	Change in the inflow angle distribution for operational transition of TSRs, with the full-scale rotor represented with the dashed line.	83
Figure 4.2	Scaling and design workflow for the Hybrid-Lambda Rotor. AoA – angle of attack; α_d – design angle of attack; β – twist angle; β_{pitch} – pitch angle; c – chord length; c_p , c_T , and c_{RBM} – power, thrust, and flapwise root bending moment coefficients; $f(\dots)$ – as a function of (...); FS – full scale; LE – leading edge; LW – light wind; λ – tip speed ratio; r – local radius; Re – Reynolds number; SW – strong wind; TE – trailing edge; $u_{\text{cut-in}}$, u_{ts} , u_{te} , and u_{rated} – wind speeds at cut-in, start of transition, end of transition, and rated power.	84
Figure 4.3	Chord (a) and twist distribution (b) for the scaled Hybrid-Lambda Rotor and the scaled NREL 5 MW turbine.	85
Figure 4.4	Control schedule for the Hybrid-Lambda model turbine (HL MT), derived from BEM simulations.	87
Figure 4.5	Axial induction (a) for the light-wind mode (at u_{ts}) and the strong-wind mode (at u_{te}) for the Hybrid-Lambda model turbine (MT), the full-scale (FS) rotor, and the conventional model turbine in BEM simulations and respective angle of attack distributions (b)	88
Figure 4.6	Reynolds number for three different operating modes, derived from BEM simulations.	89

- Figure 4.7 Experimental set-up, side **(a)** and top view **(b)**, indicating the measurement positions of the hot wires, LDA, and Prandtl tube. The coordinate system is located in the rotor centre. MoWiTO 1.8 with the Hybrid-Lambda blades **(c)**, $D = 1.8$ m, hub height of 1.5 m. 90
- Figure 4.8 Power coefficient **(a)**, thrust coefficient **(b)**, and non-dimensional flapwise RBM **(c)** from measurements and BEM simulations for various TSRs and pitch angles β_{pitch} , at a constant rotor speed of 500 rpm. 98
- Figure 4.9 Axial induction along the blade span **(a)** and angle of attack **(b)** from measurements and BEM simulations for the light-wind (LW) and strong-wind (SW) modes. 99
- Figure 4.10 Averaged radial velocity component **(a)** and envelope of the radial velocity component **(b)** in the rotor plane from FVW simulations for the two model turbines. 101
- Figure 4.11 Streamlines from FVW simulations for the Hybrid-Lambda model turbine in the LW mode and the conventional model turbine (same c_T). The rotor is indicated with the vertical black bar, and the low-induction tips are displayed in bright red. 101
- Figure 4.12 Gust in the wind tunnel: inflow hot-wire measurements in the rotor plane and scaled IEC gust, displayed 8 times slower than ideal scaling; gust amplitude is not scaled **(a)**. Flapwise RBM response of the Hybrid-Lambda Rotor and the conventional rotor. The shaded area indicates the 95% confidence interval of the 45 repetitions of the gust event **(b)**. 102
- Figure 4.13 Mean normalized wind speed **(a–d)** and turbulence intensity **(e–h)** from hot-wire measurements in the wake of the model turbines. From top to bottom: conventional rotor **(a, e)** and Hybrid-Lambda Rotor in the LW mode **(b, f)**, in the SW mode **(c, g)**, and at rated wind speed **(d, h)**. Nacelle and blades are displayed in black, and the outer 30% of the Hybrid-Lambda blades are displayed in red. The black arrows point at the second shear layer starting at the blade design blending region. . . . 104
- Figure 4.14 Wake profiles at a distance of $0.4D$ downstream for the two model rotors. At $T_i = 2\%$ for different operating modes **(a)** and in the light-wind mode for different T_i values **(b)**. 105
- Figure 4.15 Normalized wind speed **(a)** in the light-wind (left) and strong-wind modes (right). Vorticity magnitude **(b)** in the light-wind (left) and strong-wind modes (right) for the Hybrid-Lambda model turbine (top) and the conventional model turbine (bottom) from FVW simulations. . . 107

- Figure 5.1 Steady-state operating points for the Hybrid-Lambda model turbine, derived from steady-state measurement data. Background colours indicate the operating mode: green, light-wind mode (LW); yellow, transition (TS); red, strong-wind mode (SW). u_{ts} and u_{te} : wind speed at start and end of transition. 118
- Figure 5.2 **(a)** Rotational speed and generator torque as a function of wind speed, derived from BEM simulations. **(b)** Saturations and set points for the torque controller. Shaded areas indicate the permissible generator torque for a given rotational speed. 120
- Figure 5.3 Baseline pitch controller. Torque controller indicated in simplified form. Rounded rectangles: input/output of (measured) variables. Rectangles: processes. Parallelograms: data input. 122
- Figure 5.4 Load feedback (LFB) pitch controller. Torque controller indicated in simplified form. 123
- Figure 5.5 Feed-forward (FF) pitch controller. Torque controller indicated in simplified form. 124
- Figure 5.6 Wind speed measurement processing for the FF pitch controller. . 124
- Figure 5.7 Exemplary wind speed measurement processing for the FF pitch controller for a gust event. **(a)** Raw and filtered data, **(b)** final propagation and **(c)** final signal with removed propagation for visualization purpose. The final output signal detects up-ramps early but delays down-ramps. 125
- Figure 5.8 **(a)** Experimental set-up, side-view. **(b)** MoWiTO 1.8 with the Hybrid-Lambda blades, diameter of 1.8 m, hub height of 1.5 m. 129
- Figure 5.9 Turbine response with the baseline, LFB and FF controllers to the test case with wind steps: time series **(a)** and statistical analysis of RBM **(b)** and power **(c)**. Background colours indicate the operating mode: green, light-wind mode (LW); yellow, transition (TS); red, strong-wind mode (SW). Middle markers, median; boxes, 25th and 75th percentiles; whiskers, minimum and maximum of the considered data. The baseline controller works well in following the TSR of 6 in the SW mode, but the loads are higher than expected due to model uncertainties. The LFB controller uses higher pitch angles and is able to correctly constrain the loads. However, this leads to reduced aerodynamic torque and consequently lower rotational speed and lower TSRs in the SW mode. Furthermore, the power output of the LFB controller is lower in the SW mode compared to the baseline controller. 134

- Figure 5.10 Turbine response to gust events. Solid lines show the ensemble average over 50 gust repetitions. The shaded areas indicate the 95% confidence intervals. Wind speed measurements are performed 2.7 m upstream of the rotor and are not propagated in this plot. The LFB and FFLFB controllers can limit the loads in steady state perfectly to the load constraint. During the gust, the baseline and LFB controllers react too slowly and show the highest load overshoots. The FF and FFLFB controllers react in advance and reduce the load overshoot. The FF controller further reduces the variations in rotational speed and torque. 135
- Figure 5.11 Power spectral density of **(a)** the pitch signal and **(b)** the wind speed excitation for the gust test case in the wind tunnel and for aero-servo-elastic simulations with extreme operating gust for the 15 MW full-scale (FS) Hybrid-Lambda turbine. The model turbine (MT) controllers are about 10 times slower than ideally scaled ($n_t = 1/114$). This corresponds to the gust duration which is 8 times slower than ideally scaled. 137
- Figure 5.12 Turbine response to turbulent inflow. Background colours indicate the desired operating modes: green, light-wind (LW); red, strong-wind (SW); yellow, transitioning between the operating modes. All controllers are able to follow the LW-TSR of 7.5, and the torque controller can maintain the rotational speed constant in the transition region. In the SW mode, the LFB controller uses higher pitch angles, effectively constraining the loads but resulting in TSRs that are lower than the set point of 6. 139
- Figure 5.13 Top: wind speed derived from hot-wire measurements on the centre line (propagated) and derived from the wind speed estimator. Bottom: radial distance of the wake centre to the rotor centre. Only for very large wake centre displacements did the single-point hot-wire measurements converge towards the rotor effective wind speed, which is predicted by the wind speed estimator. 140
- Figure 5.14 Turbine response to waked inflow. **(a)** 200 s and **(b)** 60 s excerpt of the full test case. Background colours indicate the desired operating modes: green, light-wind; yellow, transitioning between the operating modes. The FF controller leads to the highest load overshoots for very large wake centre displacements. The baseline controller estimates the rotor-averaged wind speed much better and shows lower loads than the

FF controller. The LFB and FFLFB controllers perform best in limiting the loads.	141
Figure 5.15 DEL and pitch actuator duty cycle for the three inflow cases: gust, turbulent wind field and waked inflow. For the gust test case, the FF controller leads to around 3 times higher pitch actuation but reduces the fatigue loads. Also for the turbulent wind field test case, the FF controller shows the highest pitch actuation, although the actuation is lower than for the gust test case. The fatigue loads for the waked test case are strongly increased for all controllers due to the non-uniformity of the inflow.	143

List of Tables

Table 1.1	Generic scaling laws for wind turbines. The ratio is defined as the quantity for the scaled model turbine divided by the quantity for the full-scale turbine.	8
Table 2.1	Set of ultimate design load cases investigated in aeroelastic simulations.	26
Table 2.2	General parameter of the Hybrid-Lambda Rotor and the reference turbine.	27
Table 2.3	Weibull factors (A,k), AEP and annual economic revenue expressed as ratio to the reference turbine (ref.) for three reference sites	51
Table 3.1	Comparing the power ratio of downstream and upstream turbines in LES (operating mode 1)	71
Table 4.1	General parameter of the wind tunnel model and the full-scale Hybrid-Lambda Rotor.	87
Table 4.2	Investigated operating modes for the Hybrid-Lambda wind tunnel model.	92
Table 5.1	Scaling of controller parameters for the Hybrid-Lambda Rotor. . .	126
Table 5.2	Advantages (+) and disadvantages (–) of all tested controller versions for all test cases.	148
Table 5.3	Scaling parameters for the Hybrid-Lambda Rotor, relevant for the scaling of the aerodynamic torque.	152
Table 5.4	Data necessary for the calculation of the time constants in Eq. (5.9).	152

List of Symbols and Abbreviations

Symbol	Definition
A	Weibull scale parameter
a	Axial induction factor
a'	Tangential induction factor
α	Angle of attack
α_d	Design angle of attack
$\alpha_{\max,L/D}$	Angle of attack for maximum lift-to-drag ratio
α_{stall}	Stall angle of attack
B	Number of blades
β	Twist angle
β_{pitch}	Pitch angle
$\beta_{\text{pitch},i-1}$	Pitch angle from the last iteration
$\dot{\beta}_{\text{pitch}}$	Pitch rate
$\dot{\beta}_{\text{pitch},\max}$	Maximum pitch rate
C_l	Lift coefficient
$C_{l,d}$	Design lift coefficient
c	Chord length
c_p	Power coefficient
c_q	Torque coefficient
c_{RBM}	Flapwise blade root bending moment coefficient
c_T	Thrust coefficient
D	Rotor diameter
D_f	Diameter full-scale model

Δu	Wind speed difference
$\Delta\beta$	Pitch increment
η	Dynamic viscosity
f (as subscript)	Full-scale
$f(\dots)$	As a function of (...)
f_c	Cut-off frequency in the dynamic wake meandering model
γ	Geometrical angle between the chord of the local blade segment and the rotor plane, consisting of twist and pitch
I	Rotational inertia
k	Weibull shape parameter; constant in torque control law
L	Lever arm
l_b	Blade length
λ	Tip speed ratio
$\lambda_{d,LW}$	Design tip speed ratio for light-wind mode
$\lambda_{d,SW}$	Design tip speed ratio for strong-wind mode
$\lambda_{d,inner}$	Design tip speed ratio for inner blade section
$\lambda_{d,outer}$	Design tip speed ratio for outer blade section
M_a	Aerodynamic rotor torque
M_g	Generator torque
M_{LSS}	Low-speed shaft torque
M_l	Torque due to friction losses
M_y	Flapwise blade root bending moment
m (as subscript)	Model
N_{crit}	Critical amplification factor
n	Scaling ratio
n_l	Geometric length scaling factor
n_t	Time scaling factor
n_{tower}	Geometric scaling factor for the tower height
ω	Rotational speed
$\omega_{shift}, \omega_{trans}$	Rotational speed in transition region

P_{rated}	Rated power
ϕ	Inflow angle
R	Rotor radius
Re	Reynolds number
r	Local radius
ρ	Density
s	Wind shear
$\sigma()$	Standard deviation
T	Time constant
T_i	Turbulence intensity
t	Time
u, v	Wind speed
u_{∞}, u_1	Undisturbed inflow wind speed
u_2	Wind speed in the rotor plane
u_{ax}	Axial velocity
$u_{\text{cut-in}}$	Cut-in wind speed
u_{rated}	Rated wind speed
u_{rel}	Relative velocity
u_{te}	Wind speed at end of transition region
u_{ts}	Wind speed at start of transition region
$v_{\text{shift,end}}$	Wind speed at end of transition region
$v_{\text{shift,start}}$	Wind speed at start of transition region

Abbreviation**Definition**

ABL	Atmospheric boundary layer
ADC	Actuator duty cycle
AEP	Annual energy production
AoA	Angle of attack
BEM	Blade element momentum
BeRT	Berlin research turbine

CoVE	Cost of valued energy
DEL	Damage equivalent load
DLCs	Design load cases
DTU	Technical University of Denmark
EWSH	Extreme vertical wind shear
FF	Feed-forward
FFLFB	Combined feed-forward and load feedback controller
FS	Full-scale
FVW	Free vortex wake
HL	Hybrid-Lambda
IEA	International energy agency
LCoE	Levelized cost of energy
LDA	Laser-Doppler-Anemometer
LES	Large-eddy simulation
LFB	Load feedback
LUT	Look-up table
LW	Light-wind
MT	Model turbine
MoWiTO 1.8	Model wind turbine Oldenburg
NTM	Normal turbulence model
PI	Proportional-Integral
PS	Pressure side
RBM	Flapwise blade root bending moment
SS	Suction side
SW	Strong-wind
TS	Transition region
TSR	Tip speed ratio
WISDEM	Wind-plant Integrated System Design and Engineering Model

Chapter 1

Introduction

1.1 Motivation

Wind energy is widely seen as one of the main pillars of the energy transition towards an energy supply free of greenhouse gas emissions and nuclear waste (Wiser et al., 2011; Lee et al., 2023). A fast, large-scale exploitation of wind energy is needed to master this transition and to limit climate change to the absolutely unavoidable minimum. But, with the rising share of wind power in the energy system, the market value of wind power decreases during periods of strong winds and can be close to zero on windy days, as predicted by May et al. (2015). However, there is still a large value during light wind periods. López Prol et al. (2020) named this effect self-cannibalization of wind energy. The higher the share of wind energy in the overall energy mix, the steeper is the descending slope of the relation of market value versus wind speed. A second challenge arises with the limited available space for offshore wind farms. The close spacing leads to large cluster wakes, diminishing the available wind resource and reducing the efficiency of many wind farms, especially in light winds (Dörenkämper et al., 2023; Schneemann et al., 2020).

These problems emphasize that there is a need for a change of mindset when designing wind turbines for a reliable and profitable energy supply. Future wind turbine design should focus more on improving the value for the entire energy system by generating more power in light winds, and by providing a more evenly distributed energy generation over a wide range of wind speeds. This can be accomplished by increasing the rotor diameter in relation to the rated power, i.e. reducing the specific rating (rated power divided by rotor swept area), as stated among others by Hirth and Müller (2016), Johnson et al. (2021) and Wiser et al. (2021). Such large rotors can only be

technically and economically feasible if the extreme loads are reduced by advanced control strategies, fostering a lightweight and cost-effective blade design. Load limiting control strategies always come along with losses in efficiency on a single turbine level, and the aim is to keep them as small as possible. On the other hand, load limiting strategies can also reduce the wake effects, and improvements on a wind farm level can be expected.

It is essential to include these objectives already in the blade design. This can be seen as a compromise finding. Either maximize the power generation in low wind speeds, where the load constraint is not active. Or accept a reduction in maximal efficiency, but therefore improve the performance in operation within the load constraint region. Especially at offshore sites with a higher annual average wind speed, it is crucial to limit the losses due to load limiting strategies, since a large portion of the energy yield would be achieved in wind speed regimes with reduced aerodynamic efficiency. Thus, there is a need for novel blade design and control methodologies that enable large offshore rotors with low-specific ratings. To address these challenges, the Hybrid-Lambda Rotor concept and the accompanying control methods are developed in this thesis. They are extensively examined using simulations on different fidelity levels and wind tunnel experiments. The concept features a non-uniform distribution of axial induction along the blade span and a design for two different tip speed ratios (TSR, ratio of peripheral tip speed to inflow wind speed). This is coupled to the control strategy, as the rotor is operated at the high TSR in light-wind mode for maximum aerodynamic efficiency and at the low TSR in strong-wind mode where the load limitation technique is applied with reduced losses in efficiency compared to conventional approaches.

1.2 State of the art

This section provides a general overview of the topic. First, the trend of the specific rating of recently installed wind turbines is reported. This is followed by an overview of traditional blade design approaches and conventional wind turbine control strategies. Since this thesis also comprises a new scaling methodology for the novel rotor design to wind tunnel size, we introduce conventional scaling approaches for wind energy applications. A more comprehensive literature review can be found in the individual Chapters 2 to 5.

1.2.1 Specific rating of wind turbines

The specific rating of a wind turbine is defined as the ratio of rated power to rotor swept area. A clear trend of reduced specific rating for newly installed turbines has been reported by several authors. For the installation of offshore wind turbines in Germany, Lüers (2024) reports a reduction in specific rating from 470 W m^{-2} in 2009 to 390 W m^{-2} in 2024. For onshore turbines in the U.S., Bolinger et al. (2021) states a reduction of average specific power from 330 W m^{-2} in 2009 to 235 W m^{-2} in 2018. The mean specific power of all installed turbines in Europe has decreased from 380 W m^{-2} in 2008 to 310 W m^{-2} in 2016, as reported by Hand et al. (2018).

The higher annual average wind speed and the increased design loads at offshore sites traditionally favour higher specific ratings if a low levelized cost of energy (LCoE) is the design driver. The LCoE is the estimated cost per kWh of produced electricity over the lifetime of a wind turbine based on the ratio of the annualized total costs of the system and the expected annual energy production (Simpson et al., 2020). For the period of 1995 to 2020, Borrmann et al. (2018) report a modest decrease in the specific rating from 450 to 350 W m^{-2} for European offshore wind farms, but the study also shows a significant variance in the specific rating.

The optimal sizing, i.e. rated power and rotor diameter, of offshore wind turbines is highly dependent on the project conditions, such as the wind resource, farm parameters, grid and area constraints, and it further depends on the choice of objective function. Optimizing for a traditional metric of LCoE, Mehta et al. (2024a) found the optimum turbine size of 16 MW and 236 m (366 W m^{-2}) which is close to a current state of the art industry turbine. He further found that a constraint only on the available farm area pushes the optimum towards higher specific ratings. In contrast, a constraint only on the rated power of the wind farm pushes the optimum towards lower specific power designs, because the wake losses in the partial load range are reduced. However, LCoE cannot capture the value of wind energy and the dependency of market price vs. wind speed and time of production. Optimizing for cost of valued energy (CoVE), Mehta et al. (2024b) found the optimum at lower specific ratings. But, the outcome is highly dependent on the market scenario and the estimated dependency of price vs. wind speed. Other objective functions are used in design studies that optimize turbine sizing for the profitability in the day-ahead market (Mehta et al., 2024b) and for hydrogen production (Mehta et al., 2022). Canet et al. (2023) introduced further design metrics

which characterize the environmental impact and societal value of a wind turbine. They conclude that lower specific ratings can increase the economic and environmental value with only mild increases in the levelized cost of energy.

1.2.2 Traditional aerodynamic blade design

Nowadays, the design of wind turbine blades is highly interdisciplinary and is usually approached with systems engineering optimization routines that couple the effects of aerodynamics, structural design, control theory and economic aspects. This introduction describes only the analytical formulations for aerodynamic blade design as historically derived by Betz, 1926 and Schmitz, 1955/56.

The task of defining the aerodynamic design of a rotor blade for a wind turbine generally consists of choosing the number of blades, the rotor diameter, the aerodynamic profiles, the design TSR, and the angle of attack or the lift coefficient. With these parameters, a blade can be designed relatively straightforward and the chord and twist distribution along the blade span can be calculated with the help of the Betz or the Schmitz/Glauert approach (Schmitz, 1955/56). Betz (1926) analysed a wind turbine heavily idealized as a disk that extracts the power from the wind by decelerating the flow without any losses. He concluded, that the maximal power can be achieved if the flow in the rotor plane is retarded to 2/3 of the inflow velocity, which leads to an optimal induction factor a of 1/3. The latter is defined with

$$u_2 = u_1(1 - a) \quad (1.1)$$

where u_1 is the undisturbed inflow wind speed and u_2 is the wind speed in the rotor plane. This means that if the rotor blade is designed with a constant axial induction factor of 1/3 the maximum physically possible share of 16/27 of the energy in the stream tube with the given diameter can be extracted, neglecting all losses. Schmitz (1955/56) extended this approach by including losses due to the rotation of the wake. This approach is historically correct and has been (and still is) widely used in wind energy for the preliminary design (Burton et al., 2011). However, it does not include the rotor diameter as a free design variable, nor does it consider technically feasible load constraints or economic aspects. Chaviaropoulos and Sieros (2014) analysed how the power extraction can be maximized, if the rotor diameter and the axial induction factor are free design variables, but the turbine loads are constrained to a load level of a reference turbine with classical Betz design. He concluded, that 8.7% more power can

be extracted if the rotor diameter is enlarged by a factor of 1.136 and the axial induction factor is reduced to 0.187. Jamieson (2020) took this idea one step further and derived an optimal distribution of axial induction factor along the blade span, which led to a greater power gain with a modest increase in rotor diameter, compared to the solution with a constant axial induction factor.

Another important design parameter is the tip speed ratio (TSR, λ) which describes the ratio of peripheral tip speed to inflow wind speed:

$$\lambda = \frac{\omega R}{u} \quad (1.2)$$

The TSR consequently defines the velocity triangles along the blade span. Turbines with a high TSR have fewer and more slender blades compared to turbines with a low TSR. For high TSR turbines, the maximum power coefficient is strongly influenced by the profile drag. Hence, airfoils with a high lift to drag ratio should be used (Gasch and Twele, 2012).

1.2.3 Conventional wind turbine controllers

Since the Hybrid-Lambda Rotor design methodology is closely coupled to an adaptation of the control strategy, we first introduce the conventional control theory for horizontal axis wind turbines, as described among others by Abbas et al. (2022) and Gasch and Twele (2012). In general, five operating regions are distinguished depending on the wind speed, as depicted in Fig. 1.1. The numbering of the regions varies in the literature. In Region zero, the wind speed is below the cut-in wind speed, the turbine is at standstill (or idling) and no power is produced. In Region 1, the wind speed is sufficient to start the operation of the turbine but the rotor does not operate in the aerodynamic optimum because the rotor speed is constrained by the minimum generator speed. This means the TSR is higher than the optimum and the pitch angle is set in order to obtain the best efficiency for the given TSR. In Region 2, the turbine operates in partial load, the torque controller is used to track the optimal TSR (i.e. the rotor speed increases linearly with the wind speed) and the pitch angle is set to a constant value that leads to the optimal aerodynamic efficiency (usually called fine pitch). In this region, the power rises with the cube of the wind speed. The rotor thrust and the flapwise blade root bending moment (RBM) increase with the square of the wind speed. In region 3, the wind turbine operates above rated wind speed. The pitch controller is used to maintain a constant rotational speed. Generator torque and power are constant at their rated

values. The loads decrease above rated wind speed, because the blades are pitched towards feather. Above the cut-out wind speed, in region 4, the turbine is shut down because further operation is too risky. In addition to the torque and pitch control, the yaw angle of the turbine is controlled in order to align the rotor perpendicular to the wind direction, which is not covered in this thesis. The Hybrid-Lambda control strategy deviates from this theory in regions 2 and 3 as explained in Sect. 2.2.1.

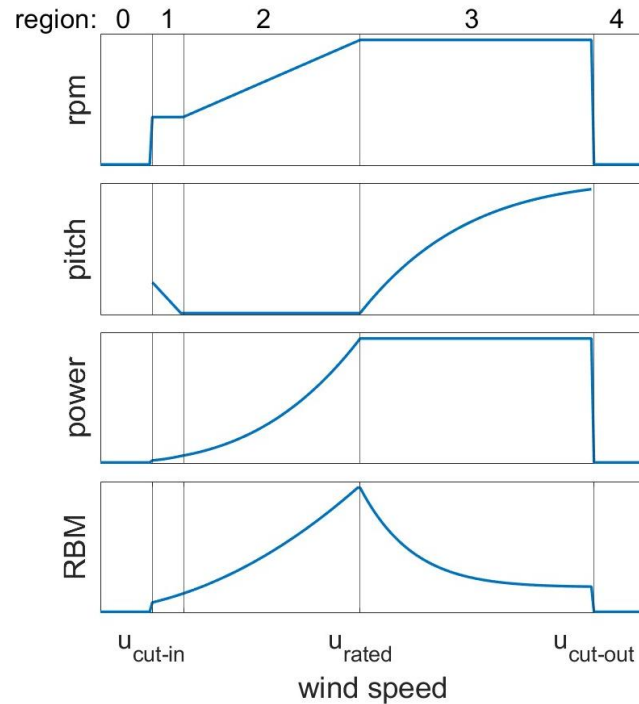


Figure 1.1: Qualitative control schedule of a conventional horizontal axis wind turbine.

In the modern design of onshore wind turbines, the rotational speed is often kept constant before rated power is reached because the maximum rotational speed is constrained by noise limitations. This results in a region 2.1 (approx. 2 to 4 ms^{-1} below rated wind speed) in which the turbine operates at a TSR below the optimum, and consequently the power coefficient is reduced. Such an approach can be viable for onshore turbines because the average wind speed lies in region 2 (before the rotational speed constraint), where the turbine operates at the optimum power coefficient. These turbines usually feature a high design TSR, leading to a very slender blade design. This results in relatively light blades and can be economically attractive, as material usage and costs can be reduced. However, the increased blade flexibility needs to be carefully considered, and thicker airfoils may ultimately be required to ensure structural integrity. For offshore turbines, the annual average wind speed is much higher and would

coincide with the region of reduced efficiency. Consequently, a better compromise is required for offshore designs, which is addressed by the Hybrid-Lambda blade design and control methodology.

1.2.4 Conventional scaling approaches in wind energy applications

In this thesis, the topic of scaling is applied in Chapter 2, where the rotor diameter is increased in order to capture more energy in light winds and in Chapter 4, where the rotor concept is transferred to wind tunnel size. In both applications, we introduce innovative and unconventional scaling approaches. Thus, we first explain the elementary methodology for scaling wind turbines, as described by Canet et al. (2021), Bottasso and Campagnolo (2021) and Gasch and Twele (2012).

Applying the theory of similarity, two rotors with different diameters will have the same characteristics (i.e. non-dimensional performance curves such as power-, thrust- and torque-coefficients) if the following rules are applied:

- the tip speed ratio is maintained
- the airfoil profiles along the blade are maintained
- the number of blades is maintained
- the same materials are used
- all three dimensions in space are scaled proportionally
- the change in Reynolds-number is small and the associated changes in aerodynamic behaviour can be neglected.

This ensures the same velocity triangles along the blade span and since the same airfoil profiles are used the lift and drag coefficients are preserved. In other words, the aerodynamic behaviour is equivalent and the non-dimensional performance curves are reproduced. Furthermore, Wang et al. (2021) show that the wake of appropriately scaled turbines are very similar.

We introduce scaling ratios n which are defined by dividing the quantity of the scaled model turbine (subscript m) by the quantity of the full-scale turbine (subscript f).

For example, the geometric length scaling factor n_l is defined by the ratio of the rotor diameters D .

$$n_l = \frac{D_m}{D_f} \quad (1.3)$$

For many wind tunnel experiments, the time is also scaled which basically defines the rotational speed of the wind tunnel model (Canet et al., 2021):

$$n_t = \frac{t_m}{t_f} = \frac{\omega_f}{\omega_m} \quad (1.4)$$

Based on these elementary scaling ratios, all matched and unmatched quantities can be fully characterised. An overview of generic scaling laws is provided in Table 1.1. In many applications, the time scaling n_t is set equal to the length scaling n_l or it is chosen in the same order of magnitude. In this case, the wind speeds remain unchanged and the scaling laws can be simplified accordingly.

Table 1.1: Generic scaling laws for wind turbines. The ratio is defined as the quantity for the scaled model turbine divided by the quantity for the full-scale turbine.

Quantity	Ratio
Length	n_l
Time (simplified)	n_t
TSR	1
Rotor speed	$1/n_t$
Natural frequencies	$1/n_t$
Wind speed	n_l/n_t
Power	n_l^5/n_t^3
Torque	n_l^5/n_t^2
Thrust	n_l^4/n_t^2
Flapwise blade root bending moment	n_l^5/n_t^2
Edgewise blade root bending moment (only gravity driven component considered)	n_l^4
Weight	n_l^3
Aerodynamic forces	n_l^4/n_t^2
Centrifugal forces	n_l^4/n_t^2
Reynolds number	n_l^2/n_t

The Reynolds number is an important non-dimensional key figure that describes the ratio of inertial forces to viscous forces in a fluid and is defined as:

$$\text{Re} = \frac{c \cdot u_{\text{rel}} \cdot \rho}{\eta} \quad (1.5)$$

Here, c is the airfoil chord length, u_{rel} is the relative velocity over the airfoil, ρ is the air density and η is the dynamic viscosity. ρ and η are usually approximately constant when the rotors are tested in air in the wind tunnel or in the field. The aerodynamic properties of airfoils, such as lift and drag behaviour for varying angles of attack, are strongly dependent on the Reynolds number. This important quantity scales with n_1^2/n_t and thus can usually not be held constant, because setting the time scaling factor to $n_t = n_1^2$ would increase the required wind speeds and rotational speeds to unfeasible values for wind tunnel applications. The Reynolds number mismatch is the largest drawback when scaling down to wind tunnel size, because the aerodynamic properties, such as stall angles, are changed and the aerodynamic efficiency is reduced.

For upscaling to larger diameters, the biggest challenge is the cubic increase of weight which leads to a linear increase of the bending stress in the blade root due to gravitational forces. In fact, it can be shown that the bending stresses due to aerodynamic and centrifugal forces remain constant for ideal scaling scenarios (Gasch and Twele, 2012). Thus, weight is the limiting factor for the turbine size and innovative, lightweight concepts are required for very large rotors. This simplified introduction to the science of wind turbine scaling does not cover the complex topic of aero-elasticity and transient responses. Again, the interested reader is referred to the three above mentioned articles.

1.3 Thesis objectives

The overall objective of this thesis is to develop methodologies for the rotor and controller design which enable very low-specific ratings for offshore wind turbines in order to capture more energy in light winds, thus increasing the value of wind energy. More specifically, the objectives are:

1. Introduction of a design methodology for very large rotors with blades that are aerodynamically optimized for the application of peak shaving.
2. Development of a method on how to scale the Hybrid-Lambda Rotor concept to wind tunnel size and the experimental characterization and validation of the

- aerodynamic design concept on wind tunnel scale.
3. Investigation of the influence of the steep gradients of axial induction along the blade span on the aerodynamics and the characterization of the wake of the Hybrid-Lambda Rotor:
 - (a) With mid-fidelity simulations and
 - (b) Experimentally in the wind tunnel.
 4. Development of control methodologies for very large turbines with a load constraint that fulfil the Hybrid-Lambda control strategy, their application on the wind tunnel model and the experimental validation with respect to extreme loads, short-term fatigue, pitch actuation and power output.

1.4 Structure of the thesis

The first objective is addressed in Chapter 2, which is published by Ribnitzky et al. (2024a). Here, the Hybrid-Lambda Rotor design methodology is introduced and the connection to the control strategy for load constraints is outlined. A substantial increase in the rotor diameter while maintaining rated power would be beneficial for the energy system and insights on how this could be realized are provided. By designing the blade for two TSRs and reducing the operational TSR for strong winds when the loads need to be constrained, the efficiency losses due to the load limiting techniques are reduced. The combination of TSR reduction and pitch angle increase leads to a beneficial redistribution of the angle of attack. The aerodynamic forces are shifted with an increase for the inner part of the blade, but a decrease for the outer part of the blade, i.e. moving the lever arm closer to the blade root. Further, an aero-structural optimization of the blade design is carried out and the concept is investigated on a systems engineering level by means of aero-servo-elastic simulations. The chapter concludes with a techno-economic evaluation with emphasis not only on conventional cost metrics, but also on the value for the energy system.

The aforementioned investigations are based on the blade-element momentum theory (BEM) which has the inherent assumption that all blade elements are independent of each other. In the Hybrid-Lambda concept, the distribution of axial induction along the blade span features a steep gradient and this assumption is violated. Therefore, free vortex wake (FVW) and Large-Eddy Simulations (LES) are used in Chapter 3 to

investigate the severity of this violation. Further, the wake of the Hybrid-Lambda Rotor is characterized. This chapter addresses the objective 3a and it is published by Ribnitzky et al. (2023).

In Chapter 4, which is published by Ribnitzky et al. (2025), the next step in the concept validation is provided. A methodology for scaling the Hybrid-Lambda Rotor to wind tunnel size is introduced, addressing the second objective. Further, the steep gradients of axial induction distribution along the blade span are experimentally investigated with Laser-Doppler-Anemometer measurements and the near wake of the Hybrid-Lambda Rotor is characterized with hot-wire measurements (objective 3b). The rotor concept is validated under reproducible turbulent inflow conditions produced with an active grid in the wind tunnel. This includes gust events and wake characterizations under various turbulence intensities in the inflow.

The tremendous increase in rotor diameter can only be feasible if an innovative blade design is accompanied by advanced control strategies that master the trade off between limiting extreme loads and maximizing the power output. Such control methodologies are developed in Chapter 5, addressing the fourth objective. Those methods are applied on the model turbine, facing the challenges that come along with the evaluation of control methods on a hardware set-up, such as the scaling of the controller characteristics and inflow test cases and the presence of model uncertainties. This chapter provides a solution on how the transition between the operating modes can be accomplished. Further, the torque and pitch controllers are active simultaneously over a wide range of wind speed, which is not the case for conventional wind turbine controllers and the associated challenges are discussed. The control methods are experimentally validated under turbulent reproducible inflow conditions in the wind tunnel. This chapter was submitted to the Wind Energy Science Journal on 30.07.2025.

Chapter 6 summarizes the main findings and conclusions of Chapters 2 to 5 and provides suggestions for future research.

Chapter 2

Hybrid-Lambda: a low-specific-rating rotor concept for offshore wind turbines

Apart from minor adjustments and corrections, the content of this chapter is identical to that of the following publication:

Ribnitzky, D., Berger, F., Petrović, V., and Kühn, M.: Hybrid-Lambda: a low-specific-rating rotor concept for offshore wind turbines, *Wind Energ. Sci.*, 9, 359–383, <https://doi.org/10.5194/wes-9-359-2024>, 2024.

Reproduced in accordance to the Creative Commons Attribution 4.0 License.

Abstract

We introduce an aerodynamic rotor concept for an offshore wind turbine which is tailored for an increased power feed-in at low wind speeds by a substantial increase in the rotor diameter while maintaining the rated power. The main objective of the conceptual design is to limit the steady-inflow loads (blade flapwise root bending moment (RBM) and thrust) to the maximum values of a reference turbine. The outer part of the blade (i.e. outer 30% span) is designed for a higher design tip speed ratio (TSR) and a lower axial induction than the inner part. By operating at the high TSR in light winds, the slender outer part fully contributes to the increased power capture. In stronger winds the TSR is reduced and the torque generation is shifted to the inner section of the rotor. Moreover, the blade design efficiently reduces the power losses when the flapwise RBM is limited through peak shaving, below rated

wind speed. This is of high importance, given the wind speed distribution at offshore sites. The characteristics of the rotor are first investigated with stationary blade element momentum simulations and further analysed with aeroelastic simulations, considering the flexibility of blades and tower to show that a structural design is feasible even for a blade of this size and complexity. The economic revenue and the cost of valued energy of the turbine are estimated and compared to the IEA 15 MW offshore reference turbine, considering a fictitious wind-speed-dependent feed-in price. Our results for the turbine concept with an increase in rotor diameter by 36 % show that the revenue can be increased by 30 % and the cost of valued energy can be reduced by 16 % compared to the reference turbine.

2.1 Introduction

In the last few decades, wind turbines have been designed extremely successfully to reduce the levelized cost of energy (LCoE) of wind power. With the rise in the proportion of wind power in the energy system, the market value of wind power decreases during periods of strong winds and the exchange price for wind power can be close to zero on windy days, as expected by May et al. (2015). López Prol et al. (2020) named this effect the self-cannibalization of wind power and emphasized that there is a need for a change in mindset in wind turbine design. Future wind turbine design should focus more on improving the value of wind power in the entire energy supply system. This should favour more steady power feed-in, higher capacity factors, reduced power forecast errors and a better utilization of the transmission system.

In the past few years, a clear trend has been observed in reducing the specific rating (i.e. the ratio of rated power to rotor swept area) for newly installed turbines, especially onshore as reported by Hand et al. (2018) and Bolinger et al. (2021). Typically, such modern three-bladed onshore turbines operate with a high design tip speed ratio (TSR) of up to 10 and a high power coefficient in the lower partial-load range, extending from the cut-in wind speed to approximately 7.5 to 9 ms^{-1} . The high aerodynamic efficiency matches perfectly with the dominant range of the wind speed distribution at light- to medium-wind sites. Due to the high TSR, such turbines reach the rated rotor speed at the aforementioned wind speed, which is well below the rated wind speed. Consequently, the power coefficient c_p and thrust coefficient c_T decrease significantly before rated power is reached (at approx. 10 to 11 ms^{-1}), which results in considerable power losses, as described in Gasch and Twele (2012). However, the high design

TSR results in slender blades and the reduced c_T values facilitate load-reduced and cost-efficient blade designs. Consequently, the swept rotor area can be significantly increased compared to traditional designs. All in all, such an onshore design philosophy has resulted in significant gains in annual energy production (AEP) and higher capacity factors, which has dramatically lowered the LCoE in recent years.

Several investigations (e.g. Hirth and Müller, 2016; Johnson et al., 2021; Wisser et al., 2021) state that turbines with larger swept rotor areas in relation to rated power are beneficial for the energy system. Thus, an increased and more steady power feed-in at low wind speeds would be desirable. In contrast, the power feed-in at strong wind speeds could be partially reduced, as sufficient power will be available from the increasing number of conventional wind energy converters. Recent studies address wind turbine concepts with very low specific ratings for onshore sites. The *Low-Wind turbine*, developed at the Technical University of Denmark (DTU) by Madsen et al. (2020), with a specific rating of 100 W m^{-2} , has a uniquely low cut-out wind speed of 13 m s^{-1} . The physical challenge of resisting increased loads is at least partially avoided, as the concept does not operate at high wind speeds. Swisher et al. (2022) discuss the economic competitiveness of such an onshore turbine. Further innovative concepts for very large rotors are discussed by Johnson et al. (2019) within the *big adaptive rotor* project. Increasing the power output in light winds but decreasing the loads in strong winds contradicts basic physical principles. A large swept rotor area would be needed in light winds, while the rotor area should be reduced to limit the loads in stronger winds. Concepts that mechanically adjust the rotor area have a long history but have never reached the level of technical feasibility on a large scale. Jamieson et al. (2005) approached this problem with telescopic blades. Among others, Agarwala and Ro (2015) introduced a separated pitch system for the blade tip and Feil et al. (2020) investigated trailing-edge flaps. Noyes et al. (2020) and Qin et al. (2020) designed and discussed downwind morphing rotors. These ideas all have in common the fact that additional actuators increase the mass and costs of the blade and introduce a complex dynamic blade response. Consequently, there is a need to approach this design problem with pure aerodynamic and control design tools without any additional mechanical actuators. Lowering the axial induction and sacrificing a high power coefficient to favour larger rotor diameters comprise a frequently discussed approach. Jamieson (2020) took the idea of the low-induction rotor developed by Chaviaropoulos and Sieros (2014) one step further and derived an optimal axial induction distribution over the blade span, which allows for greater power gain with a modest increase in rotor

diameter compared to a constant low induction factor of $1/5$. Designing a blade with variable design conditions along the blade span has sometimes been proposed. Wobben (2001) issued a patent for a blade with a step in the radial distribution of the design TSR. This concept follows the objective of reducing unintended stall effects on the blade of a variable-speed turbine in gusty winds. It was not used to enable large rotors with low specific ratings, as pointed out with the *Hybrid-Lambda* concept.

We want to take the idea of low-specific-power wind turbines one step further to offshore applications. But the transfer of the current onshore design approach to offshore sites would be inherently uneconomic. With the usage of large blades comes the need for peak shaving (e.g. pitching to feather below rated power) to limit the flapwise root bending moment (RBM). Many blade designs are optimized for one single operational point, usually zero pitch at the design TSR. Thus, peak shaving comes with great losses in the power coefficient. These losses significantly reduce the AEP as they occur close to rated wind speed, where most offshore sites see a probability of very high wind speed in the Weibull distribution. The higher annual average wind speed and the increased design loads at offshore sites traditionally favour higher specific ratings if a low LCoE is the design driver. For the period of 1995 to 2020, Borrmann et al. (2018) report a modest decrease in the specific rating from 450 to 350 W m^{-2} for European offshore wind farms, but the study also shows a significant variance in the specific rating. It is unclear whether future offshore projects will request a further reduction in specific ratings in favour of the energy system or prefer medium specific ratings and increased rated power to optimize the LCoE on the wind farm level.

We postulate that more system-friendly offshore turbines with dramatically lower specific ratings are required for the large-scale exploitation of offshore wind energy and the decarbonization of the electricity sector in the 2030s and 2040s. Therefore, we introduce an innovative concept with an increased power feed-in during light winds, which still allows for further turbine operation at higher wind speeds by finding a good compromise between load reduction and aerodynamic efficiency.

The objective of this paper is the introduction of an innovative aerodynamic rotor concept for offshore wind turbines, which allows, in combination with advanced turbine control strategies, the above-mentioned modifications in the power curve characteristics. As a reference turbine, we use the IEA 15 MW offshore wind turbine, designed by Gaertner et al. (2020). The main objectives of the conceptual design

are twofold. Firstly, the steady-inflow loads (blade flapwise RBM and thrust) are limited to the maximum values of the reference turbine while greatly increasing the swept rotor area to capture more energy in light-wind conditions. Secondly, instead of aerodynamically optimizing the blades for the operation below rated wind speed and below the maximum allowable loads, a blade design should already take the application of peak shaving into consideration. The design process should be seen as a compromise finding between power maximization below the limiting loads and minimization of losses when peak shaving is applied. We want to introduce a design methodology for blades that are aerodynamically optimized for peak shaving. The aim is to address challenges in the design process concerning aerodynamics, structural design and control strategies. We want to pinpoint the advantages of the conceptual design in transient load cases as well as design driving dynamic loads, and we address the economic competitiveness of the resulting turbine concept.

This paper is based on the design methodology and steady-state aero-static investigations of the general concept introduced by Ribnitzky et al. (2022). The current publication includes a more comprehensive development of the concept, an aero-servo-elastic optimization for the blade and tower design, a dynamic analysis of the turbine including controller design, a reduced set of design load cases, an investigation of transient extreme wind shear events, and a techno-economic evaluation.

2.2 Methodology

This section first describes the aerodynamic concept. The second subsection explains the methodology that is used to design the rotor and to simulate the aerodynamics and loads.

2.2.1 Aerodynamic concept: the Hybrid-Lambda Rotor

The main idea of the concept is to dramatically increase the rotor swept area. This is accompanied by designing the outer part of the blade (e.g. outer 30 % of the rotor) for a higher TSR (compared to the inner part) and reducing the design axial induction factor in the outer region, resulting in a much more slender outer section. The design methodology can be applied to any given wind turbine rotor by adjusting the main design variables, namely the specific rating, the TSRs for the inner and outer part of the blade, the spanwise position of the transition between the two design regions, and

the desired axial induction factors for the two blade regions (see Sect. 2.3.1). In this study, we applied the methodology to a 15 MW offshore wind turbine to simplify the understanding of the concept and to discuss a use case. The IEA 15 MW reference turbine serves as a basis for the design.

The rotor is designed to operate in a light-wind and a strong-wind mode. Figure 2.1 visualizes the desired axial induction in the two operating modes and provides an overview of the characteristic key points for the two parts of the rotor.

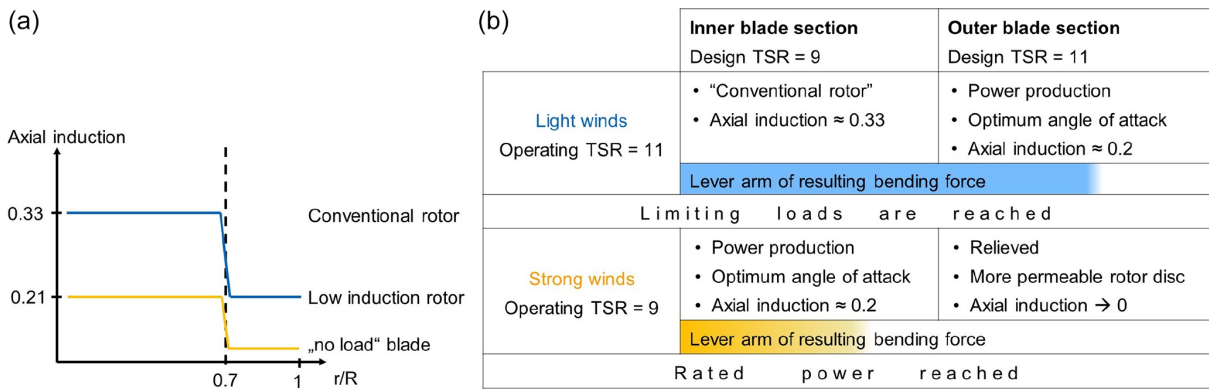


Figure 2.1: (a) Desired axial induction along the blade span for the operating modes in light wind (blue) and strong wind (yellow). (b) Schematic overview of the design criteria of the Hybrid-Lambda concept.

In light-wind conditions, the rotor operates at the high TSR of 11 and the slender outer part fully contributes to the increased power capture. The outer part is now operating at its design point, defined as the high TSR, an axial induction factor of 0.21 and the optimal angle of attack (the latter is here derived from the optimal lift-to-drag ratio). The outer part can thus be interpreted as a low-induction rotor extension. The inner part of the rotor operates like a conventional rotor with an axial induction factor close to 0.33. This is chosen in order to maximize the power output in light winds. But the reader should bear in mind that this part is not operating at its design point, as it is designed for a lower TSR of 9.

In stronger winds (but still below rated wind speed), the design value of the stationary RBM is reached. Then the TSR is reduced to a value of 9 and the torque generation is shifted to the inner section of the rotor, which is now operating at its design point, defined as the low TSR, an axial induction factor of 0.21 and the optimal angle of attack (AoA). In contrast, the outer region is significantly relieved,

as it is now operating at very low angles of attack. Ideally, the outer part of the rotor would now operate at an axial induction of zero, which means it is no longer contributing to the power production and would not produce any thrust loads. Of course, this is not feasible, but it should serve as an objective. In this way, the outer part of the rotor disc becomes more permeable and the lever arm of the resulting bending force is reduced. As the rotor is designed for and operated at two different TSRs, we refer to the concept in the following as the Hybrid-Lambda Rotor.

The transition between the operating modes introduces a new control region, since the switching of the TSR is not a sudden change but rather a continuous reduction in TSR. In this paper, it is realized with a constant rotational speed (in revolutions per minute, rpm) in region 2.2 as shown in Fig. 2.2. The reduction in TSR alone (with a constant rpm) is not enough to limit the loads. On the contrary, it is part of the design methodology to combine a reduction in TSR and pitching to feather for load limitation as further analysed in Sect. 2.3.1. Consequently, the so-called strong-wind mode cannot be described with a constant pitch angle. With increasing wind speed the pitch angle is gradually increased towards feather to limit the flapwise RBM. This action will be referred to as peak shaving in the following. Note that the transition of TSRs could also be realized in different ways (e.g. a sudden reduction or gentle increase in rpm). In fact, the optimal combination of TSR and pitch for the transition region can be found by constraining the flapwise RBM and searching for the optimum in the matrix of power coefficients for all relevant TSR and pitch values. These optimization routines resulted in a gently increasing rpm throughout region 2.2 and 2.3. However, for all wind speed bins, the increase in the power output was never larger than 0.5% of rated power compared to the constant rpm solution presented here. Consequently, the aforementioned alternative for the transition region is not presented in this paper.

Furthermore, we design the blade in a way that peak shaving is applied more efficiently. The inner section is designed with a twist offset towards stall. This comes with several advantages. The inner section does not operate in the design point in the low-wind regime. As it is twisted towards stall and operated at a higher TSR than it was designed for, a fairly conventional induction factor of 0.33 can be reached, which leads to an increase in the power coefficient in the low-wind regime. The angle for the twist offset is derived iteratively in stationary blade element momentum (BEM) simulations to reach the desired axial induction factor of 0.33 in the inner section at the high TSR. Using the twist instead of the chord length as a tool for this increase

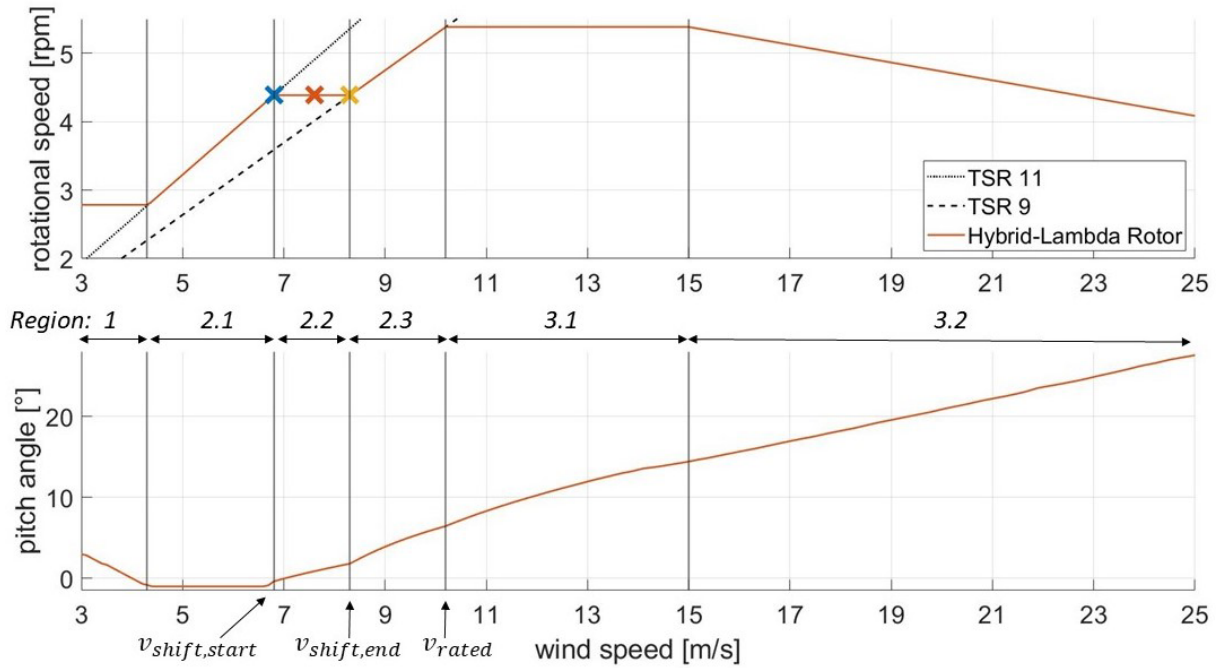


Figure 2.2: Rotational speed and pitch schedule over wind speed; crosses indicate operational points shown in Figs. 2.6 and 2.8 with corresponding colours.

in the axial induction factor allows us to use smaller chord lengths, which leads to more slender, lighter and possibly cheaper blades. Hence, the twist offset defines the difference in the axial induction factor between the light- and strong-wind mode for the inner part of the blade and it further influences the pitch angle at $v_{shift,end}$ that is needed to limit the loads. In fact, the pitch angle of 2.2° at $v_{shift,end}$ almost perfectly counterbalances the twist offset of -2.5° . Hence, the inner part of the blade operates in its optimal lift-to-drag ratio at this wind speed, although the entire blade is already pitched to feather for load reduction. When peak shaving is applied, pitching shifts the inner section to operate at its aerodynamic optimum rather than moving away from it. It reaches its design point (an induction factor of 0.21 at the low TSR), which is beneficial for load reduction. In contrast, the outer section is now operated in a “pitched-to-feather condition” and is greatly relieved. The limits to this methodology are negative lift and the stall angle. The latter is also plotted in Fig. 2.8.

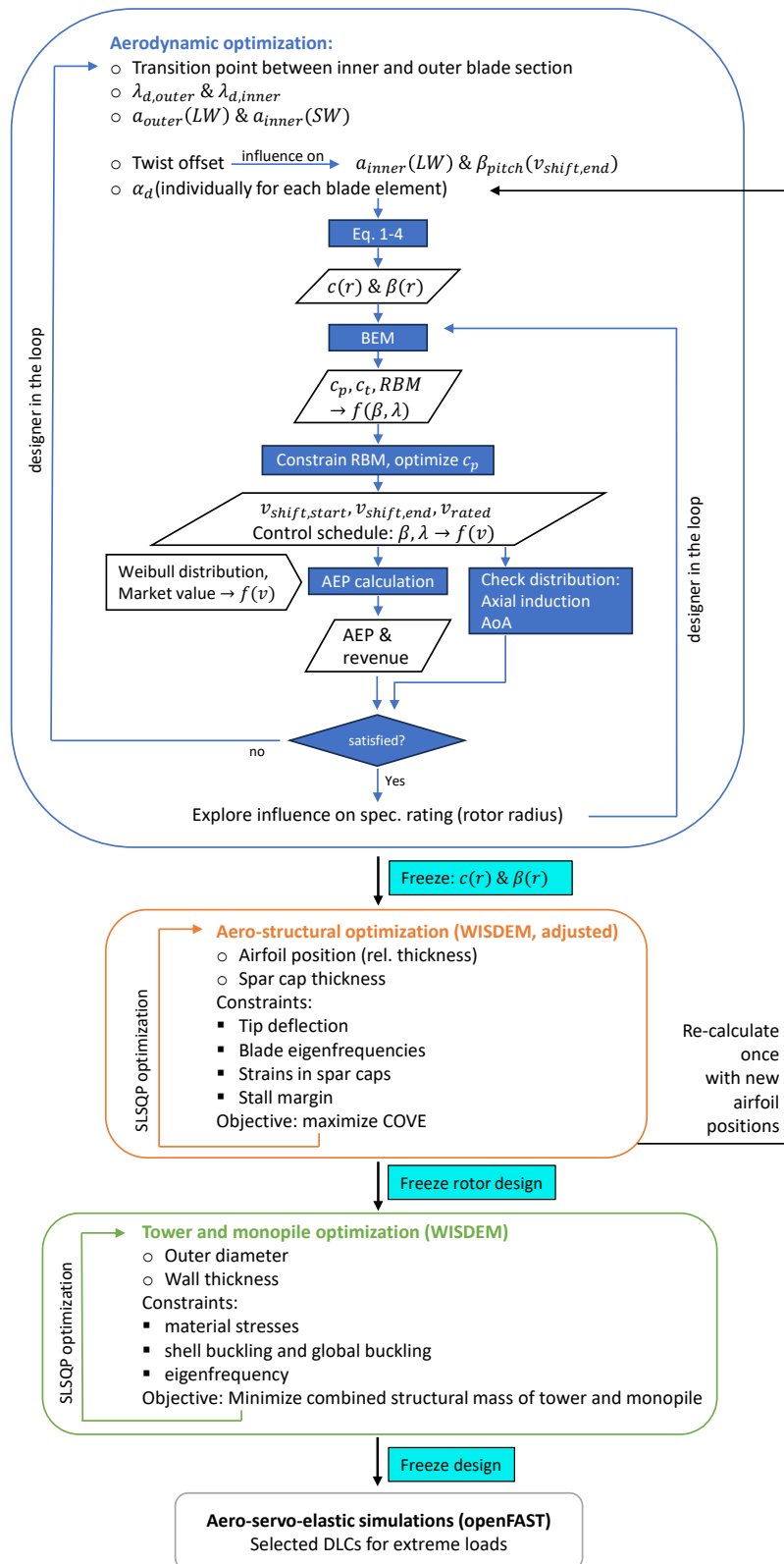


Figure 2.3: Design and optimization workflow of the Hybrid-Lambda concept. Definitions: round bullet points, free design variables; square bullet points, constraints; diamonds, outputs; $f(\dots)$, as a function of (...); LW, light wind; SW, strong wind.

The overall design and optimization workflow is illustrated in Fig. 2.3. The process can be explained in four steps: an aerodynamic blade optimization, an aero-structural optimization of the blade, a structural optimization of the tower and the aero-servo-elastic simulations. In the first step (aerodynamic optimization), the design variables are the transition point between the inner and outer blade section, the design TSRs, the design axial induction factors, the twist offset, and the design angle of attacks. Once a reasonable design is established, the influence of the rotor radius is investigated. In the second step (the aero-structural optimization), the design variables are the airfoil positions and the spar cap thickness. Once the aero-structural optimization is converged, the aerodynamic optimization is re-calculated once with the new airfoil positions. As a third step, the tower and monopile are optimized for a fixed rotor design. The resulting turbine design is then investigated in aero-servo-elastic simulations.

2.2.2 Design and simulation methodology

In the first step in the blade design, we calculated the chord and twist distribution along the blade span. As the Hybrid-Lambda Rotor is compared with the IEA 15 MW reference turbine, the same airfoil family is used and the airfoil distribution along the blade span is adopted in a first step. The airfoil position is later optimized as described in Sect. 2.2.3. With the target design TSR (λ_d), the design axial induction factor (a) and the design AoA (α_d), the corresponding chord (c) and twist distribution (β) for the two blade sections are calculated, following a procedure described by Burton et al. (2011). We chose the design AoA and the corresponding lift coefficient (C_l) as the angle with the highest lift-to-drag ratio individually for each blade station. This results in a slightly discontinuous chord and twist distribution. Therefore, smoothing with a moving average window is applied. First, the tangential induction factor (a') from Eq. (2.1) is calculated. The distribution of the inflow angle (ϕ) can be calculated as written in Eq. (2.2) and the twist distribution results according to Eq. (2.3). Finally, the chord distribution (c) is calculated with Eq. (2.4).

$$a' = \frac{a(1-a)}{\lambda_d^2 \left(\frac{r}{R}\right)^2} \quad (2.1)$$

$$\tan \phi = \frac{1-a}{\lambda_d \left(\frac{r}{R}\right) (1+a')} \quad (2.2)$$

$$\beta = \phi - \alpha_d \quad (2.3)$$

$$c = \frac{8\pi R \lambda_d \left(\frac{r}{R}\right)^2 a'}{BC_1 \sqrt{(1-a)^2 + \left(\lambda_d \left(\frac{r}{R}\right) (1+a')\right)^2}} \quad (2.4)$$

Here, R is the radius of the turbine, r is the mean radius of the local blade element and B is the number of blades.

In the second step, the twist offset towards stall is applied to the inner section and smoothing of the chord and twist distribution is applied where necessary. In the root section, the non-dimensional chord c/R is adopted from the reference turbine (which will be necessary to carry the increased torsional and edgewise bending moments) and the maximum twist is limited to 15° . The design process continues with iterations on the axial induction distribution and the twist offset to meet the requirements regarding the angle of attack and axial induction distribution in both operating modes.

To iterate the design process, we investigate the derived design concepts as rigid structures with steady-state BEM simulations (as described by Hansen, 2008), including Prandtl tip-loss and root-loss corrections as well as the Glauert high-thrust correction with the approximation by Buhl (2005). The full set of relevant TSRs and pitch angles is computed, and in a second step, the control schedule is defined, e.g. assigning the specific TSR and pitch angle over the operational range of wind speeds. We iteratively optimize the blade design on the basis of the BEM simulations. After the design criteria are satisfied, we continue investigating the rotor concept with aeroelastic simulations, as described in the next section.

2.2.3 Structural design, aeroelastic simulation and optimization methodology

To further investigate the feasibility of the Hybrid-Lambda Rotor, we develop a structural model for the blade. The workflow described in this section is carried out after freezing the design output variables' rotor radius and the chord and twist distribution. A link back to the aerodynamic optimization was only performed for a few major design versions, as indicated in Fig. 2.3. An initial layup, which is close to a scaled layup of the IEA 15 MW reference turbine, is designed in NuMAD (Berg and Resor, 2012), consisting of a blade shell, two spar caps, two shear webs, and leading-edge and trailing-edge reinforcements. Blade cross-section properties are calculated with PreComp (Bir, 2005). In the next step, the blade is optimized with the Wind-Plant Integrated System Design and Engineering Model (WISDEM; Dykes

et al., 2021). This open-source tool allows for rapid design space exploration, including the calculation of characteristic curves, steady-state load calculations, material stress assessments and optimization routines. The source code of WISDEM is adjusted to implement the control strategies of the Hybrid-Lambda Rotor, as described in the following. For each design iteration, the wind speed $v_{\text{shift,start}}$ at which the transition from the light-wind to the strong-wind mode should start is calculated first. This is done by finding the operational point at the maximum power coefficient for the given turbine design (at $\text{TSR} = 11$ and fine pitch $= -0.8^\circ$) when the limiting flapwise RBM is first reached. For higher wind speeds, the rotational speed schedule is adjusted in order to execute the transition to the low TSR. Further, a peak-shaving algorithm ensures the limitation of the flapwise RBM. In a steady-state load calculation, the strains in the spar caps are calculated according to Hansen (2008) and the maximum tip deflection is derived. Free design variables are the radial positions of the airfoils for the inner blade section (airfoils for the outer blade section are locked) and the spar cap thickness on the suction and pressure side. Constraints for the optimization process are tip deflection, blade eigenfrequencies (must be above the rated blade passing frequency, 3P), the strains in the spar caps and a stall margin. The latter would only be active if the change in the airfoil position leads to an operating angle of attack larger than the stall angle of the respective airfoil (chord and twist are not optimized in this structural design step). The objective function of the optimization process is the cost of valued energy. For each iteration the schedule of rpm, pitch, power, thrust and flapwise RBM over wind speed is re-calculated. The load case considered for the constraints is a steady inflow at the strongest wind speed in the light-wind mode $v_{\text{shift,start}}$, as calculated for each design iteration (in this case $v = 6.9 \text{ m s}^{-1}$, $\text{TSR} = 11$, $\beta_{\text{pitch}} = -0.8^\circ$). This is the operational point just before the limitation of the flapwise RBM starts by lowering the TSR and pitching, and it is found to be the most critical regarding steady-inflow tip deflection and RBM (compared to other steady-inflow wind speeds). To account for higher loads that will certainly occur under dynamic-inflow load cases, the constraints for tip deflection and strains are set relatively strictly. This way, the optimization routine can run computationally efficiently and more complex load cases are verified afterwards.

The tower of the turbine is optimized with WISDEM, too. As the main focus of this paper is the aerodynamic rotor concept, we only present a preliminary tower design and the simple choice of a monopile foundation was made, although the authors are well aware that in reality, such a large turbine will most likely be mounted on a jacket substructure. Design variables for the optimization are the tower and

monopile diameter and the material thickness. Constraints are the material stresses, shell buckling, and global buckling and the first structural natural frequency should be between 1P and 3P excitation (with a 10 % safety margin) within the operational range of the rotor speed. The objective function of the optimization routine is the combined structural mass of tower and monopile. For the optimization, a constant loading is applied at the tower top. This loading is derived with an initial aeroelastic simulation with an extreme turbulence model and a mean wind speed of 9 ms^{-1} . Safety factors are chosen according to IEC 61400-1 (2019), but the partial safety factor for loads was increased from 1.35 to $1.35 \cdot 1.2 = 1.62$ to account for the simplified load analysis for this preliminary optimization study.

The cost model implemented in WISDEM based on the work from Fingersh et al. (2006) was used to create a breakdown of the costs of major wind turbine components. The model includes a rather detailed estimation of the blade costs, as described by Bortolotti et al. (2019), including assumptions for materials, labour, tooling and many more aspects. On the contrary, the costs for parts like the pitch system and the hub are implemented as simple functions of the rotor diameter or the blade mass. The assumption of the direct drive generator costs was adjusted, since the original model only takes the machine rating as an input. In our case, the rated power remains constant but the rated torque increases, since the maximum rpm is reduced (constant maximum blade tip speed). According to Fingersh et al. (2006), the generator mass scales with $M_{g,\text{rated}}^{0.606}$, with $M_{g,\text{rated}}$ being the rated generator torque. We accounted for the mass increase in the cost estimation, assuming that the costs increase linearly with the mass. Overall, the cost model can serve to point out trends in the development of costs when increasing the turbine size, but absolute values should be handled with care.

Aeroelastic simulations are carried out with OpenFAST V3.1 (Jonkman et al., 2022). The aerodynamic modelling includes the effects of tower shadow and the aerodynamic loading on the tower, as well as the Minnema–Pierce dynamic stall model, as described by Damiani and Hayman (2019). For the purpose of this conceptual study, the authors chose ElastoDyn as a structural model which uses the Euler–Bernoulli beam theory with fitted mode shapes. This module is computationally inexpensive and allows for efficient design iterations. The shortcoming is the low modelling fidelity as the blades are modelled as straight, isotropic beams and blade torsion is neglected. For high-fidelity investigations, this assumption does not hold true for blades of this size, and further simulations are planned using the fully coupled 6×6 mass and stiffness

matrices to elaborate the impact of the simplifications made with the low-fidelity structural model. The authors are also aware that aeroelastic stability can be a main design driver for the structural design of such a long and slender blade. However, this is out of the scope of this aerodynamically focused paper.

To investigate the aeroelastic behaviour of the Hybrid-Lambda Rotor under transient inflow conditions, a set of design load cases (DLCs) are defined in Table 2.1. The DLCs are numbered according to the standard Det Norske Veritas group: DNV-GL ST-0437 (November 2016 (amended: November 2021)). From preliminary investigations, the most critical DLCs were identified as extreme wind shear, storm events with yaw misalignment and power production with the normal turbulence model (NTM). Those DLCs are simulated for the Hybrid-Lambda Rotor and the IEA 15 MW reference turbine with the same simulation methodology with the exception of DLC 6.3, which could not be simulated for the IEA 15 MW reference turbine due to stability problems for large yaw angles.

Table 2.1: Set of ultimate design load cases investigated in aeroelastic simulations.

DLC	Description	Wind speed at hub height [m s ⁻¹]
DLC 1.5	Transient extreme wind shear (vertical and horizontal wind shear positive and negative)	10
DLC 1.6	Power production, NTM	5, 7.5, 10, 13, 18, 21
DLC 6.1	Extreme wind speed model, 50-year storm, yaw misalignment of $\pm 8^\circ$	50
DLC 6.3	Extreme wind speed model, 1-year storm, yaw misalignment of $\pm 20^\circ$	40

2.3 Results

In this section, we focus on the given use case of the 15 MW offshore wind turbine, no longer generalizing the concept, in order to simplify the understanding. This means only one specific turbine diameter is presented here, although the influence of the rotor radius as a design variable was investigated and is further described below. We first

address the resulting aerodynamic blade design and the influence of certain design variables. Table 2.2 summarizes general turbine parameters. The second part deals with loads, axial induction, the angle of attack and power generation under steady- and uniform-inflow conditions. This is followed by the results of the structural design and the aero-servo-elastic investigations.

Table 2.2: General parameter of the Hybrid-Lambda Rotor and the reference turbine.

Description	Symbol	Hybrid-Lambda Rotor	IEA ref. turbine	Unit	Type of design variable
Number of rotor blades	B	3	3	–	fixed
Rated power	P_{rated}	15	15	MW	fixed
Rotor diameter	D	326	240	m	optimized
Specific rating		180	332	W m^{-2}	optimized
Hub height		193	150	m	derived from rotor diameter
Design TSR inner 70 % of blade span	$\lambda_{d,\text{inner}}$	9	9	–	optimized
Design TSR outer 30 % of blade span	$\lambda_{d,\text{outer}}$	11	9	–	optimized
Max rotor speed	ω_{max}	5.38	7.56	rpm	derived from rotor design
Min rotor speed	ω_{min}	2.8	5.0	rpm	derived from rotor design
Max blade tip speed		95	95	m s^{-1}	fixed
Cut-in wind speed	$v_{\text{cut-in}}$	3	3	m s^{-1}	fixed
Rated wind speed	v_{rated}	10.2	10.6	m s^{-1}	derived from rotor design
Cut-out wind speed	$v_{\text{cut-out}}$	25	25	m s^{-1}	fixed
Blade prebend		5.43	4.0	m	fixed/derived from diameter ratio
Unloaded tip-to-tower clearance		38	32	m	fixed/derived from diameter ratio
Rotor precone angle		4	4	$^{\circ}$	fixed
Shaft tilt angle		6	6	$^{\circ}$	fixed
Blade mass		140	65	t	optimized
Max power coefficient	c_p	0.48	0.489	–	derived from rotor design
Thrust coefficient in light-wind mode	$c_{t,\text{LW}}$	0.78	0.799	–	derived from rotor design
Thrust coefficient in strong-wind mode	$c_{t,\text{SW}}$	≤ 0.52	0.799	–	derived from rotor design

2.3.1 Aerodynamic blade design

The Hybrid-Lambda Rotor has a specific rating of 180 W m^{-2} and a rotor diameter of 326 m, which corresponds to an increase in rotor diameter and the swept area by a factor of 1.36 and 1.84, respectively. As shown in Fig. 2.4, the above-described design principles lead to a very slender blade due to the design for a lower induction factor of 0.21. The outer blade section is even more slender due to the design for the higher TSR. Nevertheless, the blade root diameter is scaled by the same factor as the rotor radius to create space for a larger pitch bearings. Figure 2.5 shows the blade twist. Of particular interest are the negative twist offset in the inner blade section and the design for optimal AoA in the outer blade section when operated at zero pitch in light winds. The twist offset is further described and investigated in Sect. 2.3.2.

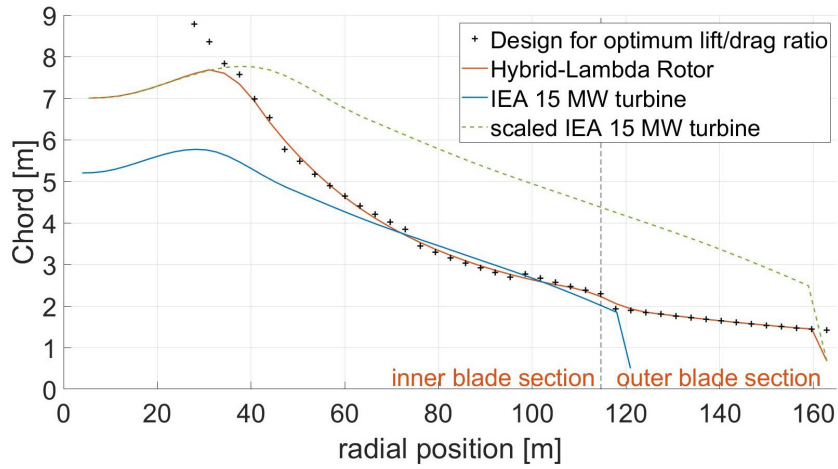


Figure 2.4: Chord distribution over radius.

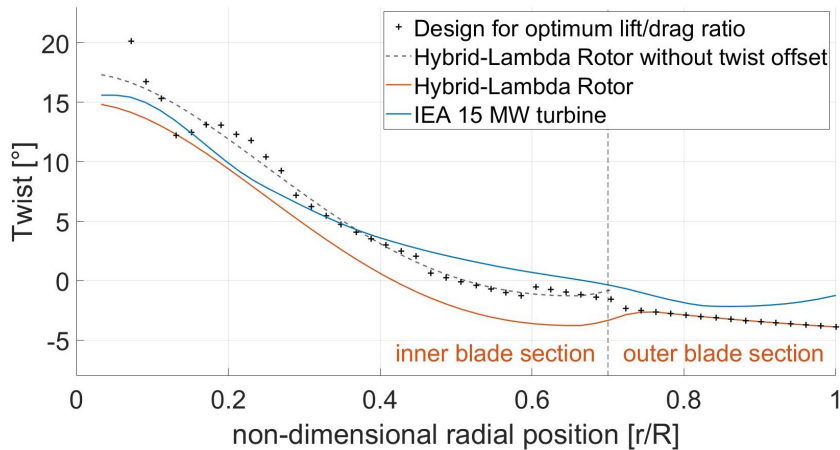


Figure 2.5: Twist over non-dimensional radius.

In the following paragraphs, we discuss some challenges in the design process and the influence of certain design parameters. First, we discuss the influence of the specific rating and thus the rotor radius. In these considerations, we assume the distribution of axial induction and the relative position of the transition point between the inner and outer blade section are unchanged. These are addressed in the next paragraphs. When varying the rotor radius, we still keep the objective of limiting the steady-inflow flapwise RBM to the maximum value of the reference turbine. If the rotor radius is enlarged, the power output is increased before the limiting loads are reached (e.g. in region 1 and 2.1). But at higher wind speeds, when peak shaving is applied (in region 2.2 and 2.3), the blade must be pitched further and power losses are more pronounced.

This can even lead to the fact that the turbine reaches rated power at higher wind speeds compared to the initial design. Furthermore, at a lower wind speed, the limiting loads are reached and the blade operates in a wider range at maximum loads (flapwise RBM). The choice of the optimal rotor radius is therefore taken by carefully choosing a reasonable value for the wind speed at which the limiting loads are reached (in this case about 70 % of rated wind speed), with the further aim of reducing the rated wind speed compared to the reference turbine. In the given case, this leads to a specific rating of 180 W m^{-2} and a diameter of 326 m for the conceptual design. Typical specific ratings for offshore turbines are on the order of magnitude of 400 W m^{-2} and are expected by Dörenkämper et al. (2023) to drop to approximately 330 W m^{-2} in the next few years. For onshore turbines, Dörenkämper et al. (2023) reported a drop in the average specific rating for newly installed turbines in Germany from around 400 W m^{-2} in 2012 to 300 W m^{-2} in 2018. These numbers highlight the extremity of the Hybrid-Lambda Rotor design and clearly show the change in design philosophy.

As a second aspect, we address the relative position of the transition point between the inner and outer blade sections. The induction distribution within the two sections is again considered unchanged. In this case, a shift of the transition point towards the blade tip increases the section of the blade that experiences higher loading. Therefore, the turbine reaches the limiting loads at lower wind speeds and the range of peak shaving becomes wider. Again, this shifts the compromise finding towards power maximization in the light-wind mode. If the transition point is moved too far towards the tip, the tip-loss effects can overshadow the beneficial aerodynamic influence of the low-loaded tip section. In the present study, we chose the transition point to be at 70 % blade span, which allows for two descriptive explanations: first, the swept areas of the two blade sections have almost identical sizes (inner rotor disc and outer rotor annulus). Second, the inner rotor disc has almost the same size as the swept area of the reference turbine, which means the slender outer section of the blade can be interpreted as an extension of the original blade.

As a third design variable, the axial induction is addressed. When a blade operates at a higher TSR than it is designed for, an undesired increase in axial induction along the blade span towards the tip is observed. This means, when plotting the axial induction vs. radius, the line tilts upwards. The design point for the inner blade section is the low TSR of 9 and an axial induction factor of 0.21 with a pitch angle of 2.2° to achieve the above-mentioned change in AoA distribution. At the same time, when operated at a

high TSR and zero pitch, an axial induction factor of 0.33 is desired with a distribution that is as uniform as possible over the inner blade section. To find a compromise between these two requirements, the induction in Eqs. (2.1), (2.2) and (2.4) is linearly lowered from 0.225 at 30 % blade span to 0.17 at the end of the inner blade section (at 70 % blade span) before the twist offset is applied. In this way, we can achieve a fairly constant axial induction in the inner section in the light-wind mode, while in the strong-wind mode a modest decrease in the axial induction towards the tip is beneficial for load reduction. Figure 2.6 shows the axial induction for various operational points as a result of stationary BEM simulations. In fact, the decreasing axial induction towards the blade tip in the strong-wind mode (see Fig. 2.6, yellow line) shows a similar trend to that derived by Jamieson (2020), which is beneficial for rated load reduction.

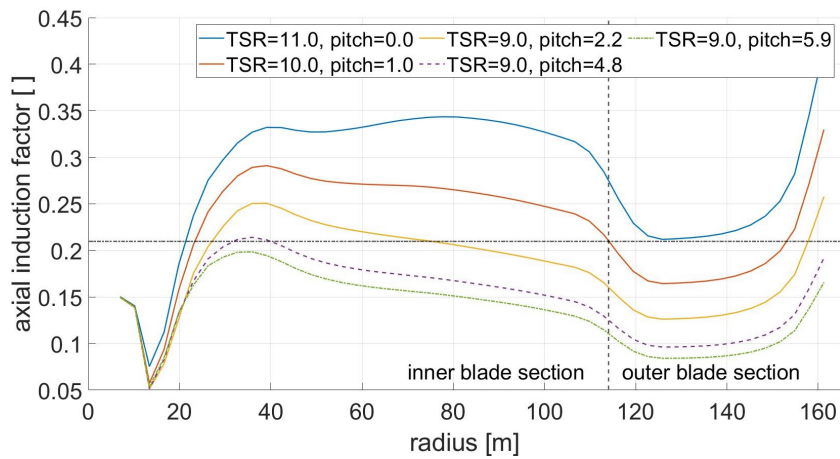


Figure 2.6: Axial induction: light-wind mode (blue), transition (red), strong-wind mode (yellow), peak shaving (dashed, purple), rated power (dash-dotted, green) and design value 0.21 (dash-dotted, black).

2.3.2 Aerodynamics, loads and power in steady-inflow BEM simulations

After addressing the blade design, we present results from the BEM simulations and the derived control strategies with steady and uniform inflow and with rigid structures. The concept is further compared to the reference turbine. Note that due to the gradients along the blade span, the assumptions made in the BEM theory can reach their limit. We used free-vortex wake methods to investigate to what extent the assumption of independent blade elements in the BEM theory is violated. Results show good agreements for rotor-integrated quantities (power and thrust), although some

differences are noticeable in the radius-resolved variables when the gradients along the blade span are large in the light-wind mode. The interested reader is referred to Ribnitzky et al. (2023).

First, the control strategy for the Hybrid-Lambda Rotor is presented in Fig. 2.2. At a cut-in wind speed of 3 ms^{-1} and above, the minimum rotational speed is set to 2.78 rpm, which is approximately half of the maximum rotational speed. From 4 ms^{-1} on, the rotor operates at the high TSR of 11 in the light-wind mode and at a fine pitch angle of -0.8° , which leads to the maximum power coefficient. This pitch angle is called fine pitch since the pitch angle for optimal c_p was derived after the blade design was concluded. The limiting loads are reached at 6.8 ms^{-1} . For higher wind speeds, peak shaving ensures the limitation of the flapwise RBM and the rotational speed is kept constant until the lower TSR of 9 is reached. During the strong-wind operation mode, this TSR is maintained until the maximum rotor speed is approached. In the pitch schedule in Fig. 2.2, it is visible that the necessary pitch angle to limit the flapwise RBM increases more slowly in region 2.2 (where the transition of the operating modes takes place) compared to region 2.3. From a wind speed of 15 ms^{-1} , rated power and the rotational speed are linearly decreased. This takes into account the oversupply of wind power from conventional turbines, and it is expected to further reduce the fatigue loads of the very slender blades.

To better understand the aerodynamic concept and to take additional benefits from the operation with two design TSRs, we take a closer look at the transition between the two design points. When the TSR is lowered (constant rpm, increasing wind speed), the AoA and therefore the lift coefficient increases because the axial flow component increases and the circumferential component remains constant. But in terms of reducing the loads, an increase in AoA is not desired. For an ideal transition from light-wind to strong-wind mode, the blade would see an increase in AoA in the inner section and a decrease in AoA in the outer section. This would shift the power generation to the inner section and reduce the lever arm of the resulting bending forces. Figure 2.7 shows the inflow angle distribution over a non-dimensional radius for a varying TSR for a certain constant axial induction factor a , as described in Eq. (2.5) according to Gasch and Twele (2012). We plotted a wider range of TSRs to emphasize the differences.

$$\phi(r) = \arctan\left(\left(1-a\right)\frac{R}{r\lambda}\right) \quad (2.5)$$

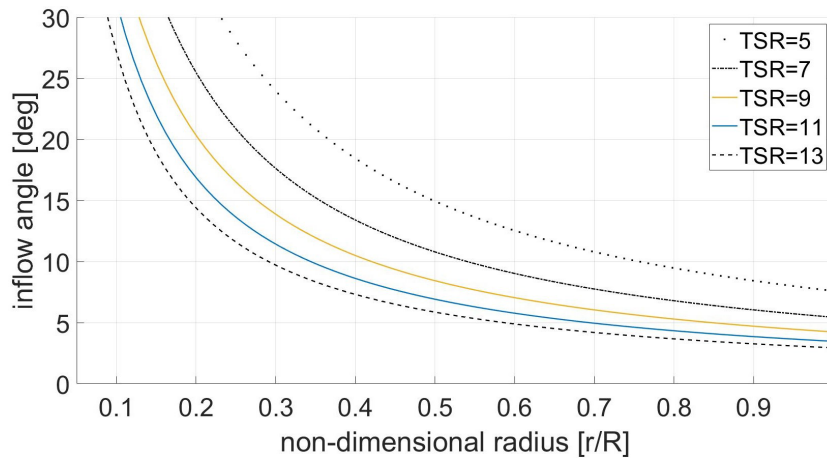


Figure 2.7: Inflow angle distribution for a varying TSR (assuming constant $a = 1/3$ over the blade length).

This formula is valid for a constant axial induction factor along the blade span, which is not the case for the given concept. But to simplify the understanding, we will use the formula for the following findings. Obviously, closer to the root the change in the inflow angle is greater than at the tip. Thus, the above-mentioned change in AoA distribution (i.e. inboard increase and outboard decrease) can be achieved if the blade is pitched towards feather while simultaneously reducing the TSR. To the authors' knowledge, this technique has never been documented before in wind energy applications, and we will use this technique to fine-tune the aerodynamic behaviour during the transition between the two operational modes, emphasizing the change in AoA. Figure 2.8 shows the angle-of-attack distribution for the Hybrid-Lambda blade. The outer blade section operates at the optimal AoA in the light-wind mode, while the inner blade section operates below the optimal AoA because it is operated at a higher TSR than it was designed for. When transitioning to the strong-wind mode (i.e. lowering the TSR and pitching to feather), the AoA decreases in the outer section but increases in the inner section. In this way, the inner section operates closer to the optimal AoA, and the change in the AoA distribution reduces the lever arm of bending forces.

In this paragraph, we analyse the power output of the Hybrid-Lambda Rotor and investigate whether the desired advantages are met. Close to cut-in wind speed, wind turbines operate at very high TSRs because the minimum rotational speed is

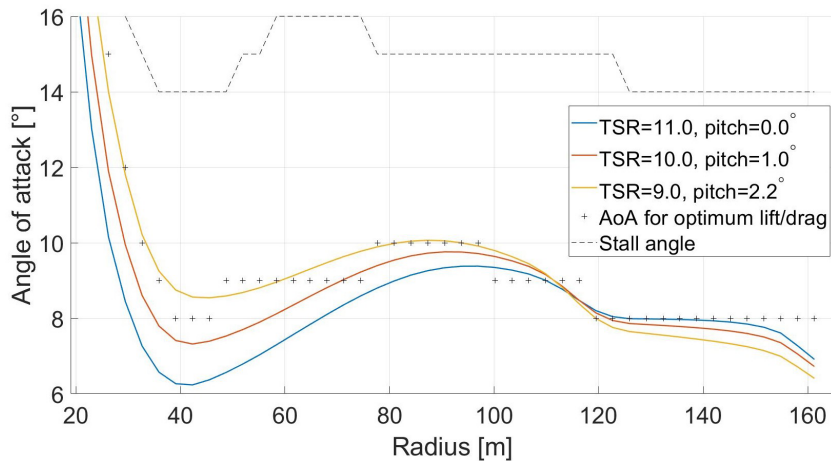


Figure 2.8: Angle of attack (BEM): light-wind mode (blue), transition to strong-wind mode (red) and strong-wind mode (yellow).

set by the generator characteristics and by the first tower eigenfrequency. As seen in the power curve, the presented concept (solid red line in Fig. 2.9) shows advantages because the light-wind design point of the blade is at a higher TSR and therefore closer to the operational TSR at cut-in. The Hybrid-Lambda Rotor operates at the high design TSR up to 6.8 ms^{-1} until the limiting flapwise RBM is reached. At this point, the turbine's power is 1.8 times greater than the reference turbine's power (blue line). The aerodynamic power coefficient in the light-wind mode is 0.481, which is only 1.7% lower than the maximum power coefficient of the reference turbine. At higher wind speeds, the turbine operates at the lower TSR and peak shaving through pitching to feather is applied to limit the loads. Here, the different efficiencies in peak shaving are visible. The potential is shown by the dotted red line, which represents the power output if the loads are not limited through peak shaving. The dashed green line indicates the power curve of the reference blade that is geometrically scaled by the same factor and where conventional peak shaving is applied to limit the flapwise RBM. This means only the pitch angle is set to a higher value to constrain the flapwise RBM while the rpm follows the design TSR. In contrast, the dotted black line represents the same blade (geometrically scaled IEA 15 MW) but peak shaving is applied in a similar manner to for the Hybrid-Lambda Rotor. This means for $v > v_{\text{shift,start}}$ the rpm is kept constant until the operational TSR is reduced from 9 to 7. For $v > v_{\text{shift,end}}$ the rpm schedule follows the TSR of 7, which is an arbitrary choice in this case and should be optimized in a detailed design study. In addition, the pitch angle is set for $v > v_{\text{shift,start}}$ in order to limit the flapwise RBM. In short, we are applying the Hybrid-Lambda control strategy to a conventional blade design. The results show that the power output

can be greatly increased if the TSR is lowered in region 2.2 and 2.3 (compare dashed green and dotted black line in Fig. 2.9). Thus, peak shaving should be accomplished not only by increasing the pitch angle, but also by optimizing the operational TSR with respect to the load constraint (as also indicated by Madsen et al., 2020). Since the results show that a reduction in the operational TSR is beneficial in the peak-shaving region, it makes sense to account for this fact already in the blade design which is integrated in the Hybrid-Lambda design methodology. Indeed, the Hybrid-Lambda Rotor enables even lower power losses in the peak-shaving region, since the TSR reduction is already accounted for in the blade design (compare solid red and dotted black line in Fig. 2.9). The turbine concept reaches its rated power at 10.2 ms^{-1} , which is 0.4 ms^{-1} lower than the reference turbine.

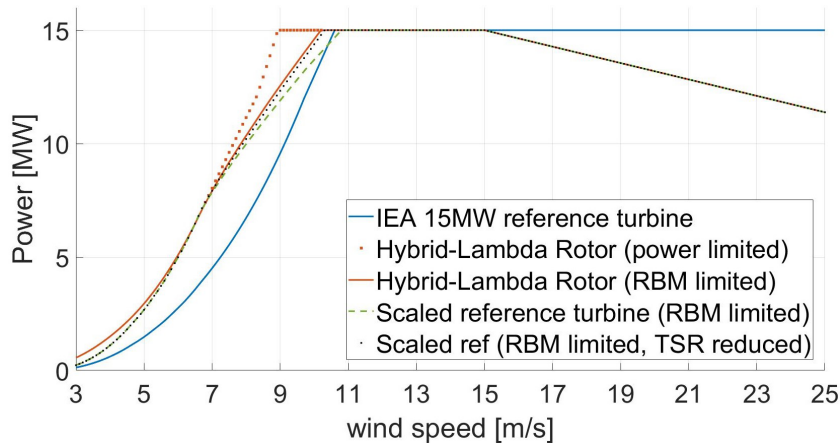


Figure 2.9: Power output of the Hybrid-Lambda Rotor (solid red) compared to the reference turbine (blue) and a scaled reference turbine (dashed green and dotted black).

Further benefits become clear when looking at the thrust characteristics of the Hybrid-Lambda Rotor in Fig. 2.10. Low thrust coefficients are beneficial in terms of design driving loads and wind farm efficiency. The maximum thrust coefficient of the conceptual rotor is comparable to the reference turbine. But the real advantage lies in the transition to the strong-wind mode. The blade is pitched and the thrust coefficient decreases rapidly, which leads to much lower wake losses for wind speeds greater than 6.8 ms^{-1} . The wake losses of the Hybrid-Lambda Rotor are addressed by Ribnitzky et al. (2023). Results show significant advantages even in a scenario with constant absolute spacing (compared to the IEA 15 MW reference turbine). The maximum dimensional steady thrust is only 3% higher than the maximum value for the reference turbine. Since the thrust is employed over the 85% larger swept area, the thrust coefficient

drops significantly. A breakdown of the contribution to the thrust coefficient of the inner and outer parts of the rotor is depicted in Fig. 2.10. Those are calculated by separately considering the respective swept area and blade span for the actual thrust force and reference force. As the inner rotor operates at higher axial induction factors (in light-wind mode) compared to the reference turbine, higher thrust coefficients are derived. But for wind speeds greater than 7.4 ms^{-1} the thrust coefficient of the inner rotor disc is lower than the value of the reference turbine due to peak shaving.

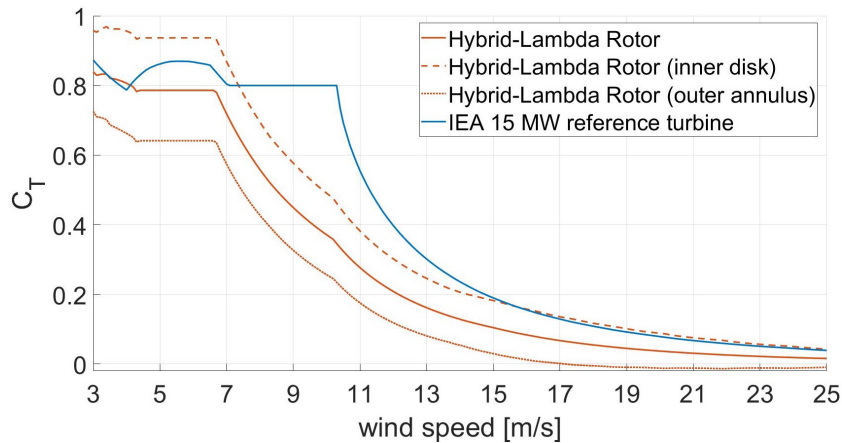


Figure 2.10: Thrust coefficient of the Hybrid-Lambda Rotor (RBM limited) compared to the reference turbine.

2.3.3 Optimization of the structural blade and tower design

Multi-disciplinary design and optimization routines are nowadays common practices in wind energy research. Consequently, the objective of this section is not to provide a new design methodology but to elaborate on a consistent and realistic system design also being possible for such an innovative and in some sense unconventional rotor design. A common problem with very long and slender blades is the low area moment of inertia that such cross-sections provide. Thus, the stiffness provided by the geometric shape is relatively low and massive reinforcements by very thick carbon spar caps need to be added. This often leads to heavy and expensive blades, which means that the advantage of a slender blade, which is expected to use less material, is counterbalanced. This thesis is supported, as the initial blade design of the Hybrid-Lambda Rotor is only 5% lighter than expected by the cubic scaling law if the reference blade were scaled geometrically (see Fig. 2.11).

A possible solution is to increase the relative thickness (which is equivalent to pushing the thicker airfoil sections closer to the tip) to increase the geometric area moment of

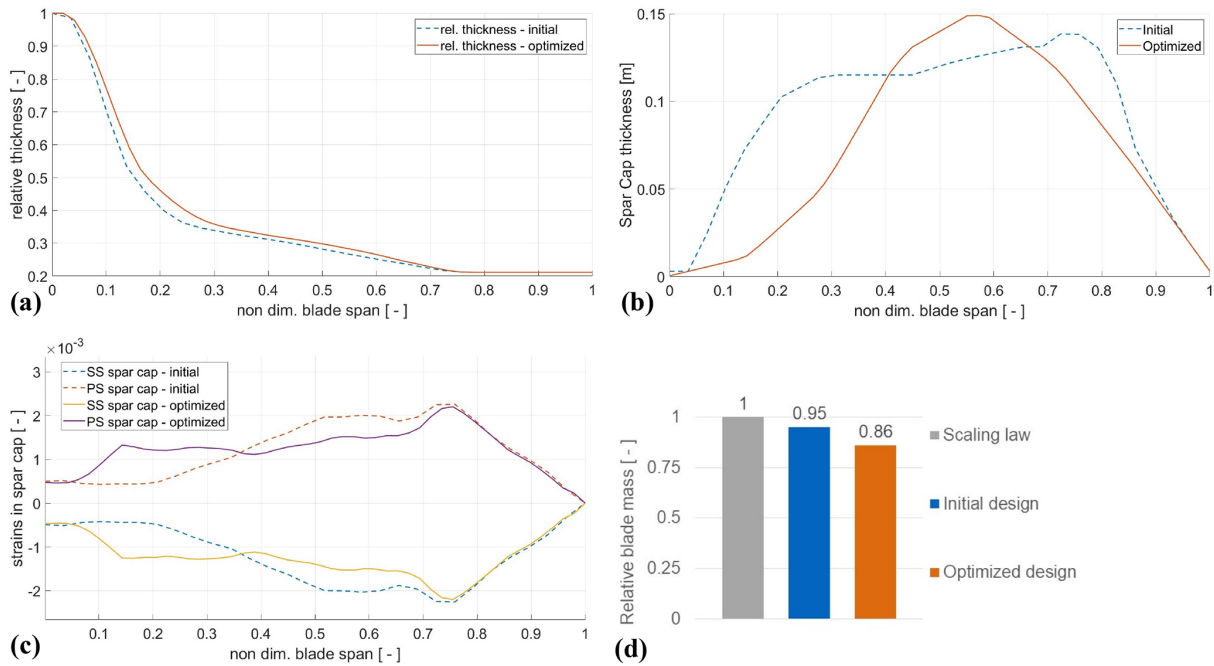


Figure 2.11: Comparison of structural parameters between initial (dashed lines) and optimized (solid lines) blade design: relative thickness distribution (a), spar cap thickness distribution (b), strains in the spar caps (SS, suction side; PS, pressure side) (c) and blade mass relative to the cubic scaling law of the IEA 15 MW blade mass (d).

inertia and reduce the spar cap thickness accordingly to save material, mass and costs. On the one hand, the designer sacrifices aerodynamic efficiency and consequently AEP, as the thicker airfoils are less efficient. On the other hand, the blade can be designed to be lighter and less costly. This trade-off is made by minimizing the cost of valued energy (COVE), using the multi-disciplinary optimization algorithm WISDEM which was adjusted by the authors to implement the Hybrid-Lambda design methodology, as described in Sect. 2.2.3. Three design parameters are compared along the blade span between the initial and the optimized blade in Fig. 2.11. The relative thickness for the inner blade section is increased while the airfoils are locked for the outer blade section in order to maintain the aerodynamic characteristics of the tip region, which is designed for the light-wind regime. The spar cap thickness is reduced, especially for the root section ($0 < r/R < 0.4$). This section sees much larger chord lengths, as the blade root diameter is scaled by the same factor as the increase in rotor diameter to create space for larger pitch bearings which will be needed to carry the increased edgewise bending moments. Due to this large chord length close to the root and the further increase in relative thickness in the optimization, the area moment of

inertia is relatively large and the spar cap thickness can be reduced significantly. This leads to a more uniform distribution of the strains in the spar caps, as shown in Fig. 2.11c.

Special care needs to be taken on the transition of the inner and the outer blade section at 70 % blade length. In this area, the chord length and the aerodynamic forces change over a small spanwise section. In the initial design, this area was reinforced by a thicker spar cap layup (see dashed blue line in Fig. 2.11) to reduce the peak that was observed in the strains in this transition area. Of course, such a distribution of spar cap thickness is not beneficial in terms of eigenfrequencies because it adds more mass closer to the tip, which drives down the eigenfrequencies and most likely has to be compensated for by a stiffer design of the inner blade section. However, the optimization algorithm reduced the spar cap thickness in this transition area at 70 % blade length, too, which did not lead to a significant increase in the strains. The resulting mass and stiffness distributions are compared to those of the IEA 15 MW turbine in Fig. 2.12, clearly showing the steeper gradient in the flapwise stiffness in the transition area of the Hybrid-Lambda blade. The reader should bear in mind that the structural solver PreComp is a 2D cross-sectional solver and does not account for stress concentration due to rapid changes in the geometry in the spanwise direction. Overall, the optimized blade is 14 % lighter compared to a geometrically scaled blade of the same size. If we were to define n as the ratio of diameters of the reference and the Hybrid-Lambda turbine, the blade mass would increase with n^3 , according to Gasch and Twele (2012), while our design leads to an exponent of 2.5 instead. Note that the reference exponent of 3 is only derived by geometric considerations. Griffith and Richards (2014) summarize recent trends for commercial and research blades and state mass scaling exponents of 2.5 for moderately innovative blades and 2.1 for highly innovative designs.

The initial tower is designed as an isotropic, tapered steel tube. The design is similar to the tower of the IEA 15 MW reference turbine with the adjusted hub height and an increase in tower diameter from 10 to 11 m at the tower base. After the optimization the tower base diameter is reduced to 8.54 m and the material thickness is increased accordingly to meet the requirements for buckling, stress constraints and eigenfrequencies. The monopile diameter is reduced to the same value. Overall, the combined structural mass of tower and monopile is reduced by 17.5 % compared to the initial design, which leads to significant cost savings, as further described in Sect. 2.3.5. As shown in Fig. 2.13, the tower design results in a classic soft–stiff design with the first

eigenfrequencies between the rotational (1P) and blade passing (3P) frequency. The first flapwise eigenfrequency of the blades is safely above 3P excitation.

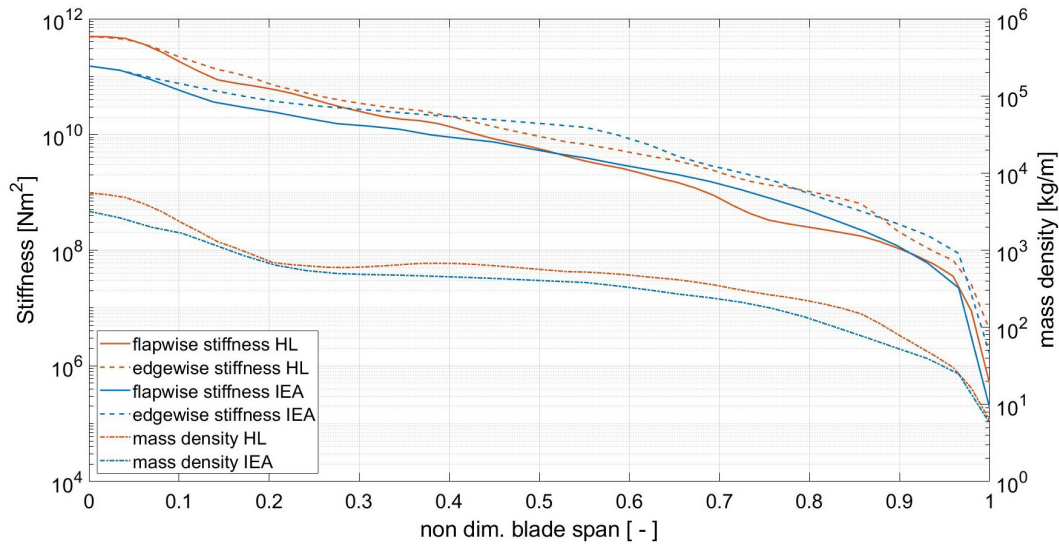


Figure 2.12: Mass and stiffness distribution for the optimized Hybrid-Lambda blade (red) and the IEA 15 MW blade (blue).

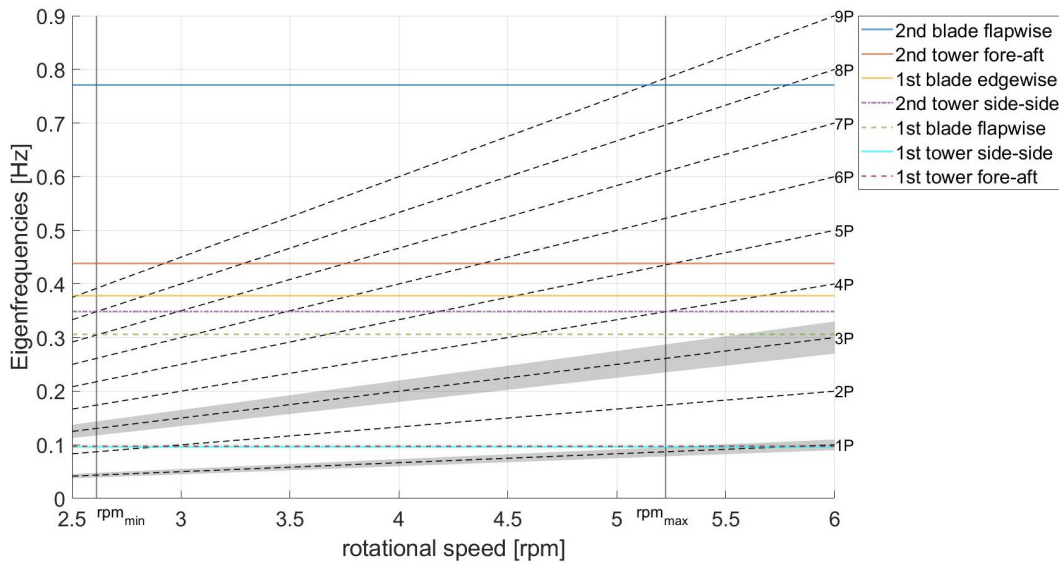


Figure 2.13: Campbell diagram for optimized blade and tower design. Safety margins of 10% for 1P and 3P excitations are shown in grey.

2.3.4 Aeroelastic load simulations

After setting up a consistent turbine model, we investigate the Hybrid-Lambda Rotor with aeroelastic simulations. First, the controller design is described. In Sect. 2.3.4.2,

we describe the transition between the operating modes in a turbulent wind field. We further investigate a set of design load cases in Sect. 2.3.4.3, and in Sect. 2.3.4.4 we examine extreme wind shear events. The presented conceptual investigation does not include a fatigue analysis. Despite its general importance, this is considered out of the scope of the paper, which is further discussed in Sect. 2.4.

Initial controller design

The innovative operating characteristics described in Sect. 2.3.2 open up new challenges and opportunities in the design of the controller. The partial-load regime below rated is no longer governed by a pure torque controller. Two newly arising challenges are the transition between the operating TSRs and the limitation of the flapwise RBM. Changing the TSR is certainly an important topic for the controller design and drive train dynamics, given an increase in the rotational inertia of the Hybrid-Lambda Rotor compared to the reference turbine by a factor of 3.5. According to generic scaling laws, the rotational inertia increases with n^5 , while the slender blades and lower radius of the centre of mass of the Hybrid-Lambda Rotor lead to an exponent of 4.1 instead. In this study, we aim for a controller that fulfils these basic requirements using only standard methods like pitch and torque control. Of course, an advanced controller design like individual pitch or observer-based feed-forward control would be beneficial for a rotor of this size, but it is not in the scope of this paper.

To better describe the control strategy, we will distinguish four regions below rated power, as depicted in Fig. 2.2. Following a certain TSR (11 in region 2.1 or 9 in region 2.3) is achieved by setting the generator torque as

$$M_g = \frac{\pi R^5 \rho c_p(\omega)}{2\lambda^3} \omega^2. \quad (2.6)$$

Note that there is no unique c_p in region 2.3 since the pitch angle is a function of wind speed. Hence, the desired c_p from steady-inflow simulations is implemented as a function of rotational speed. The transition between the two TSR values is based on a proportional and integral (PI) controller, similarly to how the transition to the full-load region is realized or how the torque control near the cut-in wind speed is done, as described by Burton et al. (2011). During the transition between the two TSR values (region 2.2), the PI controller keeps the rotor speed at the constant value ω_{shift} by setting the generator torque. To assure a smooth transition to the constant-TSR regions, the PI output is constrained by the torque values from Eq. (2.6) corresponding to $\text{TSR} = 9$ and

TSR = 11, respectively. In that way, the PI torque controller is active only during the transition region, while the constant-TSR regions are achieved by the torque control law from Eq. (2.6), similarly to conventional turbines with partial load. A similar PI-based solution is also used for conventional turbines to avoid rotor speed values near the cut-in and the rated wind speed that are too low or too high, as described in Burton et al. (2011).

For the pitch controller, two versions are implemented. The first version is referred to as the simplified controller and implements the transition of the TSR and a look-up table for the pitch signal for region 2.2 and 2.3. This simplified controller is used for the load case calculations in Sect. 2.3.4.3. A second version is developed that features a feedback from the flapwise RBMs, further referred to as the load feedback controller, and it is applied in Sect. 2.3.4.2. The functionality of the pitch controller can be described in three parts. Firstly, below rated, we use a conventional implementation with a look-up table for region 1 and a constant pitch for the maximum power output in region 2.1. The argument of the look-up table is the filtered wind speed, mimicking a wind speed estimator. Secondly, above rated, a standard PI pitch controller ensures a constant rotational speed or a linear decrease in rotational speed in region 3.2. Thirdly, in parallel to these two functionalities, we implemented a load limiter (for region 2.2 and 2.3). To do so, the mean of the three flapwise RBMs is low-pass-filtered and fed back to the controller. The RBM feedback is then compared to the maximum allowed flapwise RBM. As long as the RBM feedback is larger than the constraint, the reference pitch value (output of the controller) is increased, thus not allowing the blades to reduce their pitch angles, which would further increase the RBMs. The change in the reference pitch angle is proportional to the difference between the RBM feedback and the constraint. The output signal is saturated with the maximum pitch rate of 3°s^{-1} . The proportional gain is a controller parameter that needs to be tuned. Once the RBMs drop below the constraint, the reference pitch angle is also reduced, thus allowing the PI pitch controller to reduce the pitch angles to the optimum pitch in region 2 or to keep the rotor speed constant in region 3.1. In this way, the amplitude of load variations can be drastically reduced and load overshoots are less severe. Nevertheless, the increased pitch activity needs to be considered when sizing the actuators and bearings which will influence the resulting cost function. Instead of using the mean of all three RBMs, it is also possible to use the maximum of the three signals as a load feedback. The implementation would be identical to that described above. This results in larger pitch angles and lower loads but obviously also reduces the energy yield. The choice of the respective feedback signal and the magnitude of the constrained RBM are always a compromise between the load

limitation and power maximization. In an advanced setting of turbine control and structural health monitoring, this could also be adjusted throughout the lifetime of the turbine, considering the actual condition of the turbine.

Additionally, advanced control designs are required to further limit the loads in dynamic- and turbulent-inflow conditions. In fact, some findings from the aeroelastic simulations show a need for an improved controller design, but this is in the scope of future work.

Transition of operating modes in a turbulent wind field

From a conceptual viewpoint, the ability of the Hybrid-Lambda Rotor to switch between the light-wind and strong-wind operating modes under turbulent inflow is of special interest. For this purpose, a wind field with a normal turbulence model, a mean wind speed of 7.5 m s^{-1} and a turbulence intensity of 21 % is chosen and the ability of the load feedback controller is tested. The results are shown in Fig. 2.14 (TSR, wind speed and flapwise RBM are low-pass-filtered). Considering steady inflow, the maximum flapwise RBM (dashed black line) is reached at a wind speed of 6.9 m s^{-1} ($v_{\text{shift,start}}$ – dashed blue line) and a pitch angle of 0° , and according to the design concept, the rotor should switch to the strong-wind mode (lower TSR) for higher wind speeds. The time periods with the wind speed at hub height below $v_{\text{shift,start}}$ are marked with a green background to indicate that the rotor should be (in theory) in the light-wind mode with the high TSR. For wind speeds greater than 8.3 m s^{-1} ($v_{\text{shift,end}}$ – dash-dotted blue line) the rotor should operate at the low TSR and those time periods are marked in red. The time periods with the wind speed between $v_{\text{shift,start}}$ and $v_{\text{shift,end}}$ are marked in yellow, indicating that the rotor is transitioning between the two operating modes. Minor short-term exceedances of the transition wind speed are not highlighted.

In Fig. 2.14, three transitions from light-wind to strong-wind mode are visible. The first one, starting at 212 s, shows a sudden gust event with an increase in wind speed from 5.5 to 9.2 m s^{-1} in only 14 s. The rotor is able to reduce the TSR from 11 to 9.75 in 15 s. The attentive reader will notice that for large rotors with a high moment of rotational inertia, the TSR will decrease by default for a sudden increase in wind speed, as the rotor speed changes much more slowly than the wind speed. However, as a reaction to this gust event, the controller increases the torque rapidly (as shown with the dash-dotted red line) to keep the rotational speed constant and to even enforce the reduction in the TSR. The second ramp event takes place at 275 s, and the controller reaction is similar to the above-described case. The third transition to the strong-wind

mode occurs at 390 s, and for the following relatively long strong-wind period, the controller is able to reduce the TSR fully to the desired value of 9. However, this transition is rather slow, occurring over a time period of 37 s. The transitions from strong-wind mode back to light-wind mode take place at 175, 227 and 335 s. Especially the latter transition happens relatively quickly (12 s from TSR 10 to 11), reaching the desired TSR of 11 exactly at the time when the wind speed drops below $v_{\text{shift,start}}$.

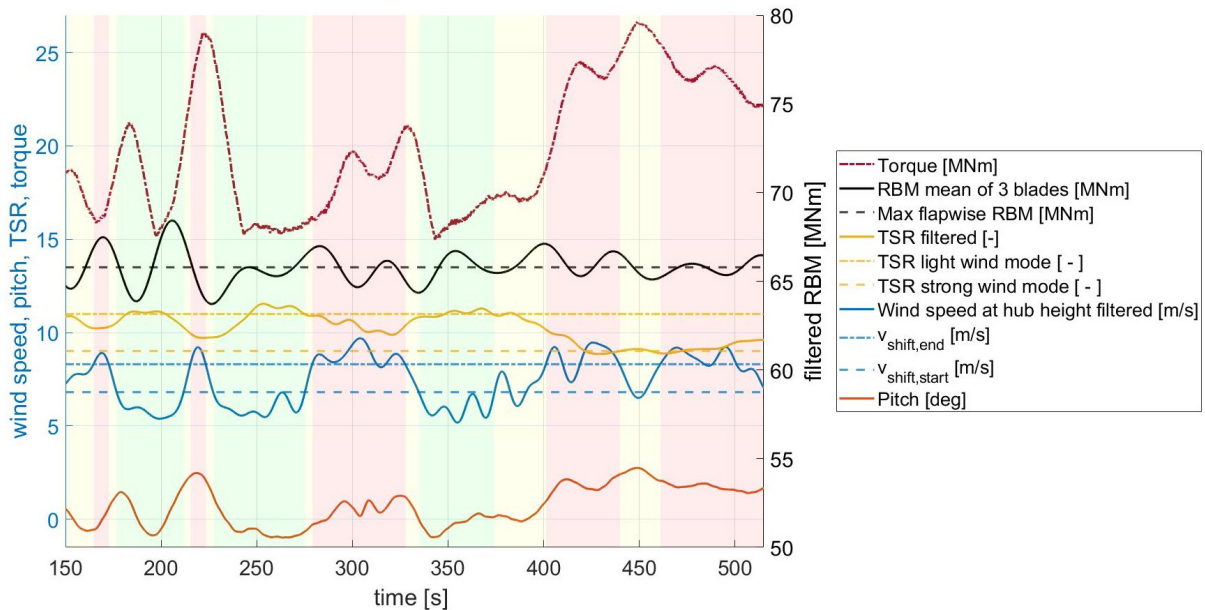


Figure 2.14: Transition of operating modes in a wind field with the normal turbulence model and a mean wind speed of 7.5 ms^{-1} ; background colours indicate the desired operating modes: green, light wind; red, strong wind; yellow, transitioning between the operating modes.

This investigation shows that it is in general possible to apply the control strategies described in Sect. 2.3.2 in a turbulent wind field in a fully aeroelastic simulation. Although the transition between the operating modes is found to be possible, this method is more suitable for slow changes in the mean wind speed. Sudden gust events, as observed at 212 s, still lead to a minor exceedance of the flapwise RBM compared to the limit that was applied in steady BEM calculations. Furthermore, it becomes clear that the current controller setup could imply large torque variations and associated high drive train fatigue loads. More advanced controller concepts (e.g. model predictive control) are likely required.

Comparison of ultimate loads with the reference turbine

After investigating the transition between the operating modes, we address ultimate loads in the set of design load cases from Table 2.1. To reveal further advantages or disadvantages of the aerodynamic design of the Hybrid-Lambda Rotor, we performed these simulations with the simplified controller without the feedback of the loads (only implementing the transition of the TSR with a look-up table for the pitch). Figure 2.15 presents the ultimate loads of the Hybrid-Lambda Rotor with solid bars and those from the reference turbine with hatched bars. Three groups are distinguished by their texture. First, the white bars illustrate the maximum loads under steady and uniform inflow including elastic deformations. Two wind speeds (rated and $v_{\text{shift,start}}$) were investigated, and the more severe case is displayed here. Second, the grey bars show the theoretical load increase according to the generic scaling law as described by Gasch and Twele (2012), which would apply to a geometrically scaled reference turbine without changing the aerodynamic concept (e.g. scaling the steady-inflow loads of the IEA 15 MW, displayed with white hatched bars). This means that flapwise RBM scales with n^3 , edgewise mass-driven RBM with n^4 , thrust with n^2 and the tower base fore–aft bending moment with $n^2 \cdot n_{\text{tower}}$ (neglecting the rotor mass increase), where n is the scaling factor of the rotor diameter and n_{tower} the scaling factor of the hub height. The out-of-plane tip deflection scales with n assuming that the aerodynamic forces scale with n^2 , geometrical dimensions scale with n and the second area moment of inertia of the blade cross-section scales with n^4 . The unloaded tip-to-tower clearance scales with n , too (neglecting gravitational effects). Thus, the loaded tip-to-tower clearance scales with n as it is the difference between two variables, both scaling with n (the unloaded tip-to-tower clearance and the maximum tip deflection with the blade in front of the tower). These scaling factors are only an indication of the upper bound, since the design methodology of the Hybrid-Lambda Rotor includes peak shaving with a constant flapwise RBM. Third, the coloured columns relate to the dynamic load quantities from aero-servo-elastic simulations.

We first address the differences between the generic scaling law and the steady-inflow loads (white and grey bars). As per definition of the design methodology, the maximum flapwise RBM moment is maintained in steady- and uniform-inflow conditions. Nevertheless, the blade length is enlarged and the edgewise mass-driven RBM has to increase. Due to the very slender and relatively light outer blade section, the lever arm of the centre of mass is shorter in relation to the total blade length. Hence,

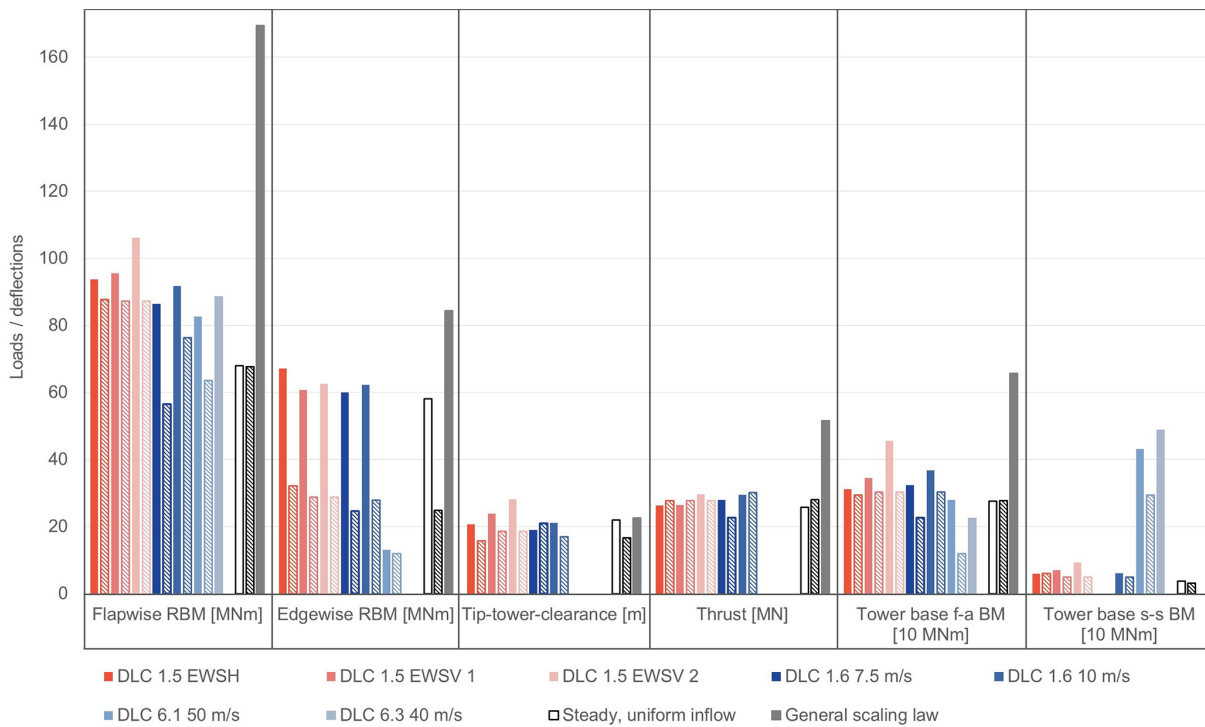


Figure 2.15: Ultimate loads in solid bars for the Hybrid-Lambda Rotor and in hatched bars for the IEA 15 MW reference turbine; only critical loads are displayed. Abbreviations: EWSH, extreme wind shear horizontal; EWSV, extreme wind shear vertical; f-a BM, fore–aft bending moment; s-s BM, side–side bending moment.

the edgewise RBM is enlarged by a factor of 2.36 (cf. the blade mass increases by a factor of 2.15). This means the edgewise RBM scales only with $n^{2.8}$ rather than with n^4 as with geometrical scaling. The tip-to-tower clearance represents a reserve; thus a higher value indicates a safer design. Note that the unloaded tip-to-tower clearance also increased as documented in Table 2.2. The loaded tip-to-tower clearance is larger for the Hybrid-Lambda Rotor under steady–uniform inflow as expected by the scaling law. The thrust is expected to be lower for the Hybrid-Lambda Rotor as a part of the blade is designed for low induction. The tower base fore–aft bending moment is approximately the same for the two turbines in steady-inflow simulations. On the one hand, a constant thrust and an increased tower length would increase the tower base bending moment. On the other hand, the increased rotor–nacelle–assembly mass introduces a counterbalancing moment. In total, this leads to an equal tower base fore–aft bending moment in steady-inflow simulations for the two turbines.

Next, we discuss the ultimate loads from the aero-servo-elastic simulations (coloured bars). For each type of loading, the most critical load cases are displayed as bars in

Fig. 2.15. If a load case is not displayed for a certain type of loading, it is considered uncritical. The objective of the Hybrid-Lambda Rotor is to limit the stationary flapwise RBM to the maximum value of the reference turbine in steady-inflow BEM simulations. Thus, it is of special interest how much this type of loading increases in transient aeroelastic simulations. The ultimate load from normal power production is indeed marginally increased compared to the load level of the reference turbine from normal power production. But, when compared to the load level of the reference turbine under extreme wind shear events, the increase is only marginal. For the storm events, the ultimate loads could be reduced by pitching to 94° instead of 90° . Still, the increase in DLC 6.3 is significant compared to the reference turbine. Due to the large yaw error of $\pm 20^\circ$, the blade experiences relatively large angles of attack (for certain azimuthal positions), which leads to an increase of 40% in the flapwise RBM. Still, for the Hybrid-Lambda Rotor the absolute values of the flapwise RBM for the storm events are lower than the maximum values for DLC 1.5 and DLC 1.6, which are the design driving load cases for the flapwise RBM. In the storm events, the slender blade design shows additional benefits. The shorter chord length reduces the lift forces arising from the complex interaction of blade twist, azimuthal position and yaw error.

The strongest increase in the ultimate edgewise RBM is observed for normal power production, extreme wind shear horizontal (EWSH) and extreme wind shear vertical (EWSV; the difference between EWSV 1 and EWSV 2 is explained in Sect. 2.3.4.4), which are the design driving load cases for both turbines. The increase is expected as much larger blades are necessarily heavier and have a longer lever arm. But, if those values are compared to the generic scaling law, the advantage of the very slender and relatively light blades of the Hybrid-Lambda Rotor becomes clear. The maximum edgewise RBM is almost twice as large as for the reference turbine, but it is still only 80% of the increase expected by the generic scaling law.

The tip-to-tower clearance turns out to be uncritical, since it is larger compared to the reference turbine. Looking at the ultimate loads for the thrust, this type of loading is uncritical, too. Since a part of the rotor is designed as a low-induction rotor and the limitation of the flapwise RBM is the stronger constraint in setting up the control schedule, the ultimate thrust is lower compared to the reference turbine for this reduced set of DLCs. The tower base fore–aft bending moment is increased for the Hybrid-Lambda Rotor in the dynamic load cases although it is constant for the steady-inflow cases, which highlights the importance of investigating transient effects.

Extreme vertical wind shear

As seen in the previous section, the Hybrid-Lambda Rotor is very sensitive to extreme wind shear, which we study in more detail. In the standard IEC 61400-1 (2019), transient extreme vertical wind shear is modelled in a way that the wind speed stays constant at hub height (here only shown for rated wind speed); the wind speed at the upper end of the rotor disc increases while the wind speed at the bottom of the rotor disc decreases. The unsteady event starts at 200 s and lasts for 12 s with a maximum wind speed at the top of the rotor disc after 6 s. We further define wind shear (s) as the slope of the wind speed (v) over the height (z), as described in Eq. (2.7).

$$s = \frac{\Delta v}{\Delta z} \quad (2.7)$$

We investigated two transient non-turbulent wind fields with different vertical wind shear. The first one (EWSV 1) implements the transient wind profiles as described in the standard IEC 61400-1 (2019) for the two turbines with the respective rated wind speed and hub height. These wind profiles are shown in Fig. 2.16, which makes clear that both turbines experience almost the same maximum wind speed at the top of the rotor disc and the wind speed at hub height remains constant at rated wind speed. In fact, the wind speed at the top increases from around 11 to 18 ms^{-1} in 6 s. As these wind profiles are modelled with the respective turbine parameters, this approach corresponds to a turbine-type-specific wind field. Consequently, the maximum wind shear after 6 s is lower for the Hybrid-Lambda Rotor than for the reference turbine (compare dashed lines in Fig. 2.16), but the wind speed at the top of the rotor disc is similar. This approach is according to the standard IEC 61400-1 (2019), but it was issued for much smaller rotors. It neglects the fact that larger rotors cover a greater spatial area and are more prone to larger differences in the spatially distributed wind speed. Therefore, we also investigated a more conservative approach. In the second case (EWSV 2), we place the Hybrid-Lambda Rotor in exactly the same wind field as for the reference turbine (blue lines in Fig. 2.16). Thus the maximum wind shear is the same, but the maximum wind speed at the top of the rotor disc is much larger for the Hybrid-Lambda Rotor due to its larger diameter. In fact, the wind speed at the top of the rotor plane increases from 12.5 to 23 ms^{-1} in 6 s, and at the bottom, it decreases from 7.7 to 0.8 ms^{-1} . Here, one should question whether this is still a realistic shear event. Further, the wind speed at hub height is larger in general and marginally increases during the transient event, as the hub height of the Hybrid-Lambda Rotor is higher. All in all, the second approach can be considered a site-specific wind field, as both turbines

experience exactly the same wind. EWSV 2 might be over-conservative, but we want to investigate the extremes in load case definitions.

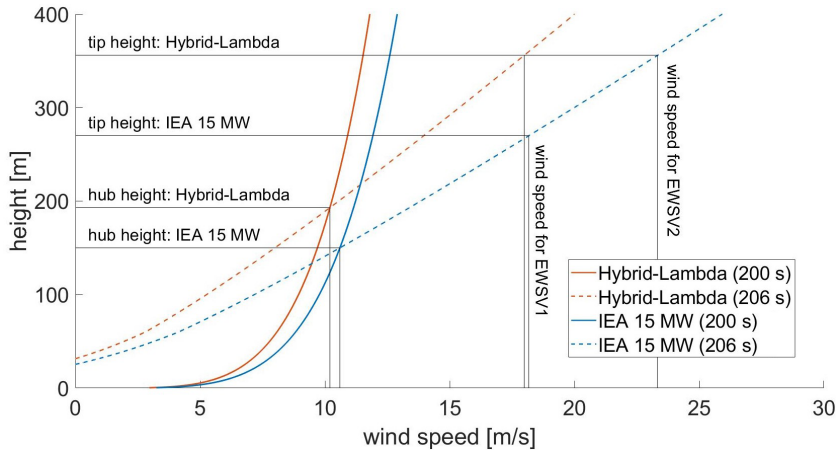


Figure 2.16: Extreme vertical wind shear profiles according to IEC 61400-1 (2019) for the Hybrid-Lambda Rotor and the IEA 15 MW reference turbine.

As seen in Fig. 2.15, the increase in flapwise RBM is very mild, with a factor of 1.09 for the turbine-type-specific approach (EWSV 1). As expected, the increase for the site-specific approach (EWSV 2) is larger, with a factor of 1.2. Still, it can be considered a great advantage that the increase in flapwise RBM is relatively low for blades of that size. Here, the low-induction design for the outer section of the blade shows additional benefits. This is the part of the blade that experiences the highest wind speeds in an extreme shear event, and it is beneficial if it is designed for a lower loading.

To support this hypothesis, we want to have a deeper look at the out-of-plane forces distributed over the blade span in Fig. 2.17. For this investigation, the site-specific wind field (EWSV 2) was used and the azimuth positions of the rotors were set in such a way that both turbines have a blade pointing up at the time of the maximum wind shear (at 206 s). In Fig. 2.17, we display the force distribution before the transient shear event happens (at 200 s) and at the time of maximum shear (206 s). The non-dimensional lever arm (L) of the resulting bending force is calculated according to Eq. (2.8) and is indicated with the vertical black lines. Here, f is the aerodynamic out-of-plane force per unit length, x is the dimensional position along the blade span and l_b is the length of the blade.

$$L = \frac{\int f(x)x dx}{l_b \int f(x) dx} \quad (2.8)$$

The force distribution of the Hybrid-Lambda Rotor shows the characteristic decrease

in the outer blade section with a maximum at approx. 65% blade length and a lower lever arm of the resulting bending force of approx. 55%. In comparison, the force distribution for the reference turbine increases more or less linearly almost until the tip, which leads to a lever arm of approx. 65%. The maximum out-of-plane force per unit length is even 1.5 times larger than for the Hybrid-Lambda Rotor. Note that the Hybrid-Lambda Rotor operates at a lower thrust coefficient at rated wind speed compared to the reference turbine. In addition, we investigated the transient wind shear event at v_{shift} to ensure a similar thrust coefficient for the two turbines. But this load case leads to less severe ultimate loads and is consequently not shown here.

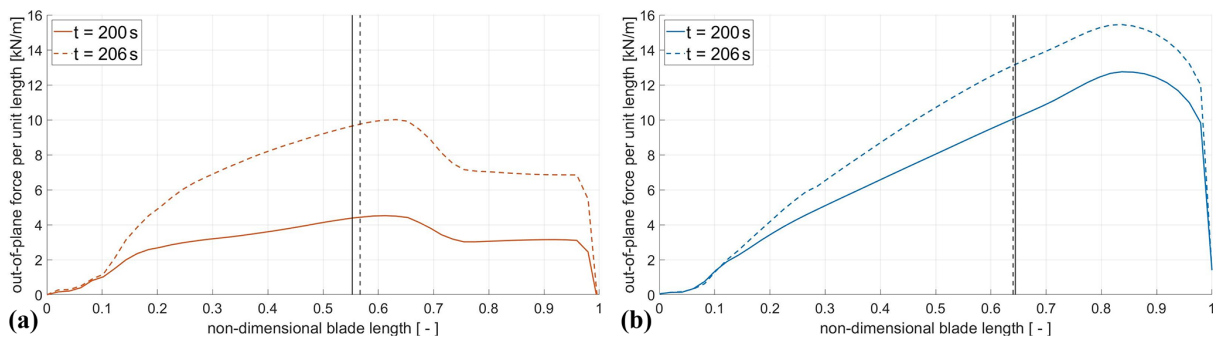


Figure 2.17: Out-of-plane forces per unit length under extreme vertical wind shear (EWSV 2): for the Hybrid-Lambda Rotor **(a)** and for the IEA reference turbine **(b)**. Resulting lever arms are indicated with vertical black lines.

Next, we look at the time-resolved change in the force distribution during the extreme shear event. For the reference turbine, the radial gradient of the force distribution increases with increasing wind shear. For the Hybrid-Lambda Rotor, the characteristic kink in the force distribution leads to lower maximum out-of-plane forces per unit length, even in the transient case. The non-dimensional lever arm is only slightly increased during the event and is still much lower than for the reference turbine. We further found the increased flexibility of the Hybrid-Lambda Rotor beneficial in this case. The increasing wind shear leads to a downwind deflection of the blade, which reduces the relative inflow in the outer part of the blade and consequently reduces the load overshoot.

All in all, the lower non-dimensional lever arm and the dynamics of the blade contribute to beneficial behaviour under extreme shear events, which leads to only mild increases in the flapwise RBM compared to the reference turbine.

2.3.5 Techno-economic evaluation

After discussing the aerodynamic characteristics of the Hybrid-Lambda Rotor and setting up a structural model for the blades and the tower, we can combine those findings in a techno-economic evaluation. We calculate the gross AEP (neglecting availability, grid and wind farm losses) for three different offshore sites with the corresponding Weibull distributions shown in Fig. 2.18. First, we chose a reference site in the German North Sea at the north-west end of zone 4 (according to Federal Maritime and Hydrographic Agency of Germany, 2020) where the application of 15 MW offshore wind turbines is expected in the near future. The Weibull distribution is derived by averaging wind data from the New European Wind Atlas for 10 years. A generic US East Coast site serves as a second reference site, as mentioned in the reference turbine report by Gaertner et al. (2020). A third site is chosen to mimic the future wind conditions in the centre of the German Bight when the increasing number of installed wind farms will influence the wind resource in the boundary layer. Here, a Weibull distribution is adopted from Pettas et al. (2021), where data from the measurement platform FINO1 are analysed after the beginning of operation of upstream wind farms.

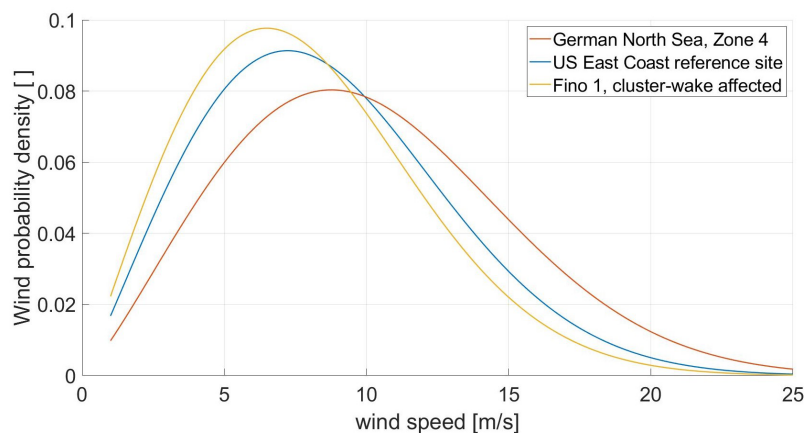


Figure 2.18: Weibull distributions for three reference sites.

First, we want to discuss how the modified power curve corresponds with the annual energy production. Figure 2.19 shows the gross energy yield per wind speed bin together with the Weibull distribution of the cluster-wake-affected reference site. It becomes clear that for wind speeds of less than 10 ms^{-1} , the energy yield is significantly increased by the Hybrid-Lambda Rotor. The financial losses due to derating the concept turbine for wind speeds greater than 15 ms^{-1} are very mild due to the low-wind-speed probability and the low market value of wind power.

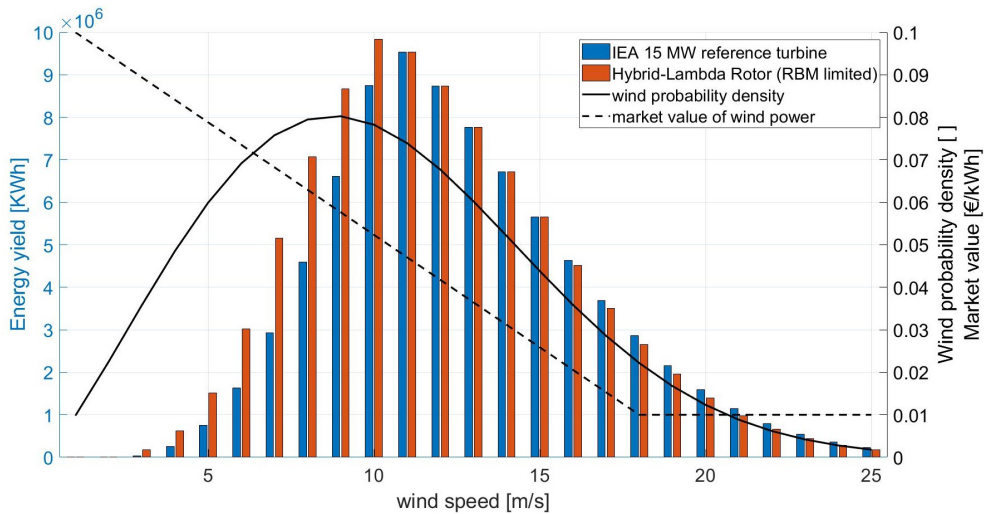


Figure 2.19: Gross energy yield, wind speed distribution (FINO1 cluster-wake affected) and market value of wind power.

As explained in Sect. 2.1, the AEP should no longer serve as merit functions because wind power will be more valuable on light-wind days. To evaluate the results from the stationary BEM simulations, we calculate the economic revenue by weighting the energy production in each wind speed bin with the market value, as predicted by May et al. (2015) and visualized in Fig. 2.19. The results for the three reference sites are reported in Table 2.3, and the investigation points out a clear trend. The increase in economic revenue is always greater than the increase in AEP because the energy yield in light winds is more valuable on the energy system level. The benefit of the concept further increases if the future development of the offshore wind resource is considered. The power characteristic of the Hybrid-Lambda Rotor becomes even more attractive if the best sites are occupied and if cluster-wake effects need to be considered. In this case, AEP and economic revenue increase by 21 % and 30 %, respectively, when compared to the reference turbine. Enlarging the rotor diameter always leads to an increased AEP. Therefore we further compare the Hybrid-Lambda Rotor to the scaled version of the reference turbine with conventionally applied peak shaving, limiting the same maximal flapwise RBM (see dashed green line in Fig. 2.9). Considering the cluster-wake-affected wind speed distribution, the AEP can be increased by 3 % and the economic revenue by 4 %.

Considering costs usually leads the designer to the objective function LCoE. But this metric neglects the variability in the market value of wind power and should not be

Table 2.3: Weibull factors (A, k), AEP and annual economic revenue expressed as ratio to the reference turbine (ref.) for three reference sites

	A	k	Ratio: Hybrid-Lambda / ref.		Ratio: Hybrid-Lambda / scaled ref. (conv. peak shaving)	
	[m s^{-1}]	[-]	Revenue	AEP	Revenue	AEP
German North Sea zone 4	11.48	2.22	1.21	1.11	1.03	1.02
Generic US East Coast site	9.77	2.12	1.27	1.17	1.036	1.027
FINO1 cluster-wake affected	8.96	2.06	1.30	1.21	1.04	1.03

used to assess turbine concepts that aim to provide a demand-oriented power feed-in. When evaluating the aero-structural optimization on an energy system level, we use the cost of valued energy (COVE). This metric is defined by dividing the annualized costs by the produced energy weighted with the normalized market value at the time of production as described by Simpson et al. (2020). With a cost model implemented in WISDEM, the annualized costs are calculated. Further, the energy yield per wind speed bin is weighted with the expected normalized market price of wind power in the corresponding wind speed bin, as depicted in Fig. 2.19. Figure 2.20 shows that the COVE could be reduced by 13 % with the initial blade and tower design (cf. Fig. 2.11) and by a further 3 % with the structural optimization of the blade and the tower for the cluster-wake-affected wind speed distribution. This figure also includes the LCoE to give an insight into how much of this reduction can be attributed to cost and AEP optimization versus the adaption of the market conditions. A breakdown of the costs for the most important turbine components is shown in Fig. 2.21. Obviously, the largest increase in costs compared to the reference turbine is seen for the blades, since this is the part that increased the most in terms of size and complexity. In fact, the costs of a blade increased by a factor of 2.8 (equals $n^{3.37}$). Related to the much heavier blades and the increased aerodynamic loading, the pitch system also needs to be sized properly. Hence, the pitch system (plotted for all three blades) sees the second highest increase with a factor of 1.8 compared to the reference turbine. The tower costs increased by a factor of 1.2. The costs for the direct drive generator have the largest share of the total turbine costs, and the derived generator costs for the reference turbine are comparable with the findings of Barter et al. (2023). For the Hybrid-Lambda Rotor, they increased by a factor of 1.22, since the rated generator torque increased. These numbers should only indicate an approximate trend of the cost breakdown, since the cost model in WISDEM relies on simplified scaling rules coupled to empirical datasets. For more insights, sophisticated models need to be set up for components like the pitch and yaw system or the generator.

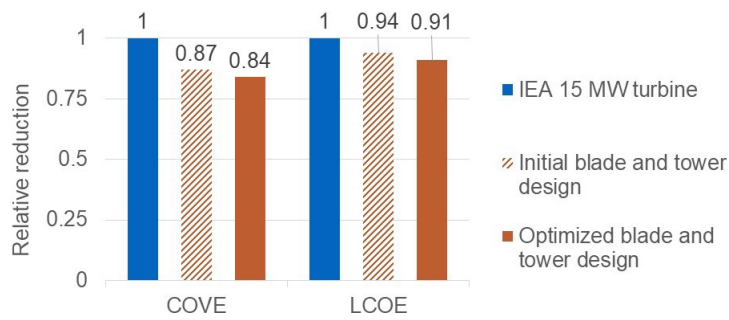


Figure 2.20: Reduction in the cost of valued energy and the LCoE relative to the reference turbine for the cluster-wake-affected wind speed distribution.

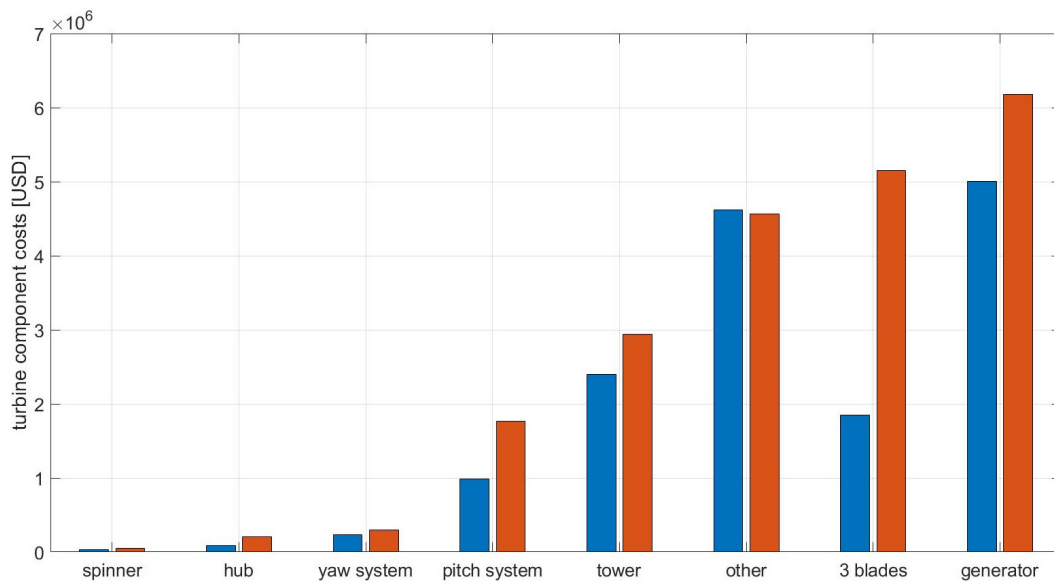


Figure 2.21: Estimation of turbine component costs for the IEA 15 MW (blue) and the optimized Hybrid-Lambda turbine (red).

2.4 Discussion

Designing blades for wind turbines usually follows several objectives and involves a multi-disciplinary approach. The novelty of our method is the dramatic reduction in the specific rating for offshore turbines. Moving away from designing the blade for one single optimized operational point, we include the application of peak shaving in the design process and introduce a design for two TSRs. This enables a unique change in the angle-of-attack distribution over the blade span when switching between the operating modes without complicating the technical implementation with additional actuators on the blade. Combined with an adapted controller, the design driving loads in transient DLCs can be reduced. The design methodology introduced should be seen as a basis for a wide range of blade design problems and can be customized accordingly.

The exemplary solution worked out in this paper, a 15 MW turbine with a specific rating of 180 W m^{-2} , should only illustrate the possibilities of the design methodology. Further, we draw the comparison once again to existing offshore turbine designs that feature specific ratings from 350 to 450 W m^{-2} , as reported by Borrmann et al. (2018). Other design problems will lead to other solutions, including different specific ratings. Moreover, the choice of design TSRs can be adopted, and the fact that we chose a stepwise implementation along the blade span with a sharp transition region should not hinder the designer's creativity. Alternatively, a continuous distribution of design TSRs along the blade span would be a possible extension of the methodology.

The Hybrid-Lambda concept can play an important role in the future path of the deployment of offshore wind energy. The increased power production in light winds will lead to a more steady power feed-in and will increase the value of wind power in the broader context of the future energy mix. This leads us to the question of the objective functions for the given design problem. Optimizing for the lowest LCoE on a single turbine level, as has mostly been done in the past, will lead to turbines with increased rated power and medium to high specific ratings. As pointed out by many other studies (e.g. Dykes et al., 2020; Simpson et al., 2020), there is the need for a change in mindset in the design objectives. The variability in the market value of wind power can no longer be neglected, and objective functions like the COVE, "system levelized cost of energy" or "value factor", just to name a few, as described in Simpson et al. (2020), should be included in future design problems. Further, wind-farm-related design objectives like wake-turbine interactions, wind farm control and large cluster wakes will influence forthcoming optimization objectives and might drive the designs in the direction of lower specific ratings and lower induction factors.

Placing the Hybrid-Lambda concept in the context of the literature, we see common trends for several design variables, especially the axial induction factor and the specific rating. In the strong-wind mode, the distribution of the axial induction over the blade span shows similarities with the one derived by Jamieson (2020). This is the analytically derived distribution that leads to the most possible extension of the rotor radius by incorporating a low-induction design that features constant loading compared to a conventional design. In terms of the specific rating, the Hybrid-Lambda concept follows similar objectives to the DTU Low-Wind turbine for onshore siting by Madsen et al. (2020), but the innovations in the presented design methodology enable the application for offshore sites. A simple transfer of a low-specific-rating turbine with

a conventional blade design to offshore sites would be inherently inefficient as the reduced aerodynamic efficiency in the upper partial-load range would coincide with the maximum wind speed distribution and associated high losses in the energy yield. The idea of designing a blade for two TSRs was first mentioned by Wobben (2001). However, the main objective of this design was the reduction of stall effects in turbulent wind conditions.

One of the main pillars of the Hybrid-Lambda concept is the ability to change the angle-of-attack distribution over the blade span by switching between the operating modes. In fact, this change seems to be very small as we are tweaking the distribution by only a few degrees. Although 1° in the change in the angle of attack can mean a lot to an aerodynamicist, these values are computed in steady-state simulations and neglect blade torsion as per definition of the structural methodologies used in this paper. Thus, we want to raise the question of whether controlling 1° in the angle of attack is at all feasible in a real application of a blade with 158 m length. Dealing with atmospheric turbulence, blade torsion, extreme shear events, low-level jets and other complex phenomena in offshore applications raises the question of whether those effects would simply dominate the uncertainties in the operation of such a blade. We owe an answer to that in this paper. The concept could possibly be supported and the effects of the angle-of-attack change could be even enhanced by the usage of distributed aerodynamic control elements on the blade. Trailing-edge flaps could increase the change in lift difference, and leading-edge slats could enlarge the operational range of the airfoils by delaying stall effects and allowing for higher angles of attack. Nevertheless, the authors decided to carry out this study without the usage of active control elements on the blade. Additional actuators introduce many problems, especially on very large blades, like additional masses, lightening issues, increased costs and reduced reliability. Although those add-ons could mitigate the dynamic loads when the turbine is in operation, storm events are still critical design load cases. The presented design method leads to only 20 % increases in flapwise RBM for the DLCs with extreme transient shear events. But storm events with a large yaw misalignment still lead to an increase of 40 % compared to the respective ultimate load from the reference turbine. Nevertheless, the absolute value of the flapwise RBM is lower for the storm events than the maximum values for normal power production and extreme shear events. Limiting the loads in storm events is a difficult exercise as the turbine is not in operation and the usage of the control system is limited in the occurrence of faults. Nevertheless, we see a benefit in the slender blade design of the Hybrid-Lambda Rotor as the shorter chord length leads

to reduced lift forces. Especially the outer part of the blade has a high lever arm and contributes the most to the RBM. But the slender design of the outer region helps to reduce the storm loads on the blade.

The consequences of the above-mentioned limitations of the methodology can be used as a guideline for further research. The blade design needs to be extended by including blade torsion, which also opens up new opportunities for further improvements in the load-limiting techniques using bend–twist coupling. Extending the structural methodology would allow us to calculate the blade torsional deformation under specific operating conditions. An iterative step back to adjust the design twist could optimize the angle-of-attack distribution for a given operational point, introducing increased loading for lower wind speeds and further relief for higher wind speeds. Finally, all those design features will not lead to a viable blade design as long as the aeroelastic stability is not given. As pointed out by Branlard et al. (2022a), aeroelastic stability is a critical issue for very large wind turbine blades and it can easily overshadow other design drivers.

As mentioned above, the analysis does not include fatigue loads. This is certainly a very important topic for large rotors. But in our opinion, including fatigue would only make sense if the conclusions lead to adjustments and improvements in the design. Achieving a fatigue-safe design could further require adapted controller strategies (like individual pitch control, model predictive control or lidar-based feed-forward control) and a thorough implementation in the aero-servo-elastic simulations, which goes beyond the scope of this publication.

As a final point, we discuss the application of design load cases to rotors of such size. In Sect. 2.3.4.4, we introduced two wind fields for the event of extreme vertical wind shear. Given the implementation of the wind profile as equated in the IEC 61400-1 (2019), a larger turbine will be tested with lower shear. Across rotors with different radii, the maximum wind speed at the top of the rotor disc is kept constant rather than accounting for larger spatially distributed wind speed changes. On the other hand, the investigations above made clear that placing a large turbine like the Hybrid-Lambda Rotor in the same wind field as the reference turbine barely leads to a realistic load case, considering a wind speed change at the top of the rotor disc from 12.5 to 23 ms^{-1} in 6 s and wind speeds close to zero at the bottom. Further metrological investigations will reveal what special inflow conditions very large wind turbines will need to face. Those

are operating in regions of the atmospheric boundary layer, like the transition to the laminar Ekman layer, where the interactions with the rotor are not yet fully understood.

2.5 Conclusions

In this paper, we introduced an innovative design method for offshore wind turbines. It can be applied to any given design problem that aims to tremendously reduce the specific rating to enable an increased power feed-in for low wind speeds while maintaining the design driving loads. The design method integrates the application of peak shaving into the design process rather than accepting peak shaving as a necessary evil. Designing the blade for two different TSRs gives the opportunity to switch between a light- and a strong-wind mode during operation. In the latter operational mode, peak shaving is applied very efficiently, thanks to a beneficial change in the AoA distribution. This can be achieved with careful consideration of three aspects: the change in the inflow angle when lowering the TSR, a twist offset applied to the inner blade section and simultaneous pitching during the transition to the lower TSR. The power characteristics of the turbine better match the demand in the power system as the energy yield in light winds is significantly increased. Putting this into the context of the future development of the wind resource, the advantages become apparent, as wind probability distributions will shift to lower wind speeds due to the increasing clustering of large wind farms in several regions. Although the peak-shaving region coincides with the maximum of the Weibull distribution for offshore sites, the losses are mild thanks to the efficient load reduction technique and the AEP is increased significantly. As energy will be (and already is) more valuable in light winds, the concept profits from a low COVE.

The presented design method was elaborated on a 15 MW offshore wind turbine to illustrate its concrete benefits. Comparing the Hybrid-Lambda Rotor to the reference turbine, the AEP and the economic revenue can be increased by 21 % and 30 %, respectively. With an optimized blade and tower design, the COVE can be reduced by 16 % compared to the reference turbine. We further compared the Hybrid-Lambda Rotor to a conventional blade design (upscaled to the same rotor radius) with a simple peak-shaving application that limits the same maximum flapwise RBM. In this case, the Hybrid-Lambda Rotor can still outperform the conventional design by 3 % in terms of AEP and by 4 % in terms of economic revenue.

Using state-of-the-art design tools, we showed that it is possible to set up a consistent system-based turbine model for such an innovative rotor concept. The aero-structural optimization resulted in a blade that is 14 % lighter compared to a geometrically scaled blade of the same size. Aeroelastic simulations showed the ability of the controller to change between the operating modes in turbulent wind, and the Hybrid-Lambda Rotor was further compared to the reference turbine in a set of design load cases. This comparison shows promising results for the flapwise RBM, blade-tip-to-tower clearance and thrust. The flapwise RBM can be limited to the same maximum value as the reference turbine in power production DLCs. In extreme shear events, the flapwise RBMs are 20 % higher and in storm events 40 % higher compared to the reference turbine. Thrust and blade-tip-to-tower clearance could be limited to the same value as for the reference turbine. The increase in edgewise RBM and tower-top movements shows open challenges in designing wind turbines of this size. It further becomes clear that advanced control strategies are needed to further limit the dynamic loads and to improve the switching between the operating modes. Nevertheless, even with a basic controller, the Hybrid-Lambda Rotor shows significant advantages in reducing the loads, although the swept rotor area is increased by 84 % compared to the reference turbine.

Data availability

For the Hybrid-Lambda Rotor, we provide the turbine model in the windIO format, the simulation model for OpenFAST and operational parameters in tabulated format under the following repository: <https://doi.org/10.5281/zenodo.10406459>, Ribnitzky, 2023.

Financial support

The work presented in this paper was funded by the Deutsche Forschungsgemeinschaft (DFG, German Research Foundation) – project ID 434502799 – SFB 1463.

Chapter 3

Rotor and wake aerodynamic analysis of the Hybrid-Lambda concept - an offshore low-specific-rating rotor concept

Apart from minor adjustments and corrections, the content of this chapter is identical to that of the following publication:

Daniel Ribnitzky, Pietro Bortolotti, Emmanuel Branlard and Martin Kühn (2023). 'Rotor and wake aerodynamic analysis of the Hybrid-Lambda concept - an offshore low-specific-rating rotor concept'. In: *Journal of Physics: Conference Series* 2626.1, p. 012008. ISSN: 1742-6588. DOI: 10.1088/1742-6596/2626/1/012008

Reproduced in accordance to the Creative Commons Attribution 3.0 License.

Abstract

The low-specific-rating rotor concept Hybrid-Lambda introduces a blade design with nonuniform distribution of design variables (design tip speed ratio and axial induction) along the blade span to alleviate loads of the outboard section in strong winds. In this paper, we validate aerodynamic design calculations, which were carried out with the blade element momentum theory by comparing the results to free vortex wake investigations (FVW). Furthermore, we investigate the wake behaviour with FVW and large-eddy simulations. The results show good agreements between the blade element momentum theory and FVW for integrated rotor quantities (power and thrust). Small

deviations are present when the gradients of axial induction along the span are large. The wake of the Hybrid-Lambda Rotor shows advantages in the near-wake region (up to 4 diameters $[D]$ downstream), especially in the outer wake annulus and in low turbulence scenarios. For further downstream positions, the wake is comparable to that of the reference turbine.

3.1 Introduction

Countries with a high share of wind power in the energy system suffer from low market values of wind power during periods of strong winds, whereas the market value during light-wind-days is comparably high (May et al., 2015). Thus, there is a demand for turbines with an increased power capture on light-wind-days. In recent years, low-specific-rating (also referred to as "low-wind") wind turbines have received increased attention (e.g. Madsen et al. (2020)), especially onshore. Large rotors increase their power capture in light winds, but they generally come with the need for load-reduction techniques when approaching rated wind speed. This is usually done by peak shaving (pitching to feather to limit the loads) and leads to large losses in the upper partial-load range. Especially for offshore sites, this coincides with the peak of the wind speed distribution. The Hybrid-Lambda Rotor, introduced by Ribnitzky et al. (2022) and further explained in Sect. 3.2, integrates the application of peak shaving into the blade design process rather than accepting it as a necessary evil. The design process is approached by balancing the two objectives of limiting power losses in the peak-shaving region and maximising power output below this region. The design features a nonuniform distribution of the axial induction along the blade span to alleviate loads of the outboard blade section in strong winds.

The enhanced wake recovery of a turbine with a nonuniformly loaded rotor was investigated by Kelley et al. (2014) and Yang et al. (2015). They found that a blade design with larger spanwise gradients of bound circulation exhibit shorter and faster mixing far wakes. Further, Madsen et al. (2021) analysed additional benefits of low-specific-rating turbines on wind farm effects. Knauer (2021) introduced a rotor design that enhances wake diffusion, using a ventilation area with negative axial induction close to the blade root.

However, the design objectives as well as the resulting blade design of the Hybrid-Lambda Rotor differ from the aforementioned studies, because it was designed

for efficient load reduction and not primarily for enhanced wake mixing. The specific aerodynamics are of interest from a scientific point of view.

First, the nonuniform distribution of the axial induction along the blade span leads to large circulation gradients. This raises the question: To what extent is the assumption of independent blade elements in the blade element momentum (BEM) algorithm violated? The application of free vortex wake (FVW) methods would be scientifically more appropriate because they do not rely on independent blade elements. Modelling of radially varying circulation is addressed by Branlard and Gaunaa (2016).

Second, a specific wake characteristic is expected, because only a part of the rotor is designed as a low-induction rotor and the rotor disc is nonuniformly loaded. Common wake engineering models can no longer be applied. We expect additional gradients in the wake profiles, and we address the question whether those will destabilize and further diffuse the wake.

The objectives of this paper are to analyse the Hybrid-Lambda Rotor with high-fidelity aerodynamic simulation tools, specifically to:

1. Investigate the Hybrid-Lambda Rotor with the FVW code and study the limits of the calculations made with the BEM theory. We compare integrated rotor quantities as well as spanwise resolved variables across the two methods.
2. Compare the wake characteristics of the Hybrid-Lambda Rotor with the International Energy Agency (IEA) 15-MW offshore reference turbine on different fidelity levels:
 - (a) FVW simulations with a steady uniform inflow and numeric turbulent wind field
 - (b) Large-eddy simulations (LES) with a neutral and stable atmospheric boundary layer (ABL)
3. Investigate a simplified wind farm layout in LES and compare the power output to assess the benefits of the Hybrid-Lambda concept.

3.2 The rotor concept

The Hybrid-Lambda Rotor is a low-specific-rating concept for offshore siting, exemplified with a 15 MW wind turbine. The uniquely low specific rating of 180 W m^{-2} corresponds to a D of 326 m. The objective of the conceptual design is to limit the stationary loads (blade flapwise root bending moment (RBM) and thrust) to the maximum values of the IEA 15-MW reference turbine (Gaertner et al., 2020) (with a D of 240 m). The main idea of the concept is to design the inner 70% of the rotor differently than the outer 30% and to operate the rotor at a tip-speed ratio (TSR) of 11 in light winds and at a TSR of 9 in stronger winds. The outer portion of the blade is designed for a TSR of 11 and an axial induction of 0.21. When operated at the TSR of 9 the outer portion should produce an axial induction below 0.15. The design for a high TSR and low induction results in a much more slender outer section compared to a traditional design. The inner portion of the rotor is designed for a TSR of 9 and an axial induction of 0.21. When operated at the TSR of 11 the inner portion should produce an axial induction close to 0.33. In light wind conditions, the rotor operates at the high TSR, and the slender outer part contributes to the increased power capture. The inner part of the rotor operates like a conventional rotor with an axial induction factor close to 0.33. The axial induction distribution and the shift in the operating mode is shown in Fig. 3.1. In stronger winds (but still below the rated wind speed), the design value of the stationary RBM is reached. Then, the TSR reduces to a value of 9, and the torque generation shifts to the inner section of the rotor, which is now operating at its design point. In contrast, the outer region is significantly relieved, because it is no longer operating at its aerodynamic optimum. This reduces the lever arm of the resulting bending force, and additional peak shaving by blade pitching ensures the limitation of the loads. For further information on the Hybrid-Lambda Rotor, the reader is referred to Ribnitzky et al. (2022).

3.3 Methods

We performed aeroelastic simulations in OpenFAST, using ElastoDyn as the elastic solver (Bonnie Jonkman et al., 2022). To address the first objective, i.e., the comparison of the BEM and FVW code, we simulated the Hybrid-Lambda Rotor using steady and uniform inflow with the standard BEM solver and the FVW module OLAF (Branlard et al., 2022b; Shaler et al., 2020). We investigated three operating modes:

- 1) Operating point 1: Light-wind mode, defined by the high TSR of 11 and maximum wind speed just before the limiting loads are reached, which is 6.8 m s^{-1}

- 2) Operating point 2: Strong-wind mode, defined by the low TSR of 9 and the corresponding wind speed when the transition from the high to low TSR completes, which is 8.3 m s^{-1}
- 3) Operating point 3: Rated power conditions, defined by the low TSR of 9 and a wind speed of 10.2 m s^{-1} .

To investigate the wake characteristics, we first isolate the effects on the wake due to the unique aerodynamic rotor design of the Hybrid-Lambda Rotor in steady and uniform inflow in FVW. Then, we can evaluate if those advantages are still present in realistic inflow conditions by simulating numeric turbulent wind fields (FVW) and full ABLs (LES).

We performed FVW simulations with both the Hybrid-Lambda Rotor and the reference turbine. We investigated steady and uniform inflow conditions in operating points 1 and 3 and turbulent wind fields, calculated with TurbSim (Jonkman and Buhl, 2006) for operating point 1. For the wind fields, we chose a relatively low turbulence intensity of 5% and a low shear exponent of 0.1. Those values are of high relevance for wake investigations, because power losses due to distinct wakes are most present in those low turbulence conditions.

We further performed LES for a single turbine with the incompressible flow solver AMR-wind (Sprague et al., 2020), using its actuator line model coupled to OpenFAST. We investigated a neutral and a stable ABL for operating point 1. In this case, both turbines (the Hybrid-Lambda Rotor and IEA 15-MW turbine) were simulated in the same ABL precursor run, resulting in slightly different mean wind speeds and wind directions at their specific hub heights. Turbines were yawed to the exact wind direction at hub height, and the resulting wind fields were turned by the yaw angle to align the wakes of the Hybrid-Lambda Rotor and the IEA 15-MW. This approach corresponds to a site-specific turbine comparison, highlighting the advantages of possibly repowering existing wind farms. The LES wind fields represent operating point 1. This means the Hybrid-Lambda Rotor is in light-wind mode and the reference turbine is in region 1.5 with an average pitch angle of 1.6° to feather (with controllers active for both turbines). This leads to averaged thrust coefficients of 0.79 for the reference turbine and 0.75 for the Hybrid-Lambda Rotor. The neutral ABL shows a turbulence intensity of around 10% and the stable ABL of around 2.4%. The average shear exponents are 0.09 and 0.14, respectively. In the turbine simulations, we used grid refinements in proximity of the

rotor to sufficiently resolve the nonuniform distribution of the variables along the span of the blade. We aimed for a grid size of 3.75 m, which corresponds to 87 points along the rotor diameter for the Hybrid-Lambda Rotor and 64 points for the reference turbine.

The wake investigations are analysed by calculating time-averaged wake profiles, normalized to the rotor diameter of the respective turbine. We further compare the mean velocity wind fields in a horizontal plane at hub height. For averaging, an output frequency of 1 Hz is used, and the time window is set to 400 seconds.

To address the performance of the Hybrid-Lambda Rotor in a wind farm configuration, we performed LES with two aligned turbines. In order to investigate the opportunity of the Hybrid-Lambda Rotor to be used as a repowering solution for existing wind farms, we chose a fixed absolute spacing of 6 of the reference turbine's diameters for both turbine simulations. This results in a relative spacing of 4.4 D for the Hybrid-Lambda Rotor. This simulation setup corresponds to a wind farm design problem when the given surface area is restricted and the ratio of rated power to surface area is kept constant rather than the relative turbine spacing.

3.4 Results

In this section, we first compare the BEM and FVW results for the Hybrid-Lambda Rotor. In the second and third part, we address the wake investigations using the FVW code and LES.

3.4.1 Comparison of BEM and FVW results

We performed aeroelastic simulations for the Hybrid-Lambda Rotor for operating points 1 and 2 using BEM and FVW methods. Results show that, for steady uniform inflow, the integrated rotor quantities (power and thrust) are in very good agreement for the two methods. For the light-wind mode, the aerodynamic power exactly matched, whereas the FVW code computed about 0.5% higher thrust. For the strong-wind mode, the FVW code computed 1.5% higher power and 0.75% higher thrust.

Next, we compare the radially resolved axial induction factor (as shown in Fig. 3.1). For the light-wind mode, the FVW code computed an axial induction factor that is about 5% lower for the inner part of the rotor and up to 15% higher for the outer part of

the rotor compared to the BEM results. Thus, the FVW code predicts a smaller change of induction between the two blade regions. The observed differences might be due to additional vortices, which are created by the strong gradients of the circulation distribution at a 0.7 nondimensional blade length. These vortices increase the induction on the outer part of the rotor and decrease the latter on the inner part. Looking at the strong-wind mode this trend persists but is much less distinctive. The axial induction distribution is in good agreement for the strong-wind mode among the two methods. As the gradients in the axial induction distribution at a 0.7 nondimensional blade length are reduced in the strong-wind mode, weaker vortices are created, which leads to reduced differences between the BEM and FVW results compared to the light-wind mode. The angle of attack distribution in Fig. 3.1 shows similar results. In the light-wind mode, the higher axial induction outboards (computed by the FVW code), leads to slower axial velocity components. Consequently, the angle of attack is reduced for the outer part of the blade in the FVW calculations. For the inner part of the blade, a similar line of arguments can be applied vice versa. Again, the differences in the angle of attack distribution in the strong wind mode between the two codes are very mild.

In summary, the FVW simulations confirm that the aerodynamic design ideas of the Hybrid-Lambda Rotor are applicable, although they reach the limit of the assumptions made in the BEM theory. The assumption of independent blade elements is violated in the transition region of the two blade regions, as strong gradients in the circulation are present. These gradients introduce additional vortices, but they act in favour of the Hybrid-Lambda concept, as the aerodynamic power computed by the FVW code slightly increased.

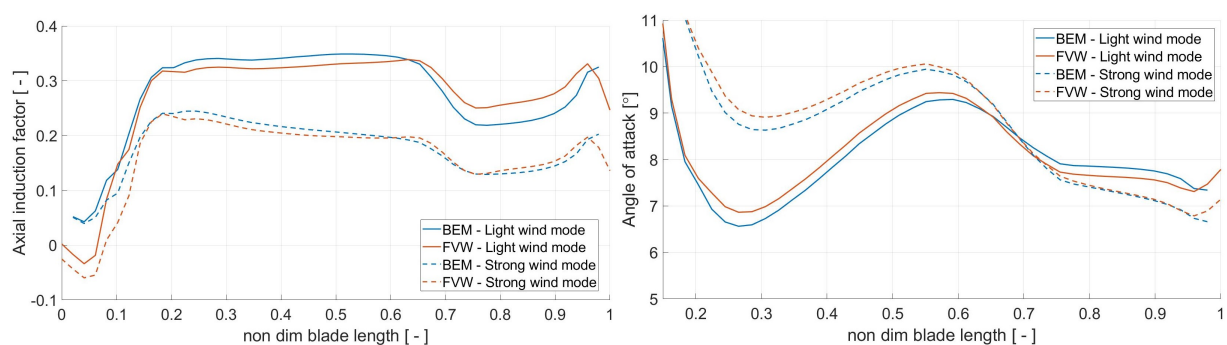


Figure 3.1: Axial induction distribution (left) and angle of attack distribution (right) for operating point 1 (solid lines) and operating point 2 (dashed lines), comparing BEM (blue) and FVW (red)

3.4.2 Wake investigations using FVW

In this section, we investigate the wake behaviour of the Hybrid-Lambda Rotor simulated by the FVW model. We first address steady and uniform inflow to identify general characteristics of the near wake. The FVW method is not ideal to investigate the far wake, and the reader is referred to section 3.4.3 for further information about the far wake. In the FVW simulations, the wake becomes unstable beyond 2.5 D. Beyond this distance, the wake profiles should be considered with care, because OLAF does not account for viscous diffusion. Further, the nacelle is not modelled in FVW, which led to an overspeed in the center of the wake within the first 1 D downstream. Nacelle effects were modelled in the LES investigations (Sect. 3.4.3).

Figure 3.2 compares the wake of the Hybrid-Lambda Rotor with the reference turbine for the light-wind mode and rated wind speed. The inner 70% of the rotor is displayed with a black bar, whereas the outer part of the rotor, which is designed for low induction, is displayed with a red bar. The axial induction distribution of the Hybrid-Lambda Rotor is reflected in the wake velocity. For the light-wind mode, the outer part of the blade causes less deceleration of the flow, which led to an outer annulus of the wake with a higher wind speed. The strong-wind mode further revealed the potential for wind farm power to increase, because the flow in the wake did not decelerate as much as the reference turbine. This is not only due to the aerodynamic rotor design but also due to operation at lower thrust coefficients in the peak-shaving region. Still, it highlights a major advantage as wake deficits are greatly reduced close to rated wind speed.

Figure 3.3 compares the wake deficit profiles for operating point 1 and 3 at different downstream locations. The profiles show a slightly higher wake deficit for the Hybrid-Lambda Rotor for the inner rotor part, compared to the reference rotor. This is also in line with the blade design, as the axial induction for the inner rotor (0.33 for the Hybrid-Lambda Rotor) is slightly higher compared to the reference turbine (0.3 for the IEA 15-MW). Further, the gradients to the inner wake core are relatively strong in the near wake and smooth out at around 3 to 4 D downstream. For rated wind speed (operating point 3), a similar behaviour can be recognized, but the gradients in the wake profiles are reduced, which is in line with the axial induction distribution (see Fig. 3.1). The wake deficit is only almost half as strong as it is for the reference turbine in the near wake, which highlights the clear advantages in the wake deployment of the

Hybrid-Lambda Rotor. The wake of the Hybrid-Lambda Rotor also shows a straight outline in the strong-wind mode. In contrast, a significant wake extension can be observed for the reference turbine, leading to a wake width (95% of the free stream velocity) of about $1.3 D$ at a downstream position of $4 D$, whereas the the wake width of the Hybrid-Lambda Rotor is still only around $1.1 D$.

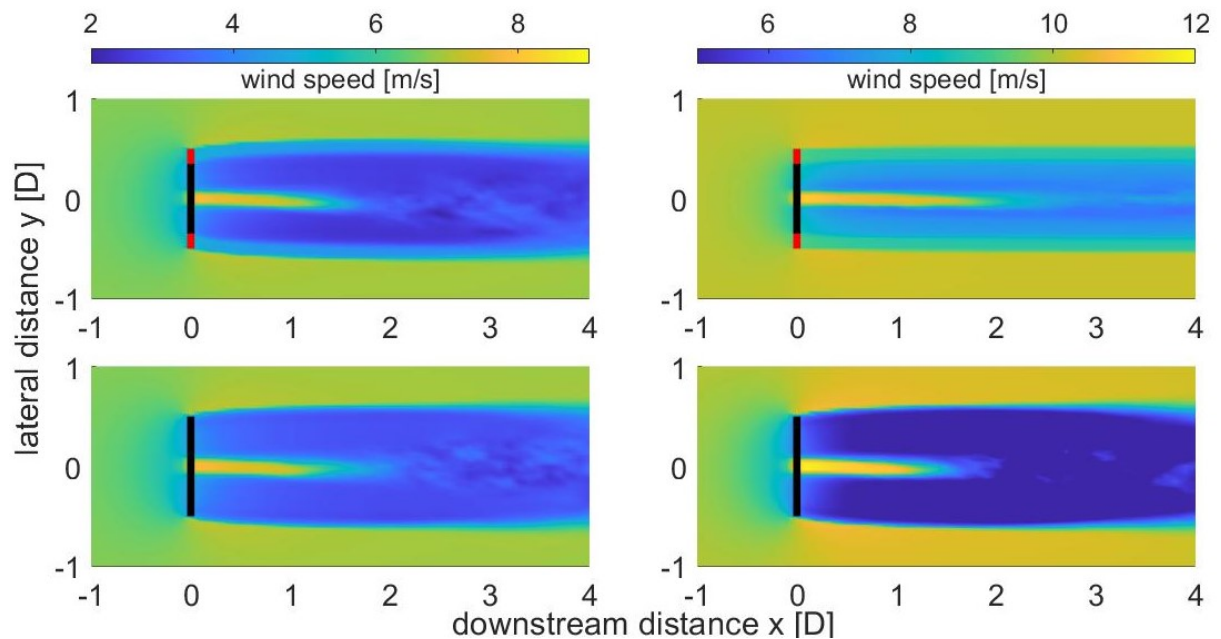


Figure 3.2: Averaged axial velocity component for steady uniform inflow (FVW). Top: Hybrid-Lambda Rotor; bottom: IEA 15-MW turbine; left: Operating point 1 (6.8 ms^{-1}); and right: Operating point 3 (10.2 ms^{-1}).

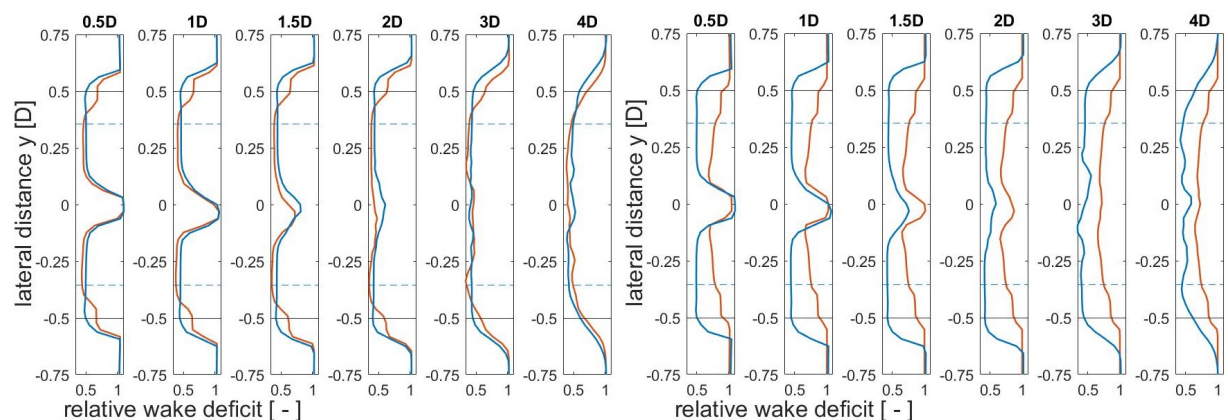


Figure 3.3: Normalized wake deficit profiles (FVW, steady uniform) for operating point 1 (left) and 3 (right). Dashed lines indicate 70% rotor radius. Red: Hybrid-Lambda Rotor; and blue: IEA 15-MW turbine.

Steady and uniform inflow does not reflect reality, but it helped us to identify and understand some basics in the wake characteristics of the Hybrid-Lambda Rotor. Next, we used numeric turbulent wind fields with the FVW code to evaluate if the characteristics, identified in the steady and uniform case, are still present when turbulence is considered. The results are shown in Fig. 3.4. The reduced wake deficit in the outer annulus is still present, but it smooths out much faster (compared to the steady case) beyond a downstream position of $1.5 D$. Turbulence is the main driver for wake diffusion and the wakes of both turbines mix much faster compared to the steady-inflow case. The wake profiles indicate a marginally better recovery for the Hybrid-Lambda Rotor at around $3 D$ downstream. For positions further downstream, both wakes seem almost fully recovered, but note that this is related to the truncation of the wake in the FVW code and does not represent a realistic behaviour for a turbulence intensity of 5%.

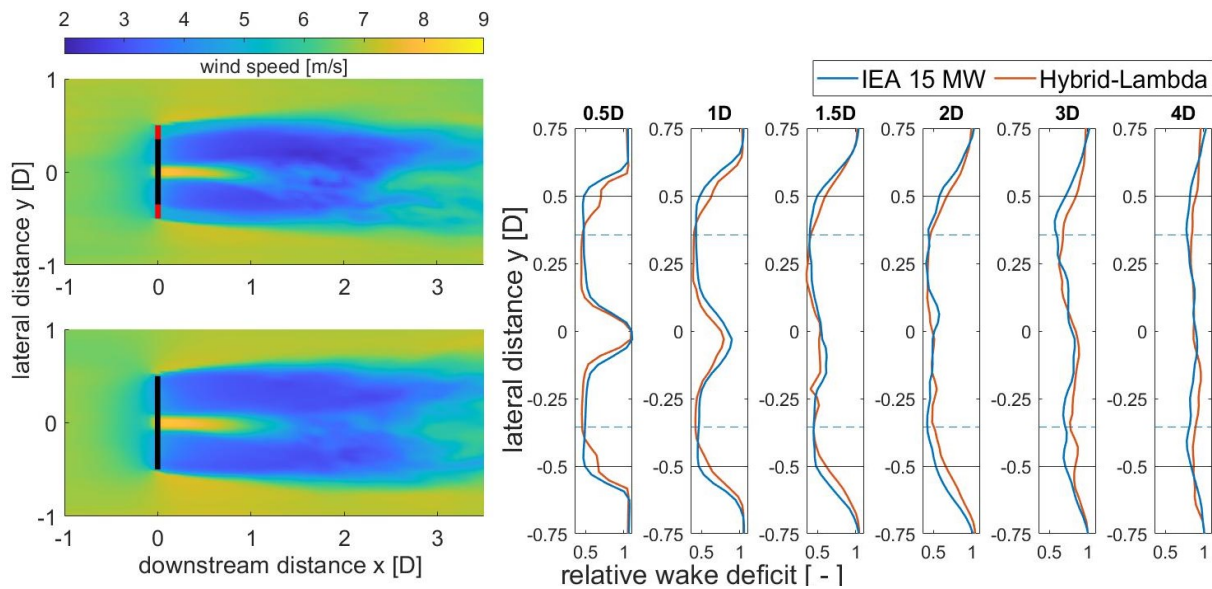


Figure 3.4: Left: Averaged axial velocity component for numeric turbulent wind field (FVW), light-wind mode (top: Hybrid-Lambda Rotor; bottom: IEA 15-MW turbine); right: Normalized wake deficit profiles

3.4.3 Wake investigations using LES and actuator line model

In a final step, we investigate the wake characteristics with LES coupled to an actuator line model and OpenFAST. We compare the wake of the two turbines and further distinguish between a neutral and a stable ABL stratification.

Starting with the neutral stratification, the corresponding wake profiles are displayed in Fig. 3.5. The gradients in the wake of the Hybrid-Lambda Rotor are comparable to the ones obtained with the FVW simulations. However, they smooth out more quickly compared to the FVW investigations. Advantages are especially distinct up to a distance of 4 D downstream and the recovery of the outer 30% of the wake is improved. In general, higher wind speeds are observed in the wake of the Hybrid-Lambda Rotor.

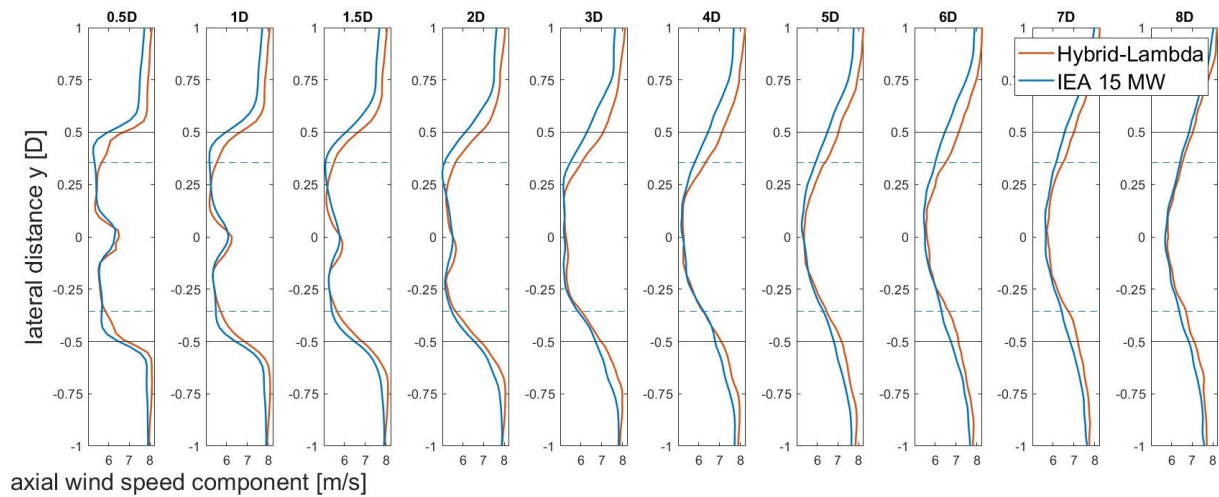


Figure 3.5: Neutral stratification: Normalized wake deficit profiles from LES (light-wind mode)

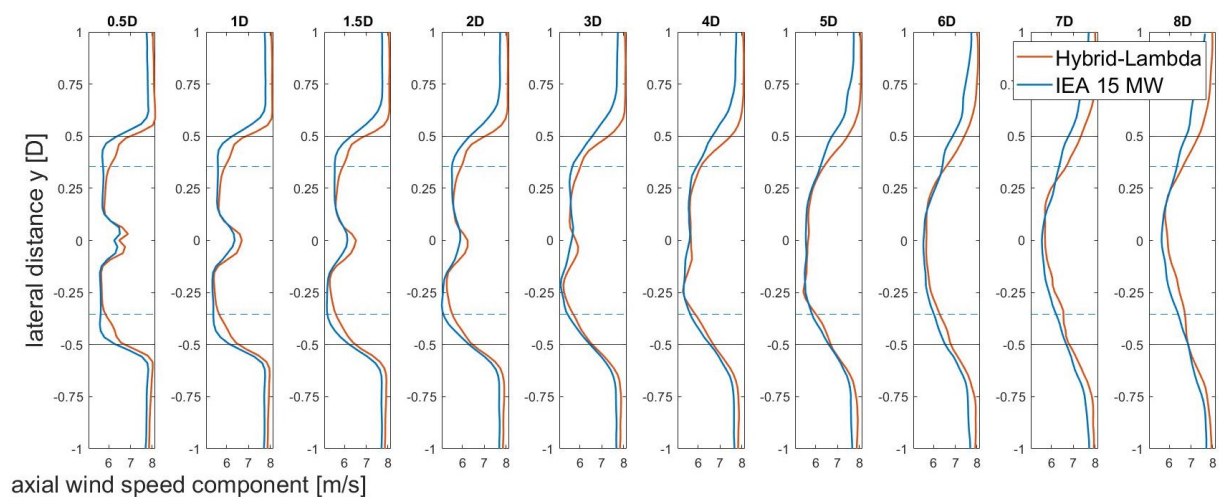


Figure 3.6: Stable stratification: Normalized wake deficit profiles from LES (light-wind mode)

Comparing these results to the stable stratification is of high interest, because wake losses are most prominent in such atmospheric conditions with a very low turbulence intensity. The results are shown in Fig. 3.6. The major driver for wake diffusion, atmospheric turbulence, is reduced, which results in wider and longer wakes. For downstream positions greater than $3 D$ the wake profiles for both turbines are wider and more plateau-like, compared to the neutral case. Further, the additional gradients in the wake of the Hybrid-Lambda Rotor persist longer. At downstream positions of 1 and $1.5 D$ (compare Fig. 3.5 and 3.6), the gradients are already smoothed out in the neutral case but still noticeable in the stable stratification. In Fig. 3.7, the averaged velocity fields are normalized with the same reference diameter for both turbines. This visualisation emphasizes the different absolute size of the wakes.

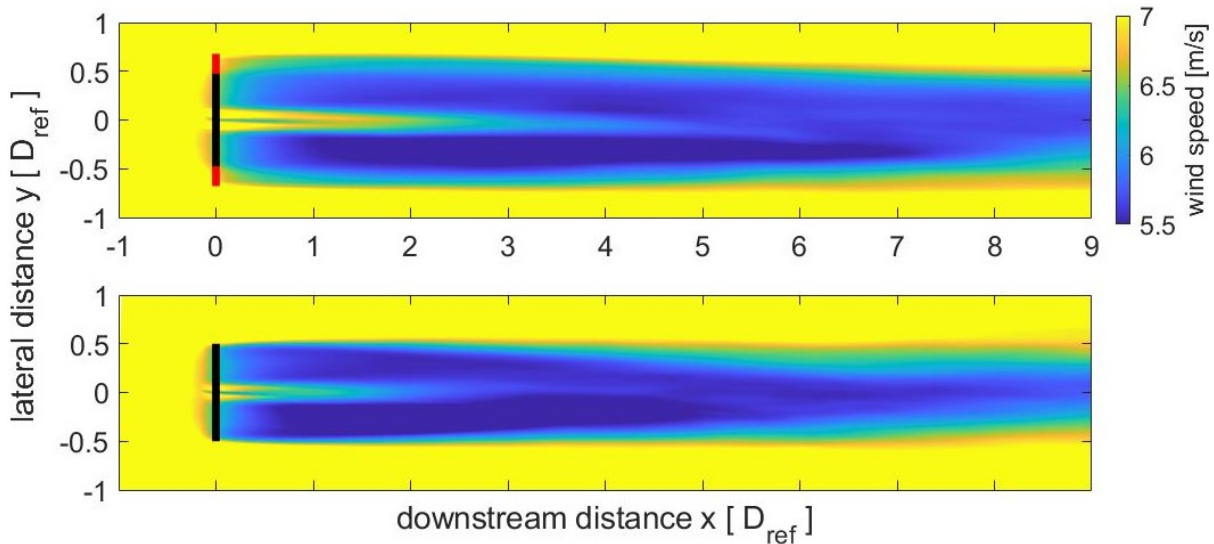


Figure 3.7: Stable stratification: Averaged axial velocity component for LES (light-wind mode); top: Hybrid-Lambda Rotor; and bottom: IEA 15-MW turbine with coordinates normalized with the diameter of the IEA 15-MW rotor for both plots

Finally, we compare configurations with two turbines in both stratifications, neutral and stable. First, we compute the energy yield by integrating the sum of the power output of the two turbines over the simulation time. The two Hybrid-Lambda Rotors can yield 1.85 times more energy in the neutral ABL and 1.91 in the stable ABL compared to the two reference turbines, respectively. Those findings are in line with the previous investigations of the wake profiles, because the advantages of the Hybrid-Lambda Rotor are more distinct in a stable ABL with a low turbulence intensity. We further compare this number to the expected scaling ratio, which results from the increase in

the swept rotor area (1.84). The additional energy yield results, apparently, from the improved wake recovery of the Hybrid-Lambda Rotor. We further compare the power ratio of the downstream and upstream turbines in Table 3.1. In the neutral ABL, the downstream Hybrid-Lambda Rotor produces 48.9% of the upstream turbine, whereas the downstream reference turbine only produces 46.8% of the upstream reference turbine. A similar trend is observed for the stable ABL with power ratios of 46.1% and 43.9%, respectively.

Table 3.1: Comparing the power ratio of downstream and upstream turbines in LES (operating mode 1)

	Neutral	Stable
Hybrid-Lambda Rotor	0.489	0.461
Reference Turbine	0.468	0.439

3.5 Discussion

The Hybrid-Lambda Rotor was not designed with the objective of enhanced wake mixing. Nevertheless, the design with a nonuniform distribution of the axial induction raises interesting scientific questions on how this affects the wake deployment. In this study, we compared two rotors of different diameters. This is a challenging comparison, but the reduction in the specific rating is the first step in the design concept of the Hybrid-Lambda Rotor. This step enables increased power capture in light winds, which is highly important for the future path of decarbonization. Blades of this size come with the need for load-reducing techniques. But applying peak thrust shaving also significantly reduces wake losses close to the turbine rated wind speed. This coincides with the maximum in the Weibull wind speed distribution (offshore) and will further increase the annual energy production on a wind farm level. Even for the light-wind mode, when no peak shaving is applied, advantages in the wake recovery are identified. To fully support this thesis, further case studies considering higher turbulence intensity and bigger farm layouts with various spacings and inflow directions should be analysed.

3.6 Conclusions

In this study, we validated the aerodynamic design concept of the Hybrid-Lambda Rotor with high-fidelity aerodynamic simulations, FVW and LES, and compared the

results to the ones predicted by BEM theory. We identified its characteristic wake behaviour and compared it to the wake of the IEA 15-MW reference turbine.

The FVW investigations support the design principles of the Hybrid-Lambda Rotor that were originally identified using the BEM theory. The integrated rotor quantities (power and thrust) obtained with the FVW and BEM methods are in very good agreement, deviating by a maximum of 1.5%. Discrepancies in the radius resolved variables are most distinct when the gradients along the blade span are large. In the light-wind mode, differences of about 15% in the axial induction distribution are observed between BEM and FVW. In the strong-wind mode, the deviations are less prominent, as the gradients along the blade span are reduced.

The wake of the Hybrid-Lambda Rotor has unique characteristics, and it shows advantages, especially in the near-wake region (up to 4 D downstream). In detail, these are higher wind speeds in the outer-wake annulus and decreased wake expansion and significantly reduced wake deficits in the strong-wind mode. Those characteristics are observed fairly consistently with both methods (FVW and LES). The advantages are most prominent in low turbulence conditions and can smear out in higher turbulence which is still the main driver for wake diffusion.

In summary, the design of a blade with strong gradients along its span is possible with the BEM theory, but a verification with a FVW code is advisable. Gradients in the axial induction distribution are reflected in the wake and can be beneficial for the wake recovery. The advantages found in this study favour an application of low-specific-rating turbines in a scenario with close spacing and low turbulence conditions. In a simplified wind farm configuration with two turbines in a fixed absolute spacing, the Hybrid-Lambda Rotor was found to yield almost twice the energy as the reference turbine (noting that both turbines have the same power rating but different diameters). Further, the ratio of the downstream to upstream turbine power production increases for the Hybrid-Lambda Rotor. This could open opportunities for repowering existing offshore wind farms with low-specific-rating turbines. Maintaining the given farm layout will save costs due to the reuse of existing infrastructure but leads to a reduced relative spacing of the larger turbines. An innovative turbine concept, like the Hybrid-Lambda Rotor, is promising for mitigating wake losses as it is better suited for close spacing.

Acknowledgements

The work presented in this paper was funded by the Deutsche Forschungsgemeinschaft (DFG, German Research Foundation) – Project-ID 434502799 – SFB 1463.

This work was authored in part by the National Renewable Energy Laboratory, operated by Alliance for Sustainable Energy, LLC, for the U.S. Department of Energy (DOE) under Contract No. DE-AC36-08GO28308. Funding provided by U.S. Department of Energy Office of Energy Efficiency and Renewable Energy Wind Energy Technologies Office. The views expressed in the article do not necessarily represent the views of the DOE or the U.S. Government. The U.S. Government retains and the publisher, by accepting the article for publication, acknowledges that the U.S. Government retains a nonexclusive, paid-up, irrevocable, worldwide license to publish or reproduce the published form of this work, or allow others to do so, for U.S. Government purposes.

Chapter 4

A scaling methodology for the Hybrid-Lambda Rotor - Characterization and validation in wind tunnel experiments

Apart from minor adjustments and corrections, the content of this chapter is identical to that of the following publication:

Daniel Ribnitzky, Vlaho Petrović and Martin Kühn (2025). 'A scaling methodology for the Hybrid-Lambda Rotor – characterization and validation in wind tunnel experiments'. In: *Wind Energy Science* 10.7, pp. 1329–1349. DOI: [10.5194/wes-10-1329-2025](https://doi.org/10.5194/wes-10-1329-2025)

Reproduced in accordance to the Creative Commons Attribution 4.0 License.

Abstract

The Hybrid-Lambda Rotor is an aerodynamic rotor concept that enables low-specific-rating offshore wind turbines in order to increase the power output in light winds and to limit the loads on the very long and slender rotor blades in strong winds. In this paper, the rotor concept is scaled to wind tunnel size and validated under reproducible inflow conditions. The objectives are to derive a scaling methodology, to investigate the influence of the steep gradients of axial induction along the blade span, and to characterize the wake of the Hybrid-Lambda Rotor in wind tunnel experiments. The

scaling objectives are to match the axial induction distribution and to incorporate the change in the angle of attack distribution when switching between the light-wind and strong-wind operating mode. The derived model rotor with a diameter of 1.8 m is experimentally investigated and compared to a conventional model wind turbine in the large turbulent wind tunnel in Oldenburg under tailored inflow conditions produced with an active grid. A two-dimensional laser Doppler anemometer is used to measure the axial induction in the rotor plane, and the wake is characterized by means of a hot-wire rig. The measurement data are supplemented with free-vortex wake simulations of both scaled rotors. The results demonstrate that switching the operating modes with the characteristic change in the angle of attack distribution works similarly for the model and the full-scale turbine. The strong gradients of axial induction along the blade span lead to complex three-dimensional flow structures, such as an increased radial flow component in the rotor plane. The low-induction design of the outer part of the rotor reduces the load overshoots in gust events compared to the conventional model turbine. The wake characterization reveals an outer annulus with reduced wake deficits, an additional shear layer and vortex system, and overall reduced wake deficits over a wide range of wind speeds below rated power. The derived results can improve the understanding of the unique flow patterns that are introduced by the Hybrid-Lambda Rotor and provide a valuable complementary data set to the simulations on the full-scale rotor.

4.1 Introduction

The large-scale employment of offshore wind energy is one of the main pillars used to fight climate change. However, integrating more and more conventional wind turbines in the energy grid will lead to an oversupply of power feed-in during strong winds, while a deficit still remains in light winds. This effect is often named self-cannibalization of wind energy (López Prol et al., 2020) as it is self-amplifying with the share of wind energy in the overall energy mix. It is further intensified by the effect of large cluster wakes, which will significantly reduce the efficiency of many wind farms, especially in light winds and in the context of limited available offshore sites and very close spacing of wind farm clusters (Dörenkämper et al., 2023; Schneemann et al., 2020). Self-cannibalization leads to high prices of electricity during light-wind days and low to zero (or sometimes negative) prices during strong-wind days, as predicted by May et al. (2015). Thus, there is a need for wind turbines that produce more power in light winds. Onshore, this aim is usually accomplished by means of larger rotor diameters in

relation to the rated power, i.e. so-called low specific power (Swisher et al., 2022). The increasing length and mass of the blades result in loads that are no longer technically feasible, which consequently leads design and control engineers to apply load-limiting techniques. The purpose is to reduce the extreme loads close to rated wind speed, but feasible solutions come with a loss in aerodynamic efficiency and thus reduced power. At offshore sites in particular, this contradicts the higher annual average wind speed since a large portion of the energy yield would be achieved in wind speed regimes with reduced aerodynamic efficiency. There is a need for novel design and control methodologies that enable large offshore rotors with low specific ratings. Such concepts limit the power losses due to load-limiting strategies, which can go hand in hand with techniques that reduce the wake losses.

For this purpose, the Hybrid-Lambda Rotor concept for offshore turbines was developed by Ribnitzky et al. (2024a). It features a rotor design for two tip speed ratios (TSRs) and a non-uniform axial induction distribution along the blade span. To limit the loads, the blades are pitched towards feather before rated wind speed, and, in addition, the rotor is switched to a strong-wind mode. Here, the rotor is operated at a lower TSR and a lower axial induction, and the spanwise angle of attack distribution is tilted with a decreasing trend towards the blade tip. When limiting the loads to a certain constraint, this novel combination of blade design and control strategies was proven to cause lower losses in power production compared to conventional blade designs and load-limiting strategies, such as solely pitching the blades to feather.

In previous studies, Ribnitzky et al. (2022) investigated the rotor concept with standard simulation methodologies such as the blade element momentum (BEM) theory. This theory relies on the assumption of independent blade elements. The rotor design with the steep gradients of the axial induction distribution along the blade span consequently reaches the limits of the applicability of the BEM theory. In subsequent investigations, Ribnitzky et al. (2023) analysed the concept using free-vortex wake (FVW) simulations and large-eddy simulations (LESs), and the results were compared to the BEM theory. Although reasonable agreement was found for rotor-integrated quantities like power, thrust, and blade root bending moment, discrepancies were noticed in the spanwise-resolved variables, like the axial induction and the angle of attack distributions. Those studies further revealed a second shear layer in the wake that trails from the mid-span blade region with the steep gradients. This raises interesting questions about the blade aerodynamics and the wake of such a rotor. To

consolidate the findings from the simulation-based studies, an experimental validation of the Hybrid-Lambda Rotor concept is lacking. This leads us to the question of how the rotor concept can be scaled to wind tunnel size.

Designing a model wind turbine blade for use in a wind tunnel usually aims to replicate certain physical characteristics of a full-scale rotor. This process involves finding a delicate compromise since an exact match of all relevant physical parameters between the model and the full-scale turbine is usually not possible. Canet et al. (2021), Bottasso and Campagnolo (2021), and Gasch and Twele (2012) thoroughly analyse the scaling of wind turbines in general. Scaling the Hybrid-Lambda Rotor involves four major challenges. First, the large geometric scaling factor of $1/181$; second, the high design TSR of 11 of the full-scale rotor; third, the non-uniform distribution of the axial induction along the blade span; and, fourth, the ability to change between a light-wind and a strong-wind operating mode. The first two aspects can lead to very low chord lengths, which is a challenge for manufacturability and which leads to very low Reynolds numbers. This would result in an undesired change in the airfoil polars and a loss in aerodynamic efficiency. The latter two aspects require a delicate blade design for two main operating conditions that can mimic the characteristics of the Hybrid-Lambda Rotor even in the small-scale environment of a wind tunnel. In this study, the emphasis is on the aerodynamic effects. Consequently, the model blades are designed over-proportionally stiff to separate aerodynamic effects from aero-elastic interactions. Further, the design and application of a transient controller for the wind tunnel model will be addressed in future studies.

Once successfully designed and manufactured, a wind tunnel model could provide valuable insights into the influence of the steep gradients of the axial induction along the blade span. It further allows us to explore the possibilities of changing the operating modes and changing the spanwise angle of attack distribution, and it enables an in-depth characterization of the wake of the Hybrid-Lambda Rotor. Wang et al. (2021) showed that wakes of scaled wind turbines can deliver a very good representation of the full-scale counterpart, with minor exceptions due to nacelle effects in the inner near-wake region. The study presented here gives valuable insights into aerodynamic effects and design methods for low-specific-rating wind turbines. This includes an understanding of the flow in the rotor area and in the near wake of rotors with a non-uniform axial induction distribution. Further, the study can serve as an example for various complex scaling problems in wind energy research and provides guidelines and

inspirations for designing scaled model turbine blades for aerodynamic investigations in the wind tunnel.

Further innovative rotor concepts have been developed in the wind energy research community. A non-uniform spanwise load distribution of the rotor can lead to enhanced wake mixing, according to Kelley et al. (2014) and Yang et al. (2015). They investigated blade designs with larger spanwise gradients of bound circulation with FVW simulations and LESs and found that those rotors exhibit shorter and faster mixing far wakes. Dong et al. (2023) compared the wake of rotors with different spanwise load distributions and found that the wake recovery rate is higher for a blade design with a load distribution that is shifted more towards the blade root. Low-specific-rating turbines that operate at lower thrust coefficients over a wide range of wind speeds can have additional advantages on a wind farm level (Madsen et al., 2020). Further rotor concepts that aim to enhance wake diffusion also exist. Knauer (2021) introduced a rotor design with a nearly inverse axial induction distribution compared to the Hybrid-Lambda Rotor, using a ventilation area with negative axial induction close to the blade root to introduce a small jet of relatively high wind speeds into the rotational centre of the wake.

The overall objective of this paper is to experimentally characterize and validate the aerodynamic design concept of the Hybrid-Lambda Rotor under reproducible, turbulent, and transient inflow conditions on a wind tunnel scale. More specifically, the contribution aims to (1) develop a method on how to scale the Hybrid-Lambda Rotor concept to wind tunnel size, (2) investigate the influence of the steep gradients of axial induction along the blade span on the aerodynamics, and (3) characterize the near wake of the Hybrid-Lambda Rotor.

4.2 Scaling methodology of the Hybrid-Lambda Rotor

In this section, we scale the Hybrid-Lambda Rotor with a rated power of 15 MW and a diameter of 326 m (Ribnitzky et al., 2024a) to the size of the Model Wind Turbine Oldenburg with a diameter of 1.8 m (MoWiTO 1.8). The model turbine is usually operated with a conventional set of blades, as described in Berger et al. (2018) and Berger et al. (2021). This rotor is an aerodynamically scaled version of the NREL 5 MW reference turbine, defined by Jonkman et al. (2009), scaled under the objective of maintaining the design TSR and the lift distribution along the blade span, and it serves as a reference rotor for this study.

4.2.1 Geometric scaling vs. aerodynamic redesign

The scaling methodology for the Hybrid-Lambda Rotor presented here differs from the aforementioned scaling approach of the reference rotor. The Hybrid-Lambda design methodology, as described by Ribnitzky et al. (2024a), aims to increase the rotor diameter compared to a reference rotor in order to increase the power in light winds. In contrast, the scaling approach presented here aims to have the same rotor diameter as the reference model turbine (1.8 m). This ensures similar boundary conditions in the wind tunnel between the two rotors, considering rotor aerodynamics and wake extension. The most straightforward approach to deriving a scaled model would be a geometric downscaling of the full-scale blade. Scaling the Hybrid-Lambda Rotor from a diameter of 326 to 1.8 m leads to a length scaling factor of $n_l = D_m/D_f = 1/181$, where D is the rotor diameter and the subscripts m and f refer to the model turbine and full-scale turbine, respectively. An exact geometric downscaling would lead to a chord length at the tip of only 8 mm and an unfeasibly low blade thickness of 0.8 mm. Further, if the internal blade shape were scaled exactly, this would lead to a blade mass of only 24 g and a tip deflection under rated conditions of 14 cm. Clearly, these values illustrate that a geometrical downscaling is not an option. Besides manufacturing constraints, the short chord length would lead to very low Reynolds numbers of about 37 000 at the blade tip at rated power, resulting in non-negligible changes in the airfoil polars and unacceptable losses in the aerodynamic efficiency. Consequently, an aerodynamic redesign of the blade is necessary. This means a new blade shape is defined that matches some pre-defined characteristics of the full-scale rotor. Choosing different airfoils and a new chord and twist distribution leads to a visually different blade, which is, however, completely irrelevant as long as the relevant aerodynamic properties are reasonably matched. The first step is to properly define the scaling objectives and to choose the aerodynamic characteristics that should be matched, since, as previously mentioned, not all characteristics can be fulfilled at the same time.

4.2.2 Scaling objectives

Common scaling approaches aim to replicate the TSR and the non-dimensional spanwise circulation distribution. However, the aforementioned challenges forced us to partially deviate from this approach. In contrast, in this study we focused on matching the axial induction distribution along the blade span for the light-wind and strong-wind operating modes of the full-scale Hybrid-Lambda Rotor, and we adapted the operational TSRs. Further, we aimed to incorporate the possibility to change the operating mode

and, consequently, to tilt the angle of attack distribution, similar to the full-scale rotor. More precisely, tilting the angle of attack distribution during the transition from the light-wind (LW) mode to the strong-wind (SW) mode means that the angle of attack is lowered in the outer part of the blade but increased for the inner part. With the focus on aerodynamic investigations, we decided to design the model blades over-proportionally stiff in order to exclude elastic effects and unintended fluid–structure interactions that could overshadow fundamental effects resulting solely from the novel blade design methodology.

4.2.3 Adaptation of design TSRs

An application of the design TSRs of 11 and 9 from the full-scale rotor is not feasible for the wind tunnel size, as the derived chord lengths and local Reynolds number (Re) would be too low, even with the choice of new airfoils. Using Eqs. (4.1)–(4.4), we explain why a reduction in design TSR will increase the Reynolds number. The latter is defined by Eq. (4.1).

$$Re = \frac{c \cdot u_{\text{rel}} \cdot \rho}{\eta} \quad (4.1)$$

Here, ρ is the air density and η is the dynamic viscosity, which are both usually constant across full-scale and wind tunnel applications. The relative velocity at the respective blade element u_{rel} is proportional to the inflow velocity u_{∞} and the design TSR λ_{d} , as denoted in Eq. (4.2). The characteristic length c is the chord length which follows the trends as expressed in Eq. (4.3) according to a Betz blade design, as described by Gasch and Twele (2012). Here, R is the rotor radius, B is the number of blades and $C_{\text{l,d}}$ is the design lift coefficient. Consequently, Re scales with the reciprocal of λ_{d} , as denoted in Eq. (4.4), and larger Reynolds numbers can be achieved by reducing the design TSR and choosing a low design lift coefficient.

$$u_{\text{rel}} \propto \lambda_{\text{d}} \cdot u_{\infty} \quad (4.2)$$

$$c \propto \frac{R}{B \cdot \lambda_{\text{d}}^2 \cdot C_{\text{l,d}}} \quad (4.3)$$

$$Re \propto \frac{R \cdot u_{\infty}}{\lambda_{\text{d}} \cdot B \cdot C_{\text{l,d}}} \quad (4.4)$$

The design TSRs from state-of-the-art model wind turbines range from 4.5 to 7.5. Examples include model wind turbines that are scaled for aero-servo (and potentially elastic) investigations, such as the MoWiTO 1.8 (Berger et al., 2018), the TU Munich G2

(Bottasso et al., 2014b), and the Polimi model turbine (Bayati et al., 2016) with a design TSR of 7.5. Model turbines that are designed for wake (and potentially wind farm) investigations are the TU Munich G1 (Campagnolo et al., 2016) with a design TSR of 7, the NTNU (Krogstad and Lund, 2012), and the MoWiTO 0.6 (Schottler et al., 2016) with a design TSR of 6. Even lower design TSRs of 5 and 4.5 are chosen for model turbines with smart blade applications, such as the TU Delft (Hulskamp et al., 2011) and the TU Berlin (BeRT) (Soto-Valle et al., 2020) turbines. Models with large diameters, like the MEXICO rotor (Schepers and Snel, 2008) or the NREL phase VI turbine (Hand et al., 2001), with diameters of 4.5 and 10 m, are also designed for relatively low TSRs of 6.7 and 5.4, respectively.

Consequently, we decided to reduce the design TSRs of the Hybrid-Lambda Rotor for the wind tunnel model. Within the iterative design process, several TSRs were investigated. We found that a design TSR for the light-wind mode $\lambda_{d,LW} = 7.5$ works well in order to fulfil the constraints of minimal chord length (3 cm) and Reynolds number (70 000). Further, there is the advantage of the comparability with the conventional blades for the MoWiTO 1.8, as they feature a design TSR of 7.5, too. The design TSR for the strong-wind mode $\lambda_{d,SW}$ was chosen in order to incorporate a similar change in the inflow angle distribution to that of the full-scale rotor when switching from the light-wind to the strong-wind mode. The aforementioned change can be calculated with Eq. (4.5) and is visualized in Fig. 4.1 using the axial induction distribution from the full-scale rotor. Here, a_{SW} and a_{LW} are the induction factors in the strong-wind and light-wind modes, respectively.

$$\Delta\phi(r) = \arctan\left(\left(1 - a_{SW}(r)\right)\frac{R}{r \cdot \lambda_{d,SW}}\right) - \arctan\left(\left(1 - a_{LW}(r)\right)\frac{R}{r \cdot \lambda_{d,LW}}\right) \quad (4.5)$$

It can be readily seen that a reduction of the TSR from 7.5 to 6.7 would lead to a similar change in the inflow angle compared to a reduction from 11 to 9 (as for the full-scale rotor) in the relevant blade region, except for the segments close to the blade root. However, we chose the strong-wind TSR to be 6 for two reasons. First, we want to enlarge the effect of the change in the angle of attack distribution in order to facilitate the measurability with the background of measurement uncertainties. Second, the transition from the light-wind to the strong-wind mode at a constant rotational speed will expand over a wider range of wind speeds if the design TSRs are further apart. For instance, with the start of the transition region at $u_{ts} = 6.3 \text{ m s}^{-1}$, the tip speed ratio in the strong-wind mode of $\lambda_{d,SW} = 6.7$ would lead to the end of the transition

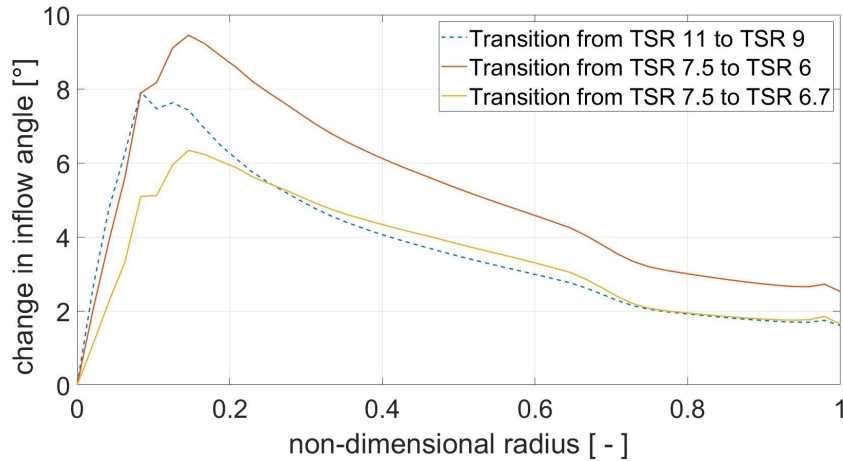


Figure 4.1: Change in the inflow angle distribution for operational transition of TSRs, with the full-scale rotor represented with the dashed line.

region at $u_{te} = 7.0 \text{ ms}^{-1}$, whereas a lower tip speed ratio $\lambda_{d,SW} = 6$ would result in a wider transition region with $u_{te} = 7.9 \text{ ms}^{-1}$. This opens up more opportunities for control-related investigations in the wind tunnel that focus on the transition between the operating modes.

4.2.4 Design and scaling constraints

With the choice of design TSRs being made, the design process continues with the application of the Hybrid-Lambda design methodology, which is visualized in Fig. 4.2. However, certain constraints need to be taken into account. The Reynolds number should be at least 70 000, as suggested by Bottasso and Campagnolo (2021), to limit the reduction in aerodynamic efficiency. The chord length directly influences the Reynolds number. In addition, the constraint of the minimal chord length due to manufacturing reasons is set to 3 cm. This is not a strict limit, but it is related to the minimal leading edge radius and the minimal trailing edge thickness of 0.5 mm within the milling process of the blade mould. The smaller the chord length, the larger the adjustments that need to be applied to the airfoil shape in order to maintain the constraints for the leading edge radius and trailing edge thickness. The blade root diameter is constrained to 35 mm in order to include the same pitch actuation mechanism and the same blade root connection to the hub as is used for the conventional blades. In theory, the maximum flapwise blade root bending moment (RBM) scales with n_1^3 . With a maximum value for steady inflow of 62.9 MNm for the full-scale model, this would result in a value of 10.6 Nm for the wind tunnel model. This is the load level where the transition from the light-wind to

strong-wind mode takes place in a steady-state assumption. However, under transient inflow conditions, higher loads are expected. Due to the load-limiting constraints of the MoWiTO 1.8, we lowered the design value for the steady-state maximum flapwise RBM to 7.5 Nm. The operational range of the rotational speed must be between 420 and 600 rpm. It is constrained by the first tower eigenfrequency (6.7 Hz) at the lower end and by the maximum rotational speed of the slip ring in the drive train at the upper end.

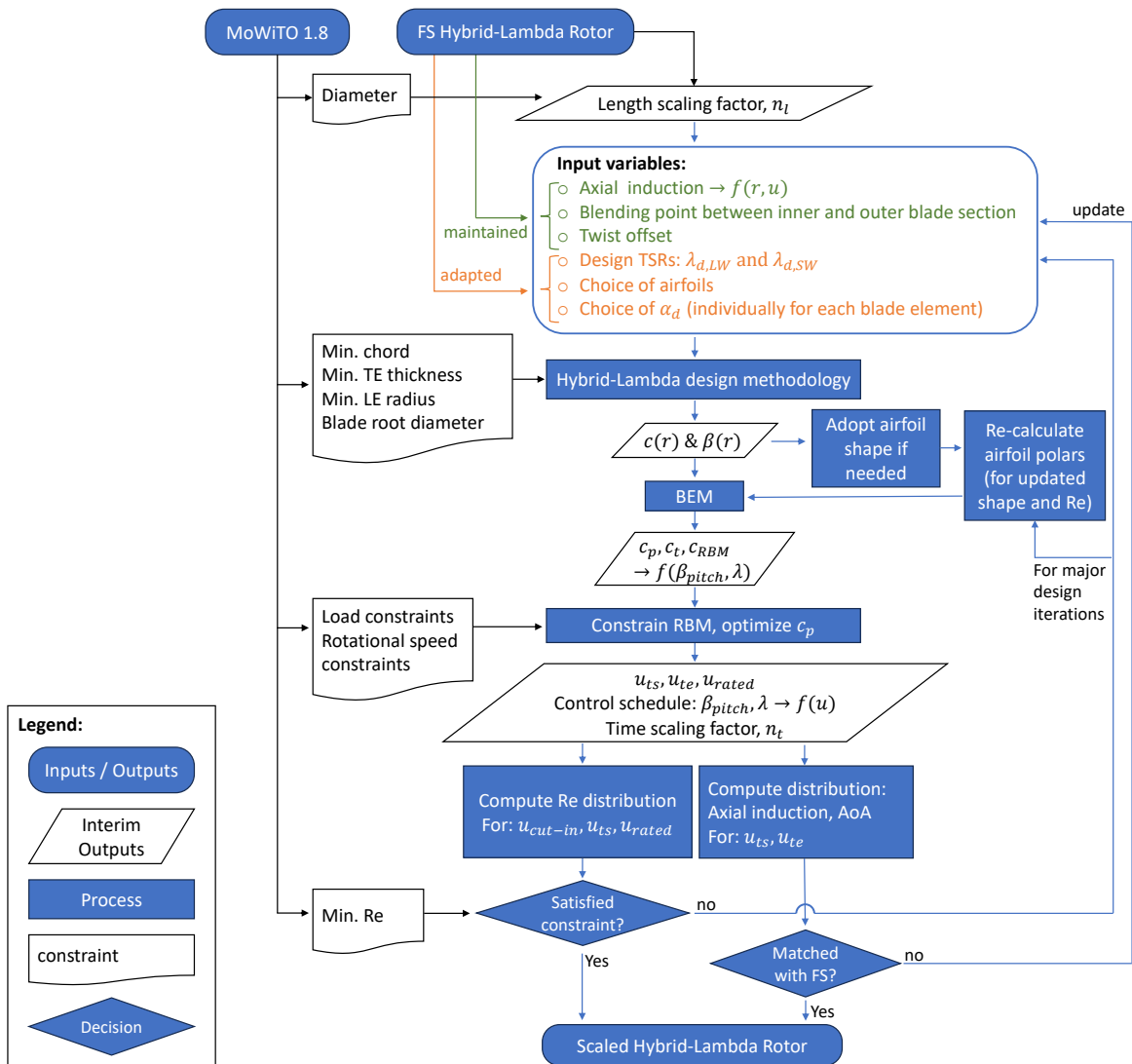


Figure 4.2: Scaling and design workflow for the Hybrid-Lambda Rotor. AoA – angle of attack; α_d – design angle of attack; β – twist angle; β_{pitch} – pitch angle; c – chord length; c_p , c_t , and c_{RBM} – power, thrust, and flapwise root bending moment coefficients; $f(\dots)$ – as a function of (\dots) ; FS – full scale; LE – leading edge; LW – light wind; λ – tip speed ratio; r – local radius; Re – Reynolds number; SW – strong wind; TE – trailing edge; u_{cut-in} , u_{ts} , u_{te} , and u_{rated} – wind speeds at cut-in, start of transition, end of transition, and rated power.

4.2.5 Inputs to the aerodynamic redesign

Before starting the design process, appropriate airfoils need to be chosen. We investigated several low-Reynolds-number airfoils and decided to use the SG6040 and SG6041 airfoils (Giguere and Selig, 1998), which were also used for the conventional blades of the MoWiTO 1.8, for the sake of comparability. The polars are simulated with XFOIL for the individual blade element with the respective Reynolds number with an N_{crit} value of 7 and without a forced transition. N_{crit} is the critical amplification factor that describes the transition between laminar and turbulent flow over the airfoil.

Next, the Hybrid-Lambda design methodology, as described by Ribnitzky et al. (2024a), is applied with the following input variables. The design TSRs are set to 7.5 and 6, as explained above. Identical to the full-scale rotor, the blending region between the inner and outer blade section is set to 70 % blade length (equivalent to 73 % rotor radius for the model turbine), and the twist offset for the inner blade region is set to -2.5° . Further information on the twist offset within the Hybrid-Lambda design methodology is given by Ribnitzky et al. (2024a). The desired axial induction distribution is adopted from the full-scale rotor, since this is the major scaling objective. The design angle of attack (α_d) is derived from a compromise between achieving good lift-to-drag ratios ($\alpha_{\text{max},L/D} \approx 4.5^\circ$), maintaining reasonable margins to the stall region ($\alpha_{\text{stall}} \approx 11.5^\circ$), and maintaining low lift coefficients that help to fulfil the minimum Reynolds number and chord length constraints. Consequently, the design angle of attack is set close to the maximum lift-to-drag ratio for the inner part of the blade where the low design TSR already ensures large enough chord lengths. For the outer part of the blade, the design angle of attack is reduced in order to enlarge the chord length, which also matches well with the angle of attack distribution of the full-scale rotor. With these input variables, the chord and twist distribution can be calculated. Those are shown in Fig. 4.3 for the final blade design.

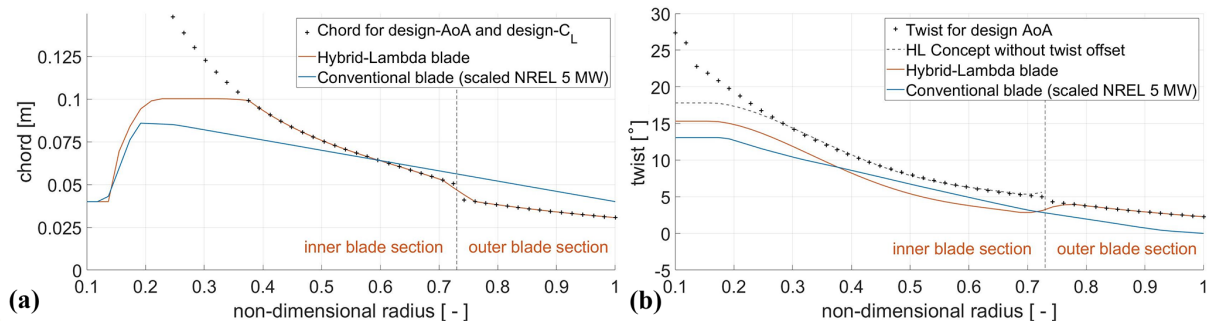


Figure 4.3: Chord (a) and twist distribution (b) for the scaled Hybrid-Lambda Rotor and the scaled NREL 5 MW turbine.

4.2.6 Deriving the control schedule and time scaling factor

BEM simulations with steady and uniform inflow provide the aerodynamic performance curves, such as the power coefficient c_p , thrust coefficient c_T and flapwise RBM as a function of pitch angle β_{pitch} , and operational TSR. Now, the constraint of flapwise RBM is applied, and the wind speed is calculated at which the limiting loads are reached (u_{ts}), which is defined as the start of the transition region. The control strategy, i.e. rotational speed and pitch angle over wind speed, as shown in Fig. 4.4 for the final scaled design, is derived as follows. For wind speeds greater than u_{ts} , the rotational speed is kept constant until λ_{SW} is reached. Then the rotational speed follows λ_{SW} until rated wind speed. The pitch angle is set in order to constrain the RBM below rated wind speed with the given operational TSRs. The wind speed at which the transition to the strong-wind mode starts, u_{ts} , and the speed at which it ends, u_{te} , are now known, as well as the respective pitch angles. Since most of the measurements are performed at these two wind speeds and with the respective rotational speed, ω_{trans} , we define the time scaling factor as

$$n_t = t_m/t_f = \omega_{\text{trans},f}/\omega_{\text{trans},m} = 1/114. \quad (4.6)$$

Note that the maximum rotational speed of 600 rpm is set by hardware constraints and is not exactly true to scale compared with the full-scale model. An overview of the actual turbine parameters and the scaling factors is provided in Table 4.1. Note that since we transferred the Hybrid-Lambda concept to lower TSRs, the scaling of the wind speed, which would be defined as n_1/n_t , does not hold true in this case. However, if we define the scaling ratios of the design TSRs as

$$n_{\lambda,LW} = \lambda_{LW,m}/\lambda_{LW,f} \quad \text{and} \quad n_{\lambda,SW} = \lambda_{SW,m}/\lambda_{SW,f}, \quad (4.7)$$

then the wind speeds can be derived from Eqs. (4.8) and (4.9):

$$u_{\text{ts},m} = u_{\text{ts},f} \cdot \frac{n_1}{n_t \cdot n_{\lambda,LW}}, \quad (4.8)$$

$$u_{\text{te},m} = u_{\text{te},f} \cdot \frac{n_1}{n_t \cdot n_{\lambda,SW}}. \quad (4.9)$$

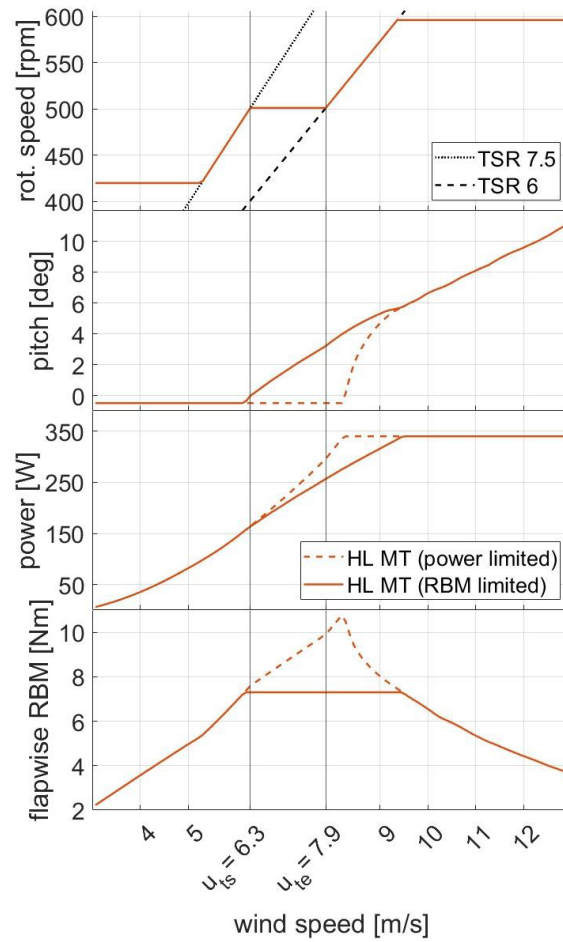


Figure 4.4: Control schedule for the Hybrid-Lambda model turbine (HL MT), derived from BEM simulations.

Table 4.1: General parameter of the wind tunnel model and the full-scale Hybrid-Lambda Rotor.

Parameter	Symbol	Model scale (subscript m)	Full scale (subscript f)	Unit	Ratio
Length scaling factor	n_l			–	1/181
Time scaling factor	n_t			–	1/114
Rotor diameter	D	1.8	326	m	1/181
Max rotor speed	ω_{\max}	600	5.38	rpm	1/111
Rotor speed at u_{ts}	ω_{trans}	500	4.39	rpm	1/114
Design TSR inner 70 % of blade span	$\lambda_{d,SW}$	6	9	–	0.67
Design TSR outer 30 % of blade span	$\lambda_{d,LW}$	7.5	11	–	0.68
Wind speed, start of transition	u_{ts}	6.3	6.9	m s^{-1}	$0.93 \approx 114/(181 \cdot 0.68)$
Wind speed, end of transition	u_{te}	7.9	8.3	m s^{-1}	$0.95 \approx 114/(181 \cdot 0.67)$
Rated power	P_{rated}	340*	15×10^6	W	$0.74/181^2$
Reynolds number at 90 % blade span at u_{ts}	Re	95×10^3	7×10^6	–	0.014

* Reduced due to hardware constraints.

4.2.7 Verifying the constraints and closing the design loop

Finally, we can check the angle of attack and axial induction distribution for the two operating points (u_{ts} and u_{te}), and we can verify the scaling objectives as follows. Is the axial induction distribution from the full-scale rotor reasonably matched (Fig. 4.5a)? Is the change in the angle of attack distribution reasonable when switching the operating modes (Fig. 4.5b)? Is the constraint for the Reynolds number achieved (see Fig. 4.6)? If one of these objectives is not met, the design optimization loop is closed by re-tuning the input parameters and calculating the next design iteration. For major design updates, we re-calculate the airfoil polars as follows. The minimum leading edge radius and trailing edge thickness is constrained due to manufacturing reasons. Consequently, the airfoil shape needs to be adapted for all blade elements where the derived chord length would lead to a violation of the constraints. Now that the relative velocity at the respective blade element is known from the BEM simulations, the airfoil polars can be re-calculated for each individual blade element, considering the expected Reynolds number and the modified airfoil shape. The largest adaptation to the airfoil shape is necessary for the blade element with the shortest chord length, consequently, at the blade tip. We observed an increase in the drag coefficient for angles of attack greater than 3.5° , which results in a reduction in the maximum lift-to-drag ratio by 15% compared to the unchanged airfoil. These numbers highlight the importance of considering the modifications to the airfoil shape, since the effect is happening in the relevant region of operational angle of attacks.

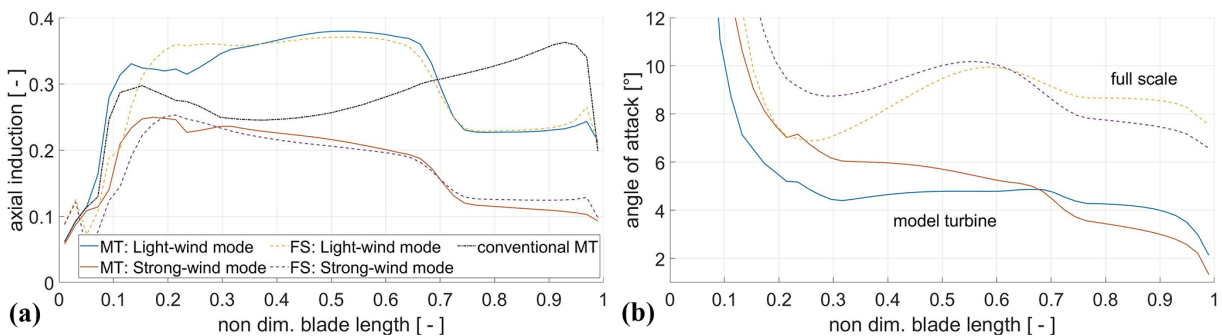


Figure 4.5: Axial induction **(a)** for the light-wind mode (at u_{ts}) and the strong-wind mode (at u_{te}) for the Hybrid-Lambda model turbine (MT), the full-scale (FS) rotor, and the conventional model turbine in BEM simulations and respective angle of attack distributions **(b)**.

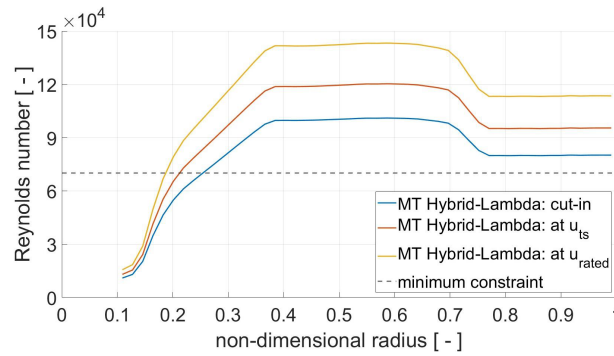


Figure 4.6: Reynolds number for three different operating modes, derived from BEM simulations.

4.3 Experimental and simulation methodology

In this section, we first explain the experimental set-up in Sect. 4.3.1, the measurement equipment in Sect. 4.3.2, and the post-processing of the measurement data in Sect. 4.3.3. Several simulations are used to derive the blade design of the scaled model, for comparison of the experimental data with simulation models and to get further insights into flow quantities that could not be measured. The simulation methodology is therefore described in Sect. 4.3.4.

4.3.1 Experimental set-up

The experiments were carried out in the turbulent wind tunnel of Oldenburg, further described by Kröger et al. (2018). It is a Göttingen-type wind tunnel, featuring a rectangular nozzle with a cross section of $3\text{ m} \times 3\text{ m}$ and a test section length of 30 m. For the purpose of this study, the open-jet test section configuration was used, as illustrated in Fig. 4.7. The wind tunnel can be equipped with an active grid to realize turbulent, reproducible flow patterns in the inflow, as further explained by Neuhaus et al. (2021). The active grid was mounted with a static open-flap configuration for the investigations of the rotor-integrated quantities (Sect. 4.4.1), the radially resolved measurements (Sect. 4.4.2), and the wake measurements (Sect. 4.4.4). This leads to a steady, uniform inflow over the rotor area with a turbulence intensity (T_i) of approximately 2%, which is used for all presented measurements if not stated differently. For the wake investigations only, four different levels of turbulence intensity (2%, 4%, 6%, and 8%) were generated with the active grid. To analyse the effect of gusts on the rotor (see Sect. 4.4.3), the active grid was used to produce a transient wind speed change that is intended to represent a scaled operating gust, as described by Neuhaus et al. (2021).

According to the IEC 61400-1 (2019) standard, the gust should last 10.5 s. With the time scaling ratio of 1 : 114 (as defined in Sect. 4.2), the ideally scaled gust in the wind tunnel would last only 0.09 s. Unfortunately, controlling the wind speed at such high frequencies is not possible, and there is always a trade-off between high frequencies and sufficient wind speed amplitudes. Neuhaus et al. (2021) found the fastest gust with a reasonable gust amplitude has a duration of 0.75 s. This means that the gust in the wind tunnel is about 8 times slower than the full-scale equivalent. The amplitude reaches from 6.3 to 7.5 ms^{-1} in the wind tunnel, while the IEC operating gust ranges from 6.3 to 8.2 ms^{-1} .

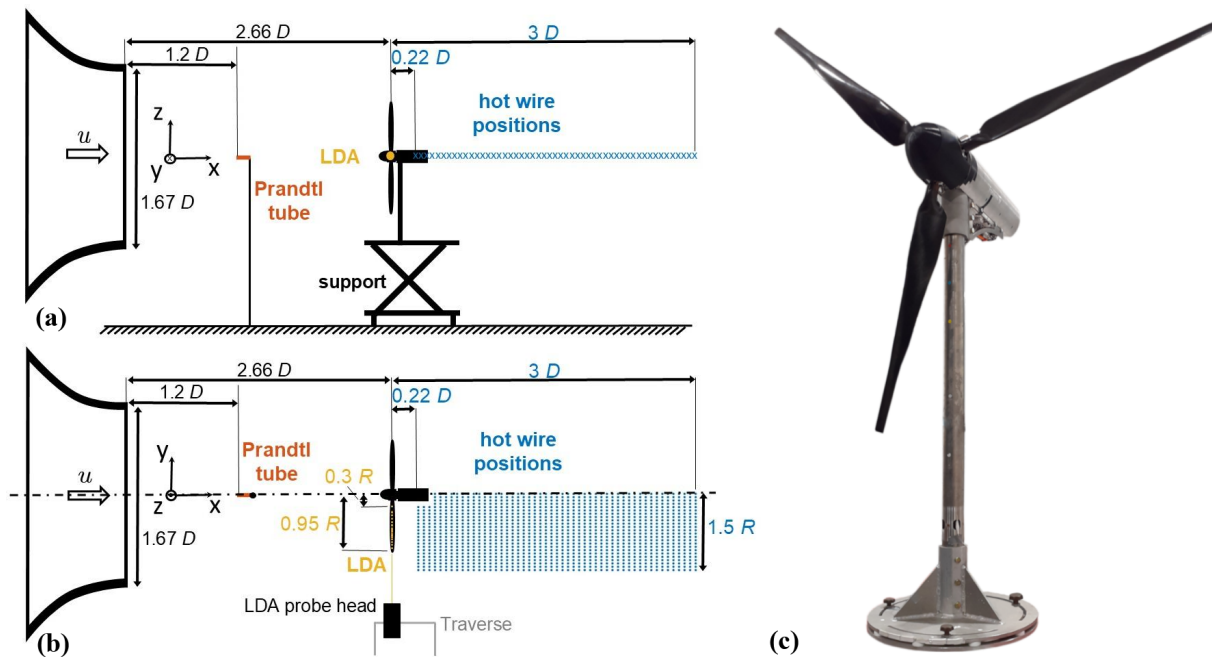


Figure 4.7: Experimental set-up, side (a) and top view (b), indicating the measurement positions of the hot wires, LDA, and Prandtl tube. The coordinate system is located in the rotor centre. MoWiTO 1.8 with the Hybrid-Lambda blades (c), $D = 1.8 \text{ m}$, hub height of 1.5 m .

In addition to the experiments with the Hybrid-Lambda Rotor, further measurements were carried out with the conventional blades to compare the load response due to gust events (see Sect. 4.4.3) and to compare the wake of the two rotor designs (see Sect. 4.4.4). Both model rotors have the same diameter of 1.8 m . The model turbine, as depicted in Fig. 4.7, is equipped with strain gauges in the blade root to measure the flapwise blade root bending moment and in the tower base to derive the rotor thrust. A torque meter and a rotational encoder in the drive train allow for measurements of the

rotor torque, azimuthal position, and rotational speed. The data acquisition system of the model turbine samples the aforementioned measurement data at 5 kHz. The blade pitch is set by three DC motors, mounted in the blade roots, allowing for individual pitch control. However, in this analysis, only collective pitch settings are used.

For this study, the turbine is operated at a fixed rotational speed of 500 rotations per minute (rpm). Changing the rotational speed would influence the operational Reynolds number, which affects the aerodynamic behaviour of the turbine. For the sake of comparability between all conducted measurement runs, a fixed reference rotational speed is chosen. For the gust investigations, the rotational speed and the blade pitch are also set to constant values. Since the focus of this study is on the aerodynamic behaviour and the impact of the different blade designs, no overshadowing of the effects by controller actions is desired.

The model turbine is placed 4.8 m ($2.66 D$) behind the wind tunnel nozzle, and the inflow velocity is measured with a Prandtl tube and a pressure transducer 2.1 m ($1.2 D$) behind the nozzle. These values were found to be best practice in order to avoid influences of the induction zone of the model turbine on the wind speed measurements and on the development of the inflow behind the active grid.

4.3.2 Measurement equipment and experimental matrix

To measure the axial and tangential induction, a two-dimensional laser Doppler anemometer (LDA) with a power of 1 W for each laser is used. A beam expander with a focus length of 2.1 m allows the LDA system to be mounted at a reasonable distance in order not to disturb the flow. In the radial direction, 16 measurement points are taken at the 3 o'clock position (looking downstream) in order to minimize the tower effects on the measurements (rotor spins clockwise looking downstream). The measurement points cover a range from 0.3 to $0.95 R$, with closer spacing in the region of the expected steep induction gradients, as indicated in Fig. 4.7. The axial and tangential induction and the angle of attack are derived from the method introduced by Herráez et al. (2018) and further applied by Berger et al. (2021). According to this method, the axial and tangential velocity components are probed in the bisectrix of two blades where the local blade induction is counterbalanced and cancelled out. Herráez et al. (2018) found that the trailed vorticity at the blade tip does play a non-negligible role, and measurements further outboard than $0.92 R$ should be treated with care. This method is only valid for

axial and uniform inflow, which is given for the studies presented here.

We analysed the wake of both the conventional and the Hybrid-Lambda Rotor. The light-wind mode of the Hybrid-Lambda Rotor leads to a thrust coefficient of 0.92. The conventional blades are investigated at the same wind speed with the same rotor speed, and the pitch is set in order to achieve the same thrust coefficient as for the Hybrid-Lambda blades in the light-wind mode. Further, the thrust coefficient is 0.61 for the strong-wind mode and 0.45 for rated wind speed. The investigated operating modes are summarized in Table 4.2. Hot-wire measurements were performed downstream of the rotors at hub height on a horizontal line along the 3 o'clock position. A hot-wire rig with 24 one-dimensional hot wires was used, covering a radial range from the centre of rotation to 1.38 m ($0.77 D$) with an equidistant spacing of 6 cm ($0.033 D$). The hot-wire rig was mounted on a traverse to realize a very fine spacing in the downstream direction, too. Measurements are taken at 51 positions downstream of the rotor, from 0.4 to 5.4 m ($0.22 D$ to $3 D$) with a spacing of 0.1 m ($0.056 D$). The first three downstream positions are located next to the nacelle. Overall, this leads to a very high spacial resolution of the wake measurements, resulting in an equidistant grid of 24×51 measurement points covering a rectangle of $1.38 \text{ m} \times 5.4 \text{ m}$, which is illustrated in Fig. 4.7. The hot-wire measurements are sampled with 6 kHz over a duration of 40 s for each point. A different hot-wire rig was used only for the investigation of varying inflow turbulence intensities. In this case, the hot wires were mounted with a spacing of 4 cm, with 16 hot wires ranging from $0.35 D$ to $0.68 D$, and only the downstream position of $0.4 D$ was investigated.

Table 4.2: Investigated operating modes for the Hybrid-Lambda wind tunnel model.

	Light-wind mode	Strong-wind mode	Rated	Unit
Abbreviation	LW	SW	rated	–
Wind speed	$u_{ts} = 6.3$	$u_{te} = 7.9$	$u_{rated} = 9.4$	ms^{-1}
Rotor speed	500	500	600	rpm
TSR	7.5	6	6	–
Pitch angle	-0.8	3.2	6.7	$^{\circ}$
c_T experiment	0.92	0.61	0.45	–
c_p experiment	0.42	0.35	0.27	–

To characterize the scaled Hybrid-Lambda Rotor and to derive the rotor-integrated quantities, a measurement matrix was performed, which consists of a grid of TSR and pitch combinations with the turbine operating under steady-state conditions. This matrix covers TSRs from 5 to 9 with a spacing of 0.5 and pitch angles from -2 to $+4^\circ$ with a spacing of 1° . Further, a finer grid is applied in the area of the highest interest around the maximum power coefficient. From -1.6 to -0.4° , the pitch angle is varied in steps of 0.4° , and the TSR is varied from 6.75 to 8.5 in steps of 0.25. The combination of very low TSR and pitch values could not be measured since the structural loads would exceed the safety constraints of the model turbine. However, according to the Hybrid-Lambda control strategy, the pitch angle is increased when the TSR is lowered. Consequently, the combination of low TSR and low pitch values is unlikely to be relevant. In total, 91 points were measured. For each point, the turbine data are averaged over 15 s, which corresponds to 125 rotor revolutions. The non-dimensional power and thrust coefficients c_p and c_T are calculated with the inflow wind speed derived from the Prandtl tube measurements and the density calculated from air temperature, humidity, and ambient pressure. Since all measurements for the rotor-integrated quantities are recorded within 1 d, the maximum variation in the air density was only 0.2 %, and the air density is considered error-free in the error propagation. For the power and thrust coefficients, the error-prone variables are thrust force, rotor torque, inflow velocity, and rotational speed.

4.3.3 Measurement data post-processing and uncertainty estimation

Certain correction methods are applied to the turbine load measurements, as described in the appendix of Berger (2022). The measured torque is corrected for the drive train friction – resulting from the bearings and the slip ring – in order to derive the rotor aerodynamic torque. The friction is derived as a linear function of rotational speed from calibration measurements, where the drive train is rotated without the blades. The thrust is corrected for the aerodynamic drag on the tower and nacelle. The drag force is derived by wind tunnel measurements with detached blades, resulting in a quadratic correction function of the thrust force over the wind speed. When calculating the wind speed at the location of the tower, induction effects are taken into account within an iterative process according to the momentum theory, as further described by Berger (2022). The strain gauge measurements are post-processed with a zero-phase digital filter, using a Butterworth infinite impulse response low-pass filter with a half-power frequency of 28 Hz, which is 12 % higher

than the blade-passing frequency (3P). This ensures that all relevant rotor dynamics are resolved but allows the data to be filtered for high-frequency vibrations and noise.

The LDA measurement data are post-processed as follows. First, the data are synchronized with the azimuth angle measurements of the MoWiTO 1.8. From the continuously acquired LDA data, only the values that lie in a sector of $\pm 3^\circ$ from the blade bisectrix are further considered. For each radial position, the data are recorded for 60 s, which corresponds to 1500 blade passings. The LDA data are not recorded in equidistant time steps but whenever a seeding particle passes through the probe volume. Due to the nature of the flow, more samples will be available for the axial component compared to the tangential component. On average, 17 000 samples were used for the calculation of the mean value of the tangential velocity and 37 500 samples for the axial velocity, for every radial position. The number of samples was never lower than 14 700 and 29 000 for the tangential and axial velocity components, respectively. Therefore, the confidence in the mean value is very high, and the 95 % confidence interval would not be visible in the plots. Consequently, we decided to plot the standard deviation over all samples, which visualizes the spread of the data but does not represent the high confidence in the mean value. In order to calculate the axial induction, precise information about the inflow is needed. Therefore, the inflow is measured with the LDA along a horizontal line at hub height in the position of the rotor plane with the turbine not installed. These measurements result in an observation of the mean wind speed and the respective standard deviation for all positions where the axial induction should be calculated. The inflow characterization reveals a slight drop in the axial inflow velocity from the centre to the edge of the rotor area of 0.25 m s^{-1} . This marginal non-uniformity is accounted for in the calculations of the axial and tangential induction and the angle of attack, since the information of the inflow at the individual radial position is used, as indicated in Eqs. (4.10)–(4.12). Here, a and a' are the axial and tangential induction factors; u_{ax} and u_{ta} are the axial and tangential velocity components in the rotor plane; u_∞ is the undisturbed axial inflow velocity component in the rotor plane; r is the radial position; ω is the rotational speed; α is the angle of attack; and γ is the geometrical angle between the chord of the local blade segment and the rotor plane, consisting of twist and pitch.

$$a(r) = 1 - \frac{u_{ax}(r)}{u_\infty(r)} \quad (4.10)$$

$$a'(r) = \frac{u_{ta}(r)}{\omega r} \quad (4.11)$$

$$\alpha(r) = \arctan\left(\frac{u_{\text{ax}}(r)}{u_{\text{ta}}(r) + \omega r}\right) - \gamma \quad (4.12)$$

Measurement uncertainties are calculated with the Gaussian error propagation, and, if not stated differently, error bars indicate the combined standard deviation of all measurement uncertainties, as indicated in Eq. (4.13). Here, ∂ refers to the partial derivative of the respective equation, $f(x_i)$ is the combined measurement value that is calculated from n measurement variables x_i , and σ is the standard deviation of the respective variable. Unless indicated differently, the latter is derived directly from the measurement data. We assume $\sigma(r) = 2 \text{ mm}$ and $\sigma(\gamma) = 0.2^\circ$.

$$\sigma(f(x_i)) = \sqrt{\sum_{i=1}^n \left(\frac{\partial f}{\partial x_i} \cdot \sigma(x_i)\right)^2} \quad (4.13)$$

For the investigation of the gust events in Sect. 4.4.3, ensemble averaging is performed. The gust event is repeated 45 times with the active grid, which is synchronized with the turbine's data acquisition system. The measurement data of the resulting flapwise blade root bending moment are aligned for all repetitions, and an average value and the standard deviation at each time step of the gust are constructed. This approach can smooth out non-deterministic variations. The same transient inflow conditions were applied to the conventional blades and to the scaled Hybrid-Lambda Rotor. In this case, we use the 95% confidence interval of the 45 repetitions to indicate the statistical significance of the different behaviours of the two blade sets. For the sake of comparability, we normalize the RBM measurements with the mean stationary value of the respective blade set. However, the difference between the two blade sets in the mean stationary value is only 0.2 Nm, which corresponds to 3% of the mean value.

4.3.4 Simulations

The scaled version of the Hybrid-Lambda Rotor was designed with an in-house BEM code, as described in Hansen (2008). The radially resolved axial induction and angle of attack distributions were derived with this simulation tool. In this paper, we define the axial induction as averaged over the annulus, which can be expressed as the local axial induction on the blade multiplied by the tip-loss factor. Additionally, aero-elastic simulations were carried out with OpenFAST v3.1 (Jonkman et al., 2022) for model validation. The rotor-integrated quantities (c_p , c_T , and flapwise RBM) shown in this study are derived from the OpenFAST simulations. The two abovementioned tools both implement the Prandtl tip and root loss models and the Glauert high thrust

correction with the approximation by Buhl (2005). Neither of them uses a dynamic stall or dynamic inflow model, since the reference simulations in this study are restricted to steady and uniform inflow. The tower shadow effect is modelled only in OpenFAST. In preliminary analyses, the blade tip deflection in front of the tower was measured with a laser distance sensor, and it did not exceed 15 mm in steady-state operations. However, the blades are modelled in OpenFAST as flexible using ElastoDyn as the elastic solver (Jonkman et al., 2022). The tower is modelled as rigid for both tools. Since the in-house BEM code is purely aerodynamic, all components are modelled as rigid in this case.

For additional investigations on the radial flow component in the rotor plane (Sect. 4.4.2) and the wake behaviour of the Hybrid-Lambda model rotor and the conventional model rotor (Sect. 4.4.4), FVW simulations are carried out with the OLAF module in OpenFAST v3.5, as described by Branlard et al. (2022b) and Shaler et al. (2020). We aimed for a representation of an undisturbed wake, focusing on the effects that result from the aerodynamic blade design. Consequently, no tower shadow model is used, and the core spread eddy viscosity (viscous diffusion parameter) is set to 100 in order to allow for a free convection of the wake for a distance of multiple diameters downstream. Further, at the time of this study, no nacelle drag model was implemented in OLAF. For all simulations, the inflow is modelled as uniform over the rotor area and constant in time without added turbulence. Similar to the experiments, the comparison of the Hybrid-Lambda Rotor and the conventional rotor is carried out at the same thrust coefficient in the light-wind mode.

4.4 Results

In this section the results from the wind tunnel experiments and the complementary simulations are presented. We first address rotor-integrated quantities in Sect. 4.4.1 and then expand to radially resolved measurements in Sect. 4.4.2. Next, we compare the dynamic response of the Hybrid-Lambda Rotor due to gusts with the response of the conventional rotor in Sect. 4.4.3. Finally, we characterize and compare the wake of the two model wind turbines in Sect. 4.4.4.

4.4.1 Rotor-integrated quantities

Characterizing the newly designed model rotor is an important step. The derived performance curves of the power coefficient, thrust coefficient, and flapwise RBM,

resolved over a fine mesh of TSR and pitch, are used to validate the blade design and define operating points for further experiments. Such a characterization is further needed for controller implementations in future studies. In total, 91 combinations of TSRs and pitch angles were measured with a constant rotational speed of 500 rpm. For the sake of clarity, only a small portion of the results is plotted in Fig. 4.8. Overall, the measured power coefficient shows good agreement with the BEM simulations. The measurement values are lower than those from the simulations, which could indicate that the simulated airfoil polars overestimated the performance at the low Reynolds numbers. Both measurements and simulations show the highest power coefficient at similar operating points, i.e. TSR and pitch combinations. The difference in maximum c_p between measurement and simulation data is about 2%. Differences are larger for off-design operational points, such as the combinations of large pitch angles with very high or very low TSRs. The curves of the thrust coefficient show a similar shape over TSR and pitch angle compared to the simulations but with a considerable offset. Although correction models for the tower drag are applied, as explained in Sect. 4.3.3, an offset in the thrust coefficient of about 13% is present for the operating point with maximal c_p . The non-dimensional flapwise RBM is plotted in Fig. 4.8 and is defined in Eq. (4.14).

$$c_{\text{RBM}} = \frac{M_y}{0.5\rho u_\infty^2 R \frac{\pi R^2}{3}} \quad (4.14)$$

Here, $0.5\rho u_\infty^2$ is the dynamic pressure, R is the rotor radius used as a characteristic length, and $\frac{\pi R^2}{3}$ is the rotor area divided by the number of blades. The measured flapwise RBMs (M_y) are in good agreement with the simulations. The relative difference between the measured RBMs and the simulations is 4% in the operational point of maximum c_p .

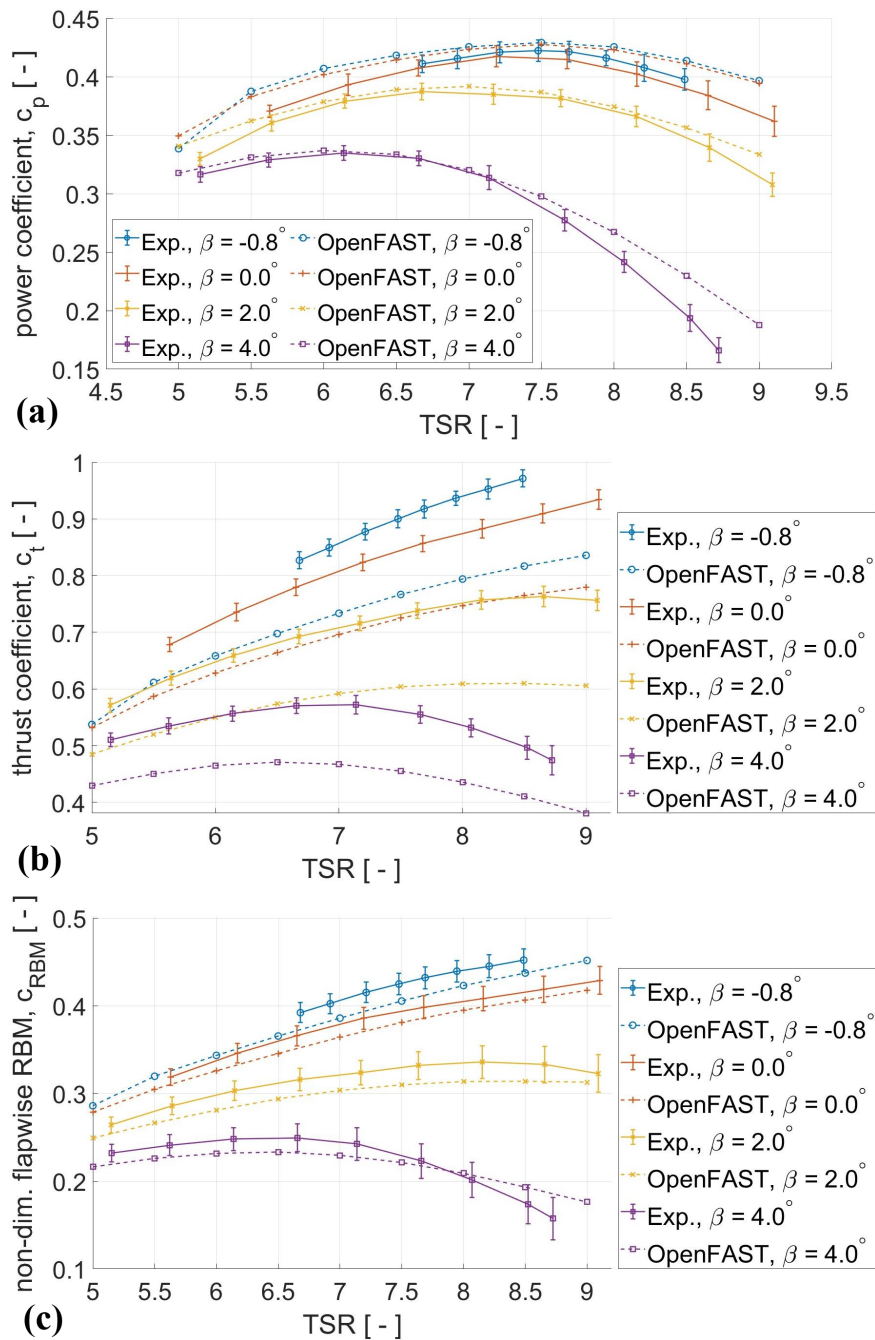


Figure 4.8: Power coefficient (a), thrust coefficient (b), and non-dimensional flapwise RBM (c) from measurements and BEM simulations for various TSRs and pitch angles β_{pitch} at a constant rotor speed of 500 rpm.

4.4.2 Radially resolved quantities

In this section, we address the measurements of the axial induction and angle of attack distribution over the blade span. We further investigate the radial velocity component in the rotor plane, as derived from FVW simulations, since this quantity was not measured within the measurement campaign. The measurements of the axial induction with the LDA show a fair match with the BEM simulations for the inner blade region ($r/R < 0.7$) for both operating modes, as displayed in Fig. 4.9a. However, the steep gradients in the blending region of the blade design are not present in the LDA measurements. The measurements show a smeared-out and less steep gradient at $r/R \approx 0.75$. Since the flow in the rotor plane is three-dimensional, the assumption of independent blade elements in the BEM theory is invalid, and the gradients can not be captured by the BEM theory. The radial velocity components are further addressed in the next paragraph. The derived angle of attack distributions are plotted in Fig. 4.9b. The measurements show that the contrary tilting of the distribution works; i.e. when switching from the light-wind to the strong-wind mode, the angle of attack increases for the inner 70% of the blade length and decreases for the outer 30%, as expected. In close vicinity to the blade tip ($0.9 < r/R < 1$), the modelling of the tip loss effect leads to deviations between the measurements and the BEM simulations. The two outermost measurement points should be treated with care since the tip loss effect influences the bisectrix method by Herráez et al. (2018). Overall, a minor offset of about 0.6° between the measurements and the simulations can be observed. However, the slopes of the angle of attack distribution match reasonably well, with the exception of the tip region.

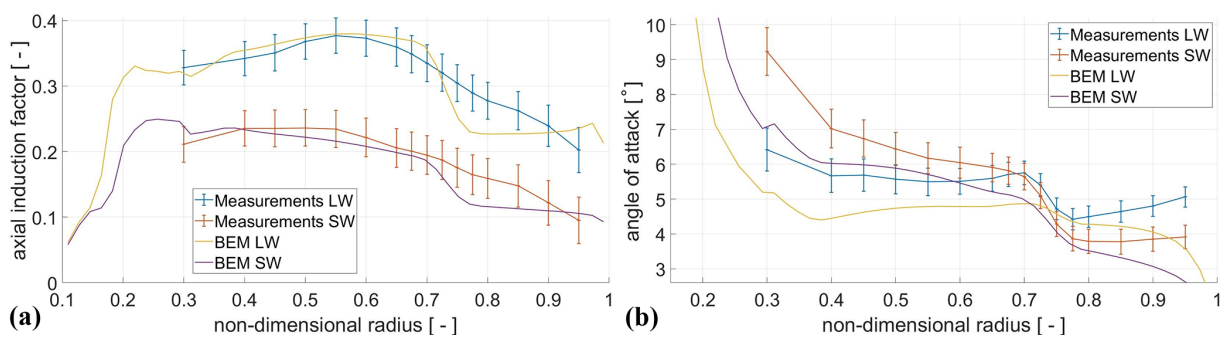


Figure 4.9: Axial induction along the blade span (a) and angle of attack (b) from measurements and BEM simulations for the light-wind (LW) and strong-wind (SW) modes.

Next, we explore possible reasons for the milder gradients in the axial induction distribution. In the BEM theory, the blade elements are treated independently of each other. This assumption is clearly violated with the blade design of the Hybrid-Lambda Rotor. To reveal further insights into the flow in the rotor plane, we use FWW simulations for the conventional and Hybrid-Lambda model turbines. The radial velocity component is extracted on a horizontal line in the rotor plane in a non-rotating coordinate system, and the average over all time steps is shown in Fig. 4.10. The time step used corresponds to an azimuthal resolution of 1.5° . Figure 4.10 shows the envelope, i.e. the minimum and maximum of the radial flow, thus displaying the impact of the passing blades and the associated vortices. A comparison of the two blade designs confirms an increased radial outboard flow component for the Hybrid-Lambda Rotor, almost over the entire rotor span. However, it is especially increased in the design blending region at 70 % blade length. The envelope shows lower extreme values at the blade tip for the Hybrid-Lambda Rotor. This is due to the increased axial wind speed component in the outer rotor annulus. Consequently, the difference in wind speed compared to the free stream is lower, and less radial flow is observed. The conventional rotor has a much higher axial induction near the blade tip (compare with Fig. 4.5a), which explains the larger magnitudes in the radial flow envelope. However, the envelope also reveals a second peak in the blending region of the Hybrid-Lambda Rotor, which means that the shear layer between the axial flow in the inner rotor disc and the outer annulus also introduces additional radial flow. This clearly highlights that the blade elements can not be treated independently, and complex, three-dimensional flow structures lead to the smearing of the steep gradients. Figure 4.10 also shows the differences in the radial flow between the operating modes. When the Hybrid-Lambda Rotor switches from the light-wind to the strong-wind mode, the radial velocity component decreases because the axial induction and the thrust coefficient are reduced, and there is less widening of the stream tubes. In contrast, the conventional rotor maintains the same operational point (same TSR and pitch angle) until rated wind speed, since no load limitation is applied. This means that the thrust coefficient and the axial induction remain constant. When the axial wind speed increases, the radial velocity component will also increase in the rotor area of the conventional turbine. Absolute velocity values are plotted in Fig. 4.10. The flow in the wake of the Hybrid-Lambda Rotor is further investigated in Sect. 4.4.4, and the influence of the trailing vortices is explained, which also heavily influence the flow in the rotor area.

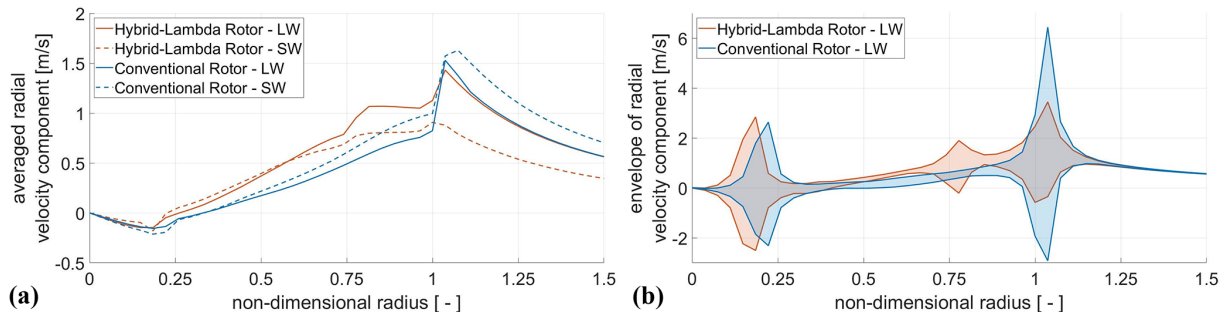


Figure 4.10: Averaged radial velocity component **(a)** and envelope of the radial velocity component **(b)** in the rotor plane from FVW simulations for the two model turbines.

From the FVW simulations we can further extract the streamlines for both model turbines, which are shown in Fig. 4.11. The streamlines that pass along the tip of the rotors are almost identical between the two turbines. This means that the outer shape of the wake is similar. In contrast, the streamlines of the Hybrid-Lambda Rotor inside the wake are pushed further outwards compared to the conventional model turbine. Here, the effect of the increased radial flow is visible. If one considers the conservation of mass flow, the slower air in the inner part of the rotor has to expand into the outer wake annulus (compare with the wake investigations in Sect. 4.4.4). Thus, the streamlines in the outer part of the wake are closer together.

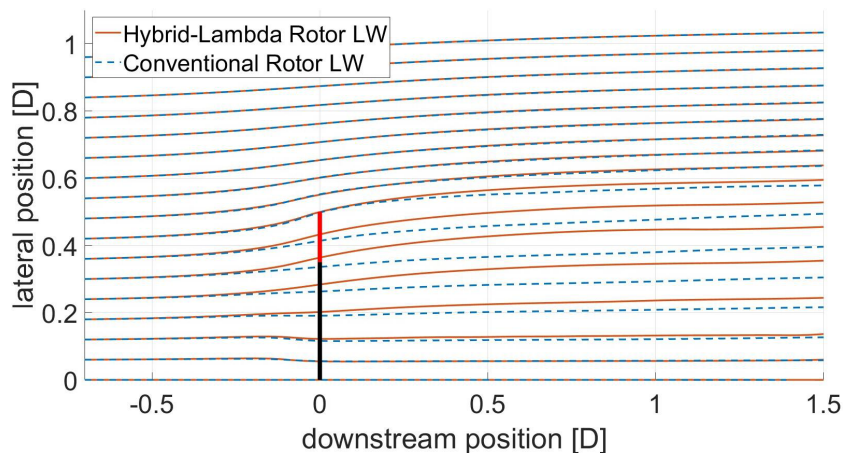


Figure 4.11: Streamlines from FVW simulations for the Hybrid-Lambda model turbine in the LW mode and the conventional model turbine (same c_T). The rotor is indicated with the vertical black bar, and the low-induction tips are displayed in bright red.

4.4.3 Dynamic response to gust events

We compared the response of the flapwise RBM to gust events between the two sets of blades. The gust events were generated with the active grid, mimicking a scaled extreme operating gust with the so-called Mexican hat shape, according to IEC 61400-1 (2019). The inflow was characterized by Neuhaus et al. (2021) with hot-wire measurements of multiple repetitions of the gust event in the centre of the rotor plane, which are plotted in Fig. 4.12. These active-grid settings were derived as the optimum trade-off between the frequency and the amplitude of the gust, as described in Sect. 4.3.1. The oscillations in the wind speed after the gust event (for $t > 3.2$ s) are a pumping effect of the flow induced by the active grid, which can not be avoided for such fast changes in the wind speed. The ensemble-averaged response in the flapwise RBM for the two rotors is displayed in Fig. 4.12. Note that no wind turbine controller was applied in this study. The pitch angle remains constant, and the rotational speed is controlled to be constant over the entire gust event. The Hybrid-Lambda Rotor is in the light-wind operating mode during the steady inflow period before the gust event. The conventional rotor is operated at the same TSR of 7.5, and the pitch is set in order to match the same flapwise RBM between the two rotors in the steady inflow period. This allows us to compare the pure aerodynamic response of the rotors. The amplitude of the load overshoot is less for the Hybrid-Lambda Rotor, and the maximum flapwise RBM is 4.3 % higher for the conventional blades. The reduced axial induction in the outer part of the Hybrid-Lambda blades helps to mitigate the load overshoot. Similar conclusions were drawn by Ribnitzky et al. (2024a) when comparing the effect of extreme-wind-shear events on the 15 MW Hybrid-Lambda Rotor and a reference rotor on a full-scale level with BEM simulations.

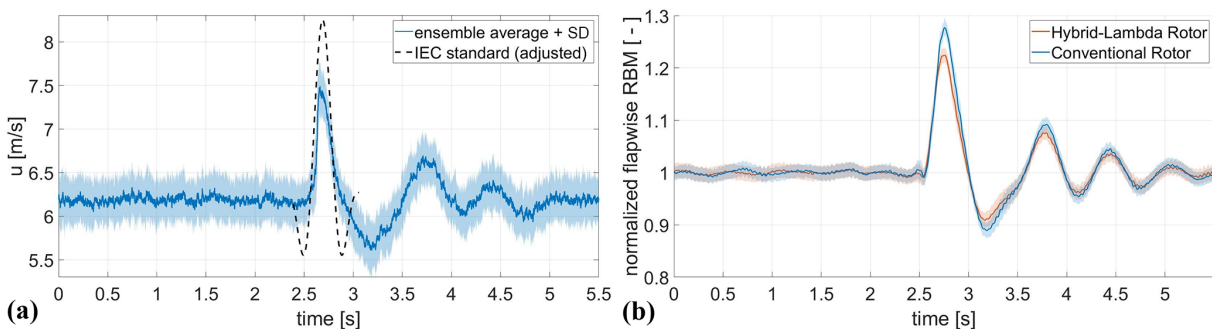


Figure 4.12: Gust in the wind tunnel: inflow hot-wire measurements in the rotor plane and scaled IEC gust, displayed 8 times slower than ideal scaling; gust amplitude is not scaled (a). Flapwise RBM response of the Hybrid-Lambda Rotor and the conventional rotor. The shaded area indicates the 95 % confidence interval of the 45 repetitions of the gust event (b).

4.4.4 Wake characterization

In this section, we provide an in-depth analysis and comparison of the wake of the two rotors, using hot-wire measurements and FVW simulations. The hot-wire measurements are performed in the open-jet configuration of the wind tunnel, as explained in Sect. 4.3.1. This means that there is a shear layer between the wind tunnel jet and the still air around the nozzle. For large distances to the wind tunnel nozzle, there is an unavoidable interaction of the wind tunnel shear layer with the wake of the turbine. Measurement data for downstream distances larger than $2D$ should be treated with care, especially for larger lateral distances to the centre line. Nevertheless, the data can provide an impression of the overall picture, and we consequently decided to plot the data up to $3D$ downstream. Figure 4.13 shows the normalized wind speed and the turbulence intensity in the wake of the two rotors. A major advantage of the Hybrid-Lambda Rotor becomes clear when comparing the wake for the different operating modes. When the wind speed increases and the rotor shifts to the strong-wind mode and further to rated conditions, the pitch angle is increased, as shown in the control schedule in Fig. 4.4. Consequently, the thrust coefficient is reduced, the wake deficits are greatly decreased (see also Fig. 4.14), and the opening angle of the wake (e.g. the expansion of the stream tube) is reduced. This is of immense importance when evaluating the rotor concept in wind farm applications. In contrast, a conventional rotor would operate with the same axial induction and thrust coefficient until rated wind speed. Consequently, the wake deficits remain unchanged, and we only provide one plot for the conventional rotor. The second aspect that we discuss is the shape of the wake. The axial induction distribution of the Hybrid-Lambda Rotor is clearly mirrored in the wake profiles. The low-induction design of the outer 30 % of the blades leads to an outer annulus with reduced wake deficits, which is highlighted in Fig. 4.13 with the contour lines. In contrast, the inner part of the blade is designed for a higher axial induction compared to the conventional rotor (see Fig. 4.5a), thus resulting in lower wind speeds in the centre of the wake. Note that the axial induction is a free design variable in the Hybrid-Lambda design methodology, and the blade design could be adjusted when optimizing for the mitigation of wake effects, e.g. choosing a slightly lower axial induction for the inner blade section. However, the wind tunnel model of the Hybrid-Lambda Rotor was not designed to outperform the conventional model in terms of wake effects but with the objective of incorporating the wake characteristics of the full-scale Hybrid-Lambda model.

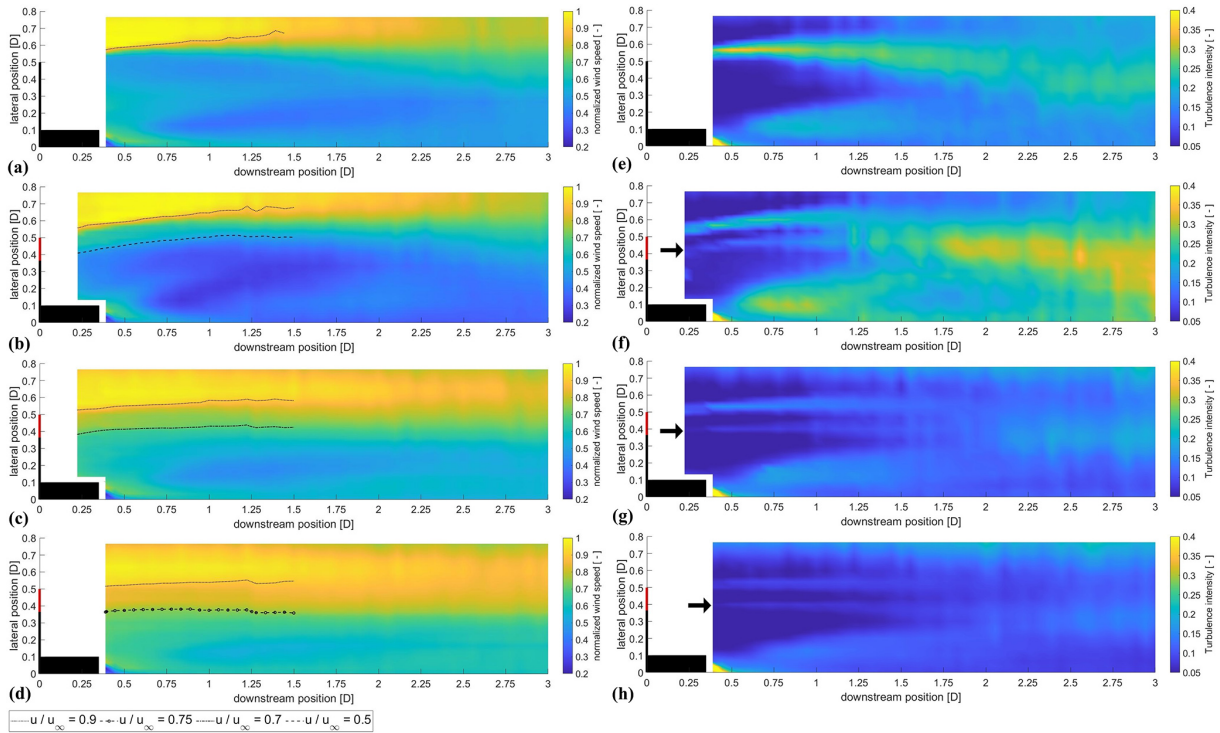


Figure 4.13: Mean normalized wind speed (a–d) and turbulence intensity (e–h) from hot-wire measurements in the wake of the model turbines. From top to bottom: conventional rotor (a, e) and Hybrid-Lambda Rotor in the LW mode (b, f), in the SW mode (c, g), and at rated wind speed (d, h). Nacelle and blades are displayed in black, and the outer 30% of the Hybrid-Lambda blades are displayed in red. The black arrows point at the second shear layer starting at the blade design blending region.

The outer annulus with reduced wake deficits leads to a second shear layer at the border to the inner wake core with lower wind speeds. This is highlighted by the black arrows in Fig. 4.13, showing the local turbulence intensity, which is defined as $T_i = \sigma(u(x,y))/u_{\text{mean}}(x,y)$. For now, we only address this as a shear layer, since the vorticity can not be derived from one-dimensional hot-wire measurements. We further look into the vorticity in the following paragraphs. The conventional rotor exhibits a single shear layer between the wake and the free stream, which leads to a single ring of increased turbulence intensity that widens up with further downstream distances. In contrast, for the Hybrid-Lambda Rotor, two rings of increased turbulence intensity can be observed. However, the magnitude of the turbulence intensity of both rings is lower compared to that of the single ring from the conventional rotor. The first ring emerges from the blade tip; the second one is shed at the blending region on the blade at 70% blade length (if one considers the opening angle of the wake). Travelling downstream,

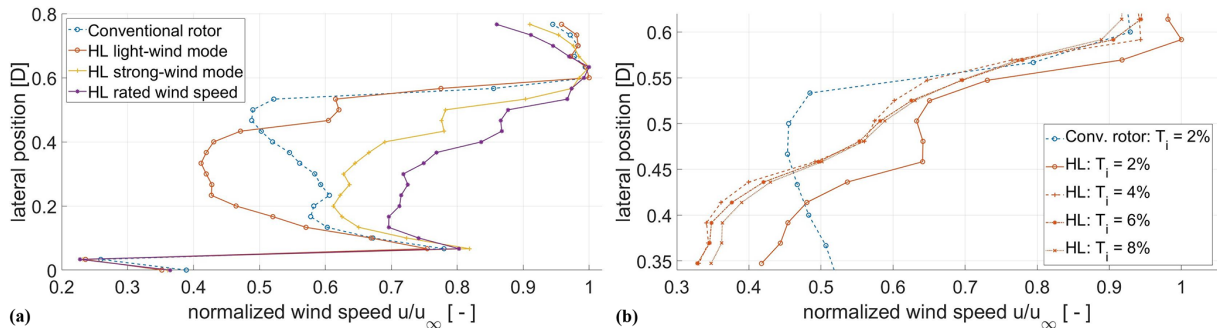


Figure 4.14: Wake profiles at a distance of $0.4D$ downstream for the two model rotors. At $T_i = 2\%$ for different operating modes **(a)** and in the light-wind mode for different T_i values **(b)**.

these two shear layers widen up and start to interact with each other, which finally leads to a region of very high turbulence intensity for downstream distances larger than $2D$. This effect is most prominent in the light-wind mode. However, the two rings of increased turbulence intensity are still noticeable in the strong-wind mode and under rated conditions. Figure 4.13 further shows how the shape of these rings changes between the operating modes. While they are bent outwards in the light-wind mode, the curvature and opening angle decrease when switching to the strong-wind mode, and the rings are almost straight. Under rated conditions, they even tend to have a slight inwards-directed taper.

From previous FVW simulations and LESs on the full-scale Hybrid-Lambda Rotor, Ribnitzky et al. (2023) discovered that with increasing turbulence intensity in the inflow, the outer annulus with reduced wake deficits smears out. This means that the step-shaped wake profile, with a region of constant high wind speed in the outer annulus, develops more into a gradual change between the inner and outer wake deficits. This transition happens closer to the rotor for higher turbulence levels. To further investigate this, hot-wire measurements were performed $0.4D$ behind the rotor with a hot-wire spacing of 4 cm (instead of 6 cm for all other cases presented before), with four different turbulence intensities in the inflow, generated with the active grid. The free-stream velocity among the different turbulence-levels was not exactly matched, since the activation of the active grid impacts the mean wind speed. Although the active-grid protocols were iterated in order to match the free-stream velocity as best as possible, small deviations of around 5% to 10% in the free-stream velocity remain. However, this does not affect the gradients of the wake profiles, which are the focus of interest in this case. The results are shown in Fig. 4.14,

and the smearing of the outer wake annulus is clearly visible. Especially for the case with 8 % inflow turbulence intensity, the plateau with higher wind speeds vanishes.

We assume that the inner shear layer is also coupled to an additional vortex system that emerges from the blending region on the blade. Since the vorticity can not be derived from one-dimensional hot-wire measurements, we use FVW simulations to investigate this assumption. First, the FVW simulations confirm the characteristics of the wake of the Hybrid-Lambda Rotor. The mean wind speed, plotted in Fig. 4.15, also shows the outer annulus with higher wind speeds in both operating modes, as well as the reduced wake deficits and reduced wake expansion in the strong-wind mode. The vorticity is computed as the magnitude of the three vorticity components. The vorticity plots clearly highlight a second ring of vortices emerging from the blending region on the blade. The magnitude of the vorticity is lower than for the tip vortex, as also observed in the turbulence intensity derived from the hot-wire measurements. The FVW simulations are set up in a way to produce a wake that is as undisturbed as possible, e.g. using laminar and uniform inflow and a relatively low core spread eddy viscosity. This simulation set-up is chosen to identify a clear representation of the vortex rings and their positions. Consequently, the vortex systems do not break up noticeably, and the interaction between the inner and outer rings of vortices is rather low.

All in all, the measurement results are in very good agreement with the FVW simulations and LESs that were carried out by Ribnitzky et al. (2023) on the 15 MW full-scale Hybrid-Lambda Rotor, where an improved wake recovery was also observed. In short, the results indicate three major advantages of the Hybrid-Lambda Rotor in wind farm applications: first, the decreased wake deficits for a large range of wind speeds below rated (for $u_{ts} < u < u_{rated}$); the increased wind speeds in the outer wake annulus, which are beneficial for partial-wake scenarios; and the enhanced wake mixing due to the additional shear layer and vortex system in the wake.

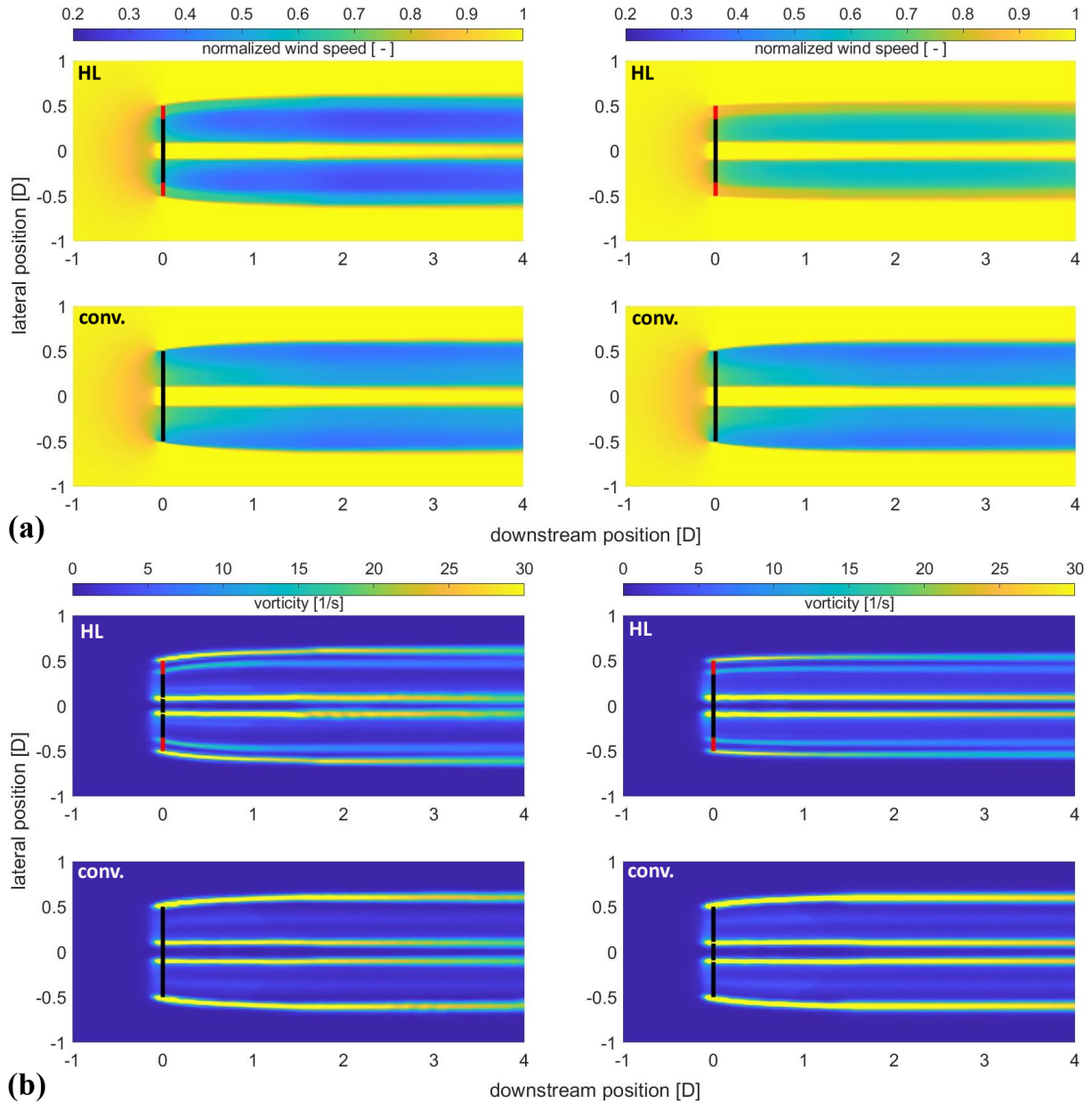


Figure 4.15: Normalized wind speed **(a)** in the light-wind (left) and strong-wind modes (right). Vorticity magnitude **(b)** in the light-wind (left) and strong-wind modes (right) for the Hybrid-Lambda model turbine (top) and the conventional model turbine (bottom) from FVW simulations.

4.5 Discussion

Scaling wind turbine rotors to wind tunnel size is a delicate scientific task since not all physical characteristics can be matched exactly. The scaling objectives need to be defined precisely, and compromises need to be made regarding the matching of classical aerodynamic non-dimensional parameters. In this paper, we developed a method on how to scale the Hybrid-Lambda Rotor to wind tunnel size with objectives that differ from those of other aerodynamic scaling approaches found in the literature, as described by Canet et al. (2021), Bottasso and Campagnolo (2021), and Gasch and Tvele (2012), among others. The concept involves a blade design for two TSRs, which is a challenge on its own. But additionally, we need to transfer the design method to lower TSRs in order to derive large enough chord lengths and Reynolds numbers. This leads to a novel scaling approach, coupled with the objective of matching the non-uniform distribution of axial induction along the blade span for two different operating modes.

This scaling approach fulfilled its aim of replicating the aerodynamic characteristics at wind tunnel scale by means of an aerodynamic redesign with low-Reynolds-number profiles. For the sake of comparability with the reference model turbine, as described in Berger et al. (2018), we chose the same airfoils: SG6040 and SG6041. Although we decided otherwise, we want to draw the attention of future designers of model wind turbines to the low-Reynolds-number airfoil SD7032, which was experimentally investigated by Fontanella et al. (2021), and for which a high-quality data set for the airfoil polars under various Reynolds numbers is available.

The investigation of the scaled rotor in the wind tunnel shows that the switching between the operating modes and the associated tilting of the spanwise angle of attack distribution work similarly to the full-scale rotor, which fulfils one of the major scaling objectives. In the measurements, the spanwise change in the axial induction distribution is smeared out, which can not be reproduced by the model assumptions inherent in the BEM simulations. Complex flow structures were identified as an increased radial flow in the rotor plane and an additional vortex system that is shed from the blending region on the blade. Here, the question arises as to how the scaling affects the rotational augmentation and the radial flow components in the rotor plane, since the Rossby number (ratio of inertia to Coriolis forces) is not matched in the given scaling approach. Further, the local blade solidity is increased for the model turbine, which can further enhance the effect of rotational augmentation compared to the full-scale rotor (Herráez

et al., 2016). However, FVW simulations for the full-scale turbines do confirm that the radial flow component is increased for the Hybrid-Lambda turbine compared to the reference turbine in a similar manner to that shown in this paper for the model turbine. Further, the additional vortex system is also found in the full-scale simulations. Full insights into the complex flow phenomena on the blade and the impact of the scaling approach could only be revealed by blade-resolved CFD simulations, which is out of the scope of this study.

Furthermore, the wind tunnel model allowed us to reveal the unique wake characteristics of the Hybrid-Lambda Rotor and underline three major advantages in the wake behaviour: first, the decreased wake deficits in the strong-wind mode; second, the increased wind speed in the outer wake annulus in the entire partial load range; and third, the additional shear layer and vortex system. To the best of the authors' knowledge, such a blade design with radially variable axial induction has never been investigated in a wind tunnel before, which includes the ability to change the operating mode by changing the operational TSR, tilting the spanwise angle of attack distribution, and reducing the axial induction. The major findings in this paper emphasize that the Hybrid-Lambda design methodology works reasonably well, but when designing a blade with such strong gradients along the blade span, one can not rely solely on the BEM theory. This was somewhat expected, since the first version of the Hybrid-Lambda Rotor was designed to separate the effects on the inner and outer parts of the blade and to push the limits of the applicability of the BEM theory, where the blade elements are treated independently.

These findings are in line with previous FVW and LES investigations on the full-scale Hybrid-Lambda Rotor by Ribnitzky et al. (2023). A smearing of the gradients in the axial induction distribution was also recognized in the FVW investigations. Further, the difference in the axial induction between the inner and outer parts of the blade was found to be reduced compared to that in the BEM simulations. Finally, the wake characteristics show very good agreement between the measurements presented in this paper and the aforementioned FVW simulations and LESs on the full-scale rotor. The outer wake annulus behaves very similarly across the simulations and the measurements, considering the wind speed distribution and turbulence intensities. It was further found with both methods that the gradients in the wake profile smear out with increasing turbulence intensity. Paulsen et al. (2024) investigated the Hybrid-Lambda Rotor using mesoscale weather research models. They showed

that the benefits of using a wind farm application even outweigh those of using a single turbine due to the reduced wake losses.

When we compare the hot-wire measurements in the wake with the LDA measurements in the rotor plane, we discover some discrepancies. The gradients in the axial induction seem to be smeared out when considering the LDA data. However, the wake profiles recorded with the hot wires reveal a relatively steep gradient in the velocity profiles. This leads us to the limitations of the applied method, which aims to derive the axial induction in the rotor plane by probing the wind speed in the bisectrix of two blades. According to Herráez et al. (2018), ideally, the induction of the rotor blades is counterbalanced, and the velocities extracted from the rotor plane are only influenced by the wake induction and not by the blade induction itself. However, this method can not capture the influence of the local trailed and shed vorticities accurately. This usually applies to the tip region ($r/R > 0.92$), where the tip vortex starts to dominate the flow. In the present study, we found a second vortex system that emerges from the blending region on the blade and that will influence the circulation distribution along the blade span. Consequently, the LDA measurements close to the design blending region are also influenced by the additional vortex, and those results should be treated with care. Since the vortex emerges from the blade, the LDA does not record steep gradients in the rotor plane. Only with some downstream distance does the vortex lead to sharp velocity gradients, which can be captured with the hot wires in the wake. Considering the outwards bending of the streamlines in Fig. 4.11, we can conclude that the inner wake core with the slower flow expands and pushes into the outer wake annulus. Consequently, the steep gradients in the wake profiles seem to develop within the first $0.5D$ downstream of the rotor. This can somehow link the low gradients from the LDA measurements in the rotor plane to the steep gradients from the hot-wire data in the wake. Nevertheless, more measurements in direct proximity to the rotor with both measurement techniques would be necessary to support this hypothesis. Despite the methodological limitations, the overall results and the combination of the hot-wire measurements in the wake with the FVW simulations give a good representation of the bigger picture concerning the flow structures in the wake of the Hybrid-Lambda Rotor.

4.6 Conclusions

In this paper, we first developed a method to scale the Hybrid-Lambda Rotor to wind tunnel size. Second, we investigated the influence of the steep gradients of axial induction along the blade span on the rotor aerodynamics. Third, we thoroughly analysed the wake characteristics of the Hybrid-Lambda Rotor and compared them to those of a conventional model rotor. We showed that it is possible to transfer a complex rotor concept to wind tunnel size and to lower design TSRs. In this delicate process of finding a compromise, it is necessary to precisely define the scaling objectives. In this case we aimed to match the axial induction distribution and reproduce the shift in the angle of attack distribution when switching between the operating modes.

With the experimental investigations in the wind tunnel, we analysed the impact of the steep spanwise gradients in the blade design, which lead to a complex three-dimensional flow. We found an additional shear layer and vortex system in the wake of the Hybrid-Lambda Rotor, and we quantified the reduced wake deficits in the strong-wind mode and under rated conditions. Further, we tested the Hybrid-Lambda Rotor in gust events, and the results show that the low-induction design of the outer part of the blade is beneficial and reduces the load overshoot by more than 4% compared to the conventional model turbine. The derived results improve our understanding of the three-dimensional flow patterns that are introduced by the Hybrid-Lambda Rotor concept and provide a valuable complementary data set to the simulations on the full-scale rotor, as described by Ribnitzky et al. (2024a). Further, the developed methodology can offer new inspirations when solving other scaling problems for complex wind turbine systems.

In this paper, we focused on aerodynamic effects and steady-state operation. In a full-scale application, reliable and safe operation of offshore low-specific-rating turbines with such large rotors can only be achieved with sophisticated control strategies. Specifically for the Hybrid-Lambda Rotor, the controller development should aim to realize the transient change in operating modes and apply techniques that limit extreme loads. The scaled model presented here offers the opportunity to test different controller versions under various reproducible turbulent inflow conditions in the wind tunnel, which will be addressed in future studies.

The successful experimental validation of the aerodynamic concept of the Hybrid-

Lambda Rotor, so far on wind tunnel scale, confirms the potential of deploying low-specific-rating turbines at offshore sites. This can favour a higher and less fluctuating power feed-in at low to medium wind speeds, thus contributing to the transition toward a reliable and economically viable wind energy supply. Load-limiting strategies are necessary to enable rotors with such large diameters, and the accompanying losses in efficiency must be carefully considered within the design process. The Hybrid-Lambda Rotor can offer a possible solution, and with the experimental work presented here, we have taken the next step in validating the concept.

Data availability

For the Hybrid-Lambda model turbine, we provide the blade geometry as a CAD file and the turbine simulation model for OpenFAST. We further provide the mean wind speeds and turbulence intensities from the hot-wire measurements in the wake, as shown in Fig. 4.13, under the following repository: <https://zenodo.org/records/14883916>, Ribnitzky (2025b).

Acknowledgements

We would like to thank Lars Neuhaus and Tom Wester for the support during the measurements.

Financial support

The work presented in this paper was funded by the Deutsche Forschungsgemeinschaft (DFG, German Research Foundation) – project ID 434502799 – SFB 1463.

Chapter 5

Experimental investigation of wind turbine controllers for the Hybrid-Lambda Rotor

Apart from minor adjustments and corrections, the content of this chapter is identical to that of the following publication:

Daniel Ribnitzky, Vlaho Petrović and Martin Kühn (2026). 'Experimental investigation of wind turbine controllers for the Hybrid-Lambda Rotor'. In: *Wind Energy Science* 11.2, pp. 469–491. DOI: [10.5194/wes-11-469-2026](https://doi.org/10.5194/wes-11-469-2026)

Reproduced in accordance to the Creative Commons Attribution 4.0 License.

Abstract

The continuous growth in rotor diameter of offshore wind turbines must be accompanied by advanced control strategies that master the trade-off between limiting the loads and maximizing power output, fostering a lightweight and cost-effective blade design. This is addressed by the Hybrid-Lambda Rotor design and control methodology which realizes two operating modes by following two different tip speed ratios (TSRs) below rated power with an overarching load constraint. Contrary to conventional wind turbine controllers, this leads to a wide range of wind speeds where the torque and pitch controllers are active simultaneously. The objective of this paper is to develop and apply such control strategies on the MoWiTO 1.8 model wind turbine and to exper-

imentally validate them under turbulent reproducible inflow conditions in the wind tunnel using an active grid. The results are examined regarding extreme loads, power production, fatigue loads and pitch actuation. Further, we discuss the scaling of the controller characteristics and inflow test cases according to the model turbine scaling. Different versions of the pitch controller are introduced: first, a baseline controller with a model-based wind speed estimator which performed well in tracking the different TSRs; second, a load feedback controller that overcame model uncertainties and performed well in setting the mean value of the loads; third, an inflow feed-forward controller which was able to reduce load overshoots in gust events. With the results presented here, we make the next step in the experimental validation of the control methodology, which unlocks the full potential of aerodynamic efficiency and ensures the structural integrity of the Hybrid-Lambda Rotor.

5.1 Introduction

The size of future wind turbine rotors is continuously increasing, and the current trend of growth in rotor diameter does not seem to saturate (Lüers, 2024; Berkhout et al., 2018; Hand et al., 2018). Rotors with a low-specific rating can capture relatively more energy in light winds, which is beneficial for a reliable and more continuous electricity supply, and it will increase the value of wind energy, as stated, among, others by Hirth and Müller (2016), Johnson et al. (2021), and Wiser et al. (2021). However, large rotors can only be designed to be economically feasible if extreme loads are limited, fostering a lightweight and cost-effective blade design. This emphasizes the necessity of advanced control algorithms which limit the extreme loads whenever needed but maximize the power output whenever possible. In other words, a close interaction of blade design and controller design methodology is needed, with the aim of achieving better power coefficients when the loads are constrained.

This problem is addressed by the Hybrid-Lambda Rotor design methodology, as first described by Ribnitzky et al. (2024a). It describes how the rotor diameter can be increased while maintaining the rated power and the extreme loads of a respective reference turbine. The optimization process can be described as the maximization of the power output over the entire partial load range while constraining the flapwise blade root bending moment. The blade design methodology includes a design for two tip speed ratios (TSRs) and two operating modes below rated power which is closely coupled to the controller design. Previous studies have successfully shown the benefits

of the concept compared to conventional upscaling approaches. The Hybrid-Lambda concept was first applied on a 15 MW offshore wind turbine with a specific rating of 180 W m^{-2} and a diameter of 326 m. In simulation environments, the concept was investigated using steady-state operating points and transient load cases including a preliminary controller (Ribnitzky et al., 2024a). Further, the concept was scaled to wind tunnel size and verified for steady-state operating points (Ribnitzky et al., 2025). A detailed explanation of the controller design and an experimental investigation of the transient behaviour of the Hybrid-Lambda controller are still missing. With this paper, we aim to fill this gap.

Limiting extreme operating loads is often addressed by conventional peak-shaving, and this paragraph serves as a brief literature review on controller design which addresses load constraints. For conventional peak-shaving the minimum pitch angle below rated power is calculated as a function of the wind speed in order to limit the load to a given value. The controller then uses a wind speed estimator and chooses the pitch angle from a look-up table (LUT), as described among others by Abbas et al. (2022), where the torque controller is not adjusted for peak-shaving purposes. Pusch et al. (2024) and Lazzerini et al. (2025) introduced frameworks to determine optimal steady-state operating points (pitch angle and rotor speed) for wind turbine control over the entire operating range of wind speeds, by solving optimization problems constrained by maximal loads or rotor speed values. Lowering the mean value of a certain load, as done for conventional peak-shaving, will reduce the peak fluctuations, too, as shown by Bottasso et al. (2014a), but it does not yet ensure that the peak fluctuations will not cross a certain limit. This can be realized by envelope protection algorithms as presented by Petrović and Bottasso (2017). Other approaches focus on feed-forward controllers that enable a preview on the inflow and allow the turbine to act in advance rather than reacting on load overshoots. Guo et al. (2023) and Fu et al. (2023) described how a feed-forward controller can be set up using preview measurements acquired with a lidar. Schlipf et al. (2013) also used model predictive control for this purpose. The advanced control methods improved the turbine response with a reduction in rotor speed and power variations, as well as a reduction in extreme and fatigue loads. Sinner et al. (2022) presented the first physical test of model predictive control for blade pitch control of a scaled wind turbine which effectively reduced rotor speed variations above rated wind speed. They used the Model Wind Turbine Oldenburg (MoWiTO 1.8) with 1.8 m diameter (Berger et al., 2018) in the $3 \times 3 \text{ m}$ wind tunnel in Oldenburg (Kröger et al., 2018) and tested the

controller under reproducible turbulent inflow conditions generated with an active grid (Neuhaus et al., 2021). This set-up is also used in the study presented here. Bottasso and Campagnolo (2021) explained fundamentals on the scaling of wind turbines and wind tunnel testing as well as the design of the controllers and actuators for scaled turbines. Experimental validation of innovative control algorithms bridges the gap between simulation-based studies and field testing. The advantage of wind tunnel tests is the ability to test under tailored and reproducible inflow conditions. However, when using model turbines, the effects of scaling must be carefully considered. Wind tunnel testing adds important value compared to simulation-based studies while avoiding administrative hurdles of full-scale tests.

The objective of this paper is to develop control methodologies for very large wind turbines with a load constraint that follow the Hybrid-Lambda operation strategy. This includes the realization of two operating modes with corresponding TSR values below rated power. The control methods are applied on a 1.8 m diameter model wind turbine, and the required scaling conditions are derived. Four controller versions are tested in the wind tunnel under reproducible turbulent inflow conditions. The experimental testing aims to answer the following six specific research aspects. First, we address how the transition between the operating modes can be accomplished. Second, we investigate how we can achieve TSR tracking while the pitch controller is simultaneously active to constrain the loads. Third, we explore different methods on how to constrain the extreme operating loads. Fourth, we discuss how to deal with model uncertainties. Fifth, we evaluate the controller versions considering extreme loads, fatigue, pitch actuation and power output. Sixth, we transfer the findings from the scaled experiments to the full-scale application and derive recommendations for controller design for very large offshore wind turbines with a load constraint.

5.2 Methodology

In this section, we first explain the Hybrid-Lambda control methodology. We then address the torque controller in Sect. 5.2.1.1, and we outline four different versions of the pitch controller in Sect. 5.2.1.2. The transferability of the experimental results from wind tunnel scale to the full-scale turbine is demonstrated in Sect. 5.2.2. The experimental set-up in the wind tunnel is described in Sect. 5.2.3, followed by an explanation of the test cases in Sect. 5.2.4 and the method to calculate damage equivalent loads and pitch actuation in Sect. 5.2.5.

5.2.1 The Hybrid-Lambda control methodology

In this section we describe the steady-state operating points for the Hybrid-Lambda Rotor, as depicted in Fig. 5.1 for the scaled wind tunnel model. We provide more information on the full-scale blade design, which is derived for considerably higher TSRs, in our previous publication (Ribnitzky et al., 2024a) and on the aerodynamic scaling to wind tunnel size in (Ribnitzky et al., 2025). A major objective of the Hybrid-Lambda Rotor design and control methodology is to achieve better power coefficients whenever loads need to be constrained. Therefore, the rotor is designed for two operating modes below rated power. In the light-wind (LW) mode, the rotor is operated at a high TSR (7.5 in the case of the model wind turbine) and with the optimum pitch angle (fine pitch is -0.8°). Since the outer 30% of the blade is designed for a TSR of 7.5, the light-wind mode ensures the maximum power coefficient. At a certain wind speed, the maximum loads are reached: in this case the maximum flapwise blade root bending moment (RBM) of 7.3 Nm. This wind speed is called $u_{ts} = 6.3 \text{ m s}^{-1}$, marking the start of the transition to the strong-wind (SW) mode for higher wind speeds. In the transition region, the rotational speed is kept constant at $\omega_{\text{trans}} = 500 \text{ rpm}$ in order to reduce the TSR and the pitch is increased to constrain the flapwise RBM. Once the lower TSR of 6 is reached, the transition ends at the wind speed $u_{te} = 7.9 \text{ m s}^{-1}$. For higher wind speeds, the rotor operates in the strong-wind mode, following the lower TSR of 6, and the pitch is increased accordingly to limit the loads. Since the inner 70% of the blade is designed for a TSR of 6, the inner part of the blade is operated in its design point in the strong-wind (SW) mode. The loads in the outer part are relieved, and the lever arm of the resulting bending forces is reduced. This is the reason why better power coefficients can be achieved compared to conventional peak-shaving strategies where the blade is conventionally optimized for one operating point and the load constraint is achieved solely by pitching to feather. These advantages are thoroughly analysed in a previous publication (Ribnitzky et al., 2024a). In contrast, this study focuses on how these steady-state operating points can be realized by a pitch and torque controller.

The Hybrid-Lambda control methodology introduces several additional features that are not present for conventional wind turbine controllers. First, the rotational speed needs to be kept constant in a defined wind speed range to incorporate the transition between the operating modes below rated wind speed. Second, the pitch angle needs to be set below rated wind speed in order to constrain the maximum loads in the transition

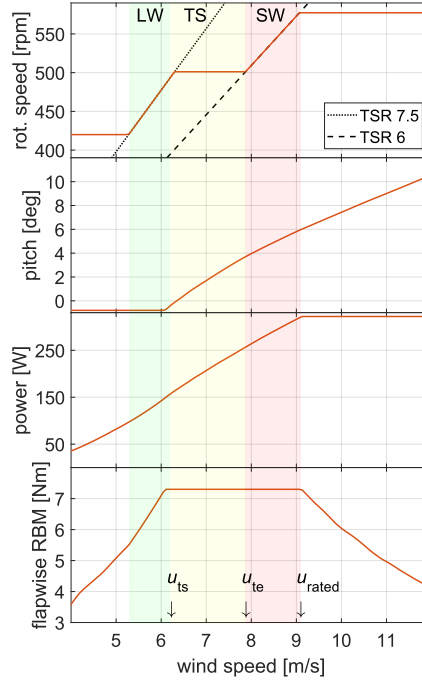


Figure 5.1: Steady-state operating points for the Hybrid-Lambda model turbine, derived from steady-state measurement data. Background colours indicate the operating mode: green, light-wind mode (LW); yellow, transition (TS); red, strong-wind mode (SW). u_{ts} and u_{te} : wind speed at start and end of transition.

region (constant rotational speed) and in strong-wind mode (variable rotational speed). Third, the torque controller is supposed to track the lower TSR in the strong-wind mode, but the pitch angle will vary with respect to the wind speed; therefore the torque coefficient c_q will not be constant, and the proportionality k in the $k\omega^2$ -law of the torque controller is not constant either. The generator torque M_g is calculated as expressed in Eq. (5.1). Here, R is the rotor radius, ρ is the air density, λ is the tip speed ratio, β_{pitch} is the pitch angle, and ω is the rotational speed. Overall, the pitch and torque controllers will be active simultaneously over a wide range of wind speeds, which is usually not the case for conventional wind turbine controllers.

$$M_g = \frac{\pi R^5 \rho c_q(\lambda, \beta_{pitch})}{2\lambda^2} \omega^2 = k\omega^2 \quad (5.1)$$

Compared to the steady-state operating points presented by Ribnitzky et al. (2025), the maximum rotational speed is reduced to 577 rpm to keep a sufficient margin to the hardware constraint of 600 rpm. Note that the pitch is not adjusted for very low wind speeds when the turbine operates at minimum rotational speed. This could further increase the power output close to cut-in.

Torque controller

The tasks of the torque controller are 4-fold, i.e. to maintain the minimum rotational speed (ω_{\min}) close to cut-in wind speed, to follow the high TSR in the light-wind mode, to keep the rotational speed constant in the transition region (ω_{trans}) and to follow the low TSR in the strong-wind mode. TSR tracking is usually accomplished by setting the generator torque according to the $k\omega^2$ -law, as described by Bossanyi (2000), while maintaining a constant rotational speed is a typical task for a PI-controller. Switching of controller types often leads to adverse transient controller reactions. Therefore, the Hybrid-Lambda torque controller is realized with one single PI-controller over the entire partial load range, but the desired behaviour is accomplished by changing the saturations and set points. Figure 5.2a shows the rotational speed and generator torque over the wind speed. However, the wind speed is generally not known by the torque controller. Instead, the input is the rotational speed and the output is the generator torque. These data (generator torque over rotational speed) are acquired a priori with blade element momentum theory (BEM) simulations and are stored in an LUT. To distinguish between the different LUTs used in this study, we refer to the table mapping generator torque over rotational speed as torque-LUT. Note that the pitch angle varies in the strong-wind mode and that the generator torque needed to track the low TSR is subject to model uncertainties. When we plot the generator torque over the rotational speed (compare with Fig. 5.2) for the Hybrid-Lambda Rotor, this function is ambiguous at ω_{trans} when the controller should switch from the light-wind to the strong-wind mode or vice versa; e.g. multiple generator torque values are assigned to the same rotational speed ω_{trans} . This is where the PI-controller is needed. To describe how the saturations and set points are derived, we introduce two rotational speeds that we chose from the middle of the light-wind and strong-wind mode, respectively:

$$\omega_{\text{middle,LW}} = \frac{\omega_{\min} + \omega_{\text{trans}}}{2} \quad (5.2)$$

$$\omega_{\text{middle,SW}} = \frac{\omega_{\text{trans}} + \omega_{\max}}{2}. \quad (5.3)$$

If the rotational speed is between ω_{\min} and $\omega_{\text{middle,LW}}$, the task of the torque controller is either to maintain ω_{\min} or to track the light-wind TSR. The reference rotational speed is set to ω_{\min} , the lower saturation is set to zero generator torque and the upper saturation is set to the torque-LUT (blue dashed-dotted line in Fig. 5.2b). This allows the torque controller to choose generator torques from the blue shaded area (A1) in Fig. 5.2b, but since the set point is ω_{\min} , the generator torque will always follow the upper saturation

(i.e. the torque-LUT for the high TSR), as desired. Only if the rotational speed gets too low will the PI-controller become active and keep the rotational speed constant at ω_{\min} . Similar methods are applied vice versa if the rotational speed is between $\omega_{\text{middle,SW}}$ and ω_{max} , although the blue shaded area (A3) in Fig. 5.2 is quite small in this case.

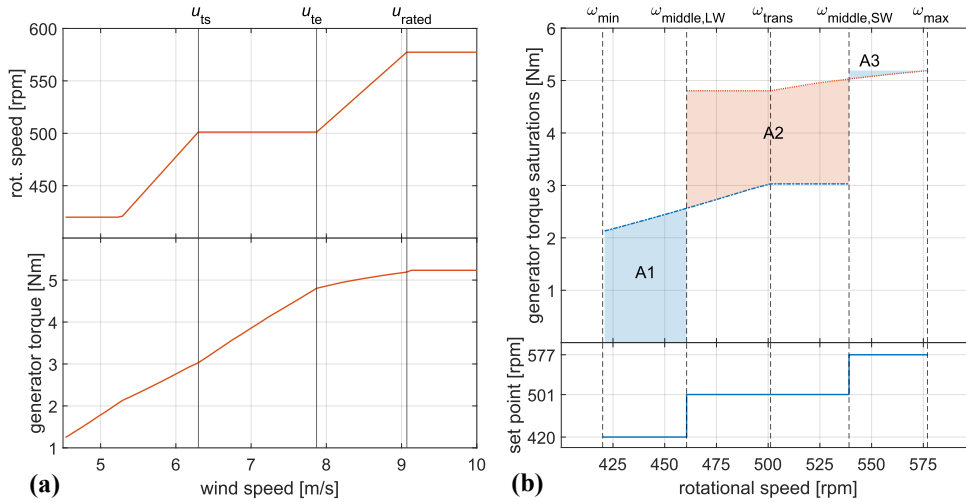


Figure 5.2: (a) Rotational speed and generator torque as a function of wind speed, derived from BEM simulations. (b) Saturations and set points for the torque controller. Shaded areas indicate the permissible generator torque for a given rotational speed.

If the rotational speed is between $\omega_{\text{middle,LW}}$ and $\omega_{\text{middle,SW}}$, the task of the torque controller is to track the light-wind TSR, to maintain ω_{trans} or to track the strong-wind TSR. The reference rotational speed is set to ω_{trans} , the lower saturation is set to the torque-LUT from the light-wind mode (blue dashed-dotted line in Fig. 5.2b) and the upper saturation is set to the torque-LUT from the strong-wind mode (red dotted line in Fig. 5.2b). This allows the torque controller to choose generator torques from the red shaded area (A2) in Fig. 5.2b. If the rotational speed is below ω_{trans} the torque controller wants to increase the rotational speed and chooses the generator torque from the lower saturation, consequently tracking the high TSR in the light-wind mode. If the rotational speed is above ω_{trans} the torque controller wants to decrease the rotational speed and chooses the generator torque from the upper saturation, consequently tracking the low TSR in the strong-wind mode. Only if the rotational speed is very close to ω_{trans} does the PI-controller keep the rotational speed constant, as desired. In other words, the PI-controller is always active. It either succeeds in maintaining ω_{trans} or (if it does not succeed due to the saturation limits) it tracks the two different TSRs.

Pitch controller

The pitch controller of a conventional wind turbine has the primary task to maintain a constant rotational speed above rated power. In the Hybrid-Lambda control methodology, it is also used to constrain the maximum loads below rated power. In this paper, we focus on the partial load range, and we discuss how the pitch angle can be set between u_{ts} and u_{rated} in order to constrain the maximum flapwise RBM. We introduce four versions of the pitch controller – a baseline controller, a load feedback (LFB) controller, a feed-forward (FF) controller and a combination of the latter two versions (FFLFB). All four versions are based on a PI-controller, tracking the maximum rotor speed (ω_{max}) as a reference, but the minimum pitch angle (β_{min}) for limiting the RBM is determined in different ways. With this architecture, the controller always wants to increase the rotational speed in the partial load range, thus reducing the pitch angle, but it is saturated by the minimum pitch angle which realizes the load constraint.

The *baseline controller* (shown in Fig. 5.3) uses a load-based pitch-LUT which maps the pitch angles to the respective wind speeds. The derived pitch angle is then set as minimum pitch for the PI-pitch controller. The pitch-LUT is calculated offline using steady-state measurement data from previous wind tunnel campaigns and data from BEM simulations. Measurement data were available for pitch angles up to 4° . For larger pitch angles, the dataset was extended with simulations. The baseline controller also includes a wind speed estimator, similar to that of a full-scale turbine. The estimator is based on filtered measurement signals from the rotor speed (ω), the pitch angle (β_{pitch}) and the measured low-speed shaft torque (M_{LSS}). The wind speed (u) can be derived from the following equations:

$$0 = \frac{1}{2} \rho \pi R^3 u^2 c_q(\beta_{pitch}, \lambda) - M_{LSS} - M_1(\omega) - I \dot{\omega}. \quad (5.4)$$

Here, M_1 is the friction losses in the drive train which are estimated from a linear fit using measurement data where the drive train was rotated without the rotor blades, which Berger (2022) describes in the Appendix of his thesis. We found that the inclusion of the rotor inertia only marginally improved the transient behaviour of the wind speed estimator for this particular wind tunnel model, and we decided to exclude the inertia term for the sake of simplicity. A comprehensive description of more sophisticated wind speed estimators is given among others by Soltani et al. (2013) and by Knudsen and Bak (2013). The torque coefficient as a function of pitch angle and TSR was also derived from steady-state measurements from previous wind tunnel campaigns. The

data were extended with BEM simulations for combinations of pitch angles and TSRs where no measurement data were available. The objective of this pitch controller is to set up a relatively simple baseline controller using only standard sensors that are also available on a conventional full-scale wind turbine. It further serves as a reference for the advanced controllers, which are described in the next paragraphs.

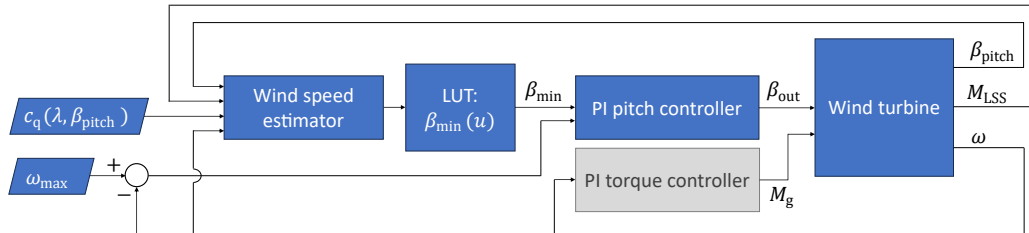


Figure 5.3: Baseline pitch controller. Torque controller indicated in simplified form. Rounded rectangles: input/output of (measured) variables. Rectangles: processes. Parallelograms: data input.

The *load feedback controller (LFB)* (shown in Fig. 5.4) uses measurements from the strain gauges at the blade root to set the individual pitch angle. The measurement signal from the flapwise RBM is low-pass filtered, the maximum allowable load is subtracted and the residual is converted with a positive controller parameter to the pitch demand. This results in a pitch increment ($\Delta\beta_{\text{pitch}}$) which can either be positive or negative, but it is saturated with the maximum allowable pitch rate. The pitch increment is then added to the previous pitch angle ($\beta_{\text{pitch},i-1}$), and if the result is larger than the minimum pitch from hardware constraints, it is set as the minimum pitch angle for the PI-pitch controller. This implementation represents an integral behaviour which has the disadvantage of slower system response times. The measurement signal from the flapwise RBM needs to be low-pass filtered because the noise in the measurement data would lead to an undesirable fluctuating controller response. We had to use a cut-off frequency of 1 Hz (which corresponds to about eight rotor revolutions at ω_{trans}) to yield a smooth controller reaction. The low-pass filter introduces further delay and additionally slows down the system response time. Most likely, a commercial full-scale turbine will provide RBM measurements with better signal-to-noise ratio and with a dedicated filter design; also, 1P load variations can be captured accurately. The described controller logic is performed for each blade individually, but, due to the slow response time, this controller does not represent a classical individual pitch controller and 1P blade load variations

cannot be alleviated. It behaves like a collective pitch controller with a rotor balancing component, which reacts on long timescales. The advantages of the LFB controller are that it is not dependent on model accuracy, there is no need for a wind speed estimator and no a priori calculation of the pitch angle (pitch-LUT) is required. The objective of this controller is to accurately constrain the mean value of the flapwise RBM.

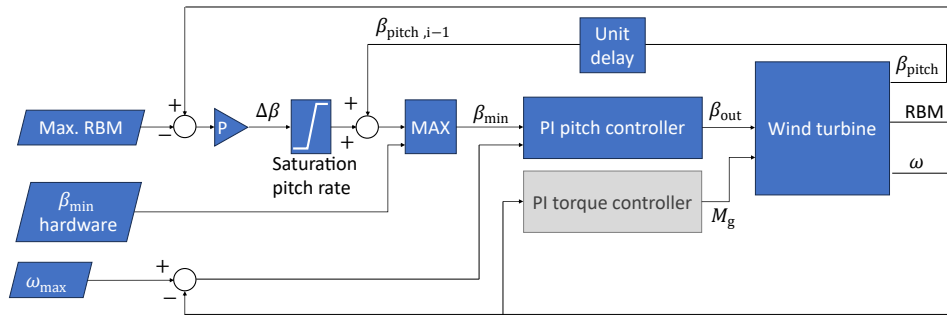


Figure 5.4: Load feedback (LFB) pitch controller. Torque controller indicated in simplified form.

The *feed-forward controller (FF)* (shown in Fig. 5.5) uses an upstream wind speed measurement to compensate for the wind disturbance. In the wind tunnel, single-point hot-wire measurements at 1.44 diameters in front of the rotor area are used to emulate a simple single beam staring mode nacelle lidar. The wind speed measurements are processed and propagated to the rotor area, as further explained in the next paragraph. The signal is then fed to the pitch-LUT to determine the required pitch angle for the respective wind speed which is set as minimum pitch angle for the PI-pitch controller. In general, the objective of this controller is to act in advance rather than reacting and specifically to reduce load overshoots in gust events.

We additionally implemented a *combined feed-forward load feedback controller (FFLFB)*. Here, the logic of both the FF and the LFB controllers run in parallel, and the larger output pitch angle is always used. In other words, β_{\min} from the FF controller (Fig. 5.5) replaces $\beta_{\min, \text{hardware}}$ in the logic of the LFB controller (Fig. 5.4). The FFLFB controller was only evaluated for the gust test case and the waked inflow.

To process the upstream hot-wire measurements for the FF controller, the signal needs to be delayed to account for the propagation time from the measurement location to the rotor plane (see Fig. 5.6), under the assumption of the frozen turbulence

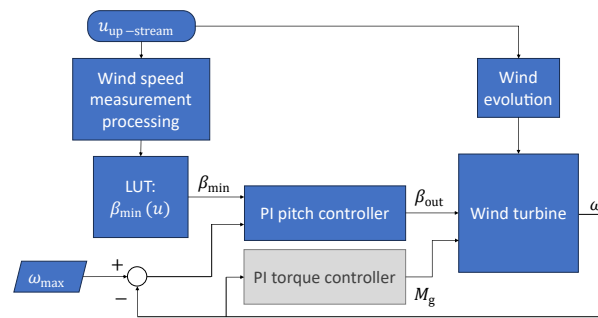


Figure 5.5: Feed-forward (FF) pitch controller. Torque controller indicated in simplified form.

hypothesis. In the case of a gust event, ideally, the pitch angle would start to increase at the exact time when the gust would hit the rotor. To account for the delay in the pitch actuation system, the controller would need to increase the reference signal slightly in advance. If we even want to account for some safety margin considering model uncertainties and the stochastic nature of turbulent gusts, we would rather like to start pitching a bit too early than too late, e.g. starting to pitch just before the gust arrives. The simplest solution would be to decrease the propagation time. In this case, the pitch would increase just before the gust arrives, but it would also start to decrease just before the gust has ended, which would lead to a load overshoot at the end of the gust event. Thus, we need to process the measurement signal in a way that the gust duration is enlarged. In other words, we would like to detect up-ramps early (increasing the pitch angle just before the gust arrives) and delay down-ramps (decreasing the pitch angle just after the gust has finished).

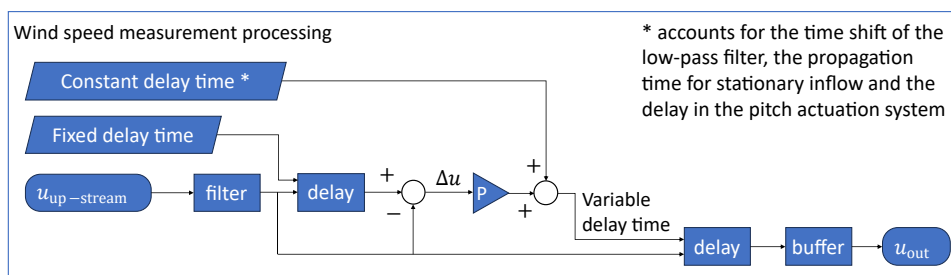


Figure 5.6: Wind speed measurement processing for the FF pitch controller.

Therefore, the hot-wire measurement signal is processed as illustrated in the flow chart in Fig. 5.6. An exemplary wind speed time series is plotted in Fig. 5.7. First, the signal is low-pass filtered (3 Hz cut-off frequency) to reduce noise (red line, labelled

“filtered” in Fig. 5.7a). Second, the signal is delayed by a fixed, short delay time (yellow line, labelled “fixed propagation” in Fig. 5.7a) and subtracted by the non-delayed signal, resulting in $\Delta u(t)$. This gives us an indication about the expected change in the signal. Third, $\Delta u(t)$ is converted with a controller parameter and added to a constant delay time that accounts for the time lag of the low-pass filter, the propagation time for stationary inflow and the delay in the pitch actuation system. Fourth, the original (filtered) signal is then delayed with this variable delay time and stored in a buffer from which the controller reads a value for each controller update iteration (yellow line, labelled “output, final propagation” in Fig. 5.7b). To visualize the effect of the processing, the resulting signal is plotted without propagation in Fig. 5.7c. Similar results could be achieved with a moving average or a Gaussian weighted moving average filter. Alternative methods and investigations on the propagation time for a model predictive controller for wind turbines in wind tunnel experiments are provided by Sinner et al. (2023).

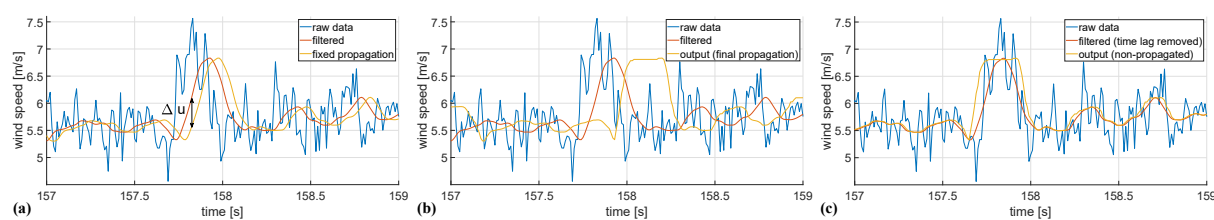


Figure 5.7: Exemplary wind speed measurement processing for the FF pitch controller for a gust event. **(a)** Raw and filtered data, **(b)** final propagation and **(c)** final signal with removed propagation for visualization purpose. The final output signal detects up-ramps early but delays down-ramps.

5.2.2 Scaling considerations

When testing wind turbine applications in the wind tunnel, we need to consider scaling effects. It has to be ensured that the experimental set-up represents the respective full-scale application reasonably well. However, not all physical characteristics can be matched simultaneously, and compromises must be found. The scaling of the rotor aerodynamics was successfully demonstrated by Ribnitzky et al. (2025). In this section, we address the scaling of parameters that are relevant for controller evaluations, which are summarized in Table 5.1.

We introduce scaling factors n which are defined by dividing the parameter of the model turbine (subscript m) by the parameter of the full-scale turbine (subscript f). The

Table 5.1: Scaling of controller parameters for the Hybrid-Lambda Rotor.

Parameter	Symbol	Model scale (subscript m)	Full-scale (subscript f)	Unit	Ratio (ideal, simplified)	Ratio (true scaling)
Geometric scaling factor	n_l			–	1/181	1/181
Time scaling factor	n_t			–	1/114	1/114
Rotor diameter	D	1.8	326	m	n_l	n_l
Rotor speed at u_{ts}	ω_{trans}	501.156	4.386	rpm	$1/n_t$	$1/n_t$
Rotational inertia	I	0.036	1.232×10^9	kg m^2	n_l^5	$n_l^5 \cdot 5.7$
Pitch rate	$\dot{\beta}_{pitch}$	85	3	$^\circ \text{s}^{-1}$	$1/n_t$	$1/n_t \cdot 0.25$
Max. aerodynamic torque	$M_{a,max}$	5.2831	2.7563×10^7	Nm	n_l^3*	$n_l^3 \cdot 1.14$
Generator torque rate	\dot{M}_g	28.84	1.5×10^6	Nm s^{-1}	n_l^3/n_t	n_l^3/n_t
Generator torque actuation time (zero to max. torque)	t_{Mg}	0.1832	18.38	s	n_t	$n_t \cdot 1.14$
Gust duration	t_{gust}	0.75	10.5	s	n_t	$n_t \cdot 8.14$
Time constant LW mode (at u_{ts})	T_{LW}	0.2259	13.35	s	n_t	$n_t \cdot 1.93$
Time constant SW mode (at u_{te})	T_{SW}	0.2812	22.21	s	n_t	$n_t \cdot 1.44$

* further clarification is given in the Appendix 5.6.

geometric length scaling factor n_l is defined by the ratio of the rotor diameters D .

$$n_l = \frac{D_m}{D_f} = \frac{1}{181} \quad (5.5)$$

Scaling the rotational inertia of the entire rotor is not possible for the given geometric scaling ratio. In theory, the rotational inertia would scale with n_l^5 . However, due to structural constraints, the scaled blades cannot be manufactured light enough to fulfil this scaling criterion. Consequently, the rotational inertia of the model turbine is about 6 times larger than required from the scaling law.

The actuation system is subjected to the time scaling n_t , which is derived by the ratio of rotational speeds in the transition region.

$$n_t = \frac{t_m}{t_f} = \frac{\omega_{trans,f}}{\omega_{trans,m}} = \frac{1}{114} \quad (5.6)$$

For the full-scale 15 MW Hybrid-Lambda turbine, Ribnitzky et al. (2024a) assumed a maximum pitch rate of 3°s^{-1} . The hardware constraint for the model turbine is at 85°s^{-1} . To match the exact time scaling, an actuation rate of 342°s^{-1} would be necessary. This means the pitch system of the model turbine is about 4 times slower than the full-scale equivalent.

The maximum aerodynamic torque would scale with n_l^3 , assuming a constant TSR, identical torque coefficients and identical inflow wind speeds. In fact, these

assumptions do not hold for the given rotor scaling, but we provide further clarification in Appendix 5.6, and we explain why the maximum rotor torque is still similar with regard to this simplified scaling. Assuming that the rotor torque scales with n_1^3 , the maximum torque of the model turbine is about 14 % higher than derived from the scaling law. For the given model turbine, the generator torque rate is ideally scaled with n_1^3/n_t and constrained through the control software. Consequently, the actuation time (e.g. time from zero to maximum torque) is 14 % slower for the model turbine compared to the full-scale equivalent. Maximal pitch and torque rates represent theoretical limits, and it is worth noting that the controller rarely operates at the said limits. Further details of the respective test cases are provided in Results.

As we will further discuss in Sect. 5.4, the inflow is also subject to scaling constraints. The inflow cannot arbitrarily be adjusted quickly, due to the inertia of the air mass and due to hardware constraints of the actuation systems in the wind tunnel. As an example, the gust event analysed in Sect. 5.3.2 lasts about 8 times longer than the full-scale equivalent.

To further compare the system behaviour, we can calculate the time constants in the equation of motion for the two rotors. Those can be modelled as a non-linear first-order system.

$$I \frac{d\omega}{dt} = M_a(\omega, u, \beta_{\text{pitch}}) - M_g(\omega) \quad (5.7)$$

Here, we neglected the friction losses in the drive train for simplicity. M_a and M_g are the aerodynamic and generator torque, respectively. If we linearize this system around an initial rotational speed ω_0 with a small perturbation of $\delta\omega$, we derive

$$I \frac{d}{dt} \delta\omega \approx \left(\frac{dM_a}{d\omega} - \frac{dM_g}{d\omega} \right) \delta\omega. \quad (5.8)$$

This is a first-order linear ordinary differential equation with the time constant T

$$T = \frac{I}{\frac{dM_g}{d\omega} - \frac{dM_a}{d\omega}} \quad (5.9)$$

and the solution

$$\omega(t) = \omega_0 + c_1 \cdot e^{-t/T}, \text{ for } t > 0. \quad (5.10)$$

The derivative of the aerodynamic torque for the perturbation in the rotational speed

under constant wind speed can be calculated as follows:

$$M_a = \frac{1}{2} \rho \pi R^3 u^2 c_q(\lambda, \beta) \quad (5.11)$$

$$\lambda = \frac{\omega R}{u} \quad (5.12)$$

$$\frac{dM_a}{d\omega} = \frac{dM_a}{d\lambda} \cdot \frac{d\lambda}{d\omega} = \frac{1}{2} \rho \pi R^4 u \frac{dc_q(\lambda, \beta)}{d\lambda}. \quad (5.13)$$

We calculate the time constants for the light-wind and strong-wind operating modes (for the wind speeds u_{ts} and u_{te}) with Eq. (5.9) and the derivative of the aerodynamic torque from Eq. (5.13). The required data can be found in Table 5.4. The derivative of the generator torque can be derived from the LUT which is used by the controller (mapping generator torque over rotational speed). Here, we use numerical backwards differentiation for u_{ts} and numerical forwards differentiation for u_{te} to avoid the ambiguity at ω_{trans} . We compare the resulting time constants for the full-scale and the model turbine in Table 5.1.

Considering the time scaling factor $n_t = 1/114$, the model turbine reacts about 2 times slower in the light-wind mode and about 1.5 times slower in the strong-wind mode to a perturbation in the inflow, compared to an ideally scaled representation of the full-scale turbine.

In conclusion, the model turbine represents a very large and heavy rotor with a high rotational inertia. Considering the change in aerodynamic torque with respect to a change in the rotational speed (or in the inflow), the time constant of the system response is also about 2 times higher for the model turbine. Furthermore, the actuation hardware represents a slow system for the full-scale application. Consequently, these scaling limitations represent a conservative approach; i.e. despite the tremendous size (15 MW, 326 m diameter) of the full-scale system, it will most likely perform equally well (if not better) in terms of controller actuations and system response times compared to the model turbine. Only the slower representation of gust events would lead to a non-conservative scaling. However, the effects of slower inflow variations are partly compensated by the slower turbine response time and slower actuation rates.

5.2.3 Measurement set-up and post-processing

The experimental controller validations were carried out in August 2024 in the turbulent wind tunnel in Oldenburg with a cross-section of 3×3 m, which is described by Kröger et al. (2018). The experimental set-up is sketched in Fig. 5.8. The open jet configuration with the active grid (Neuhaus et al., 2021) is used to investigate the controllers under turbulent reproducible inflow test cases. The control algorithms are implemented for the Model Wind Turbine Oldenburg (MoWiTO 1.8) with a diameter of 1.8 m, further described by Berger et al. (2018), equipped with blades designed by Ribnitzky et al. (2025) according to the Hybrid-Lambda Rotor design methodology. Measurement data used for the present study comprise rotational speed (azimuthal encoder), low-speed-shaft torque (torque meter), flapwise blade root bending moments (strain gauges) and upstream wind speed measurements (one-dimensional hot-wire), each sampled at 10 kHz on a National Instruments Compact RIO data acquisition system. The control algorithms are implemented on the aforementioned device with a LabVIEW real-time application. The controller update frequency is set to 100 Hz due to limitations in the computational performance of the real-time system.

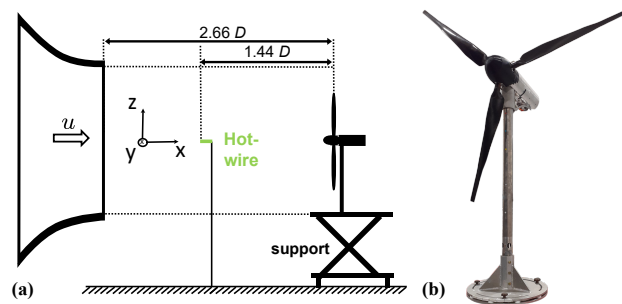


Figure 5.8: (a) Experimental set-up, side-view. (b) MoWiTO 1.8 with the Hybrid-Lambda blades, diameter of 1.8 m, hub height of 1.5 m.

The measurement data are post-processed as follows. The torque measurements are corrected for the friction in the drive train (bearings and slip ring) in order to deduce the aerodynamic rotor torque from the measured low-speed-shaft torque. To filter high-frequency vibrations and noise out of the measurement signals, we use zero-phase digital filters with a Butterworth low-pass filter in the post-processing. The corrected torque and power signals are then low-pass filtered with a half-power frequency of 10 Hz and the flapwise RBM measurements with 28 Hz, which is 3.4 times higher than the rotational frequency (1P) of 500 rpm. This ensures that all relevant rotor dynamics are resolved. In general, we show the mean of all three blade root bending moments.

The signal of the rotational speed is smoothed with a moving average window of 0.5 s length. The TSR is calculated from the filtered rotational speed and the wind speed estimate, which is also smoothed with a moving average window of the same length. The statistics of the aforementioned post-processed data are illustrated in box plots in Fig. 5.9b and c. Here, the middle markers show the median, boxes represent the 25th and 75th percentiles and the whiskers extend to the minimum and maximum of the considered data. Statistics shown in the box plots are evaluated over the stationary last 10 s of each wind step. For the time series figures, the RBM signals are filtered with a half-power frequency of 5 Hz, to increase the clarity. For the gust events, we show ensemble averages of the 50 gust repetitions with the 95 % confidence interval indicated with the shaded area. Here, we use half-power frequencies of 28 Hz for the RBM signals, 10 Hz for the corrected torque and 5 Hz for the hot-wire wind speed measurements.

5.2.4 Test cases

The controllers are experimentally investigated with four different test cases. First, wind steps are used to validate the different controller implementations. The flow is uniform and the active grid is installed with all flaps in static open configuration, which leads to a background turbulence intensity of 2 %. The wind speed is increased every 20 s by increasing the rotational speed of the wind tunnel fan.

The second test case represents coherent gust events, generated with the active grid, mimicking a scaled extreme operating gust with the so-called Mexican hat shape, according to IEC 61400-1 (2019). This inflow test case was characterized by Neuhaus et al. (2021), and it was further used in our previous publication (Ribnitzky et al., 2025) to compare the effect of different blade designs on the flapwise RBM. However, in the latter case, no wind turbine controller was used and the rotational speed was controlled to be constant, since the emphasis on the previous study was on the different blade designs. In contrast, in this study, different controller versions are compared for the same gust events.

The third test case is a turbulent inflow, mimicking the design load case 1.6 (Det Norske Veritas group: DNV-GL ST-0437, November 2016 (amended: November 2021)), normal power production with the normal turbulence model, which was also investigated with aero-servo-elastic simulations on the full-scale Hybrid-Lambda Rotor (Ribnitzky et al., 2024a). The background turbulence is produced with the

active grid, while the large wind speed fluctuations on the slow timescale are realized by dynamically changing the rotational speed of the wind tunnel fan. The mean wind speed (derived from the wind speed estimator) ranges from 5 to 11 ms^{-1} . The turbulence intensity (derived from the hot-wire measurements) is 15%. Due to the inertia of the airflow and the wind tunnel drive system, the wind speed cannot be changed infinitely fast without compromising the wind speed amplitude. Therefore, this test case is not properly scaled in time. As previously described, the time scaling factor for the Hybrid-Lambda model turbine is $n_t = t_m/t_f = 1/114$ to correctly represent the 15 MW full-scale equivalent with a diameter of $D_f = 326\text{ m}$. Here, the subscripts m and f refer to the model turbine and full-scale turbine, respectively. This means the 600 s load case with all the wind speed variations would need to be scaled to 5.3 s. Unfortunately, this is not possible if wind speed amplitudes of up to 6 ms^{-1} are desired in order to cover the whole operating range of the model turbine. This load case is therefore not scaled in time but focuses on the ability of the controllers to switch the operating modes in turbulent inflow conditions. The fast dynamics are better described by the scaled gust events mentioned before.

The fourth test case represents waked inflow conditions. A velocity deficit profile is produced with the active grid, mimicking a wake of an imaginary upstream turbine that meanders in horizontal and vertical directions on the basis of an Ornstein–Uhlenbeck process, following a method described by Onnen et al. (2024). The produced wake deficit shows a nearly axi-symmetric Gaussian profile and the spectral characteristics (e.g. the wake meandering frequency) are true to scale compared with a full-scale turbine. This means the cut-off frequency in the dynamic wake meandering model $f_c = u_\infty/(2D) = 1.67\text{ Hz}$ is representative for the wind tunnel model. The mean rotor effective wind speed in full-wake operation is set to approximately 6 ms^{-1} , which means the turbine operates mostly in light-wind mode. For large wake centre offsets, the rotor effective wind speed increases and the model turbine operates in the transition region, impinged by a partial wake scenario.

5.2.5 Calculation of pitch actuation and blade fatigue loads

Several advanced control algorithms can provide benefits in terms of power output or reduction of extreme loads, but they often come with the drawback of increased actuation activity. This can lead to increased wear, and the need for higher maintenance intervals or even component replacements can outweigh the benefits. Therefore, we

calculate the pitch actuator duty cycle (ADC), as described by Bottasso et al. (2013), according to Eq. (5.14).

$$\beta_{\text{ADC}} = \frac{1}{T} \int_0^T \frac{|\dot{\beta}_{\text{pitch}}|}{\dot{\beta}_{\text{pitch,max}}} dt \quad (5.14)$$

Here, $\dot{\beta}_{\text{pitch,max}}$ is the maximum allowable pitch rate. We further analyse the fatigue loads in terms of damage equivalent loads (DELs) for the blade root bending moments. The 28 Hz low-pass-filtered RBMs are processed, using a rainflow counting algorithm by Downing and Socie (1982) with a Wöhler curve exponent of 10 for composite materials. Note that the DELs are simply calculated for the time series of the individual test cases to express the impact of the control algorithms on the short-term fatigue loading. These numbers cannot be related to lifetime damage equivalent loads, since no wind speed probability distribution is used and not all design load cases that are required by means of the certification standards are considered.

5.3 Results

In this section, we analyse the performance of the different controller versions with the four test cases. Besides extreme loads, power output and the switching between the operating modes, we elaborate on pitch actuation and fatigue loads.

5.3.1 Wind steps

We first validate the controller implementations with wind steps. The time series of the turbine responses are shown in Fig. 5.9a. The expected set points are shown with the black lines, and the expected operating modes are indicated with the background colours. Those are derived from the steady-state operating points, i.e. the data shown in Fig. 5.1, using the rotor effective wind speed calculated with the estimator. The baseline controller works well in controlling the rotational speed and the TSR-change, i.e. following a TSR of 7.5 in the light-wind mode, maintaining a constant rotational speed of 500 rpm in the transition region and following a TSR of 6 in the strong-wind mode. In general, the loads are higher than expected in the partial load range ($60\text{ s} < t < 140\text{ s}$). For 6 ms^{-1} wind speed ($140\text{ s} < t < 160\text{ s}$), we still expect the rotor to be in light-wind mode, meaning the pitch angle is at minimum pitch and the loads are expected to be below the constraint of 7.3 Nm. However, the loads already exceed the limit which cannot be recognized by the baseline controller. For higher wind speeds ($160\text{ s} < t < 260\text{ s}$) in the transition region and in the strong-wind mode, the baseline controller starts to

increase the pitch angle and succeeds in keeping the RBM at a constant level. However, the mean value is higher than the set point (8 Nm instead of 7.3 Nm) due to model uncertainties in the pitch-LUT. Possibly, the zero pitch angle was set to a slightly lower pitch angle when evaluating the controllers in this measurement campaign, compared to the experiments when the data were recorded to set up the pitch-LUT, which were performed in 2023. Such an offset in the pitch angle could explain the increased loads.

Here, the advantages of the LFB controller become clear. With the load feedback, the controller corrects for the offset in the model and is able to correctly constrain the flapwise RBM. However, this comes with the cost of reduced power output. This is especially noticeable in the strong-wind mode ($220\text{ s} < t < 260\text{ s}$). Moreover, the TSR in the strong-wind mode is lower than the set point (5.7 instead of 6) for the LFB controller ($220\text{ s} < t < 260\text{ s}$). A higher pitch angle is used, which successfully constrains the loads, but this also reduces the aerodynamic torque. Consequently, the reference generator torque is too high, and both the rotational speed and the TSR are lower than the set point. It can be seen that the LFB controller uses lower generator torque values compared to the baseline controller, since the reduced rotational speed moves the set point in the torque-LUT to lower values. Ideally, the torque-LUT itself would need to be adapted to account for the higher-than-expected pitch angles. This could be realized by calculating the generator torque with the $k\omega^2$ -law, using the torque coefficient surface and the actual pitch angle on the fly, rather than using the a priori calculated torque-LUT with expected pitch angles.

The FF controller behaves similarly to the baseline controller, but it uses single-point hot-wire measurements instead of the wind speed estimator, and due to the aforementioned model uncertainties, the commanded pitch angle differs from the baseline controller. Since there is no feedback from the loads, the FF controller fails to keep the RBM constant in the transition and strong-wind mode. The advantages of the FF controller will become more clear in Sect. 5.3.2, which addresses the gust events. The statistical analysis of the wind steps is shown in Fig. 5.9b and c. The median is shown with the middle marker, the 25th and 75th percentiles are visualized with the boxes and the whiskers extend to the extrema of the data.

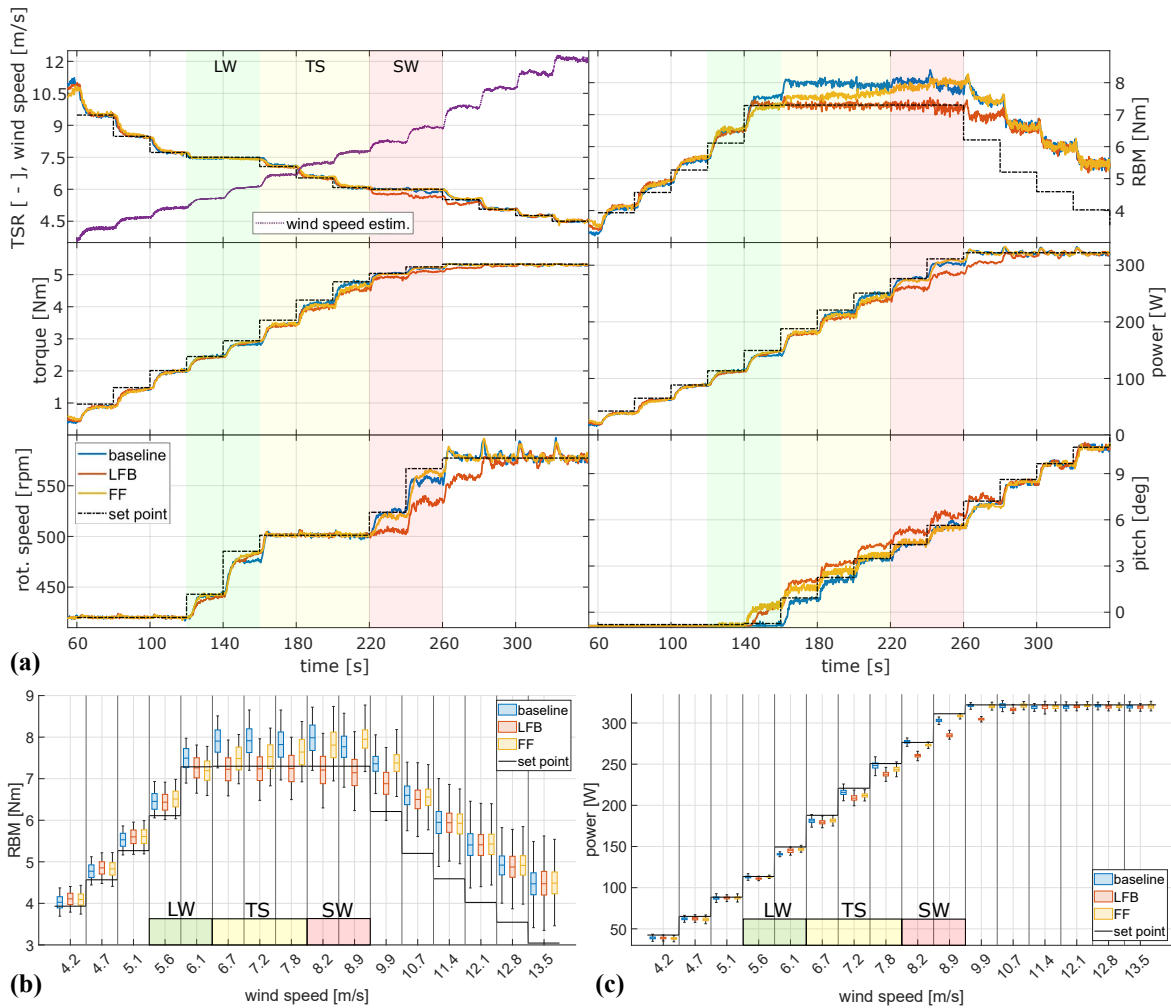


Figure 5.9: Turbine response with the baseline, LFB and FF controllers to the test case with wind steps: time series (a) and statistical analysis of RBM (b) and power (c). Background colours indicate the operating mode: green, light-wind mode (LW); yellow, transition (TS); red, strong-wind mode (SW). Middle markers, median; boxes, 25th and 75th percentiles; whiskers, minimum and maximum of the considered data. The baseline controller works well in following the TSR of 6 in the SW mode, but the loads are higher than expected due to model uncertainties. The LFB controller uses higher pitch angles and is able to correctly constrain the loads. However, this leads to reduced aerodynamic torque and consequently lower rotational speed and lower TSRs in the SW mode. Furthermore, the power output of the LFB controller is lower in the SW mode compared to the baseline controller.

5.3.2 Gusts

We use gust events to investigate the transient behaviour of the controllers. The ensemble averages of the 50 gust repetitions are shown in Fig. 5.10. The wind speed measurements are taken 1.44 D (2.7 m) upstream of the rotor, and the data are not propagated in the plot. Since only single-point measurements are available, an offset to the rotor equivalent wind speed is expected and the load level does not perfectly match with the data from the wind steps test case. However, this does not affect the presented analysis of the transient behaviour. In Fig. 5.10 the 95 % confidence intervals of the 50 gust repetitions are indicated with the shaded areas. The narrow width of the confidence intervals highlights the good repeatability of the individual gust events.

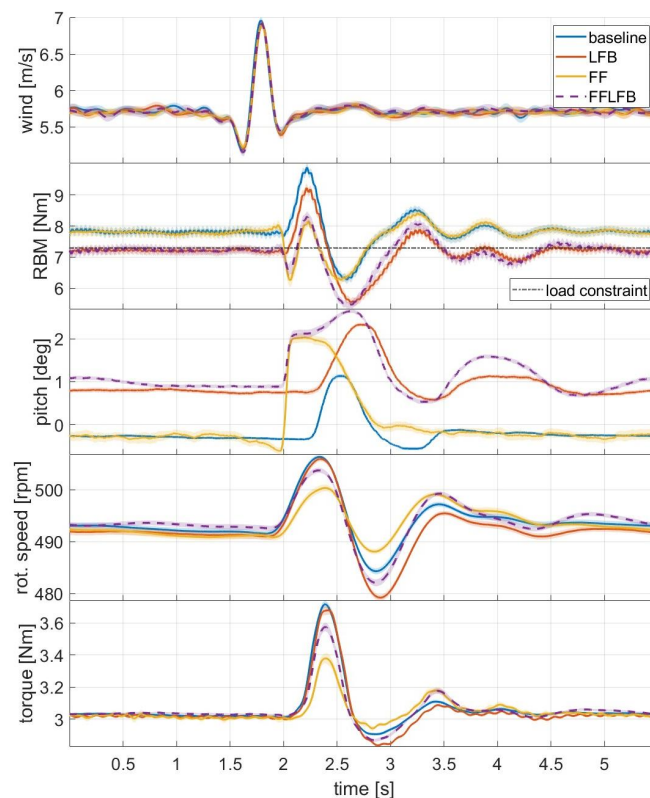


Figure 5.10: Turbine response to gust events. Solid lines show the ensemble average over 50 gust repetitions. The shaded areas indicate the 95 % confidence intervals. Wind speed measurements are performed 2.7 m upstream of the rotor and are not propagated in this plot. The LFB and FFLFB controllers can limit the loads in steady state perfectly to the load constraint. During the gust, the baseline and LFB controllers react too slowly and show the highest load overshoots. The FF and FFLFB controllers react in advance and reduce the load overshoot. The FF controller further reduces the variations in rotational speed and torque.

First of all, we notice the different steady-state values in the flapwise RBM. The controllers with the load feedback (LFB and FFLFB) can limit the loads perfectly to the constraint of 7.3 Nm in steady state. In contrast, the loads are higher than the set point for the baseline and the FF controller, as observed for the wind steps as well. Note that 1° difference in the pitch angle does not significantly change the rotor speed, which is due to a low sensitivity of the aerodynamic torque to the pitch angle in that region. During the gust event, the baseline controller shows the highest overshoot in the flapwise RBM. The maximum load is 25 % higher than the steady-state RBM because the baseline controller increases the pitch angle too late. The LFB controller shows the slowest reaction, due to the inherent integral behaviour of the controller architecture and due to the time delay associated with the low-pass filtering of the load measurements. In fact, the applied filter introduces a delay of 0.2 s for the given gust events. In contrast, the FF controller reduces the peak load almost to the same level as the steady-state loads. The feed-forward controllers (FF and FFLFB) react in advance and increase the pitch angle just before the gust arrives. This reduces the flapwise RBM in advance, and once the gust arrives, the load overshoot is significantly reduced. More precisely, for the FF controller, the peak load is 4 % higher than the steady-state value but still 11 % higher than the load constraint. The feed-forward controllers also show a longer period of high pitch angle, compared to the baseline controller. This is the intended behaviour resulting from the processing of the feed-forward signal, as described in Sect. 5.2.1. Further, the FF controller effectively reduces the variations in the rotational speed and the generator torque, which is beneficial for the drive train loads and leads to a more even power feed-in. As intended, the FFLFB controller combines the advantages of the FF and the LFB controllers. It can constrain the steady-state mean load to the desired value due to the load feedback, and additionally, it can react in advance due to the preview information. For the FF controller, the lack of load feedback is further visible, since the load overshoot after the gust event (at 3.25 s) is 4 % higher than during the gust event (at 2.25 s).

The maximum torque rate observed was 8.4 Nms^{-1} for the baseline controller, and it was similar for all four controller versions. Consequently, less than one-third of the maximum generator torque rate was used. Only the FF controller reached the maximum pitch rate of 85° s^{-1} , which happened in 14 of the 50 investigated gust events. For the ensemble average, the highest pitch rate observed was 46° s^{-1} for the FF controller. The other controllers operated far below the hardware limit. In comparison, the highest pitch rate observed for the baseline controller was 18° s^{-1} .

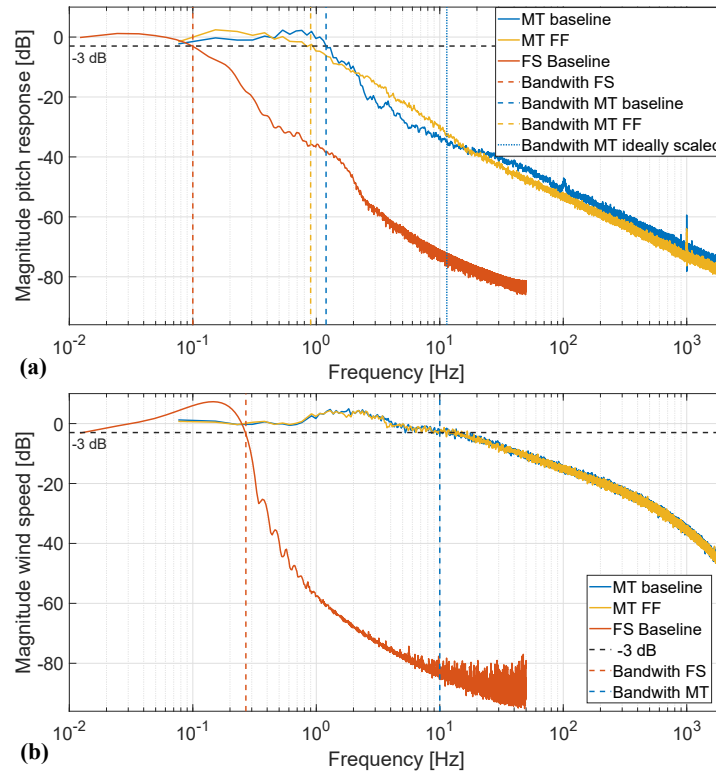


Figure 5.11: Power spectral density of (a) the pitch signal and (b) the wind speed excitation for the gust test case in the wind tunnel and for aero-servo-elastic simulations with extreme operating gust for the 15 MW full-scale (FS) Hybrid-Lambda turbine. The model turbine (MT) controllers are about 10 times slower than ideally scaled ($n_t = 1/114$). This corresponds to the gust duration which is 8 times slower than ideally scaled.

To further investigate the speed at which the pitch controllers are active, we derived the power spectral density of the pitch signal, and we compare it to the gust excitation in Fig. 5.11. In this analysis, we further include the simulation results for the full-scale 15 MW Hybrid-Lambda turbine of the design load case 2.3 extreme operating gust with a duration of 10.5 s according to IEC 61400-1 (2019), simulated with the aero-servo-elastic tool openFAST. Note that the wind speed signal from the IEC load case is not turbulent and that the inflow has not been identically scaled across all frequencies. For the model turbine, the FF controller shows higher magnitudes for frequencies between 2 and 10 Hz, compared to the baseline controller which is in line with the faster response of the FF controller, as presented above. Next, we compare the bandwidth of the scaled and the full-scale system. Note that system identification has not been the goal of the performed experiments, meaning that the system has not been

adequately excited on all frequencies. Nevertheless, the spectra of the pitch signals still give an insight into the speed of the respective systems. The pitch spectra of the model turbine drop below -3 dB at around 1.1 Hz, whereas the full-scale spectra drop at 0.1 Hz. Considering the time scaling of $n_t = 1/114$, the model turbine controllers are about 10 times slower than ideally scaled. Since the gusts are also 8 times slower than ideally scaled, as explained in Sect. 5.2.2, we can conclude that the controllers of the wind tunnel model represent a reasonable representation of the full-scale equivalent.

5.3.3 Turbulent wind fields

With this test case, we want to evaluate the controllers on their ability to switch between the operating modes in varying turbulent inflow conditions. The results are plotted in Fig. 5.12. The desired operating mode is derived on the basis of the wind speed estimator, which is indicated with the background colours. As for the previous test cases, the baseline and FF controllers set pitch angles that are too low, and the flapwise RBM exceeds the constraint, due to the model mismatch. In the transition and strong-wind modes, the average flapwise RBM is 6 % higher than the constraint for the baseline controller and 9 % higher for the FF controller. In contrast, the LFB controller can limit the loads effectively, due to the load feedback. However, the increased pitch angle also reduces the power output. On average over the entire duration of the test case, the power output of the LFB controller is 5 % lower than for the baseline controller. However, the power reduction is expected due to the controller design, which favours load limitation over power maximization.

All controller versions succeed in tracking the TSR of 7.5 in the light-wind mode, although the LFB controller seems to reach the desired TSR last when transitioning from strong-wind to light-wind mode (e.g. at 215, 260, and 380 s). As in the wind steps test case, the baseline controller works best in regulating the TSR at 6 in the strong-wind mode. In contrast, the TSR is lower than the set point for the LFB controller in strong-wind mode. Higher pitch angles are set, which reduces not only the flapwise RBM but also the aerodynamic torque and therefore the rotational speed. In general, the torque controller works well in maintaining 500 rpm in the transition region. Between 570 and 590 s, the wind speed exceeds rated. Here, the pitch controller maintains the maximum rotational speed and the TSR drops below 6 for all controllers, as expected.

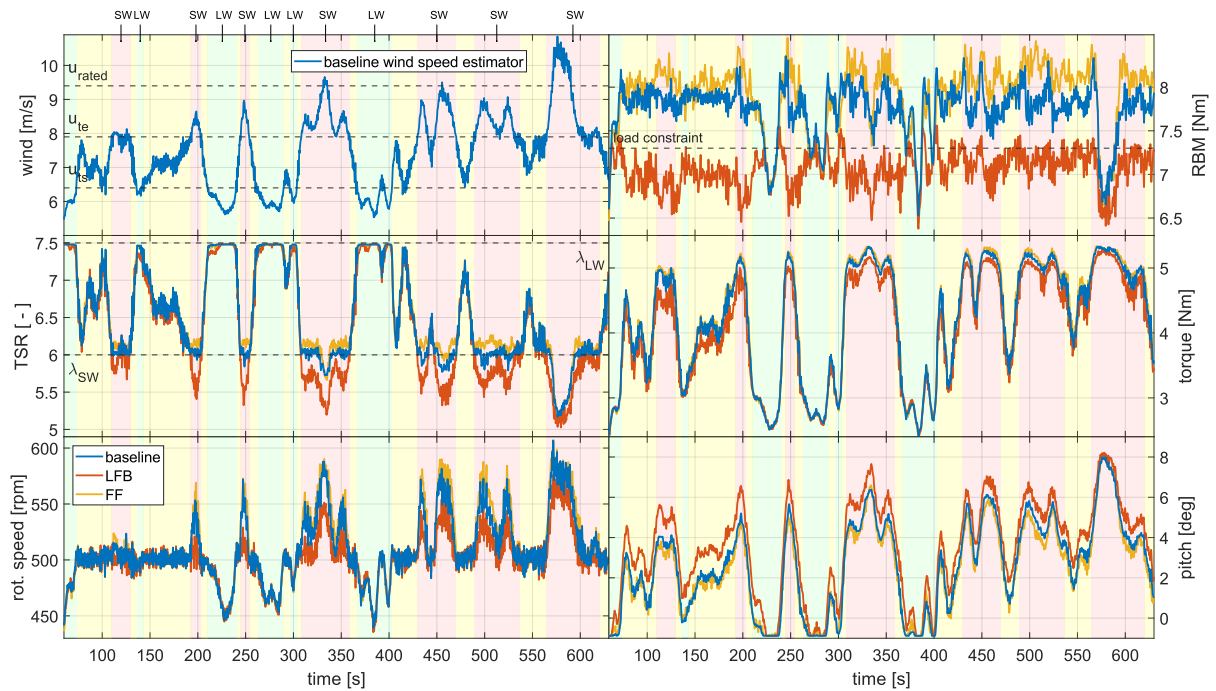


Figure 5.12: Turbine response to turbulent inflow. Background colours indicate the desired operating modes: green, light-wind (LW); red, strong-wind (SW); yellow, transitioning between the operating modes. All controllers are able to follow the LW-TSR of 7.5, and the torque controller can maintain the rotational speed constant in the transition region. In the SW mode, the LFB controller uses higher pitch angles, effectively constraining the loads but resulting in TSRs that are lower than the set point of 6.

For this test case, the FF controller used the highest pitch rate of 49°s^{-1} , which is only 60% of the hardware constraint. The maximum pitch rates for the other three controllers are below 25°s^{-1} . The maximum torque rate observed was 8.1 Nms^{-1} for the RBM controller.

5.3.4 Waked inflow

This test case addresses non-uniform inflow, and we evaluate the controller versions under a meandering wake inflow scenario. The wake produced with the active grid meanders in horizontal and vertical directions as a random walk. The radial distance of the wake centre to the rotor centre is plotted in Fig. 5.13 as an absolute value. We compare this signal to the hot-wire measurements on the centre line and the wind speed estimator. Once the signals are propagated they correlate well in time. However, the single-point hot-wire measurements fail to provide a representative rotor effective wind

speed. Whenever the wake centre distance is below $0.5D$, the hot-wire measurements are lower than the estimated wind speed and all parts of the rotor that are in the free stream are not considered by this measurement technique. Only for very large wake centre offsets (e.g. $440\text{ s} < t < 450\text{ s}$) did the hot-wire measurements converge closer to the signal of the wind speed estimator. The latter works much better in providing a rotor effective wind speed, since the rotor is used as a sensor to capture all effects over the rotor area.

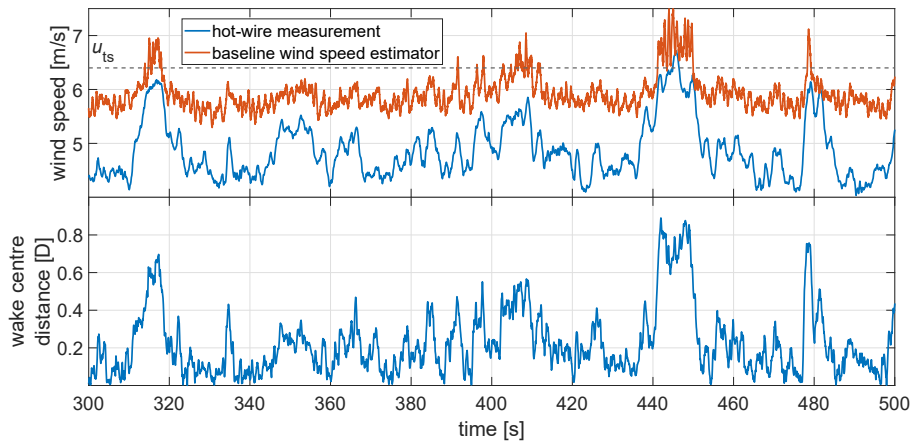


Figure 5.13: Top: wind speed derived from hot-wire measurements on the centre line (propagated) and derived from the wind speed estimator. Bottom: radial distance of the wake centre to the rotor centre. Only for very large wake centre displacements did the single-point hot-wire measurements converge towards the rotor effective wind speed, which is predicted by the wind speed estimator.

The average of the rotor effective wind speed over the duration of the test case is set to 6 ms^{-1} , which means the turbine is in light-wind mode. The time intervals where the wake centre offset is large enough that the rotor operates in the transition region are of highest interest, as shown in Fig. 5.14. All controller versions succeed in tracking the light-wind-mode TSR. Further, the reduction in TSR in the transition region works equally well for all versions. Differences are visible in the load limitation. The FF controller is blind to any non-uniformity in the flow, and for large wake centre offsets, the exceedances of the flapwise RBM are most pronounced (e.g. $t = 315\text{ s}$, $t = 410\text{ s}$, $t = 450\text{ s}$). In contrast, the baseline controller uses the estimated rotor-averaged wind speed and chooses higher pitch angles, which leads to reduced load overshoots. The LFB and FFLFB controllers again take advantage of the load feedback and perform best in limiting the flapwise RBM. In summary, the maximum load exceeds the constraint of 7.3 Nm by 17 % for the FF controller, by 12 % for the baseline, by 6 % for the FFLFB and

by 5 % for the LFB controller. Note that the load time series presented in Fig. 5.14 are low-pass filtered with a half-power frequency of 5 Hz to increase clarity and that 1 P variations are filtered out.

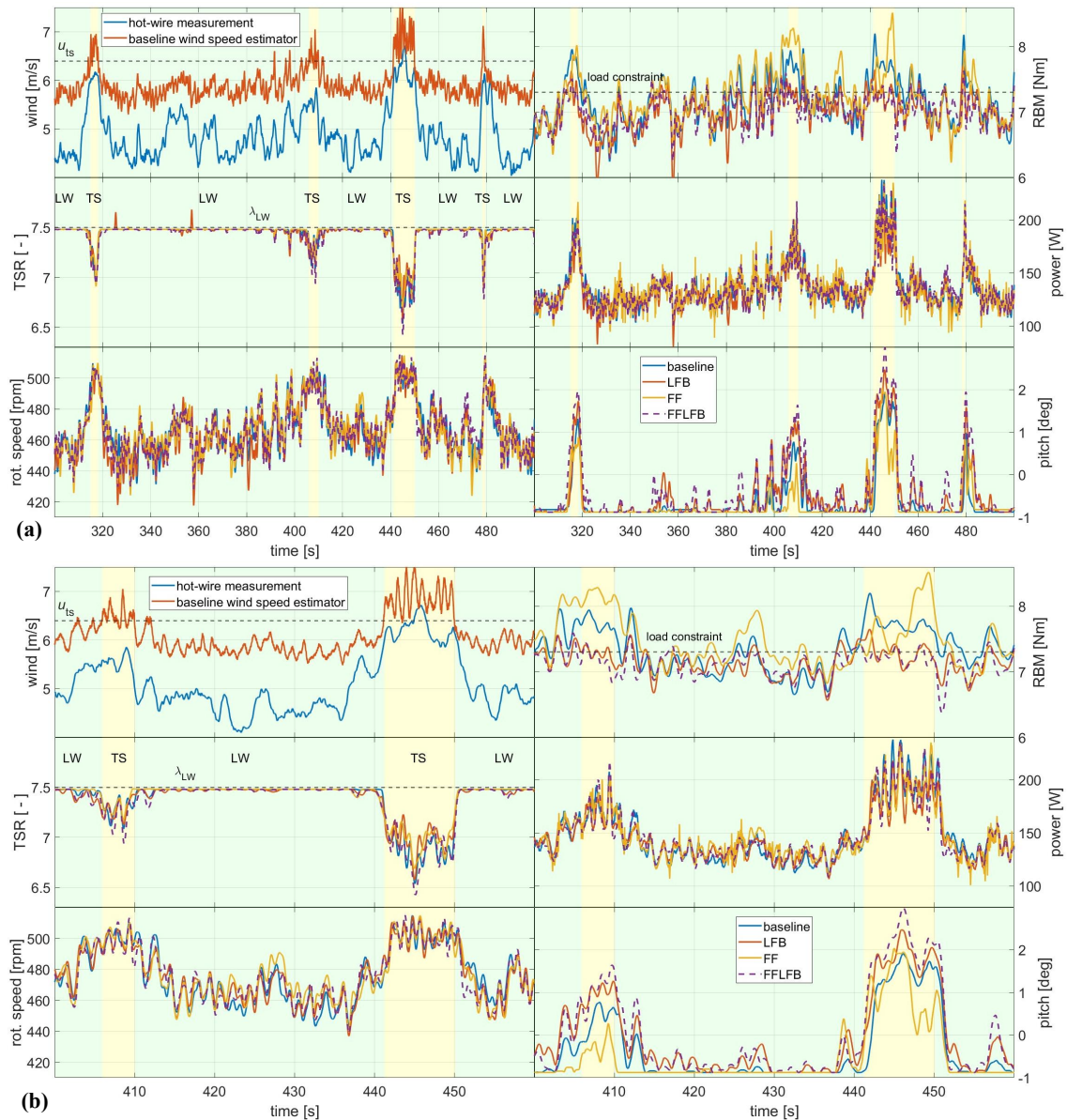


Figure 5.14: Turbine response to waked inflow. **(a)** 200 s and **(b)** 60 s excerpt of the full test case. Background colours indicate the desired operating modes: green, light-wind; yellow, transitioning between the operating modes. The FF controller leads to the highest load overshoots for very large wake centre displacements. The baseline controller estimates the rotor-averaged wind speed much better and shows lower loads than the FF controller. The LFB and FFLFB controllers perform best in limiting the loads.

Although the FF controller uses the lowest pitch angles and shows the highest loads, the power output is not increased compared to the other controllers. In contrast, the power output of the FF controller shows more fluctuations in the light-wind mode because the smaller variations in the rotor effective wind speed are not captured by the single-point measurements. Consequently, the wind speed is assumed to be below u_{ts} and the pitch actuation is not triggered (as it is for the other controller versions), which leads to higher power fluctuations (e.g. $320\text{s} < t < 405\text{s}$).

For this test case, the FF controller used the highest pitch rate of 53°s^{-1} , the FFLFB controller used 42°s^{-1} and the baseline and LFB controller used 19°s^{-1} . The maximum torque rate observed was 7.2Nm s^{-1} for the baseline controller.

5.3.5 Pitch actuation and blade fatigue loads

In the previous sections, we mainly addressed extreme loads and power output for the individual test cases. Finally, we compare all controller versions among all test cases in terms of pitch actuation and blade fatigue loads for the flapwise bending moments, as shown in Fig. 5.15. For the pitch actuation, the gust events are the most severe load case. To compute the DEL and ADC, all 50 repetitions of the gust event were used, which is not a realistic load case, but it can be used as a metric for comparison within this study. Compared to the baseline and LFB controller, the FF controller leads to around 3 times higher pitch actuation for the gust test case. As already seen in Fig. 5.10, the pitch manoeuvre for the FF controller starts with a much higher slope, which drives up the pitch actuation value. Further, for the turbulent wind field test case, the FF controller shows the highest actuation among all controller versions, although the value is only 70% of the pitch actuation from the gust events. The baseline and LFB controller show similar pitch actuations for the gusts and turbulent inflow test cases with a small increase for the turbulent inflow. This can be related to the small scale fluctuations in the inflow which are not present in between the gust events. Among all performed test cases, the waked inflow leads to the lowest pitch actuations for all controller versions because the turbine is in light-wind mode most of the time with little to no pitch actuation. Here, the FF controller shows rather low actuations because the pitch is often not triggered. The single-point measurements on the centre line do not fully capture the variations in the rotor effective wind speed, and this also leads to lower values of pitch actuation.

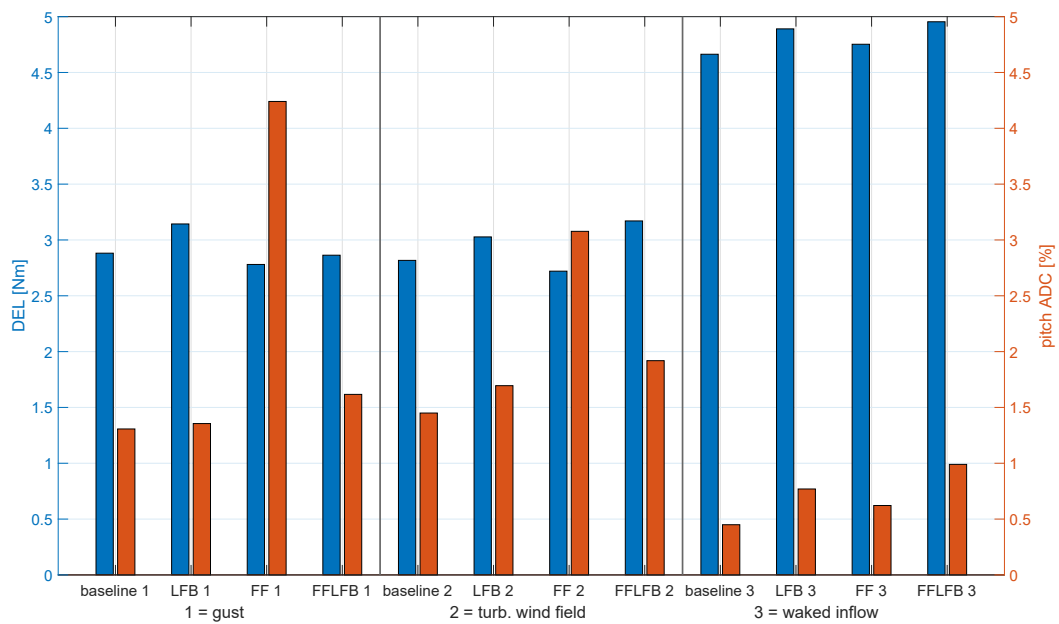


Figure 5.15: DEL and pitch actuator duty cycle for the three inflow cases: gust, turbulent wind field and waked inflow. For the gust test case, the FF controller leads to around 3 times higher pitch actuation but reduces the fatigue loads. Also for the turbulent wind field test case, the FF controller shows the highest pitch actuation, although the actuation is lower than for the gust test case. The fatigue loads for the waked test case are strongly increased for all controllers due to the non-uniformity of the inflow.

For the flapwise blade fatigue loads, the waked inflow is the most severe test case. This can be related to the non-uniformity of the flow. The blades sample through spatially inhomogeneous wind fields, and the individual blade loads are excited with higher harmonics of the blade passing frequency, which is not present for the other two test cases with uniform inflow. For the gust test case, the strategy of the FF controller seems to pay off not only in terms of reduced extreme loads: the DELs are also the lowest among the four controller versions for this test case. In general, the turbulent inflow test case leads to similar DELs, compared to the gust events. For the turbulent inflow, the LFB controller works best in reducing the extreme loads, but it leads to higher blade fatigue loads (7% increase compared to the baseline controller).

5.4 Discussion

The novelty of the Hybrid-Lambda control strategy is the objective of tracking two different TSRs below rated wind speed and the realization of the transition between the operating modes with an overarching load constraint. Contrary to conventional wind turbine controllers, the pitch and torque controllers are active simultaneously over a wide range of wind speeds below rated. The wind tunnel validation clearly showed that it is possible to realize the Hybrid-Lambda control strategy. The latter has so far only been designed with steady-state analysis and tested in transient aero-servo-elastic simulations. With the research presented here, we evaluated the controller methods on a fully actuated scaled wind turbine.

We first discuss the achievement of the six research questions outlined in the introduction. We give recommendations on controller design for very large wind turbines with a load constrain, and we address challenges in the scaling approach. We conclude the Discussion by comparing our finding to related research.

The results confirm the original research questions outlined in the Introduction. First, the transition between the operating modes (i.e. keeping the rotor speed constant while the pitch controller is active for the load constraint) can be accomplished by using the torque PI-controller. Despite the large rotor inertia, variations of only $\pm 2\%$ in rotor speed are present for turbulent inflow when the turbine operates in the transition region.

The second objective of tracking a desired TSR and simultaneously achieving a load constraint introduced a challenge to the controller design. In the present study, we tested two controller architectures that can accomplish one of the objectives but struggle to fulfil both simultaneously. The baseline controller succeeded best in tracking the strong-wind TSR but, due to a model mismatch, led to loads that were too high. The LFB controller was able to limit the loads to the desired constraint. However, by choosing higher pitch angles, the operating points of the aerodynamic model deviated from the expected ones, resulting in a poor tracking of the strong-wind TSR by the torque controller. To overcome this and to achieve both objectives independently of each other, the $k\omega^2$ -law in the torque controller would need to be adapted with a k value that is a function of the actual pitch angle and which needs to be calculated on the fly.

The third objective was to limit extreme flapwise RBM loads. If the mean value

should be set correctly, a load feedback is necessary and the LFB controller performed best. However, due to its integral behaviour, this controller architecture cannot handle transient events on a small timescale like gusts. In this case, the FF controller performed best in limiting the extreme loads. Further, controller designs without additional sensor equipment, like the baseline controller, can keep the loads constant in the transition and strong-wind mode. However, one needs to take model uncertainties into account, which leads us to the fourth objective.

Model uncertainties can lead to an offset in the load response, as it is present for the baseline controller. The LFB controller can overcome this challenge thanks to the measurement data from the flapwise RBMs. Alternatively, a model calibration or model update procedure would be needed to improve the baseline controller, as among others described by Mulders et al. (2023). Model uncertainties will also be present for a commercial full-scale turbine. The inflow is not controllable nor repeatable in the field. However, the aerodynamic model might be more reliable due to higher chord-based Reynolds numbers. Further, the manufacturing and assembling accuracy will be higher for a full-scale turbine because the ratio of tolerances to product size is simply more favourable.

With the fifth research question, we addressed further impacts on the wind turbine as an engineering system, such as the pitch actuator duty cycle and fatigue loads. Besides limiting the extreme loads, the FF controller could also reduce the fatigue loads on the blade root bending moments but comes at the cost of an increased pitch actuation. In contrast, other studies have reported reduced pitch actuation for feed-forward-based model predictive controllers, since the anticipation of future events can also lead to an avoidance of pitch manoeuvres if the wind speed increase is only temporary (Sinner et al., 2022).

The sixth research objective was to outline recommendations on controller design for very large wind turbines with a load constraint. First, model uncertainties need to be taken into account by a calibration or model update procedure. Second, a feedback from load measurements is crucial to fulfil the load constraint in spite of uncertainties. Third, a wind preview will be required to reduce extreme loads on small timescales. Although load-limiting control concepts without a preview already exist on commercial turbines, both the tremendous size of the turbines addressed in this study (diameter of more than 300 m) and the wide wind speed range in which the load constraint is active

(upper half of the partial load range) will require more sophisticated techniques to achieve an economical viable design. Fourth, the TSR tracking needs to account for the actual pitch angle, which might be different than the expected pitch angle due to the advanced control methods that react on the turbine state and the environmental conditions.

Testing wind turbine applications in the wind tunnel always comes with the challenge of appropriate scaling (Canet et al., 2021). While the aerodynamic scaling of the wind turbine model was successfully described by Ribnitzky et al. (2025), the temporal scaling of the inflow conditions remains difficult to satisfy. One limitation of the methodology presented here is that the turbulent inflow test case is not true to scale in time, compared to a full-scale equivalent. The wind speed variations cannot be accomplished arbitrarily fast, since the flow itself and the wind tunnel actuators are subject to inertias. However, we can investigate the transient controller reactions with the test case of gust events. The fastest gust that can be produced with the active grid and that still shows a reasonable wind speed amplitude has a duration of 0.75 s (Neuhaus et al., 2021). Due to the large time scaling factor of the model turbine ($n_t = 1/114$), this gust is still about 8 times slower than the full-scale equivalent, which should have a duration of 10.5 s according to the IEC 61400-1 (2019). However, for the model turbine, the rotational inertia and the pitch and torque actuation times are larger compared to an ideally scaled version of the full-scale turbine. Consequently, the transient controller reactions can be assessed reasonably well with this compromise.

In this study, we derived the steady-state operating points by prescribing a schedule of rotational speed which consists of tracking the light-wind and strong-wind TSR and a transition region with constant rotational speed in between. The pitch angle was then derived by optimizing the power coefficient with respect to the load constraint. Here, we want to emphasize that other approaches are also possible. Frameworks for the steady-state operating points, as described, for example, by Pusch et al. (2024) and Lazzerini et al. (2025), enable the optimization of both the rotational speed and the pitch angle for the entire operating range. The control philosophy described by Lazzerini et al. (2025) drops the assumption of constant TSR, or it could be interpreted as a control strategy with an infinite number of TSRs. This approach could be promising for the Hybrid-Lambda concept and could be implemented in future studies. However, special care needs to be taken considering model uncertainties because the control algorithm proposed by Lazzerini et al. (2025) is essentially based on a reliable wind speed estimator. Possibly, a load feedback would be a necessary addition.

5.5 Conclusions

In this paper, we set up a control methodology for the Hybrid-Lambda Rotor concept and validated it on a scaled wind turbine model in wind tunnel experiments under various turbulent inflow conditions. We showed how two different TSRs can be tracked below rated wind speed by using three different rotor speed set points (ω_{\min} , ω_{trans} and ω_{\max}) and by defining the generator torque saturations according to the TSRs. With this method, we can further realize a transition region with constant rotational speed (ω_{trans}) to switch between the two operational TSRs. Four versions of the pitch controller, which aim to satisfy the constraint on the flapwise RBM, were investigated. An overview of the findings is provided in Table 5.2. First, we presented a baseline controller which uses only standard sensors that are also available on a conventional full-scale wind turbine. It performed well in tracking the different TSRs and managed to constrain the loads to a constant value, which was, however, 10% higher than the desired level (in the test case with wind steps) due to a mismatch in the zero pitch position. Second, a load feedback controller that uses measurements from the strain gauges at the blade root. This version was able to correctly set the mean value of the flapwise RBM, but reducing the loads always comes with the drawback of reduced power feed-in. Further, due to its integral behaviour, the response was too slow for sudden gust events. Third, a feed-forward controller was tested that uses single-point wind speed measurements 1.44 D upstream of the rotor as a preview signal. A special signal processing algorithm was developed which enabled the controller to detect up-ramps early but also takes into account the slower advection time of down-ramps. As a result, the load overshoots in gust events have been significantly reduced, which, however, comes with the price of increased pitch actuation. The fourth controller version is a combination of the LFB and the FF controller.

To close the loop, we transfer the presented findings to the full-scale application. We need to evaluate the control strategies in the context of very large rotors that are closely spaced in offshore wind farm applications. As explained in the introduction, we need larger rotors to generate more energy in light winds and thus achieve a more continuous and reliable supply of wind energy. To fulfil the goals of installed capacity, those large rotors will need to be spaced relatively closely to each other and economic competitiveness can only be achieved by a lightweight and cost-effective turbine design. This can be supported by advanced control strategies that effectively reduce extreme loads during operation. The close spacing of the turbines will make

Table 5.2: Advantages (+) and disadvantages (–) of all tested controller versions for all test cases.

	Baseline	LFB	FF	FFLFB
Wind steps	+ Good tracking of LW and SW TSR (+) RBM constant in transition region and SW mode – RBM constraint exceeded by 10 %	+ RBM correctly constrained – TSR in SW mode too low – Reduced power output	+ Good tracking of LW and SW TSR – RBM increasing with wind speed in transition region and SW mode – RBM constraint exceeded by 10 %	(not evaluated)
Gusts	– Highest load overshoot. RBM constraint exceeded by 35 %	+ Steady state RBM correct – Slowest pitch reaction – Load overshoot. RBM constraint exceeded by 26 %	+ Pitch is increased just before the gust arrives + Lowest load overshoot of 11 % + Lowest variation in rotational speed – Highest pitch actuation	+ Steady state RBM correctly set + Longest period of increased pitch + Reduced load overshoot of 14 %
Turbulent inflow	+ Good tracking of LW and SW TSR – Average RBM in transition and SW mode exceeds constraint by 6 %	+ RBM correctly constrained – Reduced power output – TSR in SW mode too low	– Average RBM in transition and SW mode exceeds constraint by 9 %	(not evaluated)
Waked inflow	+ Load overshoots are lower than for FF – RBM constraint exceeded by 12 %	+ Lowest load overshoot, RBM constraint exceeded by 5 %	– Highest load overshoots – RBM constraint exceeded by 17 % – Power output is not increased – Higher power variations	+ Lowest load overshoot, RBM constraint exceeded by 6 %

highly turbulent partial wake scenarios more likely. That means that spatially resolved information about the inflow needs to be provided to the controller and that individual pitch strategies will possibly be needed to reduce unsymmetrical rotor loadings. A load feedback will be essential to correct for model uncertainties and to adapt the controller to changes in the system behaviour. Such changes could be present to the aerodynamic behaviour, e.g. due to leading edge erosion, or to the actuation and sensor system, e.g. due to long-term drift.

Unconventional rotor concepts like the Hybrid-Lambda Rotor will need advanced control algorithms to unlock the full potential of aerodynamic efficiency and to ensure structural integrity. Wind tunnel experiments are a powerful tool to test the newly developed control strategies under tailored reproducible inflow conditions. With the results presented here, we have completed an important step in the validation of the Hybrid-Lambda Rotor design and control methodology.

Data availability

The data shown in all figures of this paper are available in the following repository: <https://zenodo.org/records/16598897> (Ribnitzky, 2025a).

5.6 Appendix

Scaling of aerodynamic rotor torque

In this appendix, the scaling of the aerodynamic rotor torque M_a is explained, which is defined as

$$M_a = \frac{1}{2} \rho \pi R^3 u^2 c_q. \quad (5.15)$$

Subject to scaling are the rotor radius R , the wind speed u and the torque coefficient c_q .

Rotor radius

The scaling of the rotor radius can be expressed with

$$n_1 = \frac{R_m}{R_f}, \quad (5.16)$$

and this scaling criterion is satisfied.

Time scaling

The time scaling is defined by the ratio of rotational speeds in the transition region:

$$n_t = \frac{t_m}{t_f} = \frac{\omega_{\text{trans},f}}{\omega_{\text{trans},m}}, \quad (5.17)$$

and this scaling criterion is satisfied in the transition region.

Torque coefficient

The torque coefficient can be derived from the power coefficient c_p and the TSR.

$$c_q = \frac{c_p}{\lambda} \quad (5.18)$$

The torque and power coefficients are non-dimensional, and they would be constant for an ideal scaling (identical aerodynamic characteristics and constant TSR). However,

this is not the case for the given model turbine. The power coefficient is reduced due to aerodynamic losses associated with the lower Reynolds number. Thus, we introduce a scaling factor for the power coefficient:

$$n_{cp} = \frac{c_{p,m}}{c_{p,f}}. \quad (5.19)$$

Further, the TSR is reduced in order to derive larger chord lengths and higher Reynolds numbers for the model turbine. We can define a scaling ratio for the TSRs in light-wind mode (λ_{LW}) and strong-wind mode (λ_{SW}). Since we address the maximum aerodynamic torque at rated wind speed, only the strong-wind mode is used here.

$$n_{\lambda,SW} = \frac{\lambda_{SW,m}}{\lambda_{SW,f}} \quad (5.20)$$

Consequently, we can define the following for the scaling of the torque coefficient:

$$n_{cq} = \frac{c_{q,m}}{c_{q,f}} = \frac{n_{cp}}{n_{\lambda}}. \quad (5.21)$$

Wind speeds

For an ideal scaling (constant TSR), the wind speeds would scale with

$$n_{u,ideal} = \frac{u_m}{u_f} = \frac{n_l}{n_t}. \quad (5.22)$$

Since we transferred the rotor design to lower TSRs, the wind speed scales with

$$n_u = \frac{u_m}{u_f} = \frac{n_l}{n_t n_{\lambda}}. \quad (5.23)$$

The maximum rotational speed (ω_{rated}) of the model turbine is constrained due to hardware limitations. When the maximum rotational speed is reached with the strong-wind TSR, this wind speed is considered to be the rated wind speed. Thus, the rated wind speed, rated torque and rated power change compared to the scaling theory, or in other words, the model turbine is de-rated. This can be incorporated by defining a new time scaling for rated power:

$$n_{t,rated} = \frac{\omega_{rated,f}}{\omega_{rated,m}}. \quad (5.24)$$

The rated wind speed consequently scales with

$$n_{u,\text{rated}} = \frac{u_{\text{rated,m}}}{u_{\text{rated,f}}} = \frac{n_1}{n_{t,\text{rated}} n_{\lambda,\text{SW}}}. \quad (5.25)$$

Aerodynamic torque

If we combine Eqs. (5.15), (5.16), (5.21) and (5.25) we can define a scaling ratio for the aerodynamic torque:

$$\begin{aligned} n_{\text{Ma}} &= n_1^3 n_{u,\text{rated}}^2 n_{\text{cq,rated}} \\ &= n_1^3 \left(\frac{n_1}{n_{t,\text{rated}} n_{\lambda,\text{SW}}} \right)^2 \frac{n_{\text{cp,rated}}}{n_{\lambda,\text{SW}}}. \end{aligned} \quad (5.26)$$

For the ideal scaling (constant TSR and constant c_p), Eq. (5.26) simplifies to

$$n_{\text{Ma}}^* = \frac{n_1^5}{n_t^2}. \quad (5.27)$$

If the time scaling equals the geometric scaling, Eq. (5.26) simplifies to

$$n_{\text{Ma}}^{**} = n_1^3. \quad (5.28)$$

For the given model turbine, the required parameters are given in Table 5.3 and the coefficients from Eq. (5.26) result in

$$n_{u,\text{rated}}^2 n_{\text{cq,rated}} = 1.14. \quad (5.29)$$

This is why the maximum aerodynamic torque of the model turbine is 14 % higher, compared to the ideal and simplified scaling, where only the change in radius is considered.

These scaling laws can be extended from the aerodynamic torque to the generator torque, considering the different mechanical losses in the drive train, which we exclude here for the sake of brevity.

Table 5.3: Scaling parameters for the Hybrid-Lambda Rotor, relevant for the scaling of the aerodynamic torque.

Parameter	Symbol	Model scale (subscript m)	Full-scale (subscript f)	Unit	Scaling coefficient
Rotor diameter	D	1.8	326	m	n_l
Power coefficient at rated wind speed	$c_{p,\text{rated}}$	0.2805	0.2923	–	$n_{c_p,\text{rated}}$
Maximum rotor speed	ω_{rated}	577.3317	5.3824	rpm	$1/n_{t,\text{rated}}$
Rated wind speed	u_{rated}	9.0687	10.2	m s^{-1}	$n_{u,\text{rated}}$
TSR at rated (SW mode)	λ_{SW}	6	9	–	$n_{\lambda,\text{SW}}$
Max. aerodynamic torque	$M_{a,\text{max}}$	5.2831	2.7563×10^7	Nm	n_{Ma}

Table 5.4: Data necessary for the calculation of the time constants in Eq. (5.9).

Parameter	Symbol	Model scale (subscript m)	Full-scale (subscript f)	Unit
Wind speed at the start of transition region	u_{ts}	6.3	6.8	m s^{-1}
Wind speed at the end of transition region	u_{te}	7.9	8.3	m s^{-1}
Derivative of aerodynamic torque coefficient at u_{ts}	$\frac{dc_{q,ts}}{d\lambda}$	-7.6×10^{-3}	-3.7×10^{-3}	–
Derivative of aerodynamic torque coefficient at u_{te}	$\frac{dc_{q,te}}{d\lambda}$	-6.6×10^{-3}	-6.9×10^{-4}	–
Derivative of generator torque at u_{ts}	$\frac{dM_{g,ts}}{d\omega}$	0.1	5.9×10^7	Nm s rad^{-1}
Derivative of generator torque at u_{te}	$\frac{dM_{g,te}}{d\omega}$	0.06	4.8×10^7	Nm s rad^{-1}
Air density	ρ	1.2	1.2	kg m^{-3}

Financial support

The work presented in this paper was funded by the Deutsche Forschungsgemeinschaft (DFG, German Research Foundation) – project ID 434502799 – SFB 1463.

Chapter 6

Conclusions and Outlook

In this chapter, the major findings and conclusions of this thesis are summarized and the research questions stated in the introduction are addressed. Additionally, suggestions for further research are discussed in Sect. 6.2.

6.1 Conclusions

The value of wind energy does not solely depend on a low levelized cost of energy. It is of high importance at which time the energy is produced and how much wind energy is already available in the grid at that given time. Further, the variability of the produced energy directly impacts the value. We identified two major problems of the large-scale exploitation of wind energy, especially in the German Bight. First, the self-cannibalization (May et al., 2015; López Prol et al., 2020) addresses the fact that the higher the share of wind energy in the entire energy mix is, the larger is the decrease of the market value with increasing wind speeds. In other words, wind energy is very valuable at times of low wind speeds, but the value decreases significantly or even drops below zero during strong wind periods. Second, the increasing clustering of offshore wind farms heavily reduces the efficiency of downstream wind farms due to cluster wake effects, which predominantly occur when the turbines operate in the partial load range, i.e. at wind speeds below rated. These cluster wakes can persist for several tens of kilometres under certain atmospheric conditions (Dörenkämper et al., 2023; Schneemann et al., 2020). Thus, there is a demand for an increased power feed-in in light winds, which is usually accomplished by means of larger rotors and lower specific ratings, at onshore sites. But especially at strong wind sites, large rotors come with the need for load reduction techniques which inherently reduce the aerodynamic

efficiency of the individual turbines. For offshore sites, the wind speed regime where the load reduction is active, e.g. from around 7 to 11 ms^{-1} , coincides with the annual average wind speed and a large portion of the produced energy would suffer from the reduced efficiency during load limitation. Innovative rotor concepts are required which enable very large rotors to capture more energy in light winds, but which also limit the loads to a feasible level. The goal is to foster a lightweight and cost-effective rotor design, while compromising the aerodynamic efficiency as little as possible. Further, load reduction techniques can reduce the wake losses and a deficit on the individual turbine efficiency can be at least partly counterbalanced with improvements for downstream turbines.

This delicate compromise finding is addressed with the Hybrid-Lambda Rotor design methodology which was developed and extensively examined within this thesis. In the following, we summarize the major findings, structured according to the main objectives outlined in the introduction.

1. *Introduction of a design methodology for very large rotors with blades that are aerodynamically optimized for the application of peak shaving:*

The Hybrid-Lambda Rotor design methodology can be applied to any given design problem which targets a very low-specific rating in order to increase the power in light winds while maintaining the design driving loads. The design features a non-uniform distribution of axial induction along the blade span, with a design value of 0.36 for the inner 70 % of the blade and 0.23 for the outer 30 %. Further, the blade is designed for two different TSRs, which is coupled to the control strategy for which two operating modes, light-wind (LW) and strong-wind (SW), are implemented. In the SW mode, peak shaving is applied with less reductions in the aerodynamic efficiency, compared to conventional peak shaving strategies, such as solely pitching to feather. This is due to a beneficial change in the AoA distribution which can be achieved by considering the following three aspects: First, when lowering the TSR, the increase in the inflow angle is larger for the inner part of the blade than for the outer part. Second, when pitching the blade to feather, the AoA decreases evenly over the entire blade length. And third, a twist offset for the inner part of the blade ensures that this part operates closer to the optimal AoA when peak shaving is applied. By reducing the TSR and simultaneously pitching to feather, we can achieve the following: When switching from the LW to the SW mode, the AoA decreases for the outer part of the blade (which reduces the loading) but increases closer towards the optimal AoA for the

inner part of the blade. This reduces the lever arm of the resulting bending forces and the contribution to the rotor torque production is concentrated closer to the blade root.

Due to the larger rotor diameter, the energy yield in light winds is significantly increased and the power characteristics of the turbine better match the demand in the energy system which results in a lower cost of valued energy. The mass of the blades could be significantly reduced compared to conventional scaling approaches by applying an aero-elastic optimization of the structural blade design and due to the inherent slender blade design for high TSRs. A sophisticated aero-servo-elastic simulation model was set up and the concept revealed several advantages when investigated in transient, turbulent design load cases. Finally, a cost model was introduced which enabled a techno-economic evaluation.

2. *Development of a method on how to scale the Hybrid-Lambda Rotor concept to wind tunnel size and the experimental characterization and validation of the aerodynamic design concept on wind tunnel scale:*

When scaling wind turbines to wind tunnel size, usually not all physical characteristics can be matched exactly. In this study, the scaling objectives were twofold: First, we aimed to match the non-uniform axial induction distribution over the blade span for two different operating modes. Second, we incorporated the change in the AoA distribution when switching between the LW and SW operating mode, as described above. Additionally, we transferred the design method to lower TSRs to derive larger chord lengths and higher Reynolds numbers. The experimental investigation of the scaled model showed that switching between the operating modes with the associated change in the AoA distribution works similar to the full-scale model and the aerodynamic characteristics are successfully replicated. The scaled model was further tested in gust events which were produced with an active grid in the wind tunnel. For this purpose, no controller action was applied to compare the pure aerodynamic response of different blade designs. When compared to a model turbine with the same diameter and with conventional blade design (replicating the NREL 5 MW reference turbine), the load overshoot in the normalized flapwise RBM was 4 % lower for the Hybrid-Lambda model turbine, due to the beneficial low-induction design of the outer part of the blades.

3. *Investigation of the influence of the steep gradients of axial induction along the blade span on the aerodynamics and the characterization of the wake of the Hybrid-Lambda Rotor:*

This objective was addressed by means of experimental investigations with the scaled wind tunnel model and by means of mid-fidelity simulations. Both methods revealed the unique wake characteristics of the Hybrid-Lambda Rotor which enable three major advantages: First, the wake deficit in the SW mode is significantly reduced. In this wind speed region, conventional turbines still operate in the partial load range, i.e. with a high thrust coefficient and with strong wake deficits. Second, the low-induction design of the outer part of the blade leads to an outer annulus in the wake with increased wind speeds, compared to a wake deficit profile of a conventional turbine. This feature is present for the entire partial load range and can be beneficial in partial wake scenarios, when only mild deficits from the outer wake annulus impinge the downstream rotor. And third, an additional shear layer and an associated vortex system shed from the blending region on the blade due to the change in the design axial induction. The shear layer further increases the turbulence intensity between the inner wake core and the outer annulus which enhances wake diffusion.

The BEM theory inherently assumes that the blade elements are independent of each other, at all radial positions. Therefore, strong gradients in the axial induction distribution at the blade design blending region are predicted. In contrast, the LDA measurements in the rotor plane show that the steep gradients are smeared out. However, in the hot-wire measurements in the near-wake of the model turbine, the steep gradients and the stepwise velocity change in radial direction are present. We therefore conclude, that the gradients need to develop from a uniform distribution in the inflow via a smeared out distribution in the rotor plane to a stepwise profile with the steep gradients in the close vicinity downstream of the rotor. This development can not be predicted by the inherent model assumptions in the BEM theory. Due to the conservation of mass, the inner wake core with the slower flow expands and pushes into the outer wake annulus with higher wind speeds. This further supports the steep gradients and the stepwise velocity change in radial direction in the near-wake. All applied methods (experiments, LES and FVW simulations) revealed that the gradients in the wake profile smear out with increasing turbulence intensity in the inflow.

We further compared the power output of a simplified wind farm layout with two turbines in LES with actuator line model with a fixed absolute spacing of 1.44 km among two Hybrid-Lambda turbines ($P_{\text{rated}} = 15 \text{ MW}$, $D = 326 \text{ m}$) and two IEA reference turbines ($P_{\text{rated}} = 15 \text{ MW}$, $D = 240 \text{ m}$). We used a very high spatial resolution that allows to resolve the non-uniform axial induction distribution

along the blade span. For a wind speed of 6.8 ms^{-1} , the Hybrid-Lambda turbines produce twice the power than the reference turbines. This advantage even outperforms the benefits on a single turbine level, due to the beneficial wake characteristics. Similar results were found by Paulsen et al. (2024), who compared the performance of the turbine concepts in large-scale wind farm clusters by means of mesoscale simulations.

4. *Development of control methodologies for very large turbines with a load constraint that fulfil the Hybrid-Lambda control strategy, their application on the wind tunnel model and the experimental validation with respect to extreme loads, fatigue, pitch actuation and power output:*

We set up a control methodology for the Hybrid-Lambda Rotor concept which succeeded in tracking two different TSRs below rated wind speed. This is achieved by a smart arrangement of the rotor speed set points and the generator torque saturations for the PI torque controller. It further enables a transition region with constant rotational speed to switch between the two operational TSRs. Four versions of the pitch controller were introduced which approach the objective of limiting the flapwise RBM in different ways. First, a baseline controller which uses a wind speed estimator and a look-up table for the pitch angle, without the need for additional sensor equipment that might not be available on commercial turbines. Second, a load feedback (LFB) controller which uses measurements from the flapwise RBM to set the pitch angle. Third, a feed-forward (FF) controller which uses wind speed measurements upstream of the rotor as a preview, allowing the pitch actuation to react in advance to sudden gust events. The fourth controller is a combination of the LFB and the FF controller.

The baseline controller succeeded well in tracking the two TSRs in the LW and SW operating modes and the flapwise RBM was held constant in the peak shaving region in steady-state test cases. However, due to model uncertainties, the resulting RBM was 10% higher than desired. The LFB controller was able to overcome this challenge. The measurements from the blade root allowed to correct for the model mismatch. The pitch angle was set higher and the RBM was constrained well in steady-state. But, due to the inherent integral behaviour of the feedback implementation, the response was too slow for sudden gust events. Those were handled much better by the FF controller, which was able to entirely remove the load overshoot by pitching just before the gust impacts the rotor. By thoroughly explaining the scaling of the controller concepts, we ensure the transferability of

the results from the wind tunnel tests to full-scale applications.

We therefore conclude, that controller development for very large wind turbines with a load constraint should include a model calibration or model update procedure, a feedback from the load measurements and a preview of the inflow. Those characteristics need to be combined and implemented in a controller framework that ensures structural integrity of the turbine while unlocking the full potential of aerodynamic efficiency and load mitigation features of the Hybrid-Lambda Rotor.

6.2 Suggestions for further research

There are five implications of those results for future work on the Hybrid-Lambda Rotor concept.

First, future design versions could incorporate a more gradual change of the design TSR and axial induction along the blade span. This could include an application of the axial induction distribution as derived by Jamieson (2020), which is found to be optimal in terms of rotor size increase with a load constraint. Instead of a stepwise change in the axial induction distribution, as proposed by the Hybrid-Lambda concept, and instead of a constant low induction of 0.187, as described by Chaviaropoulos and Sieros (2014), Jamieson (2020) derived an axial induction distribution that gradually decreases from $1/3$ at the blade root to very low values at the blade tip. Such a design would probably not provoke the additional vortex system, as it was found for the Hybrid-Lambda concept described in this thesis. A comparison of those two design variations would also enable a detailed analysis of the impact of the second vortex system on the wake diffusion.

Second, the torsional degree of freedom needs to be included in the blade design. Bend-twist coupling can help to reduce the loads and it will further reduce the lever arm of bending forces, since the torsional deflection increases towards the blade tip. However, the blade design as well as the controller strategy needs to be adapted. Considering that the blade will deflect torsionally towards feather means that the angle of attack will reduce gradually towards the blade tip which can help to reduce the losses associated with load limiting strategies due to the reduced lever arm. But, this also means that the aerodynamic operating point will move away from the optimum and this can be counterbalanced by adjusting the twist angle in the blade design and the control strategy. In this way, the aerodynamic optimum can be at least preserved for one chosen operating point, preferably for the end of the light wind mode at u_{ts} .

Third, the Hybrid-Lambda concept offers further benefits on a wind farm level which should be evaluated in detail. Paulsen et al. (2024) investigated the concept using meso scale simulations. They showed that the benefits in a wind farm application even outperform those of the single turbine due to the reduced wake losses. Paulsen et al. (2026) further compared prospective expansion scenarios where the entire available area in the German Bight is either equipped with IEA 15 MW turbines or with the same amount of 15 MW Hybrid-Lambda turbines. Over the course of a representative year, the annual energy production is increased by 19.4% with the use of Hybrid-Lambda turbines. This simulation method can cover a very large area, like the entire available area of the German Bight, and a very long time span, like a representative year. But the coarse spatial resolution cannot resolve the non-uniform axial induction distribution over the rotor plane. It is therefore unable to fully model the unique wake characteristics of the Hybrid-Lambda Rotor. Since LES is computationally expensive, conventional wake engineering models should be adapted to fit the wake shape of the Hybrid-Lambda Rotor. This would enable wind farm and cluster layout optimization studies with the integration of the Hybrid-Lambda Rotor. Also mixed layouts could be investigated, i.e. using the amount of deployed Hybrid-Lambda turbines and the amount of conventional turbines as free design variables. Thus, not only the layout and the spacing is optimized, but also the best ratio of Hybrid-Lambda and conventional turbines in one wind farm (or in the entire German Bight) would be investigated. With the different hub heights and operational strategies, i.e. thrust coefficients vs. wind speed, interesting wake mixing phenomena are expected, which could be investigated with LES in the next stage.

Fourth, the Hybrid-Lambda Rotor design methodology could be extended with wind farm related aspects. An important design parameter is the wind speed u_{ts} , at which the limiting loads are reached and the transition to the SW mode starts. For stronger wind speeds, the efficiency of the individual turbine decreases but the wake deficits in the wind farm are greatly reduced. The wind speed u_{ts} can be influenced within the blade design by the axial induction distribution along the blade span. If larger parts of the blade are designed for a higher axial induction (closer to 1/3), the efficiency will be higher in the LW mode, but the limiting loads will be reached at lower wind speeds and the peak shaving in the SW mode will be accompanied with larger losses. However, the reduced wake deficits will expand over a wider range of wind speeds. These complex interactions need to be addressed with an optimization routine,

connecting the rotor and controller design of individual turbines with implications on the wind farm level. Incorporating the transition wind speed as a key design variable into wind farm oriented turbine design could open an interesting research field. This seems to become increasingly important with the advancing clustering of offshore wind sites in northern Europe and other suitable locations worldwide.

And fifth, the control concept for the Hybrid-Lambda Rotor could be further refined and extended. By optimizing steady state operating points, the transition between the operating modes can be improved. Incorporating model predictive control could prevent unnecessary switches between modes if, for example, a wind speed reduction is only temporary. Further, the control concept could be extended to the level of wind farm control, enabled by a communication between the individual turbines with the aim of improving energy capture and focusing on demand oriented power feed-in. Nevertheless, the limitation of structural loads needs to be guaranteed and the health state of individual turbines could be included in the control concept. The control algorithm would then adapt to changing properties and the damage level of individual turbines, aiming on an equal distribution of damage among the entire wind farm.

References

- Abbas, Nikhar J., Daniel S. Zalkind, Lucy Pao and Alan Wright (2022). 'A reference open-source controller for fixed and floating offshore wind turbines'. In: *Wind Energy Science* 7.1, pp. 53–73. DOI: 10.5194/wes-7-53-2022.
- Agarwala, Ranjeet and Paul I. Ro (2015). 'Separated Pitch Control at Tip: Innovative Blade Design Explorations for Large MW Wind Turbine Blades'. In: *Journal of Wind Energy* 2015, pp. 1–12. ISSN: 2356-7732. DOI: 10.1155/2015/895974.
- Barter, Garrett E., Latha Sethuraman, Pietro Bortolotti, Jonathan Keller and David A. Torrey (2023). 'Beyond 15 MW: A cost of energy perspective on the next generation of drivetrain technologies for offshore wind turbines'. In: *Applied Energy* 344, p. 121272. ISSN: 03062619. DOI: 10.1016/j.apenergy.2023.121272.
- Bayati, I., M. Belloli, L. Bernini, R. Mikkelsen and A. Zasso (2016). 'On the aero-elastic design of the DTU 10MW wind turbine blade for the LIFES50+ wind tunnel scale model'. In: *Journal of Physics: Conference Series* 753, p. 022028. ISSN: 1742-6588. DOI: 10.1088/1742-6596/753/2/022028.
- Berg, Jonathan and Brian Resor (2012). *Numerical Manufacturing And Design Tool (NuMAD v2.0) for Wind Turbine Blades: User's Guide*. Albuquerque: Sandia Report, SAND2012-7028. DOI: 10.2172/1051715.
- Berger, Frederik (2022). 'Wind tunnel experiments with a model turbine: Dynamic inflow investigation: Dissertation'. In: URL: <https://oops.uni-oldenburg.de/id/eprint/5516> (visited on 01/08/2025).
- Berger, Frederik, Lars Kröger, David Onnen, Vlaho Petrović and Martin Kühn (2018). 'Scaled wind turbine setup in a turbulent wind tunnel'. In: *Journal of Physics: Conference Series* 1104, p. 012026. ISSN: 1742-6588. DOI: 10.1088/1742-6596/1104/1/012026.
- Berger, Frederik, David Onnen, Gerard Schepers and Martin Kühn (2021). 'Experimental analysis of radially resolved dynamic inflow effects due to pitch steps'. In: *Wind Energy Science* 6.6, pp. 1341–1361. DOI: 10.5194/wes-6-1341-2021.

- Berkhout, Volker, André Bisevic, Michael Claußner, Martin Dörenkämper, Michael Durstewitz, Stefan Faulstich, Philip Görg, Laura Große, Berthold Hahn, Fabian Huneke, Detlef Kuhl, Marc-Alexander Lutz, Jochen Mayer, Julia Mergner, Miriam Noonan, Sebastian Pfaffel, Florian Rehwald, Jonas Schmidt, Susann Spriestersbach, Bernhard Stoevesandt and Lukas Vollmer (2018). 'Windenergie Report Deutschland 2018'. In: *Fraunhofer-Gesellschaft*. DOI: 10.24406/publica-fhg-299720.
- Betz, Albert (1926). *Wind-Energie und ihre Ausnutzung durch Windmühlen (Wind energy and its utilization through windmills)*. unchanged from the original edition [Göttingen, Vandenhoeck u. Ruprecht, 1926]. Staufen bei Freiburg: Ökobuch, 1994. ISBN: 9783922964117.
- Bir, Gunjit (2005). *User's Guide to PreComp (Pre-Processor for Computing Composite Blade Properties)*. Golden (US): National Renewable Energy Laboratory, NREL/TP-500-38929. DOI: 10.2172/876556.
- Bolinger, Mark, Eric Lantz, Ryan Wisser, Ben Hoen, Joseph Rand and Robert Hammond (2021). 'Opportunities for and challenges to further reductions in the "specific power" rating of wind turbines installed in the United States'. In: *Wind Engineering* 45.2, pp. 351–368. ISSN: 0309-524X. DOI: 10.1177/0309524X19901012.
- Bonnie Jonkman, Rafael M Mudafort, Andy Platt, E. Branlard, Mike Sprague, Matt Hall, Ganesh Vijayakumar, Marshall Buhl, Hannah Ross, Pietro Bortolotti, Shreyas Ananthan, Jon Rood, Derek Slaughter, Stein Housner, Kurt Bendl, Lucas Carmo and Eliot Quon (2022). 'OpenFAST release v3.3.0, Zenodo [code]'. In: DOI: 10.5281/zenodo.7262094.
- Borrmann, Rasmus, Knud Rehfeldt, Anna-Kathrin Wallasch and Silke Lüers (2018). 'Capacity densities of European offshore wind farms'. In: *Report conducted by Deutsche WindGuard GmbH*. URL: https://vasab.org/wp-content/uploads/2018/06/BalticLINes_CapacityDensityStudy_June2018-2.pdf (visited on 01/08/2025).
- Bortolotti, P., D. Berry, R. Murray, E. Gaertner, D. Jenne, R. Damiani, G. Barter and K. Dykes (2019). 'A Detailed Wind Turbine Blade Cost Model'. In: *National Renewable Energy Laboratory, NREL/TP-5000-73585*. DOI: 10.2172/1529217.
- Bossanyi, E. A. (2000). 'The Design of closed loop controllers for wind turbines'. In: *Wind Energy* 3.3, pp. 149–163. ISSN: 10954244. DOI: 10.1002/we.34.
- Bottasso, C. L., F. Campagnolo, A. Croce and C. Tibaldi (2013). 'Optimization-based study of bend-twist coupled rotor blades for passive and integrated passive/active load alleviation'. In: *Wind Energy* 16.8, pp. 1149–1166. ISSN: 10954244. DOI: 10.1002/we.1543.

- Bottasso, C. L., A. Croce, C. E. D. Riboldi and M. Salvetti (2014a). 'Cyclic pitch control for the reduction of ultimate loads on wind turbines'. In: *Journal of Physics: Conference Series* 524, p. 012063. DOI: 10.1088/1742-6596/524/1/012063.
- Bottasso, Carlo L. and Filippo Campagnolo (2021). *Wind Tunnel Testing of Wind Turbines and Farms*. In: Stoevesandt, B., Schepers, G., Fuglsang, P., Yuping, S. (eds) *Handbook of Wind Energy Aerodynamics*. Springer. DOI: 10.1007/978-3-030-05455-7_54-1.
- Bottasso, Carlo L., Filippo Campagnolo and Vlaho Petrović (2014b). 'Wind tunnel testing of scaled wind turbine models: Beyond aerodynamics'. In: *Journal of Wind Engineering and Industrial Aerodynamics* 127, pp. 11–28. ISSN: 01676105. DOI: 10.1016/j.jweia.2014.01.009.
- Branlard, E. and M. Gaunaa (2016). 'Superposition of vortex cylinders for steady and unsteady simulation of rotors of finite tip-speed ratio'. In: *Wind Energy* 19.7, pp. 1307–1323. ISSN: 10954244. DOI: 10.1002/we.1899.
- Branlard, E., B. Jonkman, G. R. Pirrung, K. Dixon and J. Jonkman (2022a). 'Dynamic inflow and unsteady aerodynamics models for modal and stability analyses in OpenFAST'. In: *Journal of Physics: Conference Series* 2265.3, p. 032044. ISSN: 1742-6588. DOI: 10.1088/1742-6596/2265/3/032044.
- Branlard, Emmanuel, Ian Brownstein, Benjamin Strom, Jason Jonkman, Scott Dana and Edward Ian Baring-Gould (2022b). 'A multipurpose lifting-line flow solver for arbitrary wind energy concepts'. In: *Wind Energy Science* 7.2, pp. 455–467. DOI: 10.5194/wes-7-455-2022.
- Buhl, L. (2005). 'A New Empirical Relationship between Thrust Coefficient and Induction Factor for the Turbulent Windmill State'. In: *National Renewable Energy Laboratory, NREL/TP-500-36834*. DOI: 10.2172/15016819.
- Burton, Tony, Nicholas Jenkins, David Sharpe and Ervin Bossanyi (2011). *Wind Energy Handbook*. 2nd. Chichester: Wiley. ISBN: 978-1-119-99272-1.
- Campagnolo, Filippo, Vlaho Petrović, Johannes Schreiber, Emmanouil M. Nanos, Alessandro Croce and Carlo L. Bottasso (2016). 'Wind tunnel testing of a closed-loop wake deflection controller for wind farm power maximization'. In: *Journal of Physics: Conference Series* 753, p. 032006. ISSN: 1742-6588. DOI: 10.1088/1742-6596/753/3/032006.
- Canet, Helena, Pietro Bortolotti and Carlo L. Bottasso (2021). 'On the scaling of wind turbine rotors'. In: *Wind Energy Science* 6.3, pp. 601–626. DOI: 10.5194/wes-6-601-2021.

- Canet, Helena, Adrien Guilloré and Carlo L. Bottasso (2023). 'The eco-conscious wind turbine: design beyond purely economic metrics'. In: *Wind Energy Science* 8.6, pp. 1029–1047. DOI: 10.5194/wes-8-1029-2023.
- Chaviaropoulos, P. K. and G. Sieros (2014). 'Design of low induction rotors for use in large offshore wind farms'. In: *EWEA Conf., 10-13 March 2014*. URL: https://www.researchgate.net/publication/263209536_Design_of_Low_Induction_Rotors_for_use_in_large_offshore_wind_farms (visited on 15/11/2023).
- Damiani, R. and G. Hayman (2019). 'The Unsteady Aerodynamics Module for FAST 8'. In: *National Renewable Energy Laboratory, NREL/TP-5000-66347*. DOI: 10.2172/1576488.
- Det Norske Veritas group: DNV-GL ST-0437 (November 2016 (amended: November 2021)). *Loads and site conditions for wind turbines, standard*. URL: <https://www.dnv.com/energy/standards-guidelines/dnv-st-0437-loads-and-site-conditions-for-wind-turbines/> (visited on 15/11/2023).
- Dong, Guodan, Jianhua Qin, Zhaobin Li and Xiaolei Yang (2023). 'Characteristics of wind turbine wakes for different blade designs'. In: *Journal of Fluid Mechanics* 965. ISSN: 0022-1120. DOI: 10.1017/jfm.2023.385.
- Dörenkämper, Martin, Tobias Meyer, David Baumgärtner, Johanna Borowski, Christian Deters, Enno Dietrich, Johannes Fricke, Florian Hans, Torben Jersch, Mareike Leimeister, Mohammad Mohsen Neshati, Georg Pangalos, Tulio Ernesto Quiroz López, Gesa Quistorf, Niklas Requate, Kevin Vincent Schalk, Jonas Schmidt, Marco Schnackenberg, Sandra Schwegmann, Philipp Thomas, Lukas Vollmer, Julia Walgern, Viktor Widerspan and Hanna Zotieieva (2023). 'Weiterentwicklung der Rahmenbedingungen zur Planung von Windenergieanlagen auf See und Netzanbindungssystemen'. In: *Fraunhofer-Institut für Windenergiesysteme*. DOI: 10.24406/publica-2202.
- Downing, S. and D. Socie (1982). 'Simple rainflow counting algorithms'. In: *International Journal of Fatigue* 4.1, pp. 31–40. ISSN: 01421123. DOI: 10.1016/0142-1123(82)90018-4.
- Dykes, K., L. Kitzing, M. Andersson, C. Pons-Seres de Brauwer and H. Canét (2020). 'Beyond LCOE: New Assessment Criteria for Evaluating Wind Energy R&I: A SETWind workshop report'. In.
- Dykes, Katherine, S. Andrew Ning, George Scott and Peter Graf (2021). *WISDEM® (Wind-Plant Integrated System Design and Engineering Model)*. DOI: 10.11578/dc.20211208.2.

- Federal Maritime and Hydrographic Agency of Germany (2020). *Flächenentwicklungsplan 2020 für die deutsche Nord- und Ostsee*. Hamburg: BSH 7608. URL: https://www.bsh.de/DE/THEMEN/Offshore/Meeresfachplanung/Flaechenentwicklungsplan/_Anlagen/Downloads/Downloads_Publikationsslider/FEP_2020_Flaechenentwicklungsplan_2020.pdf?__blob=publicationFile&v=6 (visited on 15/11/2023).
- Feil, Roland, Nikhar Abbas, Pietro Bortolotti, Nick Johnson and Ben Mertz (2020). 'Distributed Aerodynamic Control using Active Trailing-Edge Flaps for Large Wind Turbines'. In: *Journal of Physics: Conference Series* 1618.4, p. 042026. ISSN: 1742-6588. DOI: 10.1088/1742-6596/1618/4/042026.
- Fingersh, L., M. Hand and A. Laxson (2006). 'Wind Turbine Design Cost and Scaling Model'. In: *National Renewable Energy Laboratory, NREL/TP-500-40566*. DOI: 10.2172/897434.
- Fontanella, Alessandro, Ilmas Bayati, Robert Mikkelsen, Marco Belloli and Alberto Zasso (2021). 'UNAFLOW: a holistic wind tunnel experiment about the aerodynamic response of floating wind turbines under imposed surge motion'. In: *Wind Energy Science* 6.5, pp. 1169–1190. DOI: 10.5194/wes-6-1169-2021.
- Fu, Wei, Feng Guo, David Schlipf and Alfredo Peña (2023). 'Feedforward pitch control for a 15 MW wind turbine using a spinner-mounted single-beam lidar'. In: *Wind Energy Science* 8.12, pp. 1893–1907. DOI: 10.5194/wes-8-1893-2023.
- Gaertner, Evan, Jennifer Rinker, Latha Sethuraman, Frederik Zahle, Benjamin Anderson, Garrett Barter, Nikhar Abbas, Fanzhong Meng, Pietro Bortolotti, Witold Skrzypinski, George Scott, Roland Feil, Henrik Bredmose, Katherine Dykes, Matt Shields, Christopher Allen and Anthony Viselli (2020). *Definition of the IEA 15-Megawatt Offshore Reference Wind turbine, NREL/TP-5000-75698*. Golden (US): National Renewable Energy Laboratory. DOI: 10.2172/1603478.
- Gasch, Robert and Jochen Twele (2012). *Wind Power Plants: Fundamentals, Design, Construction and Operation*. 2nd. Berlin: Springer. ISBN: 978-3-642-22937-4.
- Giguere, P. and M. S. Selig (1998). 'New Airfoils for Small Horizontal Axis Wind Turbines'. In: *ASME Journal of Solar Energy Engineering* 120, pp. 108–114.
- Griffith, T. and P. Richards (2014). 'The SNL100-03 Blade: Design Studies with Flatback Airfoils for the Sandia 100-meter Blade'. In: *Sandia report: SAND2014-18129*. DOI: 10.2172/1159116.
- Guo, Feng, David Schlipf and Po Wen Cheng (2023). 'Evaluation of lidar-assisted wind turbine control under various turbulence characteristics'. In: *Wind Energy Science* 8.2, pp. 149–171. DOI: 10.5194/wes-8-149-2023.

- Hand, M., A. Hethy, S. Lüers, A. Wallasch, K. Rehfeldt, A. Duffy, D. Weir, M. Stenkvis, A. Uihlein, T. Stehly, E. Lantz and R. Wiser (2018). *IEA Wind TCP Task 26 – Wind Technology, Cost, and Performance Trends in Denmark, Germany, Ireland, Norway, Sweden, the European Union, and the United States: 2008–2016*. Golden (US): National Renewable Energy Laboratory, NREL/TP-6A20-71844. DOI: 10.2172/1525772.
- Hand, M. M., D. A. Simms, L. J. Fingersh, D. W. Jager, J. R. Cotrell, S. Schreck and S. M. Larwood (2001). 'Unsteady Aerodynamics Experiment Phase VI: Wind Tunnel Test Configurations and Available Data Campaigns'. In: *National Renewable Energy Laboratory NREL/TP-500-29955*. DOI: 10.2172/15000240.
- Hansen, Martin (2008). *Aerodynamics of wind turbines*. 2nd. London: Earthscan. ISBN: 978-1-84407-438-9.
- Herráez, Iván, Buşra Akay, Gerard J. W. van Bussel, Joachim Peinke and Bernhard Stoevesandt (2016). 'Detailed analysis of the blade root flow of a horizontal axis wind turbine'. In: *Wind Energy Science* 1.2, pp. 89–100. DOI: 10.5194/wes-1-89-2016.
- Herráez, Iván, Elia Daniele and J. Gerard Schepers (2018). 'Extraction of the wake induction and angle of attack on rotating wind turbine blades from PIV and CFD results'. In: *Wind Energy Science* 3.1, pp. 1–9. DOI: 10.5194/wes-3-1-2018.
- Hirth, Lion and Simon Müller (2016). 'System-friendly wind power'. In: *Energy Economics* 56, pp. 51–63. ISSN: 01409883. DOI: 10.1016/j.eneco.2016.02.016.
- Huebler, C., B. Schmidt, S. Voß, C. Hente, C. Gebhardt, D. Ribnitzky and R. Rolfes (2022). 'Entwurf von Offshore-Windenergieanlagen neuer Größenordnung als Grundpfeiler unserer zukünftigen Energieversorgung'. In: 26. *Dresdner Baustatik Seminar (14.10.2022), Conference Paper*. URL: https://www.researchgate.net/publication/364751477_Entwurf_von_Offshore-Windenergieanlagen_neuer_Grossenordnung_als_Grundpfeiler_unserer_zukunfftigen_Energieversorgung (visited on 01/08/2025).
- Hulskamp, A. W., J. W. van Wingerden, T. Barlas, H. Champlaud, G. A. M. van Kuik, H. E. N. Bersee and M. Verhaegen (2011). 'Design of a scaled wind turbine with a smart rotor for dynamic load control experiments'. In: *Wind Energy* 14.3, pp. 339–354. ISSN: 10954244. DOI: 10.1002/we.424.
- IEC 61400-1 (2019). *Wind energy generation systems - Part 1: Design requirements, International Electrotechnical Commission, ed. 4*.
- Jamieson, P., C. Hornzee-Jones, E. Moroz and R. Blakemore (2005). 'Variable diameter wind turbine rotor blades, US patent: US 6,972,498 B2'. Pat.

-
- Jamieson, Peter (2020). 'Top-level rotor optimisations based on actuator disc theory'. In: *Wind Energy Science* 5.2, pp. 807–818. DOI: 10.5194/wes-5-807-2020.
- Johnson, Nick, Pietro Bortolotti, Katherine Dykes, Garrett Barter, Patrick Moriarty, Scott Carron, Fabian Wendt, Paul Veers, Josh Paquette, Chris Kelly and Brandon Ennis (2019). 'Investigation of Innovative Rotor Concepts for the Big Adaptive Rotor Project'. In: *National Renewable Energy Laboratory, NREL/TP-5000-73605*. DOI: 10.2172/1563139.
- Johnson, Nick, Josh Paquette, Pietro Bortolotti, Nicole Mendoza, Mark Bolinger, Ernesto Camarena, Evan Anderson and Brandon Ennis (2021). 'Big Adaptive Rotor Phase I Final Report'. In: *National Renewable Energy Laboratory, NREL/TP-5000-79855*. DOI: 10.2172/1835259.
- Jonkman, B., R. Mudafort, A. Platt, E. Branlard, M. Sprague, G. Vijayakumar, M. Buhl, H. Ross, P. Bortolotti, M. Masciola, D. Ananthan, M. Schmidt, J. Rood, M. Hall, K. Bendl and T. Martinez (2022). 'OpenFAST release v3.1.0, Zenodo [code]'. In: DOI: 10.5281/zenodo.6324288.
- Jonkman, J., S. Butterfield, W. Musial and G. Scott (2009). 'Definition of a 5-MW Reference Wind Turbine for Offshore System Development'. In: *National Renewable Energy Laboratory, NREL/TP-500-38060*. DOI: 10.2172/947422.
- Jonkman, Jason and M. L. Buhl (2006). 'TurbSim User's Guide'. In: *Technical Report NREL/TP-500-39797*. DOI: 10.2172/891594.
- Kelley, Christopher., David. Maniaci and Brian Resor (2014). 'Horizontal-Axis Wind Turbine Wake Sensitivity to Different Blade Load Distributions'. In: *AIAA SciTech, SAND2014-20587C*. DOI: 10.2514/6.2015-0490.
- Knauer, Andreas (2021). 'Rotor blade shaped to enhance wake diffusion: European patent, EP 3 308 014 B1'. Pat.
- Knudsen, Torben and Thomas Bak (2013). 'Simple model for describing and estimating wind turbine dynamic inflow'. In: *American Control Conference - Institute of electrical and electronics engineering*, pp. 640–646. DOI: 10.1109/ACC.2013.6579909.
- Kröger, Lars, Joeri Frederik, Jan-Willem van Wingerden, Joachim Peinke and Michael Hölling (2018). 'Generation of user defined turbulent inflow conditions by an active grid for validation experiments'. In: *Journal of Physics: Conference Series* 1037, p. 052002. ISSN: 1742-6588. DOI: 10.1088/1742-6596/1037/5/052002.
- Krogstad, P. Å. and J. A. Lund (2012). 'An experimental and numerical study of the performance of a model turbine'. In: *Wind Energy* 15.3, pp. 443–457. ISSN: 10954244. DOI: 10.1002/we.482.

- Lazzerini, Guido, Jacob Deleuran Grunnet, Tobias Gybel Hovgaard, Fabio Caponetti, Vasu Datta Madireddi, Delphine de Tavernier and Sebastiaan Paul Mulders (2025). 'COFLEX: a novel set point optimiser and feedforward–feedback control scheme for large, flexible wind turbines'. In: *Wind Energy Science* 10.7, pp. 1303–1327. DOI: 10.5194/wes-10-1303-2025.
- Lee, Hoesung et al. (2023). 'IPCC, 2023: Summary for Policymakers. In: Climate Change 2023: Synthesis Report. Contribution of Working Groups I, II and III to the Sixth Assessment Report of the Intergovernmental Panel on Climate Change'. In: *IPCC, Geneva, Switzerland*, pp. 1–34. DOI: 10.59327/IPCC/AR6-9789291691647.001.
- López Prol, Javier, Karl W. Steininger and David Zilberman (2020). 'The cannibalization effect of wind and solar in the California wholesale electricity market'. In: *Energy Economics* 85, p. 104552. ISSN: 01409883. DOI: 10.1016/j.eneco.2019.104552.
- Lüers, Silke (2024). 'Status of Offshore Wind Energy Development in Germany Year 2024'. In: *Deutsche Windguard*. URL: <https://www.windguard.de/jahr-2024.html> (lastaccess:3.11.2025).
- Madsen, H. Aa, F. Zahle, F. Meng, T. Barlas, F. Rasmussen and R. T. Rudolf (2020). 'Initial performance and load analysis of the LowWind turbine in comparison with a conventional turbine'. In: *Journal of Physics: Conference Series* 1618.3, p. 032011. ISSN: 1742-6588. DOI: 10.1088/1742-6596/1618/3/032011.
- Madsen, Helge, Frederik Zahle, Thanasis Barlas, Flemming Rasmussen, Fanzhong Meng, Riccardo Riva, Franck Bertagnolio and Kenneth Lonbaek (2021). *The LowWind project - an update: EERA - Low Specific Power and Low Wind Workshop (September 22-23, 2021)*. URL: https://www.researchgate.net/publication/355859693_The_LowWind_project_-an_update (visited on 01/08/2025).
- May, Nils, Karsten Heuhoff and Frieder Borggreffe (2015). 'Market incentives for system-friendly designs of wind turbines'. In: *DIW Economic Bulletin No. 24/2015* 24, pp. 313–321.
- Mehta, Mihir, Michiel Zaaier and Dominic von Terzi (2022). 'Optimum Turbine Design for Hydrogen Production from Offshore Wind'. In: *Journal of Physics: Conference Series* 4, p. 042061. ISSN: 1742-6588. DOI: 10.1088/1742-6596/2265/4/042061.
- (2024a). 'Drivers for optimum sizing of wind turbines for offshore wind farms'. In: *Wind Energy Science* 9.1, pp. 141–163. DOI: 10.5194/wes-9-141-2024.
- Mehta, Mihir Kishore, Michiel Zaaier and Dominic von Terzi (2024b). 'Designing wind turbines for profitability in the day-ahead market'. In: *Wind Energy Science* 9.12, pp. 2283–2300. DOI: 10.5194/wes-9-2283-2024.

- Mulders, Sebastiaan P., Yichao Liu, Fabio Spagnolo, Poul B. Christensen and Jan-Willem van Wingerden (2023). 'An iterative data-driven learning algorithm for calibration of the internal model in advanced wind turbine controllers'. In: *IFAC-PapersOnLine* 56.2, pp. 8406–8413. ISSN: 24058963. DOI: 10.1016/j.ifacol.2023.10.1035.
- Neuhaus, Lars, Frederik Berger, Joachim Peinke and Michael Hölling (2021). 'Exploring the capabilities of active grids'. In: *Experiments in Fluids* 62, 130.6. ISSN: 0723-4864. DOI: 10.1007/s00348-021-03224-5.
- Neuhaus, Lars, Daniel Ribnitzky, Michael Hölling, Matthias Wächter, Kerstin Avila, Martin Kühn and Joachim Peinke (2024). 'Model wind turbine performance in turbulent–non-turbulent boundary layer flow'. In: *Journal of Physics: Conference Series* 2767.4, p. 042018. ISSN: 1742-6588. DOI: 10.1088/1742-6596/2767/4/042018.
- Noyes, Carlos, Chao Qin and Eric Loth (2020). 'Analytic analysis of load alignment for coning extreme–scale rotors'. In: *Wind Energy* 23.2, pp. 357–369. ISSN: 10954244. DOI: 10.1002/we.2435.
- Onnen, D., L. Neuhaus, V. Petrović, D. Ribnitzky and M. Kühn (2024). 'Dynamic wake conditions tailored by an active grid in the wind tunnel'. In: *Journal of Physics: Conference Series* 2767.4, p. 042038. DOI: 10.1088/1742-6596/2767/4/042038.
- Paulsen, Johannes, Martin Dörenkämper and Gerald Steinfeld (2024). 'Power production and large-scale wake effects of offshore wind turbines with low specific rating'. In: *Journal of Physics: Conference Series* 2767.9, p. 092060. ISSN: 1742-6588. DOI: 10.1088/1742-6596/2767/9/092060.
- Paulsen, Johannes, Gerald Steinfeld, Martin Kühn and Martin Dörenkämper (2026). 'Mitigation of offshore wind farm cluster wake effects by low-specific-rating, low-induction turbines'. In: *Wind Energ. Sci. Discuss. [preprint]*. DOI: 10.5194/wes-2026-23.
- Petrović, Vlaho and Carlo L. Bottasso (2017). 'Wind turbine envelope protection control over the full wind speed range'. In: *Renewable Energy* 111, pp. 836–848. ISSN: 09601481. DOI: 10.1016/j.renene.2017.04.021.
- Pettas, Vasilis, Matthias Kretschmer, Andrew Clifton and Po Wen Cheng (2021). 'On the effects of inter-farm interactions at the offshore wind farm Alpha Ventus'. In: *Wind Energy Science* 6.6, pp. 1455–1472. DOI: 10.5194/wes-6-1455-2021.
- Pusch, Manuel, David Stockhouse, Nikhar Abbas, Mandar Phadnis and Lucy Pao (2024). 'Optimal operating points for wind turbine control and co–design'. In: *Wind Energy* 27.11, pp. 1286–1301. ISSN: 10954244. DOI: 10.1002/we.2879.
- Qin, Chao, Eric Loth, Daniel S. Zalkind, Lucy Y. Pao, Shulong Yao, D. Todd Griffith, Michael S. Selig and Rick Damiani (2020). 'Downwind coning concept rotor for a 25

- MW offshore wind turbine'. In: *Renewable Energy* 156, pp. 314–327. ISSN: 09601481. DOI: 10.1016/j.renene.2020.04.039.
- Ribnitzky, Daniel (2023). *Hybrid-Lambda Rotor (low specific rating offshore wind turbine) - simulation model: Zenodo [data set]*. DOI: 10.5281/zenodo.10406459.
- (2025a). *Dataset: Experimental investigation of wind turbine controllers for the Hybrid-Lambda Rotor: Zenodo [data set]*. DOI: 10.5281/zenodo.16598897.
- (2025b). *Hybrid-Lambda model turbine - blade geometry, openFAST model and wake measurement data: Zenodo [data set]*. DOI: 10.5281/zenodo.14883915.
- Ribnitzky, Daniel, Frederik Berger and Martin Kühn (2022). 'Innovative aerodynamic rotor concept for demand-oriented power feed-in of offshore wind turbines'. In: *Journal of Physics: Conference Series* 2265.3, p. 032017. ISSN: 1742-6588. DOI: 10.1088/1742-6596/2265/3/032017.
- Ribnitzky, Daniel, Frederik Berger, Vlaho Petrović and Martin Kühn (2024a). 'Hybrid-Lambda: a low-specific-rating rotor concept for offshore wind turbines'. In: *Wind Energy Science* 9.2, pp. 359–383. DOI: 10.5194/wes-9-359-2024.
- Ribnitzky, Daniel, Pietro Bortolotti, Emmanuel Branlard and Martin Kühn (2023). 'Rotor and wake aerodynamic analysis of the Hybrid-Lambda concept - an offshore low-specific-rating rotor concept'. In: *Journal of Physics: Conference Series* 2626.1, p. 012008. ISSN: 1742-6588. DOI: 10.1088/1742-6596/2626/1/012008.
- Ribnitzky, Daniel, Vlaho Petrović and Martin Kühn (2025). 'A scaling methodology for the Hybrid-Lambda Rotor – characterization and validation in wind tunnel experiments'. In: *Wind Energy Science* 10.7, pp. 1329–1349. DOI: 10.5194/wes-10-1329-2025.
- (2026). 'Experimental investigation of wind turbine controllers for the Hybrid-Lambda Rotor'. In: *Wind Energy Science* 11.2, pp. 469–491. DOI: 10.5194/wes-11-469-2026.
- Ribnitzky, Daniel, Sören Voß, Anna Rode, Mareille Wynants, Jann-Eike Saathoff, Khaled Yassin, David Märtings, Daniel Schuster, Normann Goldau, Lars Neuhaus, Jannik Meyer, Edgar Werthen, Matthias Wächter, Clemens Hübler, Raimund Rolfes, Claudio Balzani, Arndt Hildebrandt, Joachim Peinke, Torsten Schlurmann, Boso Schmidt and Martin Kühn (2024b). *Design Basis Offshore Megastructures - CRC 1463: Zenodo [data set]*. DOI: 10.5281/zenodo.10666475.
- Schepers, J. P. and H. Snel (2008). 'Model Experiments in Controlled Conditions - Final Report'. In: *Energy research Center of the Netherlands (ECN), Tech. rep. ECN-E-07-042, Petten*. URL: <https://publications.tno.nl/publication/34628817/8d6E4g/e07042.pdf> (visited on 01/08/2025).

- Schlipf, David, Dominik Johannes Schlipf and Martin Kühn (2013). 'Nonlinear model predictive control of wind turbines using LIDAR'. In: *Wind Energy* 16.7, pp. 1107–1129. ISSN: 10954244. DOI: 10.1002/we.1533.
- Schmitz, G. (1955/56). 'Theorie und Entwurf von Windrädern optimaler Leistung (Theory and design of windwheels with an optimum performance)'. In: *Wiss. Zeitschrift der Universität Rostock, 5. Jahrgang*.
- Schneemann, Jörg, Andreas Rott, Martin Dörenkämper, Gerald Steinfeld and Martin Kühn (2020). 'Cluster wakes impact on a far-distant offshore wind farm's power'. In: *Wind Energy Science* 5.1, pp. 29–49. DOI: 10.5194/wes-5-29-2020.
- Schottler, J., A. Hölling, J. Peinke and M. Hölling (2016). 'Design and implementation of a controllable model wind turbine for experimental studies'. In: *Journal of Physics: Conference Series* 753, p. 072030. ISSN: 1742-6588. DOI: 10.1088/1742-6596/753/7/072030.
- Shaler, Kelsey, Emmanuel Branlard and Andrew Platt (2020). 'OLAF User's Guide and Theory Manual'. In: *National Renewable Energy Laboratory, NREL/TP-5000-75959*. DOI: 10.2172/1659853.
- Simpson, Juliet, Eric Loth and Katherine Dykes (2020). 'Cost of Valued Energy for design of renewable energy systems'. In: *Renewable Energy* 153, pp. 290–300. ISSN: 09601481. DOI: 10.1016/j.renene.2020.01.131.
- Sinner, Michael, Vlaho Petrovic, Apostolos Langidis, Lars Neuhaus, Michael Holling, Martin Kuhn and Lucy Y. Pao (2022). 'Experimental Testing of a Preview-Enabled Model Predictive Controller for Blade Pitch Control of Wind Turbines'. In: *IEEE Transactions on Control Systems Technology* 30.2, pp. 583–597. ISSN: 1063-6536. DOI: 10.1109/TCST.2021.3070342.
- Sinner, Michael, Vlaho Petrović, David Stockhouse, Apostolos Langidis, Manuel Pusch, Martin Kühn and Lucy Y. Pao (2023). 'Insensitivity to propagation timing in a preview-enabled wind turbine control experiment'. In: *Frontiers in Mechanical Engineering* 9. DOI: 10.3389/fmech.2023.1145305.
- Soltani, Mohsen Nourbakhsh, Torben Knudsen, Mikael Svenstrup, Rafael Wisniewski, Per Brath, Romeo Ortega and Kathryn Johnson (2013). 'Estimation of Rotor Effective Wind Speed: A Comparison'. In: *IEEE Transactions on Control Systems Technology* 21.4, pp. 1155–1167. ISSN: 1063-6536. DOI: 10.1109/TCST.2013.2260751.
- Soto-Valle, Rodrigo, Sirko Bartholomay, Jörg Alber, Marinos Manolesos, Christian Navid Nayeri and Christian Oliver Paschereit (2020). 'Determination of the angle of attack on a research wind turbine rotor blade using surface pressure measurements'. In: *Wind Energy Science* 5.4, pp. 1771–1792. DOI: 10.5194/wes-5-1771-2020.

- Sprague, M. A., S. Ananthan, G. Vijayakumar and M. Robinson (2020). 'ExaWind: A multifidelity modeling and simulation environment for wind energy'. In: *Journal of Physics: Conference Series* 1452.1, p. 012071. ISSN: 1742-6588. DOI: 10.1088/1742-6596/1452/1/012071.
- Swisher, Philip, Juan Pablo Murcia Leon, Juan Gea-Bermúdez, Matti Koivisto, Helge Aagaard Madsen and Marie Münster (2022). 'Competitiveness of a low specific power, low cut-out wind speed wind turbine in North and Central Europe towards 2050'. In: *Applied Energy* 306, p. 118043. ISSN: 03062619. DOI: 10.1016/j.apenergy.2021.118043.
- Wang, Chengyu, Filippo Campagnolo, Helena Canet, Daniel J. Barreiro and Carlo L. Bottasso (2021). 'How realistic are the wakes of scaled wind turbine models?' In: *Wind Energy Science* 6.3, pp. 961–981. DOI: 10.5194/wes-6-961-2021.
- Werthen, Edgar and Daniel Ribnitzky (2024). *CRC1463 Initial digital twin - 25MW Wind Turbine CRC-25-310: Zenodo [data set]*. DOI: 10.5281/zenodo.10694008.
- Werthen, Edgar, Daniel Ribnitzky, David Zerbst, Martin Kühn and Christian Hühne (2023). 'Aero-structural coupled optimization of a rotor blade for an upscaled 25 MW reference wind turbine'. In: *Journal of Physics: Conference Series* 2626.1, p. 012012. ISSN: 1742-6588. DOI: 10.1088/1742-6596/2626/1/012012.
- Wiser, Ryan, Dev Millstein, Mark Bolinger, Seongeun Jeong and Andrew Mills (2021). 'The hidden value of large-rotor, tall-tower wind turbines in the United States'. In: *Wind Engineering* 45.4, pp. 857–871. ISSN: 0309-524X. DOI: 10.1177/0309524X20933949.
- Wiser, Ryan, Zhenbin Yang, Maureen Hand, Olav Hohmeyer, David Infield, Peter H. Jensen, Vladimir Nikolaev, Mark O'Malley, Graham Sinden and Arthouros Zervos (2011). 'Wind Energy. In IPCC Special Report on Renewable Energy Sources and Climate Change Mitigation'. In: *Cambridge University Press*, pp. 535–608. DOI: 10.1017/CBO9781139151153.011.
- Wobben, Aloys (2001). 'Rotor blade for a wind power installation, international patent: WO 01/48377 A1'. Pat.
- Yang, Xiaolei, Aaron Boomsma, Fotis Sotiropoulos, Brian Resor, David Maniaci and Christopher Kelley (2015). 'Effects of spanwise blade load distribution on wind turbine wake evolution'. In: *AIAA SciTech* 2015-0492. DOI: 10.2514/6.2015-0492.

List of publications

Publications this thesis is based on

Journal peer-reviewed publications

- Daniel Ribnitzky, Frederik Berger, Vlaho Petrović and Martin Kühn (2024a). ‘Hybrid-Lambda: a low-specific-rating rotor concept for offshore wind turbines’. In: *Wind Energy Science* 9.2, pp. 359–383. DOI: 10.5194/wes-9-359-2024
Reproduced in accordance to the Creative Commons Attribution 4.0 License.

Author contributions: DR realized and implemented the idea of the Hybrid-Lambda Rotor, added the conceptual idea of the change in the angle of attack and axial induction distribution, carried out the investigations and wrote the paper. FB assisted in developing the conceptual idea of the rotor concept. VP realized the initial controller for the OpenFAST model and supervised further controller developments. MK suggested the conceptual idea of designing a low-specific-rating rotor for two TSRs, contributed with fruitful discussions from an early planning stage and supervised the investigations. All co-authors thoroughly reviewed the paper.

The content of this paper is reproduced in Chapter 2.

- Daniel Ribnitzky, Vlaho Petrović and Martin Kühn (2025). ‘A scaling methodology for the Hybrid-Lambda Rotor – characterization and validation in wind tunnel experiments’. In: *Wind Energy Science* 10.7, pp. 1329–1349. DOI: 10.5194/wes-10-1329-2025
Reproduced in accordance to the Creative Commons Attribution 4.0 License.

Author contributions: DR developed the scaling methodology, designed the Hybrid-Lambda model turbine blades, conducted the experiments and simulations, post-processed the data and wrote the paper, VP supervised the experiments and the post-processing, MK contributed with effective discussions to the scaling

methodology and to the blade design and supervised the investigations. All co-authors thoroughly reviewed the paper.

The content of this paper is reproduced in Chapter 4

- Daniel Ribnitzky, Vlaho Petrović and Martin Kühn (2026). 'Experimental investigation of wind turbine controllers for the Hybrid-Lambda Rotor'. In: *Wind Energy Science* 11.2, pp. 469–491. DOI: 10.5194/wes-11-469-2026

Author contributions: DR developed the control methodology for the Hybrid-Lambda Rotor; realized the controller versions on the real-time platform for the model turbine; planned, conducted and post-processed the experiments and wrote the paper. VP initiated the torque control concept for the Hybrid-Lambda Rotor; supervised the controller development and assisted in the controller tuning during the wind tunnel experiments. MK contributed to the control methodology with supporting discussions and supervised the investigations. All co-authors thoroughly reviewed the paper.

The content of this paper is reproduced in Chapter 5.

Conference peer-reviewed publications

- Daniel Ribnitzky, Pietro Bortolotti, Emmanuel Branlard and Martin Kühn (2023). 'Rotor and wake aerodynamic analysis of the Hybrid-Lambda concept - an offshore low-specific-rating rotor concept'. In: *Journal of Physics: Conference Series* 2626.1, p. 012008. ISSN: 1742-6588. DOI: 10.1088/1742-6596/2626/1/012008

Reproduced in accordance to the Creative Commons Attribution 3.0 License.

Author contributions: DR realized and implemented the idea of the Hybrid-Lambda Rotor. DR set-up the simulation models, carried out the investigations and wrote the paper. PB and EB supported the model set-up and post-processing and contributed with purposeful discussions. MK supervised the investigations and suggested the conceptual idea of a low-specific-rating rotor. All co-authors thoroughly reviewed the paper.

The content of this paper is reproduced in Chapter 3.

Further publications

Conference peer-reviewed publications

- Daniel Ribnitzky, Frederik Berger and Martin Kühn (2022). ‘Innovative aerodynamic rotor concept for demand-oriented power feed-in of offshore wind turbines’. In: *Journal of Physics: Conference Series* 2265.3, p. 032017. ISSN: 1742-6588. DOI: 10.1088/1742-6596/2265/3/032017
- Edgar Werthen, Daniel Ribnitzky, David Zerbst, Martin Kühn and Christian Hühne (2023). ‘Aero-structural coupled optimization of a rotor blade for an upscaled 25 MW reference wind turbine’. In: *Journal of Physics: Conference Series* 2626.1, p. 012012. ISSN: 1742-6588. DOI: 10.1088/1742-6596/2626/1/012012
- Lars Neuhaus, Daniel Ribnitzky, Michael Hölling, Matthias Wächter, Kerstin Avila, Martin Kühn and Joachim Peinke (2024). ‘Model wind turbine performance in turbulent–non-turbulent boundary layer flow’. In: *Journal of Physics: Conference Series* 2767.4, p. 042018. ISSN: 1742-6588. DOI: 10.1088/1742-6596/2767/4/042018
- D. Onnen, L. Neuhaus, V. Petrović, D. Ribnitzky and M. Kühn (2024). ‘Dynamic wake conditions tailored by an active grid in the wind tunnel’. In: *Journal of Physics: Conference Series* 2767.4, p. 042038. DOI: 10.1088/1742-6596/2767/4/042038

Further conference publications

- C. Huebler, B. Schmidt, S. Voß, C. Hente, C. Gebhardt, D. Ribnitzky and R. Rolfes (2022). ‘Entwurf von Offshore-Windenergieanlagen neuer Größenordnung als Grundpfeiler unserer zukünftigen Energieversorgung’. In: 26. *Dresdner Baustatik Seminar (14.10.2022), Conference Paper*. URL: https://www.researchgate.net/publication/364751477_Entwurf_von_Offshore_-_Windenergieanlagen_neuer_Grossenordnung_als_Grundpfeiler_unserer_zukunftigen_Energieversorgung (visited on 01/08/2025)

Conference presentations

- Daniel Ribnitzky, Martin Kühn: 'Offshore megastructures - innovative rotor concepts for demand-oriented power feed-in'. IEA task 37, low wind workshop, 24.09.2021
- Daniel Ribnitzky, Martin Kühn: 'Innovative rotor concept for demand-oriented power feed-in'. EAWC PhD Seminar, Porto, 03.11.2021
- Daniel Ribnitzky, Frederik Berger and Martin Kühn (2022). 'Innovative aerodynamic rotor concept for demand-oriented power feed-in of offshore wind turbines'. In: *Journal of Physics: Conference Series* 2265.3, p. 032017. ISSN: 1742-6588. DOI: 10.1088/1742-6596/2265/3/032017, The Science of Making Torque from Wind, Delft, 12.05.2022
- Daniel Ribnitzky, Pietro Bortolotti, Emmanuel Branlard and Martin Kühn (2023). 'Rotor and wake aerodynamic analysis of the Hybrid-Lambda concept - an offshore low-specific-rating rotor concept'. In: *Journal of Physics: Conference Series* 2626.1, p. 012008. ISSN: 1742-6588. DOI: 10.1088/1742-6596/2626/1/012008, Poster at EERA DeepWind conference, Trondheim, 19.01.2023
- Daniel Ribnitzky, Pietro Bortolotti, Emmanuel Branlard, Vlaho Petrović, Martin Kühn: 'Wake deployment and wind farm value of the Hybrid-Lambda low-specific-rating offshore wind turbine'. Wind energy science conference, Glasgow, 26.05.2023
- Daniel Ribnitzky, Vlaho Petrović, Martin Kühn: 'The Hybrid-Lambda rotor: A concept overview and wind tunnel validations'. EAWC PhD Seminar, Hannover, 07.09.2023
- Daniel Ribnitzky, Vlaho Petrović, Martin Kühn: 'Rotor concept for demand-driven power feed-in of offshore wind turbines - The Hybrid-Lambda Rotor concept'. Wind physics symposium, Oldenburg, 14.06.2024
- Daniel Ribnitzky, Vlaho Petrović, Martin Kühn: 'Advancements on the Hybrid-Lambda blade design and control methodology'. EAWC PhD Seminar, Visby, 24.09.2024
- Daniel Ribnitzky, Johannes Paulsen, Lars Neuhaus, Vlaho Petrović, Martin Kühn: 'The Hybrid-Lambda rotor design and control methodology - Enabling low-

specific-rating offshore wind energy'. IEA task 55 systems engineering workshop, Roskilde, 03.12.2024

- Daniel Ribnitzky, Iván Herráez, Vlaho Petrović, Martin Kühn: 'Near-wake and rotor aerodynamics of the Hybrid-Lambda Rotor in wind tunnel experiments'. Wind energy science conference, Nantes, 25.06.2025

Code and data availability

- Daniel Ribnitzky (2023). *Hybrid-Lambda Rotor (low specific rating offshore wind turbine) - simulation model: Zenodo [data set]*. DOI: 10.5281/zenodo.10406459
- Daniel Ribnitzky, Sören Voß, Anna Rode, Mareille Wynants, Jann-Eike Saathoff, Khaled Yassin, David Märtns, Daniel Schuster, Normann Goldau, Lars Neuhaus, Jannik Meyer, Edgar Werthen, Matthias Wächter, Clemens Hübler, Raimund Rolfes, Claudio Balzani, Arndt Hildebrandt, Joachim Peinke, Torsten Schlurmann, Boso Schmidt and Martin Kühn (2024b). *Design Basis Offshore Megastructures - CRC 1463: Zenodo [data set]*. DOI: 10.5281/zenodo.10666475
- Daniel Ribnitzky (2025b). *Hybrid-Lambda model turbine - blade geometry, openFAST model and wake measurement data: Zenodo [data set]*. DOI: 10.5281/zenodo.14883915
- Daniel Ribnitzky (2025a). *Dataset: Experimental investigation of wind turbine controllers for the Hybrid-Lambda Rotor: Zenodo [data set]*. DOI: 10.5281/zenodo.16598897
- Edgar Werthen and Daniel Ribnitzky (2024). *CRC1463 Initial digital twin - 25MW Wind Turbine CRC-25-310: Zenodo [data set]*. DOI: 10.5281/zenodo.10694008

Acknowledgements

First of all, I would like to thank my supervisor and first referee Prof. Dr. Martin Kühn for granting me the opportunity to carry out this most interesting research in the highly proficient and lively research group Wind Energy Systems at the Institute of Physics, University of Oldenburg and part of ForWind. His encouragement to think out of the box, the countless fruitful discussions and his supportive supervision contributed substantially to the outcome of this work. I am also grateful to Dr. Vlaho Petrović, my second supervisor, for guiding me along the path of control theory and his motivating support in the preparation and execution of the numerous wind tunnel measurement campaigns. Furthermore, I want to thank the second referee, Prof. Dr. Gerard Schepers, for the effort to review this thesis.

During my PhD, I had the outstanding opportunity of a three-month research exchange with the National Renewable Energy Laboratory in Boulder, Colorado. My sincere thanks go to Dr. Pietro Bortolotti for initiating this research visit and for his dedicated supervision, from which I learned a lot. Furthermore, I would like to thank the colleagues in the US, namely Prof. Emmanuel Branlard, Dr. Garret Barter, Dr. Daniel Zahlkind and Prof. Dr. Lucy Pao for their support and patient answers to my countless questions.

Scaling the rotor and designing the blades for the model turbine in the wind tunnel would not have been possible without the guidance from Dr. Frederik Berger who substantially helped me to familiarize with the topic in the early stage of my research. For the majority of this period I had the honour to share an office with David Onnen. Not only his outstanding humour, but also his helpful advice whenever something did not go to plan in the wind tunnel, and our countless scientific discussions made this time quite enjoyable.

I thank all my colleagues at ForWind, in particular Thomas Messmer, Gabriele Centurelli, Dr. Lars Neuhaus, Dr. Tom Wester, Dr. Michael Hölling, Apostolos Langidis, Johannes Paulsen, Raghawendra Joshi, Manuel Zúñiga and Dr. Hendrik Heißelmann for either bringing me forward in scientific questions, providing constructive feedback

or helping in the preparation and execution of wind tunnel experiments. Further, the collaborative research centre 'Offshore Megastructures' built an excellent working environment and I want to thank in particular Edgar Werthen and Dr. Claudio Balzani for the fruitful cooperation. All those small supportive puzzle pieces built an excellent foundation for this work. I also enjoyed working with Calvin Schrader and Johannes Seesing who supported me as students with manual work in the wind tunnel and by carrying out helpful simulation studies.

Furthermore, I appreciate the financial support given by the Deutsche Forschungsgemeinschaft (DFG, German Research Foundation) which funded the project Offshore Megastructures (Project-ID 434502799 – SFB 1463).

Finally, I am deeply thankful to my parents who have opened up all the marvellous opportunities on my way here. Thank you, Martina and Peter for your love and for the life I love to live!

Curriculum Vitae

Personal information:

Name Daniel Ribnitzky
Place of birth Herrenberg, Germany

Education:

10/2017 – 04/2020 Master study „Mechanical and Process Engineering“
TU Darmstadt, Germany
10/2013 – 08/2016 Bachelor study „Mechanical and Process Engineering“
TU Darmstadt, Germany
2003 – 2012 High School Diploma (Abitur)
Gymnasium Neureut, Karlsruhe, Germany

Scientific experience:

10/2020 – 12/2025 Doctoral Candidate in group Wind Energy Systems
Carl von Ossietzky University Oldenburg
Supervision: Prof. Dr. Martin Kühn

Work Experience:

- 02/2021 – 12/2025 Research Assistant in group Wind Energy Systems
Carl von Ossietzky University Oldenburg
Project CRC 1463 Offshore Megastructures: Aerodynamically adaptive rotor concepts for very large offshore wind turbines.
- 10/2020 – 02/2021 Research Assistant in group Wind Energy Systems
Carl von Ossietzky University Oldenburg
Project WindRamp: Investigation of short-term forecasts for offshore wind power with lidar measurements.
- 10/2017 – 10/2019 Scientific assistant (working student) at the institute of aerodynamics, TU Darmstadt

Erklärung

Ich erkläre hiermit, dass

- (a) eine Promotion zum Dr.-Ing. angestrebt wird,
- (b) ich diese Arbeit selbständig verfasst und nur die angegebenen Hilfsmittel benutzt habe, und dass die Arbeit in Teilen bereits veröffentlicht bzw. zur Veröffentlichung eingereicht wurde,
- (c) diese Dissertation weder in ihrer Gesamtheit noch in Teilen einer anderen Hochschule zur Begutachtung in einem Promotionsverfahren vorgelegen hat.

Oldenburg, 06.08.2025

.....
(Daniel Ribnitzky)

